GEOCHEMICAL STUDIES ON CUMULUS PHASES OF SOME LAYERED IGNEOUS ROCKS.

Charles Terence Williams B.Sc.

ABSTRACT

This thesis presents the results of an investigation into the non-equilibrium distribution of trace constituents as a function of crystal growth. The ultrabasic igneous complex of Rhum (Scotland) with its relative uniformity of mineral composition, but variety of mineral habits was used in the investigation.

For this, the distributions of elements of contrasting behaviour have been studied, and especially uranium which strongly partitions into the melt, and strontium, which partitions into the feldspar on fractional crystallisation of a basaltic magma.

The technique of fission track analysis for uranium is fully described, and further developments have been introduced in order to accurately map the inter- and intra-mineral uranium distributions in polished rock sections. Results of uranium, strontium, nickel and calcium concentrations in the cumulus phases olivine, clinopyroxene and plagioclase feldspar are given.

There is a good correlation between the partition coefficients of uranium and the morphologies of the major cumulus phases. Calculations of crystal growth rates for different olivine morphologies have been determined. On these observations, a model is proposed relating both the mode and variation in nucleation rates of the individual morphologies to the degree of supercooling of the melt. Data on other elements are presented to substantiate these arguments. It is shown that olivines of spinifex (harristic) type have grown at a relatively fast rate and not slowly as suggested by some workers. The mode of crystallisation of certain morphologies, as to whether by diffusion-controlled growth, or by interface-controlled growth is discussed.

The distributions of uranium and other geochemically compatible elements in the intercumulus minerals are described, and the results of reaction of the cumulus with the intercumulus material studied. Zirconolite (or zirkelite) is recorded in a terrestrial basic intrusion for the first time.

CONTENTS

LIST OF FIGURES

LIST OF PLATES

CHAPTER 1. INTRODUCTION

1.1. Aims of thesis

Early experimental work by Bowen clearly showed that many interdependent factors are involved in the crystallisation of minerals from silicate melts. These factors include the physico-chemical conditions prevailing at the onset of nucleation and during growth of the mineral (for example, the composition and degree of supersaturation and supercooling of the melt), and the extent to which variations in these conditions affect the morphology and chemical composition of the mineral. Before attempts can be made to elucidate the role that each plays, geochemical, textural and experimental data need to be accumulated. Any proposed model of crystal growth must adequately account for these observations.

In an attempt to provide more of these required data, the work for this thesis was done. There were two principal aims. Firstly, to contribute some knowledge to the distribution of trace constituents in accumulative rocks of basic igneous intrusions, using as an example, the layered igneous complex of Rhum (Inner Hebrides). Secondly, to examine the role of uranium as a potential indicator of crystal growth rates and mechanisms in igneous cumulates, and to discuss its behaviour in the late-stage crystallisation of basic igneous rocks.

1.1.1. The distribution of trace constituents

By combining geochemical and textural data with published experimental observations, the intermineral partitioning of certain trace constituents has been studied as a function of the nucleation, supercooling and growth rates of the mineral phases, and their observed crystal morphologies.

In theoretical models that describe the crystallisation of minerals from silicate melts, the assumption is often incorporated that equilibrium conditions existed throughout the crystallisation process (e.g. Greenland, 1970). Crystallisation is, in itself, a combination of three basic operations:- a nucleation process (with an associated energy change designated $\Delta G_{nucleation}$); a growth process occurring at the crystal/melt interface ($\Delta G_{interface}$), and a diffusion process involving transport of heat and material away from, or towards the interface ($\Delta G_{diffusion}$). The growth rate (Y) of a mineral can then be represented by an overall expression:-

$$Y = f\ (\Delta G_{nucleation} + \Delta G_{interface} + \Delta G_{diffusion}).$$

where f is a constant for the particular system. However, both nucleation (e.g. Strickland-Constable, 1968) and growth processes at the interface (e.g. Kirkpatrick, 1974) require the existence of metastable, or disequilibrium conditions in the melt, thus apparently negating models based upon thermodynamical equilibrium conditions. A major reason why such models are often applicable (e.g. those of McIntire, 1963 and Albarede and Bottinga, 1972) lies in the fact that for most conditions observed in nature, the $\Delta G_{diffusion}$ factor predominates, and the diffusion coefficient (D) for the majority of elements in silicate melts is usually sufficient to maintain equilibrium conditions of growth. (Albarede and Bottinga, ibid., in fact recognised the need to take into consideration kinetic disequilibrium, but based their models on thermodynamical equilibrium conditions - i.e. constant partition coefficients for elements during crystal growth).

The degree and extent of the supercooling of the melt can be related to both the energy processes involved in crystal

growth (e.g. Tiller, 1970), and the rate of crystal growth (Tammann, 1925). When therefore, increasing energy contributions to the system are made from the nucleation and crystal/melt interface processes, expressed in terms of variations in the supercooling, then the resulting growth rate will deviate increasingly from the "equilibrium" rate allowed by element diffusion. The outcome will be that the observed partition coefficients for these elements will no longer be equal to their equilibrium partition coefficients. Hart and Brooks (1974) and Sinha and Sastri (1969) have in fact reported variations in the observed partition coefficients in basalts, which they attribute to changes in crystal growth rates.

Lofgren (1974) noted that the morphologies of experimentally grown feldspars (and pyroxenes) depend markedly on the degree of supercooling in the melt. He observed a progression of morphologies from tabular (or equant) at low supercoolings, to acicular (or spherulitic) at high supercoolings. In the literature, there are reported many examples of morphological variations within one mineralogical type occurring in natural environments. Minerals with skeletal, dendritic or acicular morphologies are usually associated with rocks which have undergone rapid coolings, e.g. Drever and Johnston (1957) and Brett et al.(1971), whereas more equant or polyhedral morphologies are generally associated with slower cooling. Bryan (1972), observed a change in morphology from euhedral, equidimensional olivine and feldspar crystals in the inner (central) zone of a pillow lava, to a skeletal morphology at the outer rim. Morphologies similar to those from rapidly cooled rocks but occurring in deep seated rocks have, however been described. Donaldson et al.(1973) observed olivine with a spherulitic morphology in the Rhum basic intrusion. Donaldson '

(1974) compared the dendritic morphology of the harrisitic olivines from Rhum with Archaean spinifex textures (e.g. Nesbitt, 1971) and he discussed the possibility that rapid cooling is not an essential prerequisite for the formation of such textures, and that crystallisation from a highly supercooled magma may have been responsible.

In the light of these experimental and field observations, a study of the distribution of trace elements in minerals displaying a variety of crystal morphologies would prove instructive. Examples of such elements are uranium, strontium, nickel and calcium, and such minerals are olivine, feldspar and pyroxene. Uranium has the additional advantage in that it possesses a much slower diffusion rate, e.g. Seitz (1973,b) than most other elements which would suggest it to be a more sensitive indicator of variations in crystal growth rates. The Rhum layered igneous intrusion is particularly suitable for such a study in that there is present a wide variety of crystal morphologies, and, in addition, the major element compositions of the cumulus minerals are relatively constant (Brown, 1956).

1.1.2. Growth rates and mechanisms in cumulates - the role of uranium.

The recognition that large intrusive volumes of magma have consolidated by a process of crystal accumulation and that the resulting solidified body possesses characteristic textures, has led to the introduction of a specific nomenclature. Wager *et al.* (1960) termed such rocks *cumulates* - a shortened version of Bowen's (1928) term "accumulative rocks". In essence, cumulates are the product of accumulation of minerals (termed cumulus crystals) from a magma, either by a flotation, or a gravity settling process, and subsequently consolidated by crystallisation of the intercumulus magma.

Studies of the cumulates from the Stillwater Complex, Montana, U.S.A., (Hess, 1939) and the Skaergaard Intrusion, East Greenland (Wager and Deer, 1939) showed that post-depositional enlargement of cumulus crystals at the same temperature as at initial formation, was a frequent occurrence. Hess (ibid.) suggested that this could have resulted from diffusion of elements from the overlying magma, through the intercumulus liquid to growing crystals in the upper layers of the crystal pile, and that simultaneously, there was diffusion of unwanted material in the opposite direction. Such a diffusional overgrowth has been termed adcumulus growth (Wager et al.,1960), and rocks in which much adcumulus growth occurred, are called adcumulates. In the absence of adcumulus growth, the intercumulus liquid becomes trapped and crystallises as lower-temperature minerals or zones. Rocks of this nature are termed orthocumulates and are recognised texturally by the presence of lower-temperature zones around the original cumulus crystals, and/or the presence of late-stage crystallising minerals such as apatite, zircon etc. Rocks intermediate between these two cases are called mesocumulates.

Two other important textures have been recognised in cumulates giving additional rock types viz. heteradcumulates and crescumulates.

Heteradcumulate is the name given to a cumulate containing large unzoned poikilitic crystals of one or more minerals enclosing many smaller cumulus crystals. The poikilitic minerals have the same composition as their cumulus counterparts elsewhere in the intrusion. Such rocks are relatively common in the Rhum layered intrusion and are considered (e.g. Wager and Brown, 1968, p.267) to have developed in a manner similar to that proposed for adcumulus growth.

Crescumulates are recognised by the appearance of the predominant mineral displaying an elongated and branching habit. These crystals are often orientated with their longer axis parallel to the plane of layering - although Drever and Johnston (1972) report randomly orientated branching olivine crystals in the Rhum western layered series. Wager and Brown (1968 p.554) suggest that crescumulates have grown upwards from a carpet of cumulus crystals during temporary periods of magma stagnation. Specimens from the Harris Bay area (Rhum western layered series) have been studied in this work, and the olivine habit is described here as a harrisitic morphology. It should be noted that the term crescumulate has not gained general acceptance (e.g. Drever and Johnston ibid.).

In the Rhum layered series, a variety of cumulate rock types occur, the major cumulus minerals exhibiting a wide range of morphologies, but with essentially constant major element compositions. In olivine, for example, there is a marked development of contrasting morphologies, ranging from poikilitic (heteradcumulus olivine) through equant, rounded, irregular and tabular (cumulus olivine), to harrisitic (crescumulus olivine). From textural considerations, it would be unusual to expect that identical growth processes (and growth rates) produced such differing morphologies. The major element geochemistry however, shows no variation with morphological type, and in terms of the major elements, the growth of olivine in all of the above situations may be considered to have been controlled by a diffusion process. By studying the distribution of a low-partitioning trace element (i.e. an element which plays no significant role in the continued growth of the mineral), variations in the growth processes (or growth rates) may be detected. Since a low-

partitioning element is essentially "rejected" from a growing crystal, a build-up of that element adjacent to the crystal/melt interface occurs. If, in addition, the growth rate of the crystal is greater than the rate of diffusion of that element away from the interface, the element will become incorporated into the crystal in a non-equilibrium manner. The incorporation in this case, will be controlled not by a diffusion process, but by the rate of attachment at the interface. Thus, a more sensitive indicator of both the growth rate and growth mechanism would be a low-partitioning, slowly diffusing, trace element.

To test such a hypothesis, the distribution of uranium between various olivine morphologies was studied. The results show (chapters 3 and 4), that a correlation exists between the observed partition coefficients and the olivine (and to a lesser extent, plagioclase) morphologies.

The relative growth rates of the adcumulus, heteradcumulus and crescumulus producing processes have from time to time come under discussion. Using a simple model incorporating estimates of rates of crystal settling and packing of the cumulus minerals, Wager et al. (1960) calculated that a growth velocity of approximately 0.12 millimetres/day was necessary for the formation of adcumulates. Donaldson (1975) however, suggested a faster rate of the order of 0.45 millimetres/day for the Skaergaard adcumulates. Campbell (1968) in describing the Jimberlana layered cumulates, argued that the heteradcumulates of the intrusion crystallised more rapidly than did the adcumulates. Wadsworth (1961) proposed that the olivine crescumulates of Rhum grew at a comparatively rapid rate, whereas Donaldson (1974) favoured the idea of crystallisation of crescumulates from a highly supercooled magma.

Using a model proposed by Burton et al. (1953), the relative growth rates of the six olivine morphologies have been determined from the observed partition coefficients of uranium. The calculated growth rates agree well with experimentally grown olivines (Donaldson, 1975), and with the estimated growth rates from packing models (e.g. Wager et al. 1960 and Wager, 1963).

1.1.3. Late-stage crystallisation in cumulates - the behaviour of uranium.

Wager and Brown (1968) in discussing the Skaergaard intrusion, suggested that since uranium resided preferentially in the residual magma during crystallisation of a basic magma (e.g. Adams et al. 1959), its concentration within the rock would be a guide to the amount of trapped liquid, and hence the extent of adcumulus growth. Henderson (1970) used the term "mesostasis" to describe the trapped (or pore) material, and Henderson (ibid) and Henderson et al. (1971) calculated the amount of mesostasis in specimens from Skaergaard, Rhum and Bushveld cumulates using whole rock uranium concentrations. Henderson (1975) showed also that uranium could be used to determine the degree of fractionation efficiency within cumulates.

In relating the concentration of uranium to the amount of mesostasis in the cumulates, Henderson et al. (1971) showed that quite considerable variations can occur in volumes separated by only a few centimetres. This indicates that the mesostasis is not distributed homogeneously even in hand sized specimens, and an indication of the location of the uranium (and hence where mesostasis areas occur) in cumulates would prove instructive in relation to post-cumulus crystallisation processes.

The presence of late-stage crystallisation minerals from basic cumulate rocks is well documented. In Skaergaard for

example, a wide range of minerals such as zircon, apatite, quartz, chlorite etc., occur (Wager and Brown, 1968, p.52), these being considered as products of crystallisation from trapped magma. The behaviour of uranium in such an environment is discussed (chapter 5), and many features recorded from uranium - distribution studies of lunar rocks are seen also in the Rhum cumulates. Such features are the geochemical compatibility of uranium with Zr, P and Rare Earth Elements (e.g. Thiel et al., 1972), and the quite frequent appearance of unusual uranium-enriched phases such as baddeyelite (ZrO_2) and zirconolite ($CaZrTi_2O_7$) (or zirkelite - e.g. Lovering and Wark, 1971). In addition reports are presented of a uranium-concentration gradient in an apparantly unzoned ilmenite grain, and a concentric uranium distribution pattern within a large poikilitic chrome spinel grain.

1.2. The cumulates of the Rhum and Carlingford intrusions

The majority of specimens described in this thesis are from the eastern series of the layered igneous cumulates of Rhum (Inner Hebrides). Recently, a plea for the spelling "Rhum", to be reverted to its original form, i.e. "Rum", was made (Bruce, 1975). In fact, earliest geological references e.g. Judd (1874, 1885) and Harker (1908) use the Gaelic spelling "Rum", as do Phillips (1938) and Tomkeieff (1942). Tilley (1944) and Bailey (1945) changed the spelling to "Rhum", and in line with subsequent literature and with recent Ordnance Survey publications, this later Anglicized version (viz. Rhum) is used throughout this thesis.

The layered cumulates of both the eastern and western series of Rhum are Tertiary in age (Bailey, 1945), intrude into Pre-Cambrian (mainly Torridonian) rocks, are closely associated with bodies of eucrite and gabbro, and with separate complexes of felsite, granophyre and explosion breccia (Harker, 1908).

Brown (1956) was able to map 15 major rhythmic layers, termed "units", in the eastern part of the complex to a height of over 800 metres. The units are numbered sequentially upwards from 1 at the base of the exposed eastern series. Each unit consists of an olivine-rich rock (olivine-cumulate) at the base grading upwards to a plagioclase-rich rock (plagioclase-cumulate) at the top, with locally developed chrome-spinel seams occasionally seen at the junctions of units. Clinopyroxene occurs throughout the intrusion averaging 10 to 15 modal percentage. Orthopyroxene is rare or absent.

A significant feature of the complex is the constancy in composition of olivine, feldspar and clinopyroxene in the 15 units. To a slightly lesser extent, this lack of cryptic layering is mirrored in the western layered series described by Wadsworth (1961). The two series are separated by a north-south fault (the Long Loch fault), but Wager and Brown (1968) considered that they both originated in the same magma chamber. The total exposed thickness of the intrusion is probably more than the sum of the two series (i.e. greater than 2300 metres) since no layered units east and west of the fault can be equated (Wager and Brown, ibid.). Brown (1956) and Wager and Brown (ibid.) attributed the constancy in mineral composition throughout the intrusion, and the regularity of the layering, to each unit resulting from an influx of a fresh pulse of basaltic magma. The sub-crustal magma chamber was probably connected to an active sub-aerial volcano. A recent paper by Gibb (1976), discusses the possibility of the Rhum cumulates crystallising from a eucritic rather than a basaltic magma. This would eliminate some of the problems involved in expelling vast amounts of magma from the site of crystallisation, and provide a clearer understanding as

to the lack of cryptic variation within the original cumulus crystals. It does not however, detract from the theory regarding adcumulus (or heteradcumulus) growth mechanisms.

Although mineralogically there is little variation in the major cumulus minerals - olivine essentially Fo_{86-82} (chrysolite); plagioclase feldspar An_{88-84} (bytownite), and clinopyroxene $Ca_{44}Mg_{49}Fe_{7}$ (endiopside) - there are significant differences in the textures and morphologies of these phases. To a certain extent, these can be related to the cumulate rock type. Using the nomenclature of Wager et al. (1960), all five cumulate rock types occur in the layered series of Rhum, i.e. ortho-, meso-, ad-, heterad- and crescumulates. In the lower regions of each unit in the eastern series, olivine, as a cumulus phase exhibits an equant, rounded, irregular and tabular morphology, whereas plagioclase feldspar usually occurs intercumulus, enclosing many olivine crystals and possessing a poikilitic morphology. In the feldspar-cumulates higher up in each unit, the roles are reversed with plagioclase, a cumulus phase, having a tabular morphology, and olivine becoming more intercumulus and occasionally developing a poikilitic morphology. Clinopyroxene, in general, maintains a poikilitic morphology through this reversal, but is sometimes seen as a cumulus phase - in these latter cases, all three minerals are cumulus in origin.

Two field excursions to the eastern layered series were undertaken to obtain a collection of samples of various cumulate types from different units. The samples obtained from these excursions were then augmented with a batch of samples previously collected by Henderson in 1968.

Initially, a comparison of the Rhum cumulates with those from the Carlingford (Co. Louth) layered basic intrusion was

intended. Le Bas (1960) recognised the existence of four layers in this intrusion where, like Rhum the ratio of cumulus olivine to cumulus feldspar decreases upwards. Unlike Rhum however, the major minerals present i.e. olivine, plagioclase feldspar, clinopyroxene and orthopyroxene, show a quite substantial degree of cryptic variation within each layer. Examination of thin sections collected from a field excursion to Carlingford showed that, in addition, some degree of post-depositional tectonic activity had affected the intrusion. This manifested itself by the appearance of secondary serpentinisation and alteration, veining and microfaulting. Since uranium is a relatively labile element (e.g. Cherdyntsev, 1971), there exists the strong possibility that loss (or indeed introduction) of this element had occurred during the tectonic activity. These two factors meant that the Carlingford cumulates would not have provided suitable specimens regarding the aims of this thesis, where aspects of the primary crystallisation history, with emphasis on the distribution of uranium was investigated.

1.3. Selection of analytical techniques.

The major part of this thesis involved studying the distribution of uranium in minerals containing concentrations of that element at the sub-p.p.m. (10^{-9} gm/gm) level. The analytical technique chosen should incorporate several factors:-

(1) a high sensitivity,

(2) neither mineral separation nor sample decomposition,

(3) the ability to produce concentration gradients, and to locate areas within the rock enriched in uranium.

(1) A high sensitivity is required since greater than 95% of the minerals present in the Rhum cumulates (i.e. olivine,

plagioclase, clinopyroxene and chrome spinel) contain uranium concentrations of the order of a few p.p.b. Previously reported values for the olivines from various environments range from 0.2 p.p.b., (lherzolite inclusions, Kleeman et al.,1969) to 46 p.p.b. (dunites, Fisher, 1970); for plagioclase feldspar from 10 p.p.b. (lunar basalts, Thiel et al. 1972) to 43 p.p.b. (Bushveld cumulates, Gijbels et al.,1974); for clinopyroxene from 15 p.p.b. (lherzolite inclusions, Kleeman et al.,1969) to 60 p.p.b. (Rhum cumulates, Henderson et al.,1971), and for chrome spinel from 20 to 30 p.p.b. Gijbels et al. ibid.).

(2) The uses of a technique which does not require mineral separation is necessary for two reasons. Firstly, because outer rims of minerals are often removed during preliminary crushing of the sample; Henderson et al. (1971) reported that the outer rims of some zoned plagioclase feldspars from the lower units of the Rhum cumulates contained a higher uranium concentration than did the cores of the crystals. Secondly, contamination from micron-sized uraniferous inclusions (e.g. Thiel et al.,1972) becomes a possible (and serious) source of error using mineral separates.

(3) Since the research for this thesis included a study of the behaviour of uranium both within the intrusion as a whole (i.e. in terms of the late-stage crystallisation products), and within individual crystals (i.e. in terms of crystal growth behaviour), the chosen technique requires the ability to determine both intra- and inter-mineral uranium distributions.

The only analytical technique currently available which satisfied the above requirements is that of fission track (or particle track) analysis. Reviews by Fleischer et al.(1969) and Fisher (1975) have shown this technique to be readily

applicable to many of the natural sciences since it combines a relatively simple sample preparation with a high sensitivity (to sub-p.p.b. levels). The method used in this study, details of which are given in chapter 2, was based initially on the "Lexan print" technique of Kleeman and Lovering (1967 (a) and (b)). In outline the method is one of irradiating a polished section of the rock in contact with a detector capable of recording the induced fission fragments from the nuclear fission of ^{235}U, and comparing the number of resulting fission tracks with those from a substance of known uranium concentration.

A modification of Kleeman and Lovering's (ibid.) technique was introduced since a print of the rock surface on the detector was not obtained. This entailed producing a photographic record (contact print) of the detector, previously inscribed with a location grid, in place on the rock surface.

The potential improvement of having a print of the rock surface on the detector (as in Kleeman and Lovering, ibid.) would, nevertheless have simplified the above procedure, and reasons for not obtaining such a print are discussed. With the final irradiated batch of samples however, Lexan prints were formed and the reactor conditions for their production are given in Appendix 1.

In conjunction with fission track analysis, additional instrumental analytical techniques were employed - viz. electron probe microanalysis, (details given in chapter 2, section 2.8.) and to a lesser extent, x-ray fluorescence.

Electron probe microanalysis was used to determine the compositions of the major mineral phases and distributions of trace elements Ni and Ca in olivines (chapter 4, section 4.3.), and to detect whether any zoning was apparent in the minerals

(chapter 4, sections 4.3., 4.5, and 4.6.).

In studying the distribution of uranium in unusual late-stage crystallising minerals, a combination of fission track analysis (for locating) the high-uranium minerals, Scanning electron microanalysis (for identifying)the mineral and electron probe microanalysis (for a quantitative analysis) was used (chapter 5, section 5.4.).

An X-ray fluorescence analytical technique was used to determine concentrations of Sr in separated feldspars from differing cumulate rock types in the Rhum layered intrusion. A previous study of feldspars from the Rhum cumulates (Williams, 1971) showed a relationship between the Sr concentrations and the type of crystal growth. These results are detailed in Appendix 2, and a comparison is drawn between the Sr and U concentrations in the feldspar phases (chapter 4, section 4.5.).

CHAPTER 2 EXPERIMENTAL TECHNIQUES

1: URANIUM DISTRIBUTION MAPS

2.1. Introduction and Theory

Natural uranium consists of 3 isotopes; ^{234}U, ^{235}U, and ^{238}U, which all undergo spontaneous fission. The 238 and 235 isotopes are parent isotopes, and the 234 an intermediate product in the 238 decay series.

Of practical importance is the ability of these isotopes to undergo induced fission (see table 2.1). Under bombardment from "energetic" neutrons, the above isotopes fission to produce two highly-charged, fast-moving ions:-

$$\text{e.g. } {}^{235}_{92}U \xrightarrow{\text{thermal neutrons } {}^{1}_{0}n \text{ energy} < .5\text{MeV}} {}^{236}_{92}U \longrightarrow 82\text{-}100_X + 125\text{-}150_Y \text{ fission fragments}$$

$$+ 3 \text{ or } 4 \text{ neutrons} \qquad (1)$$

Table 2.1

Isotope	% abundance	$t_{\frac{1}{2}}$ (yrs) Spontaneous fission	induced fission capture cross-section (σ_f)	energy for fission (MeV)
234	.0056	2.5×10^5	.65 barns	.1 - 2
235	.72	7.1×10^8	5807 "	.01 - 2*
238	99.27	4.5×10^9	0.55 "	1
^{232}Th	100	1.4×10^{10}	.391 "	1

* neutrons with energy up to . 5 MeV are termed "thermal" . neutrons.

neutrons with energy > . 5 MeV are termed "fast" neutrons.

The fission fragments formed are unequal in mass (Katkoff, 1960), the most probable heavy mass of 139, and the most probable light mass of 95. The momentum of fission fragments

X and Y are equal and opposite, separating with kinetic energies of up to 150 MeV, and with initial charges as high as +16 (Chadderton and Torrens, 1969).

It has long been known that the passage of a fission fragment through an insulating material will produce localised damage, which, under certain conditions, can be detected (e.g. Silk and Barnes, 1959). Price and Walker (1962, a) chemically etched material which had been subjected to bombardment by fission tracks, and found that the rate of chemical attack was greater along the damaged paths, so making them visible (under suitable magnification) to the fission "tracks". For the wide range of insulating materials, in which the paths of energetic particles have been observed and can be microscopically revealed, Fleisher et al. (1964) collectively termed Solid State Nuclear Track Detectors (S.S.T.D.). They can broadly be divided into three groups:-

(a) Crystalline solids (including minerals)

(b) Amorphous solids (glasses)

(c) Organic polymer plastics.

2.1.1. Theory of fissioning

Bohr and Wheeler (1939) initially proposed a theory of fissioning based on the liquid drop model. The nucleus of the element is visualised as a spherical drop of liquid. On contact with a bombarding neutron, oscillations are set up producing an asymmetrical distribution of positively charged protons. The resulting repulsion can lead to a splitting of the nuclear drop (fig. 2.1). Since ^{235}U contains an odd number of neutrons, considerable energy is released when it gains a further neutron. This kinetic energy starts the disturbance within the nucleus that leads to fission. The ^{238}U and ^{232}Th isotopes already contain an even number of neutrons, and in this case collision with a fast neutron has to occur

(table 2.1), in order to bring considerable kinetic energy to the nucleus for fissioning to occur.

The liquid drop model is of course a simplified one and many modifications, particularly to account for defects in the prediction of certain events, have been proposed. In the liquid drop theory symmetrical splitting of the nucleus should occur, whereas in practice, asymmetrical splitting is observed (equation (1)). However, most theories explaining fission are at best semi-quantitative since adequate models of complex atomic nuclei do not, at the present, exist.

2.1.2. Theories of track formation

Observations showed that almost any energentic nuclei - including fission fragments - may produce narrow trails of radiation damage in insulating material (Fleischer et al. 1964). In addition, different materials (S.S.T.D.s) are sensitive to a variety of different nuclear particles, (Fleischer et al. 1967). Some organic detectors (e.g. cellulose nitrate) are able to detect low energy protons, deuterons and alpha particles, whereas in others - in general the inorganic detectors e.g. mica - only heavy, highly-charged nuclei are detected (Katz and Kobetich, 1968).

Any theory which attempts to explain (or predict) the production of latent particle tracks in S.S.T.D.'s must account for the following major characteristics (Fleischer et al.1965 a).

1) The damage region is narrow ($\simeq 50$ Å in diameter) and continuous atomically, or nearly so.
2) Tracks are not formed in metals or "good" semiconductors.
3) Different detectors have different threshold energies below which tracks are not revealed.
4) Tracks are highly stable and their fading is controlled by,

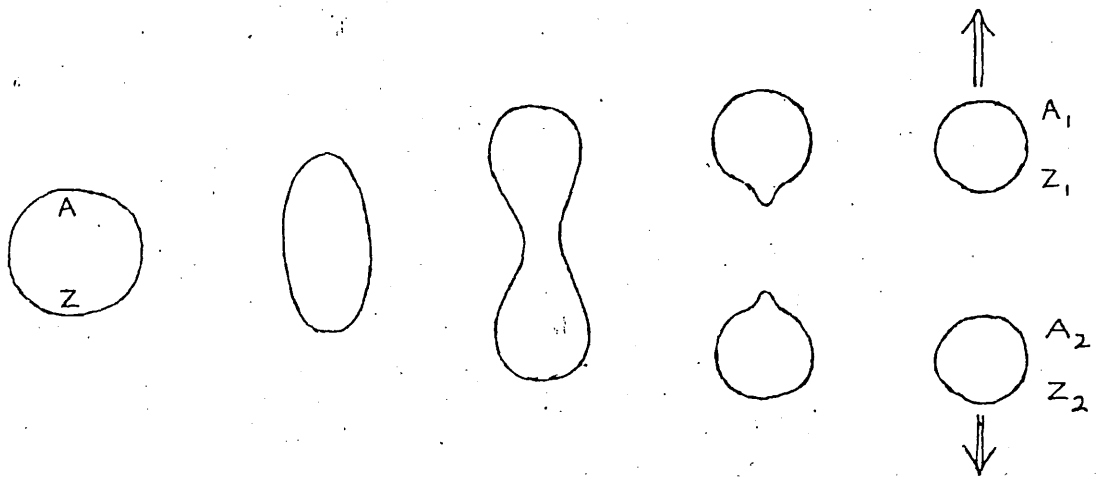

Figure 2.1. Schematic representation of the fission of a nucleus on the basis of the "liquid drop" model (from Chadderton and Torrens, 1969).

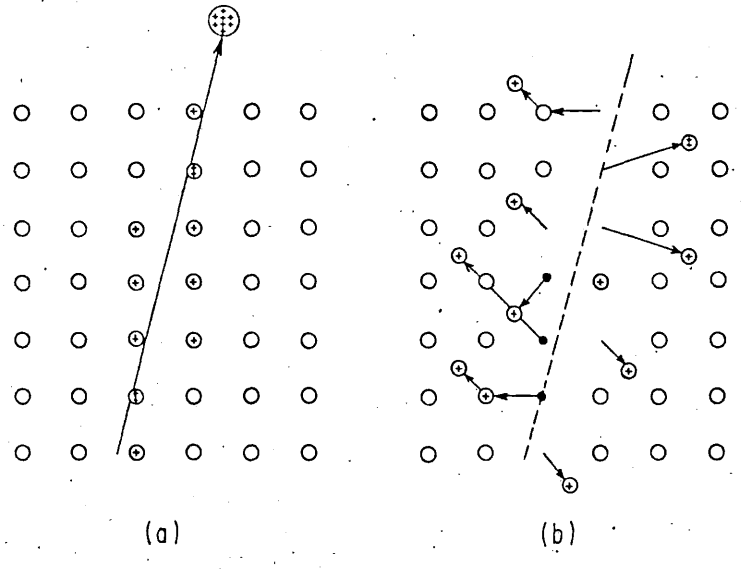

Figure 2.2. Ion-explosion spike model (from Fleischer et al., 1965, a).

the motion of atoms and not electronic defects. Parameters involving the incident particle, properties of the individual S.S.T.D., and etching procedure have similarly to be taken into account.

The energy processes involved to form a latent track, and damaging mechanisms in both inorganic and organic S.S.T.D.s are discussed below. However, a comprehensive theory for both inorganic and organic detectors has not been proposed.

2.1.2.1. Energy processes involved.

There are basically three energy processes involved in the formation of etchable tracks by energetic particles in S.S.T.D.s. These are:-

(a) Energy loss of the particle

(b) Transfer of energy from the particle to the detector.

(c) Production of damage in the detector caused by this energy such that the rate of chemical attack along the particle's track (R_t) is greater than the corresponding rate of attack of the bulk of the detector (R_b).

(a) A particle loses energy by three main methods. The principal mode of energy loss is due to interactions of the particle with atomic electrons (ionisation and excitation) of the medium in which the particle is travelling - $\left(-\frac{dE}{dx}\right)$ electronic. Less important, until the particle nears the end of its path, is the contribution to energy loss of the particle when in direct collision with the nuclei of the stopping medium - $\left(-\frac{dE}{dx}\right)_{\text{nuclear}}$. The third energy loss method, $\left(-\frac{dE}{dx}\right)_{\text{radiation}}$, is small in comparison with the others. Here loss of energy is by the emission of Bremsstrahling and Cerenkov radiation. The total rate of energy loss, or absolute stopping power, $\left(\frac{dE}{dx}\right)_{\text{total}}$, may then

be written:-

$$\left(-\frac{dE}{dx}\right)_{total} = \left(-\frac{dE}{dx}\right)_{electronic} + \left(-\frac{dE}{dx}\right)_{nuclear} + \left(-\frac{dE}{dx}\right)_{radiation}$$

(b) The transfer of energy from the incident particle to the detector can conveniently be divided into two types: energy absorption by the detector, and energy conversion within the detector to more specific modes.

Algar (1965) has shown that three modes of energy absorption exist: electron displacement (ionisation and excitation); nuclear displacement, and the generation of impurity atoms as a result of radiation damage. These correl ate with the three energy loss processes described above in (a), and, as in (a), the primary mechanism for energy absoption is considered to be electronic displacement. However, the probability of nuclear displacement as the particle nears the end of its path increases. The probability of energy transfer by nuclear radiation is small.

(c) Energy conversion within the detector produces the damage whereby the condition $R_t/R_b > 1$ exists, and an etchable track is formed. Energy is converted by means of molecular and atomic vibrations and may be emitted in the form of luminescence, or heat, or it may be stored as potential energy in the form of chemically reactive species. Luminescence accounts for only a few % of the total energy converted, some of which will in any case be locally absorbed. Heat accounts for the vast proportion of energy converted. The temperature in the immediate vicinity (a few Å) of the particle may exceed several hundred degrees C (Chadderton and Torrens, 1969), resulting in extensive atomic and molecular rearrangements. At these locally high temperatures, a small proportion of the energy may be stored as potential energy in the form of free electrons, free radicals and free ions,

perceptible to chemical attack, they being stabilized by a cage effect (an unbonded situation where a molecule, ion or radical is wholly or partly locked within the host crystal lattice).

Several models have been proposed by various authors to interpret the molecular and ionic arrangement produced by an energetic particle via energy-transfer and absorption in both inorganic and organic detectors. A brief résumé of these follows.

2.1.2. 2. Inorganic detectors.

Models for inorganic detectors revolve around a spike concept - large local amplitudes of vibration as a result of the deposition of a large amount of energy within a locally confined volume.

Fleischer et al.(1965,a) proposed an ion-explosion spike model. It is postulated that a charged particle produces within the detector a positively charged cylindrical region. Electrostatic repulsion of the positive ions occur forming a region locally rich in interstitial ions and vacancies (fig.2.2). The model predicts that tracks will not be formed in materials having (1) a high density of free electrons (i.e. in metals), (2) high hole mobilities (i.e. in good semi-conductors such as silicon and germanium). The predictions agree well with experiment.

The thermal spike model (Billington and Crawford, 1961) suggests that all the energy of the incident charged particle is coverted locally to heat. The charged particle interacts with electrons in the detector and sets the atoms in vibration. The vibrations are subsequently spread to neighbouring atoms by "Rutherford" collisions - mutual repulsions of similarly-charged particles. Temperatures in excess of 10^4 °C within a cylindrical volume of 100 Å radius and several millimetres in length can be attained within a time of the order of 10^{-1} seconds. This model corresponds in effect to energy transfer by electronic displacement

Brinkmann (1954,1959) proposed a displacement spike model whereby many interstitial and displaced atoms (and ions) are produced by "hard sphere" collisions (fig.2.3). Here energy transfer is by nuclear displacement both by atoms being "knocked on" by collision with the incident particle, and also by secondary (or higher order) displacements - the primary knocked on atom undergoing collision with neighbouring atoms thus initiating a cascade effect.

Chadderton and Torrens (1969) combined the latter two models to give a fission-spike model. They envisaged (fig.2.4). a gradual transition from Rutherford collisions of interatomic vibrations (thermal spike concept) to hard sphere collisions (displacement spike concept).

In general, for inorganic detectors, predictions by different models agree well with experimental observations. When applied to the more sensitive organic detectors though, agreement between predictions and observations is not so precise.

2.1.2.3. Organic detectors

Tracks in organic detectors are the result of broken chemical chains (and bonds) and the formation of free radicals and gas inclusions (Becker, 1968), schematically shown in fig.2.5. These may be attributed to electronic ionisation and excitation via energy transfer and absorption, in the region of the particle track.

A review of theories covering organic detectors has been published by Benton (1970). They all depend on there being a critical, or threshold, particle energy value characteristic of the detector. Katz and Kobetich (1968, 1970) favoured the formation of a track through the deposition of secondary electrons (δ-rays), in the particle's immediate vicinity producing local molecular fragmentation in the detector. An etchable track is then formed if sufficient fragmentation has occurred over a sufficiently large area to allow the etchant to pass freely along the damaged

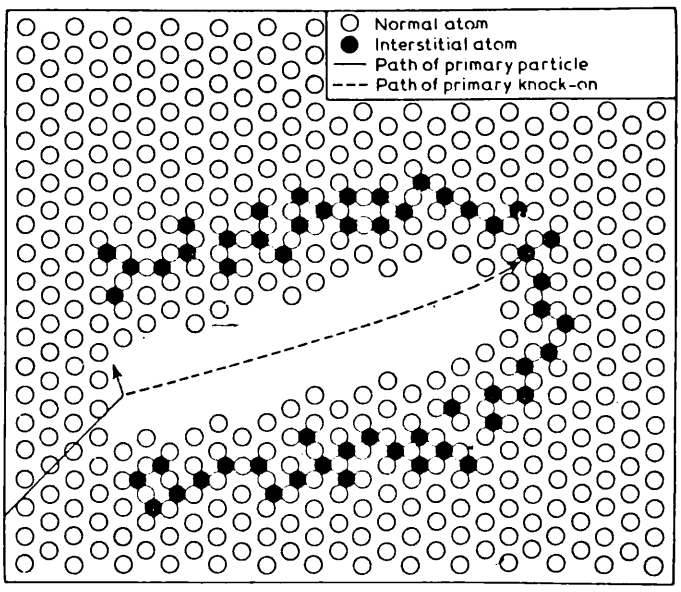

Figure 2.3. Displacement spike model (from Chadderton and Torrens, 1969).

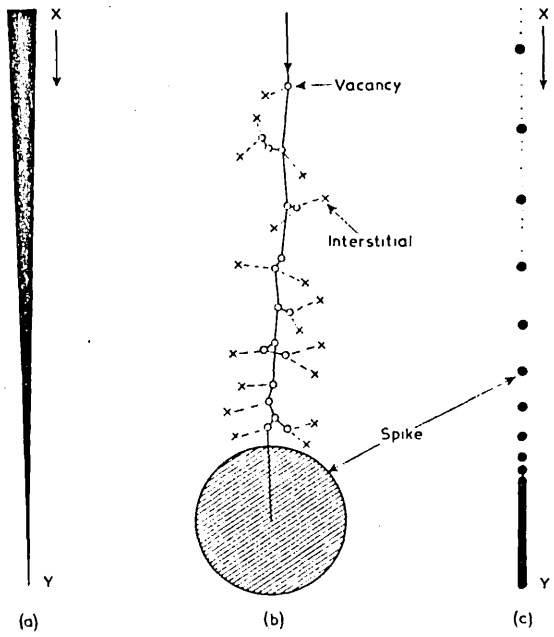

Figure 10. Schematic representation of the fission spike. (a) The fragment enters the crystal at X and comes to rest at the point Y. The intensity of the thermal spike at any point along this 'track' is given by the radius of a right circular cone (seen here in section) at that point. (b) Diagram showing the formation of a displacement spike by an energetic knock-on deriving from a collision between the fragment and a lattice atom. When the mean-free-path for atomic displacement falls below an interatomic distance a displacement spike is formed. (c) The frequency of displacement spike formation increases as the fragment slows down and there is a gradual transition from 'Rutherford' to 'hard sphere' collisions. The statistical nature of the frequency of collision events is considered to be understood and is omitted from the diagram.

Figure 2.4. Fission spike model (from Chadderton and Torrens, 1969).

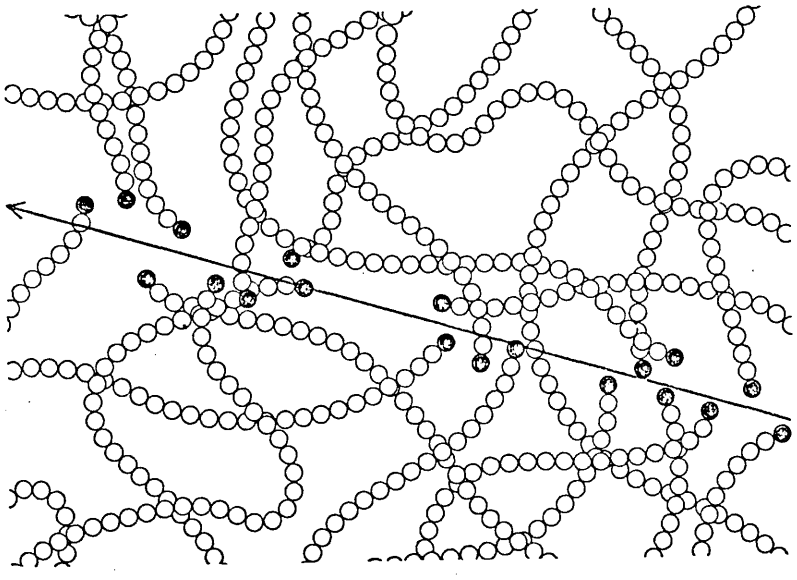

Figure 2.5. Schematic representation of Fission fragment entering an organic S.S.T.D. (from Becker, 1968).

trail. Primary ionisations or excitations within the detector are not, however, taken into account.

Fleischer et al. (1967) showed that there is a critical primary ionisation rate for a detector (R_{crit}), such that only particles having primary ionisation rates above this will produce etchable tracks. Price et al. (1968) found that for Lexan polycarbonate S.S.T.D., the rate of chemical etching of a track (R_t) increased exponentially with the ionisation rate of the particle (above the value R_{crit}). Theories based on primary ionisation rates however ignore secondary or δ-ray effects. It is likely then that contributions from both primary and secondary effects are necessary to the formation of etchable tracks.

2.1.3. Development of Particle Tracks.

Although latent tracks may be observed using both a Transmission Electron Microscope (Silk and Barnes, 1959) and a Scanning Electron Microscope (Burnett et al., 1970), the most widely used and simplest method of observation is by use of an optical microscope. Conversion from a latent particle track in a S.S.T.D. to a particle track which may be viewed optically necessitates enlargement, by chemical action, of the narrow radiation damaged trail.

The region of radiation damage (described above) is chemically more reactive than the bulk of the detector. Thus, when the detector is immersed in a solvent, the rate of chemical attack along the track (R_t) is greater than the rate of chemical attack perpendicular to the undamaged surface (R_b). The resulting etch figure is a hollow cylinder lying along the trajectory of the charged particle, and having ideally, a length close to the range of the particle. Upon attaining a diameter of size comparable to the wavelength of visible light (·4 to ·8 μ), the etch figure acts as a strong scattering centre appearing white in reflected

light and dark in transmitted light (fig. 2.6).

An important factor in chemical etching is the existance of a critical angle θ_c , the angle below which particles striking the S.S.T.D. will not be revealed by etching. Fleischer and Price (1964) showed that $\theta_c = \sin^{-1} R_b/R_t$,and that for some inorganic glasses, the value of θ_c can be as high as 50°. For S.S.T.D.'s such as Lexan, mica and makrofol, θ_c is very low (of the order of $2\text{-}5^\circ$). This in effect means that for the latter S.S.T.D.'s, a very high percentage of latent tracks will be revealed - i.e. the etching efficiency approaches unity.

Etching chemicals and conditions vary for individual detectors. A review by Fleischer and Hart(1970) details etching conditions for over 90 minerals, glasses and plastics. In general, minerals and glasses may be etched under acid (particularly HF) conditions, and plastics under alkali conditions.

Various environmental factors such as treatment of the detector with ultraviolet radiation (Benton and Henke, 1968) may influence the formation of tracks in S.S.T.D.'s either prior to, or after irradiation. Experiments performed have been aimed primarily at enhancing the sensitivity of the S.S.T.D. to detectlower energy particles, and to increasing the value of R_t with respect to R_b so as to improve the quality of the tracks. These are reviewed by Benton (1970).

2.1.4. Track Counting Procedures.

For quantitative work, the number of etch pits per unit area of detector is required. Previous workers have employed a variety of track counting procedures. Visual track counting using a microscope has, for much routine work, been superseded by automatic track counting procedures. Schultz (1968) measured the light scattered by fission tracks in a S.S.T.D. via a photomultiplier coupled with an amplifier. The scattered light was found to be proportional to the track density, up to a point

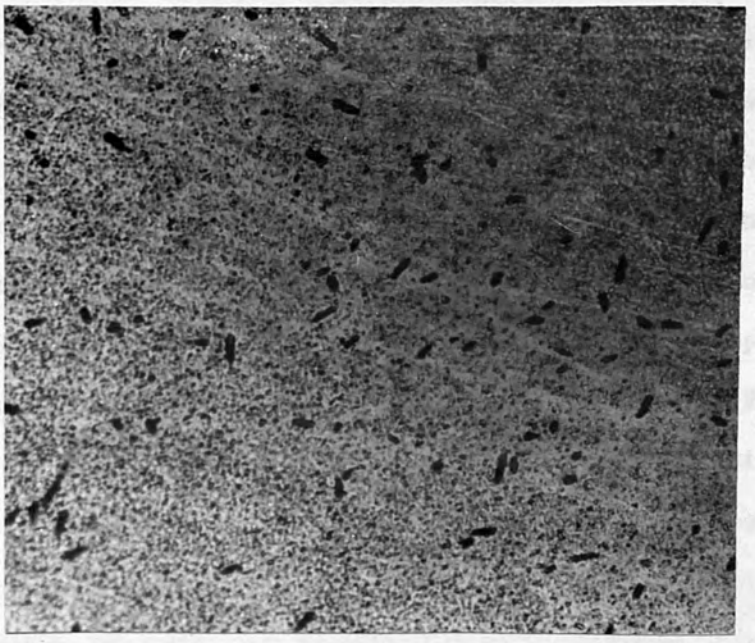

Figure 2.6. Fission tracks developed in makrofol - an organic S.S.T.D. - viewed in transmitted light.

where tracks overlap. Becker (1966) utilised the fact that under dark field illumination, tracks appeared bright on a dark background. The amount of light may then be measured by placing a photomultiplier at the location of the eyepiece. Again the photomultiplier reponse was proportional to the number of tracks. Besant and Ipsom (1970) counted tracks using an image analysing computer (Quantimet). The microscope image of the detector is monitored by a television camera to a cathode ray screen. On the basis of optical intensity, a discriminator unit selects those features which are to be counted. The threshold of detection may be varied to exclude background marks on the detector.

For measurement of low track densities, various techniques have been employed to enlarge a fission track such that it becomes visible to the naked eye. They all entail the use of S.S.T.D.'s thin enough to allow the etched track to penetrate through the detector so creating an etched "hole". Fleischer . (1966) coated one side of a thin film (15 μm) of organic S.S.T.D. with aluminium. The detector was then etched from the other side with NaOH solution. The etchant passed through the holes and dissolved relatively large areas of aluminium around the holes making them visible to the eye. Dye solutions that are forced through the fission holes onto filter paper is a technique used by Cross and Tommasinno (1967). These workers (ibid. 1969) also developed a method of rapid, automatic track counting by an electrical arrangement. An electrical discharge (or spark) is passed through the fission hole evaporating a corresponding hole in an adjacent thin aluminium sheet. The number of resulting pulses may be counted directly by a scaler, and the pattern of holes in the aluminium provides a visible replica of the pattern of tracks in the S.S.T.D.

High track densities (where automatic counting techniques are unsuitable because of overlapping of the tracks) have been

measured using a Scanning Electron Microscope (Seitz et al., 1973) with mica as the S.S.T.D.. When, however tracks are distributed inhomogeneously and over small areas, visual track counting with a microscope is usually employed. The magnification used depends on the shape and length of the track, and on the individual researcher. A considerable range in magnification from x300 to x2000 has been used, e.g. Nagpal et al. (1973) and Seitz et al.(1973).

2.1.5. Applications of S.S.T.D.'s to the Sciences.

In the last decade and a half, S.S.T.D.'s have been used extensively in several of the sciences. The advantages of S.S.T.D.'s are their ease of use; insensitivity to light; selectivity of charged particles from a high background of neutrons, X-rays and γ-rays; stability of tracks to severe environmental conditions (temperature and pressu re etc.), and a high track recording efficiency. Their applications are multifarious and include microanalysis (for uranium - e.g. Fleischer, 1968; for thorium - e.g. Hair et al., 1971; for boron - e.g. Carpenter, 1972, and for lithium - e.g. Kleeman, 1973); nuclear physics (e.g. Fleischer et al., 1969); geochronology (e.g. Hurford,1973); cosmology (e.g. Price et al., 1969); archeology (Fleischer et al., 1965c), and as evidence of extinct (e.g. Fleischer et al., 1965b) and "new" elements (Fleischer et al., 1969). Not least is their applicability in obtaining information regarding the distribution, within a rock specimen, of fissionable elements - viz. uranium-distribution maps (section 2.2.).

2.1.6. Quantitative aspects of the fission track technique.

The uranium or thorium content in a mineral may be determined quantitatively since the number of induced fission tracks produced is, for an isotope, proportional to the neutron dose. This can be represented by formula (2) below (from Kleeman and

Lovering, 1970) :-

$$(\rho i)_x = n.\sigma.I.(N)_y.K_{xy}.\alpha_x.g_x. \qquad \text{——————(2)}$$

where $(\rho i)_x$ = number of induced tracks per unit area observed on the etched surface of x.

n = neutron dose

I = isotopic abundance

σ = fission cross section of element (in barns)

$(N)_y$ = atomic density of the element in host phase y

K_{xy} = a geometric depth factor approximately equal to the range of the fission fragment in the host solid. (Fleischer et.al., 1967). Subscripts x and y denote tracks formed in y and recorded in x.

α_x = "the etching efficiency of order unity" (Fleischer ibid. p.334) of the detector.

g_x = a geometric factor (Kleeman and Lovering, ibid.), and is equal to 0.5 for tracks formed only on one side of the detector.

The concentration of an element (A) having a fissionable isotope (B) may, in a specimen, be determined if irradiated under identical conditions to a standard with known isotopic composition and content, when :-

$$\frac{(\rho i)_{stand.}}{(N)_A \text{ stand.}(N)_B \text{ stand.}} + \text{constant} = \frac{(\rho i)_{spec.}}{(N)_A \text{ spec.}(I)_B \text{ spec.}}$$

where $(\rho i)_{stand.}$ = n.° of induced tracks per unit area from isotope B in the standard.

$(\rho i)_{spec.}$ = n.° of induced tracks per unit area from isotope B in the specimen.

$(N)_A$ stand. = atomic density of element A in the standard.

$(N)_A$ spec. = atomic density of element A in the specimen.

$(I)_B$ stand. = isotopic abundance of B in the standard.

$(I)_B$ spec. = isotopic abundance of B in the specimen.

$$\text{then, } (N)_A \text{ spec.} = \frac{(\rho i)_{spec.}}{(\rho i)_{stand.}} \cdot \frac{(I)_B \text{ stand.}}{(I)_B \text{ spec.}} \cdot (N)_A \text{ stand.} \qquad \text{——(3)}$$

The concentration (C), in g/g of element A may be calculated :-

$$C = \frac{(N)_A \text{ spec.}}{N_o \cdot D} (Aw) \qquad \text{——(4)}$$

where Aw = atomic weight of element A

N_o = Avagadro's Number (approx. 6×10^{23})

D = density of host phase

The values α_x, g_x and K_{xy} need an explanation as to their functions.

α_x, an etching efficiency factor, is the fraction of those fission fragments impinging on the detector which may be revealed as tracks. This term is analogous to Fleischer and Prices' (1964) $\cos^2\theta_c$ term relating to the critical angle θ_c, below which particles striking the detector will not be revealed by etching. Since for Makrofol θ_c is very low (2^o), in effect all the fission fragments will be revealed as tracks (Fleischer et al., 1967).

g_x, a geometry factor, simply expresses whether tracks have crossed the detector from the host phase on one side ($g = \frac{1}{2}$), or from two sides ($g = 1$).

When tracks from a standard are compared with those from an unknown specimen under identical conditions, the values α_x and g_x may be cancelled out. However, the value K_{xy} (a depth factor) is strictly not constant for different materials.

K_{xy} has been defined (Kleeman and Lovering, 1970) as the maximum depth from which a median fission fragment can produce a recognisable track. Mory et al. (1970) measured the mean ranges of ^{235}U fission fragments through various metals. Except for a few exceptions they noted a linear relationship between the mean ranges (R) - measured in units of milligrams.cm^{-2} - and the square

root of the atomic number of the elements under study. Values (recalculated to microns) varied from 10.54 μm. for aluminium to 4.44 μm. for gold (compared to Kleeman and Loverings', 1970 value of $K_{xy} = 8.11 \mu m.$).

The measured ranges depended also upon the crystallographic texture of the material. More research is required before the effect of K_{xy} (or R) may be evaluated in a variety of materials (particularly silicates), and before the proper significance of this factor in the equation is understood. However, if one uses Mory's et al. (ibid.) results - i.e. that R is proportional to $Z^{\frac{1}{2}}$, and assumes that R may be proportionally summed for elements in a compound material (i.e. minerals), equations (3) and (4) may be modified (for uranium):-

$$(U)\text{spec.} = \frac{(\rho i)_{\text{spec.}}}{(\rho i)_{\text{stand.}}} \cdot \frac{(I)\text{stand.}}{(I)\text{spec.}} \cdot \frac{(R)\text{stand.}}{(R)\text{spec.}} (U)\text{stand} \quad -(5)$$

where (U)spec. = uranium content in g/g in the specimen

(U)stand. = uranium content in g/g in the standard

(I)spec. = isotopic abundance of ^{235}U in the specimen

(I)stand. = isotopic abundance of ^{235}U in the standard

(R)spec. = mean fission fragment range (in $mg.cm^{-2}$) for the specimen

(R)stand. = mean fission fragment range (in $mg.cm^{-2}$) for the standard

$(\rho i)_{\text{spec.}}$ = number of induced tracks per unit area (from ^{235}U) in the specimen

$(\rho i)_{\text{stand.}}$ = number of induced tracks per unit area (from ^{235}U) in the standard

and, where $R = \sum_i c_i r_i$ ——————(6)

c_i = weight fraction of the ith element having atomic number Zi

r_i = range of fission fragments (in $mg.cm^{-2}$) for the ith element where $r_i = 0.8(Zi)^{\frac{1}{2}}$ (Mory et al., 1970).

For most of the major rock-forming minerals and using glass standards however, (R)spec $\simeq$ (R)stand and the term $\frac{(R)\text{stand.}}{(R)\text{spec.}}$ in equation (5) approximates to 1.

2.2. Uranium Distribution Maps - technique.

Uranium (or more accurately, fission track) distribution mapping is a technique utilising S.S.T.D.'s to record accurately the distribution and concentration, within a rock or mineral section, of those elements which undergo induced fission. Under neutron bombardment, S.S.T.D.'s detect only fission fragments from uranium and thorium (table 2.1).High energy fluxes, γ-rays, neutrons and high energy protons in general, do not produce tracks. The technique is as follows:- a thin film of the detector is placed onto a polished rock section and irradiated in a thermal neutron flux. After an appropriate period has elapsed to allow most of the radioactivity to decay, the detector is detached from the rock surface and the induced fission tracks revealed by chemical etching. Fig 2.7, from Kleeman and Lovering (1967,b) schematically shows the principle.

Fleischer, using both inorganic (mica, 1965a) and organic S.S.T.D.'s (Lexan plastic, 1966) first obtained uranium distribution maps from polished rock sections. The limitations and usefulness of the technique however, depend upon solving the problem of the spatial relationship between the etched detector and the rock section.

2.2.1. Spatial relatioship problems in uranium distribution maps

The small size of the tracks (10-20μm. in length) mean that variations of distributed uranium may be studied over small areas and within, in fact, individual crystals. However, in practice, the usefulness of the distribution technique over very small areas and with low-uranium minerals, depends upon the ability

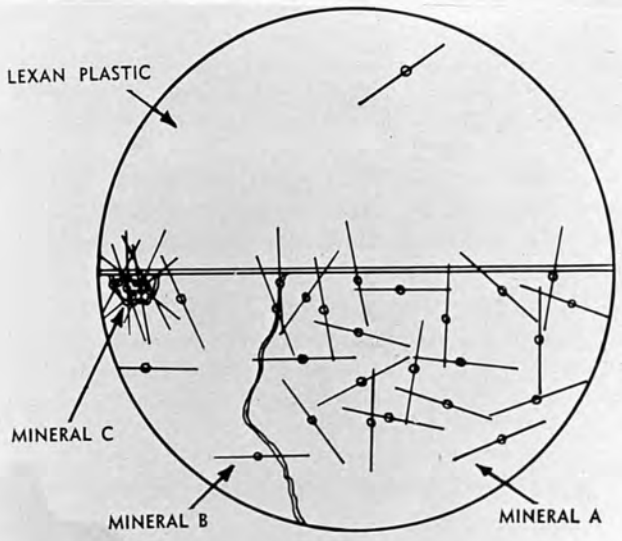

Figure 4. A representation of fission track registration in Lexan plastic. Hypothetical examples of three mineral phases of different uranium abundances are A with moderate content, B with low abundance, and C represents a small grain of high concentration. The fissioning atoms are shown, with the direction of the two products.

Figure 2.7.

Uranium mapping - Principle.

(From Kleeman and Lovering, 1967, a).

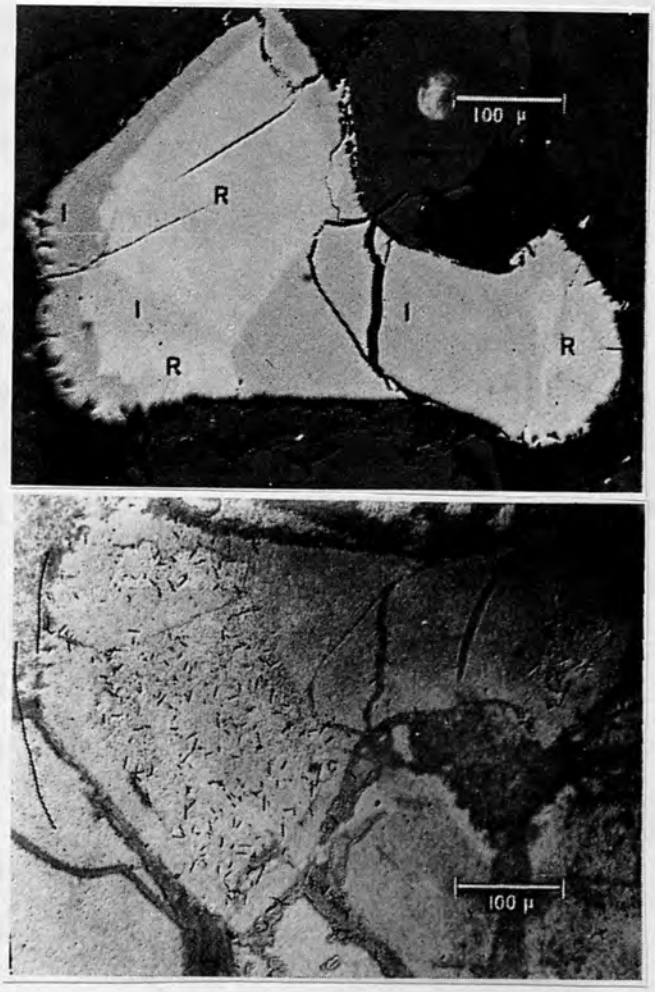

Figure 2.8.

"Lexan Print" (from Kleeman and Lovering 1967, a).

to relate accurately the induced fission track in the S.S.T.D. to its source position in the rock or mineral. Owing to the small size of the fission track, and since the detector is detached from the rock prior to etching, the determination of the spatial relationship between the etched detector and the rock's surface becomes a problem. As most of this work was concerned with trace uranium concentrations, some method of recording accurately the rock/S.S.T.D. couple was required to solve the spatial relationship problem.

Kleeman and Lovering (1967a,b) effectively eliminated the problem when they reported obtaining a Lexan plastic print - a print of the rock's surface permanently imaged on Lexan plastic S.S.T.D. (fig2.8). They suggested (ibid. 1970b) the image to be the result of α-particles and ^{7}Li recoil ions from lithium and boron (n,α) reactions:-

$$^{6}Li + n \longrightarrow {}^{3}H + {}^{4}He$$

$$^{10}B + n \longrightarrow {}^{7}Li + {}^{4}He$$

The different concentrations of these elements in adjacent minerals produce different quantities of α-particle pits (less than 1μm. in depth) giving rise to a mineral contrast and hence print fabric.

Although the Lexan plastic print method is widely known (Kleeman and Lovering, 1967b was published in Science N.Y.) and is both an effective and (apparently) very simple method of distribution mapping, the appearance in the literature of several methods suggests that other workers may have had difficulty in obtaining such prints. Dooley et al. (1970) devised a dual microscope whereby both detector and rock specimen could be viewed simultaneously; Fleischer (1966) used a very thin layer of detector (approx. 3μm.) on the rock surface, which was then etched in situ; Haines (1972) devised a method whereby location marks were made on both rock surface and detector prior to

irradiation, these being assigned coordinates, and then, by vector analysis, the coordinates of other points were calculated. Marking the rock with uranium-doped ink or with uranium-enriched scribes has also been reported (Szabo et al., 1970).

In view of the many apparent advantages provided by the Lexan plastic print method, several attempts were made during this work to obtain such prints.

2.2.2. Lexan plastic prints - their production.

This section is a report of my attempts to produce a Lexan plastic print (see also Appendix 1).

From correspondence exchanged with Professor Lovering and D.A. Wark (Lovering's research assistant), it would appear that several factors come into play in the formation of these prints. Several points are discussed and their roles investigated.

(a) The α-track registering properties of Lexan may be greater than that for makrofol (the organic S.S.T.D. routinely used throughout this work).

(b) Nuclear heating may occur and result in the α-tracks being annealed (temperatures above 90°C would anneal the α-tracks - Lovering, private communication).

(c) Pressure on the detector may be too high or low.

(d) The Li and B content of the minerals may not be high enough to provide an adequate contrast.

(e) The type of adhesive used in preparing the polished thin sections may affect the α-track registering properties of the detector.

(f) Reactor conditions may differ.

The inclusion of factor (e) - the type of adhesive used - was made since Wark (private communication) occasionally found that certain epoxy resins outgas an unidentified substance during irradiation which prevented the detector from registering

either a print or fission tracks. This he overcame by vacuum-evaporating a thin film of pure aluminium (a few hundred Å thick) onto the S.S.T.D. which effectively protected it from the gas and provided the desired print (the aluminium film was rapidly removed by the NaOH etching solution).

In an attempt to obtain a Lexan plastic print, irradiations were performed aimed at eliminating the factors (a) to (f) which could possibly inhibit the formation of such a print. Factors (a), (d) and (e) were eliminated by using a variety of different aluminium-coated detectors including organic S.S.T.D.s (makrofol; Lexan provided by Dr.C. Rice (I.G.S), and Lexan provided by Professor Lovering) on a range of different rock types. Adjustments of detector pressure were made with the tension screws on the irradiation canisters (factor (c)), and, since reactor temperatures in both the University of London Reactor Centre (U.L.R.C.) and the Atomic Weapons Research Establishment (A.W.R.E.) are similar to that in the Hifar reactor (the reactor in which Kleeman and Lovering obtain their Lexan plastic prints) - table 4.2-factor (b) was eliminated. Thus, after these irradiations, factors (a) to (e) were eliminated and a print was not obtained. After a sample of Rhum crescumalate was irradiated (with kind permission of D. Wark) in the Hifar reactor (Sydney, W. Australia) and a Lexan plastic print produced, it was considered that reactor conditions in Hifar were in some way more conducive to print formation than either of the reactors at the U.L.R.C. or the Herald reactor at the A.W.R.E. (factor (f)). When however, the reactor variables (temperature and flux) were compared for the three reactors, they were found to be similar (table 4.2). Kleeman (1973) however, obtained Lexan prints from samples irradiated in a thermal neutron flux of 3×10^{12} neutron.cm^{-2}.sec^{-1}, but with a low fast neutron componant of 3×10^{5} neutron.cm^{-2}.sec^{-1} (see also Appendix 1).

Table 2.2

Reactor	working temperature	thermal neutron flux (cm^{-2})	fast neutron flux (cm^{-2})
Hifar (Sydney	40°C	3×10^{12}	$1\text{-}5 \times 10^{10}$
U.L.R.C. (through tube)	30°C	5.5×10^{10}	2×10^{10}
A.W.R.E. (VT-1)	35°C	1 to 2 $\times 10^{12}$	1×10^{10}

The possibility that a high γ-flux was a critical factor was dispelled when aluminium irradiation canisters were used in the A.W.R.E. VT-1 facility.

Since for most of this work, a Lexan plastic print was not obtained (see also Appendix 1), the spatial relationship problem needed to be tackled from another angle - the contact print method.

2.2.3. Contact Print Method.

The contact print method routinely used throughout this work was conceived by the author to resolve the spatial resolution problem. Although not as elegant, nor indeed as precise as the Lexan plastic print method it was relatively simple to use, and the errors have been quantitatively analysed. It is based on recording photographically, on a grid basis, the rock/S.S.T.D. couple. A grid of approximately 4 millimetre divisions was cut into the makrofol S.S.T.D. and affixed to the rock section. A photographic "contact print" (details section 2.3.1.) was made of the rock/S.S.T.D. couple. After irradiation, etching and mounting on a glass slide, the S.S.T.D. grid was numbered in the form A1 - iB, . A1 - jC. The squares of the S.S.T.D. which corresponded to areas in the rock section could then be rapidly found by reference to the contact print (similarly numbered), or alternatively, areas of interesting uranium-

distributions could be related to the corresponding areas of the rock section.

A mineral whose uranium content was required, was located on the contact print and the grid square noted. Its precise coordinates (x_1, y_1) within that square were transformed to the coordinates (X, Y) on an x - y microscope stage (attached to the Zeiss photomicroscope) upon which the S.S.T.D. was placed.

If the grid square on the contact print has dimensions a millimetres by b millimetres (along the x and y axes respectively) and the point to be transformed lies p millimetres and q millimetres along x and y, then the coordinates of the point $(x,y,) = {}^{p}/_{a}, {}^{q}/_{b})$. The stage coordinates corresponding to the position of the grid-square corners on the S.S.T.D. can be measured:- A, B along x and C, D along y. The coordinates of the transformed point on the S.S.T.D. (X,Y) can be found when:

$$X = A + x_1(B - A)$$

$$Y = C + y_1(D - C)$$

It was important to know how accurately the transformation process could be performed and hence to know the minimum mineral area, and minimum S.S.T.D. area which could be analysed by the contact print method. This was related mainly to the error involved in measuring the contact print coordinates (x_1, y_1) i.e. $\pm$ 0.5 millimetres. This was termed the "relocation error", R. R, when transformed to the S.S.T.D. is a function of the magnification of the contact print (routinely x5). An area of high probability of locating the point on the contact print (w_{cp}) exists with

$$w_{cp} = (2 \times R_{cp})^2 \quad \text{where } R_{cp} = \text{relocation accuracy} = 500\ \mu m$$

$= \underline{1 \times 10^6 \mu m^2}$ (at x5 magnification).

The corresponding area of high probability on the S.S.T.D. (w_d with mid point XY) of locating the transformed point is then:-

$$w_d = \left(2 \times \frac{R_{cp}}{5}\right)^2 = (2 \times 100)^2$$

$$= \underline{4 \times 10^4 \mu m^2} \text{ (at zero magnification)}$$

So, within the square w_d (centre XY) the probability of finding the transformed point (x,y,) approaches 1. w_d then was taken to be the minimum S.S.T.D. area which can be counted for fission tracks. But since this is a finite area, it must relate to a finite area of the mineral. To ensure that all fission tracks within w_d related only to the mineral under investigation, the minimum mineral area (w_{min}) was required where:-

$$w_d = \left[(R_{cp} + \frac{R_{cp}}{5}) 2\right]^2$$

$$= \left[(500 + 100) 2\right]^2$$

$$= 1.44 \times 10^6 \mu m^2 \quad \text{(at x 5 magnification).}$$

(Equivalent to approximately $5.8 \times 10^4 \mu m^2$ at zero magnification). Minerals then having dimension on the contact print less than $1.4 \times 10^6 \mu m^2$ (approx $1.2 \mu m^2$) should not be chosen for analysis unless either of the two following conditions apply:-

(1) The fission track distribution is so distinctly shaped and there exists a similarly shaped mineral such that correlation between mineral and S.S.T.D. area is obvious (chapter 5, section 5.2.3)

(2) The distribution is such that a high-uranium phase gives a fission track "star" which can be related back to the rock section by its unusual mineralogy and/or geochemical compatability with elements such as Zr or P. (Chapter 5, section 5.4).

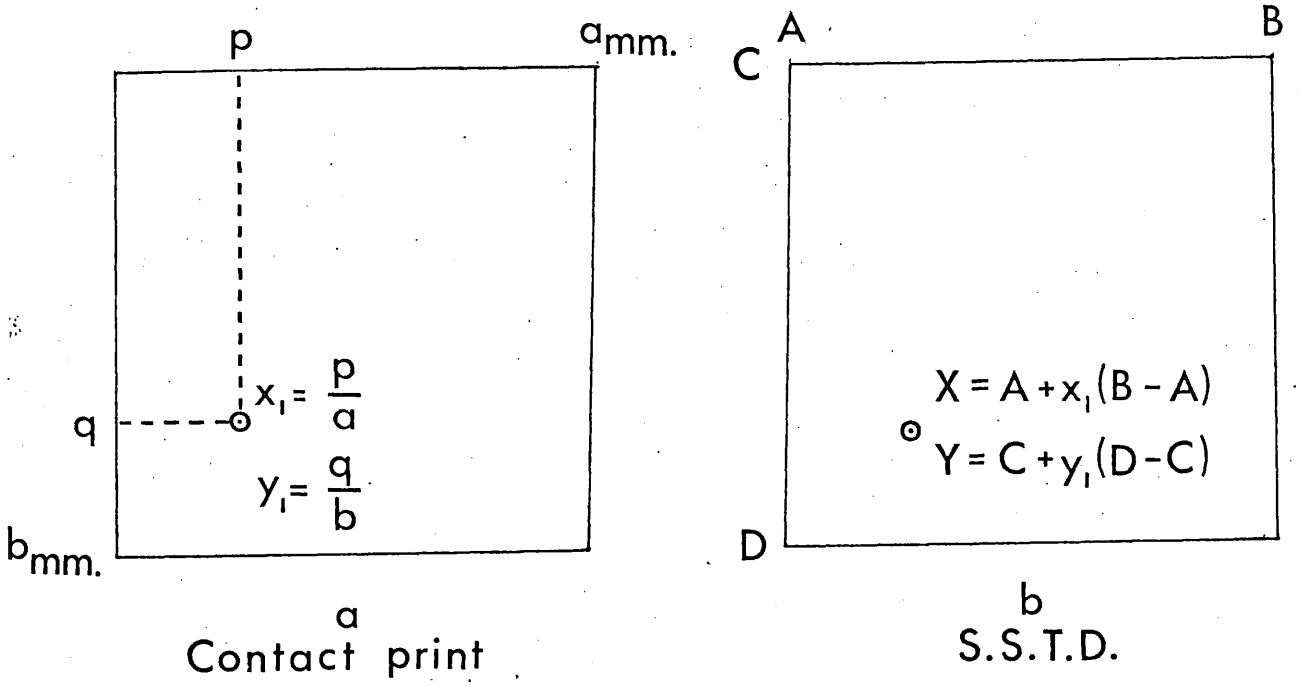
p
a mm.
q
$x_1 = \frac{p}{a}$
$y_1 = \frac{q}{b}$
b mm.
a
Contact print
A
B
C
D
$X = A + x_1(B - A)$
$Y = C + y_1(D - C)$
b
S.S.T.D.

Figure 2.9

2.3. Uranium Distribution Maps - procedure

The principle of the technique is as follows: simultaneous irradiation of the detector/rock section and detector/standard couples in a thermal neutron flux, chemically etching the detached dectectors and comparing the number of fission tracks from the specimen to that from the standard.

Prior to sample irradiation, initial factors such as the time required for the irradiation plus an appropriate cooling-off period (γ-radiation decay of mainly ^{24}Na, $t_{\frac{1}{2}}$ = 15 hours), practical sensitivity and the expected uranium concentrations of the rocks and minerals under investigation must be considered. The expected concentration range for the Rhum rocks (and minerals) is of the order of 10 - 100 p.p.b. uranium (1p.p.b. = 10^{-3} p.p.m.) and the practical sensitivity of the method is dependant largely upon the attainment of reasonable counting statistics of the order of 10^4 tracks. cm^{-2} (Besant and Ipsom,1970).

For this work, four irradiation facilities had been made available; two initially at the University of London Reactor Centre (U.L.R.C.) and a further two at the Atomic Weapons Research Establishment (A.W.R.E.). A comparison of the four facilities is shown in table 2.3.

Table 2.3

facility		thermal neutron flux (neutrons. $cm^{-2}.sec^{-1}$).	max.^{m} convenient dose (neutrons $cm^{-2}.sec^{-1}$).	sensitivity.* expected uranium concentration (p.p.b.) for 10^4 tracks.cm^{-2}.
U.L.R.C.	through tube	approx. 1×10^{11}	3.6×10^{16} (100 hours)	21
	core tube **	$0.5 - 1 \times 10^{12}$	1.4×10^{17} (40 hours)	4
A.W.R.E.	J.2.	2×10^{11}	7.2×10^{16}	13
	VT-1	2×10^{12}	2.0×10^{17}	3

* calculated from formula (2)

** unsuitable for 2 x 1 inch sections due to the small diameter of the tube.

The maximum convenient dose is a loose term combining several factors: safety considerations towards reactor personnel (against γ-radiation from ^{24}Na); real time taken to accumulate 100 reactor hours (to allow a reasonable sample turnround), and a maximum viable dose of 2×10^{17} neutrons. cm^{-2}.

Nylon irradiation canisters were designed and constructed for both the U.L.R.C. through tube (fig 2.10) and the A.W.R.E. J2 facility (fig 2.11). The U.L.R.C. canister can accommodate up to seven polished thin sections plus standards, and the J2 canister up to four. The specimen/detector or standard/detector couple was, in each case, sandwiched between nylon spacer discs and tensioned by means of the attached screw. In the higher flux facilities (U.L.R.C. core tube and A.W.R.E. VT - 1) standard aluminium canisters were used.

The processes involved in obtaining distribution maps can conveniently be divided into four stages:-

1. Preparation of material
2. Irradiation
3. Etching procedure.
4. Counting procedure.

2.3.1. Preparation of material

Thin sections of the specimen were prepared by mounting the material in an epoxy resin (Ciba-Geigy A103 and HY 951 hardener in a 10 to 1 ratio) and grinding down to a thickness of 35 μm. The dimensions of the slide were 2 x 1 inches and chosen to be compatible for use both with the Geoscan microanalyser (at Imperial College) and the Jeol scanning electron microscope (at Chelsea College). The sections were polished on a Metaserv motorised polishing instrument with Hyprez diamond abrasives to a final $\frac{1}{4}$ μm grade, washed in a minimum quantity (1-2 mls) of distilled water and in I.M.S. It has been suggested (Wark, personal communication)

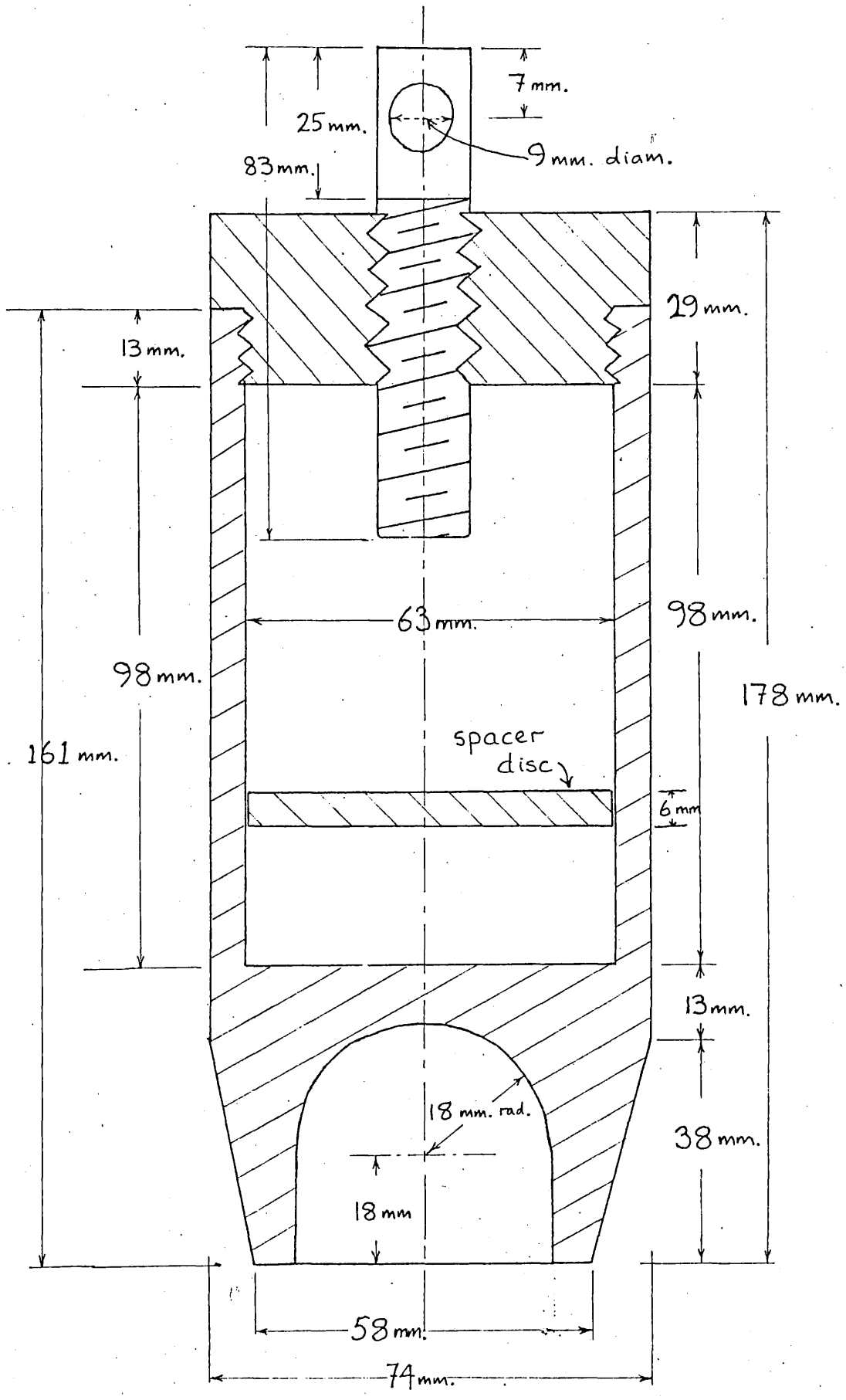

Figure 2.10

U.L.R.C. irradiation canister

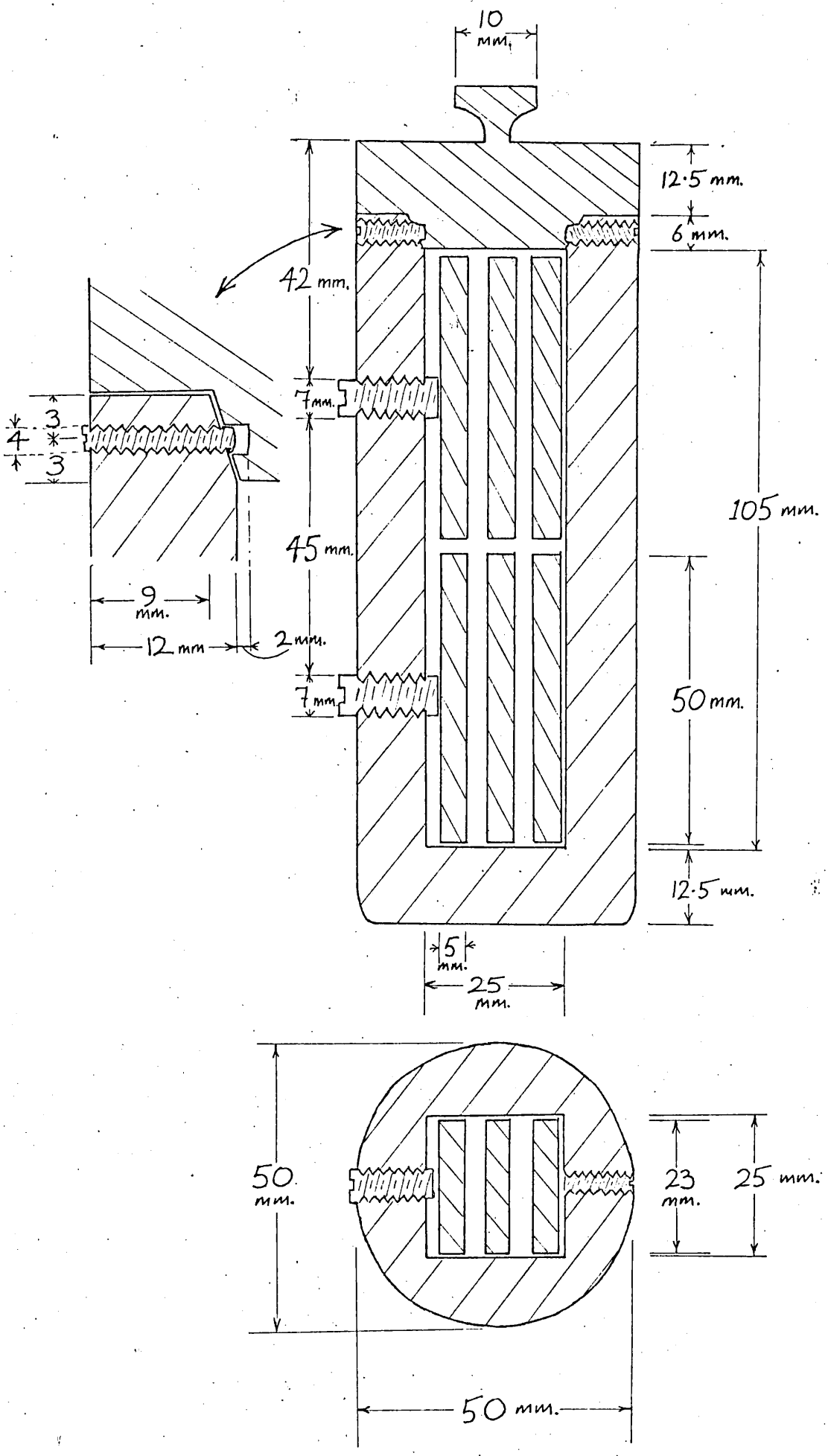

Figure 2.11

A.W.R.E. irradiation canister

that with excessive sample washing leaching of uranium into the aqueous phase may occur. A minimum amount of washing was, therefore, undertaken, and ultrasonic cleaning in a sonic bath not used.

Detector material, makrofol KG*, an organic (bis-phenyl A polycarbonate resin **) S.S.T.D., was supplied in 50μm thick transparent sheets. One surface of the sheet was uniformly smooth and, in order to obtain maximum surface contact with the rock section, was consequently used as the detector surface. Pieces of makrofol were cut to cover the rock section and a location grid of approximately 4 mm^2 divisions cut into the detector surface with a clean, new scalpel blade. An old, or blunt blade scratched, rather than cut the surface, causing the makrofol to buckle. The detector was then washed in a similar manner to the thin sections and allowed to dry before being attached to the rock section by means of spots of adhesive (Bostik 1) at each corner.

A contact print (section 2.2.2.) was prepared using Kodak photographic fine grain positive film (fig 2.12). A contact negative was firstly produced by pressing the film onto the rock detector couple (by means of magnetised clips) and exposing for a suitable period of time (4 -6 seconds at f.11) and developing the negative in 1 + 4 Kodak DPC developer. The film was chosen for its slow speed (5 ASA) so that it could be handled near a safe light, and for its high

*Supplied by: C.M.C. Klebetechnik-Ireland Ltd.,
Waterford Industrial Estate,
Waterford, Eire.

**formula:- $-OC_6H_4C(CH_3)_2C_6H_4O\overset{\overset{O}{\|}}{C}-$

identical to Lexan plastic except that makrofol contains a small amount of green dye and is prepared by a casting process (Paretzke etal. 1973).

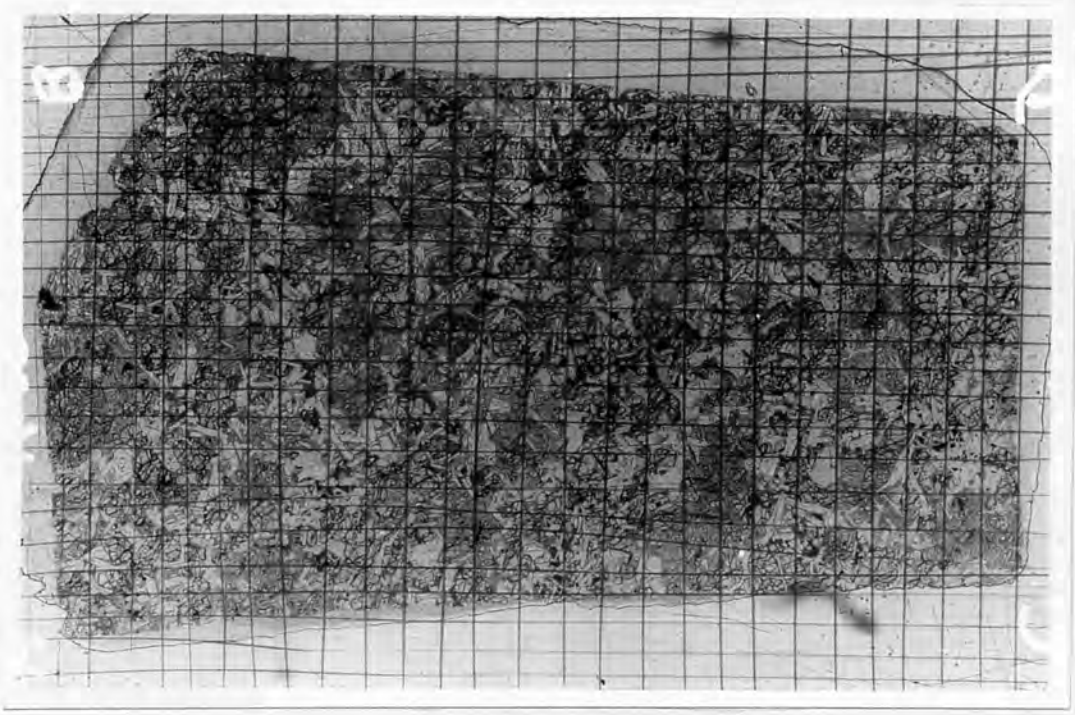

Figure 2.12 (a). Contact print (R.90).

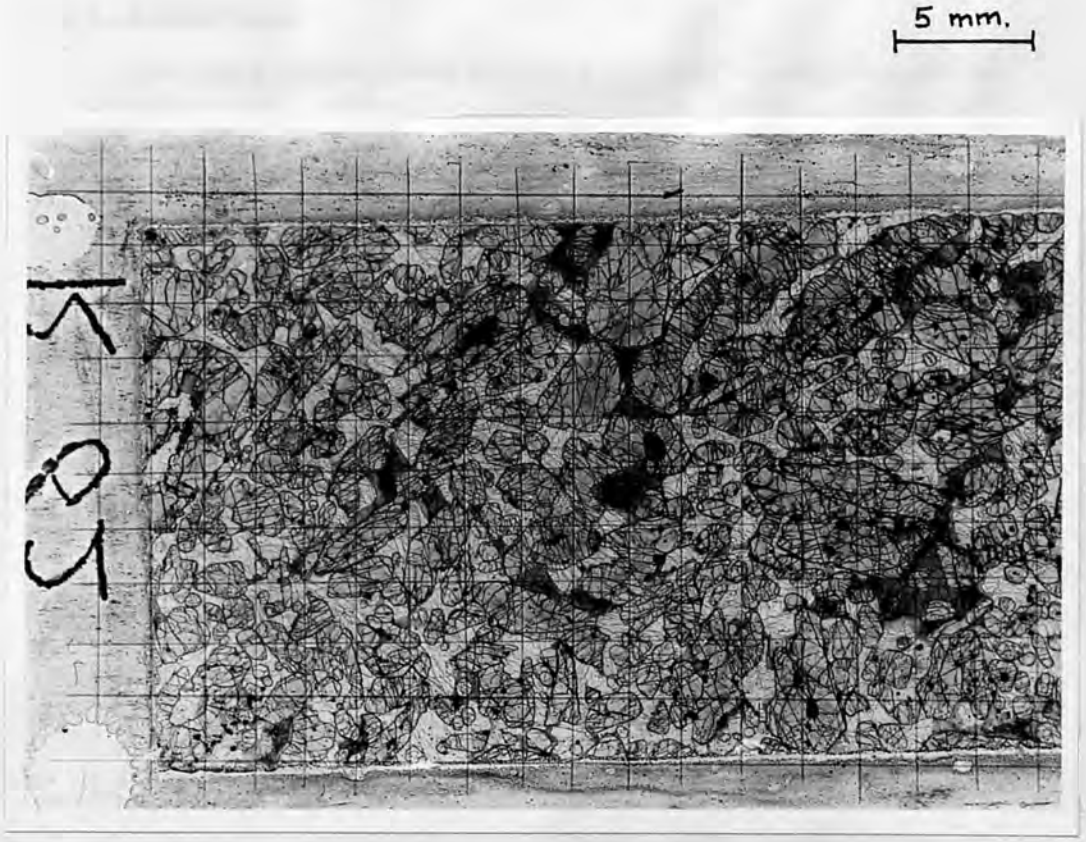

Figure 2.12 (b). Contact print (R.62).

definition so that objects of size approximately 25 μm were resolved. Preselected areas of interest were then photographed using a Zeiss photomicroscope (Ilford Pan-F film and 1 + 29 Perceptol developer) at a total magnification of not less than x100 (routinely x125).

Glass standards (calibrated microscope glass slides and U.S.G.S. standards - Section 2.3.5.) were washed in a similar manner to the specimens. Pieces of makrofol were cut, washed and dried, and placed on the surfaces of the standards. Neither a location grid nor a photographic record of the standard/detector couple was required.

The materials were packed prior to irradiation, the positions of the standards arranged such that they were in close proximity to the positions of the specimens. The arrangement varied slightly with the type of irradiation canister that was used, but in general was as shown in figure 2.13.Blanks were used in each irradiation in order to monitor the uranium concentration in the S.S.T.D.'s.

2.3.2. Irradiation

The total thermal dose required depended uponthe amount of uranium estimated to be in the photographed pre-selected areas of the rock. The maximum limit attainable was 2×10^{17} neutrons.cm^{-2}. At doses above this, the makrofol S.S.T.D. became increasingly brittle and hence less manageable. Similarly, above 2×10^{17} neutrons.cm^{-2}, the epoxy resin bonding the rock section to the glass slide deteriorated rapidly, and the rock section started to crumble. The best choice of reactor facility for the irradiation may rapidly be made on the basis of the data in table 2.3. Since the concentration of uranium in the major mineral phases of Rhum cumulates are in the p.p.b. range, the maximum permitted dose was generally applied.

In both the A.W.R.E. facilities, monitoring to obtain values of both the thermal and fast neutron doses for each irradiation, was undertaken.

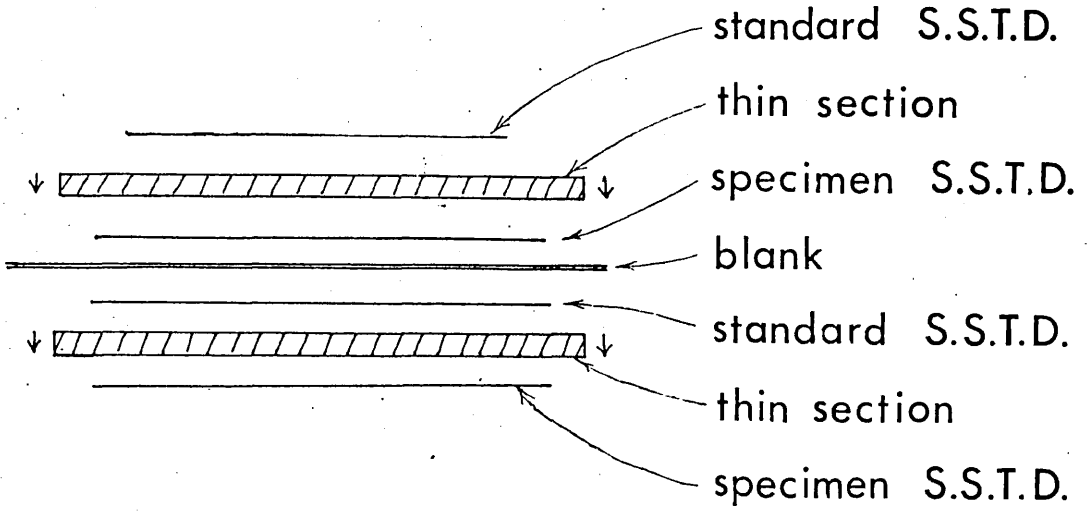

Figure 2.13

Packing arrangement for irradiation

FIG. 4.—Lexan recorder counted on Quantimet with × 10 Objective × 1·5 Magnification Changer (recorder etched for 16 hr in this case).

Figure 2.14

from Besant and Ipson, 1970

2.3.3. Etching procedure

The paths of the fission fragments in the makrofol S.S.T.D. were made optically visible by chemical etching with NaOH solution. The etching parameters, i.e. etchant concentration, time and temperature, when varied affect the quality of the etched fission tracks. Variations of the parameters have however been well investigated, and guide lines to the optimum conditions established.

Khan (1973) showed that the general etching velocity (Vg) of a plastic detector (cellulose nitrate) increased with increasing etchant concentration to a point where Vg remains constant. Frank and Benton (1969) suggested the optimum NaOH solution concentration for etching Lexan S.S.T.D. to be approximately 20%. The "generally accepted" NaOH solution concentration is 6N or 6.25N (e.g. Fleischer et al. 1969). The solution concentration used routinely in this work was 6N NaOH.

Frank and Benton (ibid) found that the bulk etch rate R_b (equivalent to Khan's, 1973 term, Vg) increased exponentially with temperature of etching solution. Etching times at room temperature can be as long as 16 hours (Besant and Ipsom, 1970). This was considered inconvenient when dealing with batches of samples, and since the track definition is in no way enhanced (and may in fact deteriorate, Khan, 1973), a temperature of 70°C was subsequently chosen as this required etching times of only 10 minutes.

A drop of Decon 90 wetting agent was added to the distilled water prior to the preparation of the etching solution as it was reported by Besant and Ipsom (ibid) to give a more uniform attack on the detector. The S.S.T.D. was agitated with a glass rod during the etching procedure at

intervals of approximately 60 seconds. This ensured that chemical etch products did not accumulate on the surface of the detector and impede the solution reaching the site of the attack (Khan, 1973). Identical etching conditions were followed for both standard and specimen S.S.T.D.s. Upon completion of the etching time, the S.S.T.D. was immediately immersed in a dilute solution of acetic acid in order to halt the etching reaction. The S.S.T.D. was washed with distilled water and IMS. Drying was completed with the assistance of the heat from a tungsten lamp.

After drying, a brownish residue of phenol or quinone-type compounds (Paretzke et al., 1973) coated the surface of the makrofol S.S.T.D. This had the result of making the detector non-transparent and the tracks indistinct. The clarity of the tracks increased when the detector was fixed face up on a glass slide with a solution of durafix in isopropanol. The effect of the durafix mount on the clarity of the tracks was considered to be two-fold. Durafix is a solution of cellulose acetate in dicholorethylene, and the thin layer of cellulose acetate bonding the detector to the glass produced less scattered light since its refractive index is similar to that of makrofol. It also appeared to dissolve the residue.

2.2.4. Counting procedures

Track counts (i.e. the number of induced fission tracks per unit area of detector) were carried out both automatically and visually.

Automatic track counting was carried out with a Quantimet 720B Image Analyser (at Birkbeck College, London). A microscrope image (x400 magnification) was transmitted, via suitable electronics, to a cathode ray tube and screen. A

discriminator then analyses the screen for areas of light and dark (fig 2.14),the track count per analysed area printed on a teletype output. This enabled homogeneously distributed tracks to be rapidly counted.

Heterogeneously distributed tracks (such as found in most rock sections) were counted visually using a Zeiss photomicroscope and transmitted light at a magnification of X450. The area in the field of view was projected onto a ground glass projection head screen attached to the photomicroscope. Tracing paper with a grid of 4 centimetre squared (cm^2) divisions marked on it was placed on the screen and the number of fission tracks per division recorded. Tracks from both specimen and standard were counted in this manner.

Tracks were also counted directly from photographs. Since photomicrographs of several areas of the detector/rock section couple had been taken prior to irradiation (section 2.3.1.), after irradiation and etching, these same areas of the detector were rephotographed, and the number of tracks in a given area counted from the photographs. Photomicrographs were similarly taken (at the same magnification) of the standard S.S.T.D. and the tracks counted over a similar area.

2.4. Standard calibration

In order to determine quantitatively the concentration of uranium in a specimen by fission track analysis, a standard of known uranium content and isotopic composition is required. After irradiating both standard and specimen under identical conditions, the uranium content (in the specimen) may be calculated by comparing the number of induced tracks per unit area in the standard S.S.T.D. with the number in the specimen S.S.T.D. (Section 2.1.6.). In this work two standards were used to calculate uranium concentrations of various mineral

phases. These were N.B.S. standard glasses (SRM 614, Carpenter, 1972) plus calibrated batches of Chance microscope glass slides, as secondary standards. The calibrated glass slides were then used in the preparation of those polished rock sections which were to be irradiated for fission track analysis.

Two analytical methods were used to determine the uranium content in the glass slides - fission track analysis and delayed neutron activation analysis (D.N.A.A.) as described by Gale (1967).

Six specimens from a batch of 50 Chance 50 x 24 cm microscope glass slides were randomly sampled and cut in half. The uranium content in one half was calculated by fission track analysis using SRM-614 glass as standard. Pieces of makrofol S.S.T.D. were placed against the specimen and the standard and irradiated with a total thermal neutron dose of 6.3×10^{16} neutrons. cm^{-2}. Etching was performed in 6N NaOH for 10 minutes at $70 \pm 1^{\circ}C$ (Section 2.3.3.). The track density was determined with the Quantimet 720 at Birkbeck College (Section 2.2.4.). The other half of the glass slide was powdered in an agate pestle and mortar, the U content being determined at Harwell by the D.N.A.A. Method. A batch of "Geoscan" 48 x 24 cm glass slides were similarly calibrated by the fission track method.

In order to calculate the uranium content by fission track analysis, equation (5) (Section 2.1.6.) was used:-

$$(U)_{spec.} = \frac{(\rho i)_{spec.}}{(\rho i)_{stand.}} \times \frac{(I)_{stand.}}{(I)_{spec.}} \times \frac{(R)_{stand.}}{(R)_{spec.}} \times (U)_{stand.}$$

The standard in this case was the N.B.S. (SRM-614) glass, where:-

$(I)_{stand.} = 1.173 \times 10^{-3}$ (Isotopic content of ^{235}U)

$(U)_{stand.} = 0.828 \pm .002$ p.p.m. U

The specimens were the 50 x 24 millimetre Chance microscope glass slides, where

(I) spec. = 7.26×10^{-3} (natural isotopic content of ^{235}U)

To determine the values (R)stand. and (R)spec, the major element concentrations of both specimen and standard were required. Then, from equation (6),

$$R = \sum_i c_i r_i \qquad \text{where } r_i = 0.8(Z)^{\frac{1}{2}}$$

Table 2.4.

element	N.B.S. (SRM-614) stand		Chance 50 x 24 cm		"Geoscan" 48 x 26 cm	
	c_i	$c_i r_i$	c_i	$c_i r_i$	c_i	$c_i r_i$
Si	.33	.987	.33	.987	.32	.958
Ca	.08	.286	.11	.393	.12	.429
Na	.10	.253	.07	.177	.07	.77
Al	.01	.029	.02	.057	.02	.057
O	.48	1.085	.47	1.063	.47	1.063
Total	1.00	2.664	.99	2.677	.99	2.684

where c_i = weight fraction of the element

r_i = the mean fission fragment range in $mg.cm^{-2}$

To determine the values of $(\rho i)_{spec.}$ and $(\rho i)_{stand.}$ track densities at x 400 magnification were obtained using the Quantimet :-

$(\rho i)_{stand.} = 1.106 \times 10^5$ (mean of 6)

$(\rho i)_{spec.} = 2.884 \times 10^5$ (mean of 6)

Then substituting the appropriate values into equation (5), the concentration of uranium in the Chance (50 x 24 mm.) slides i.e. (U)spec., was calculated - table 2.5.

Table 2.5.

slide n°. (50 x 24 mm.)	D.N.A.A. (p.p.m. U)	fission track (p.p.m. U)
S1	.346	.343
S2	.382	.345
S3	.333	.345
S4	.367	.350
S5	.373	.343
S6	.369	.341
Average	.362	.344

Over 100 track counts each over an area of $1.746 \times 10^5 \mu m^2$ were recorded on both standard and specimens. The low mean standard deviations and subsequent chi-squared (χ^2) tests (table 2.6) showed that, in addition to obtaining extremely good reproducibility (table 2.5, the uranium was distributed homogeneously throughout both the U.S.G.S. standards and the microscope glass secondary standards.

Table 2.6

specimen	track density ($\times 10^5$ cm^{-2})	Mean S.D. 100 area counts	χ^2	normal deviate (n.d.)
N.B.S. (SRM-614)	3.370	.380	111.684	.873
50 x 24 mm.	8.667	.377	108.931	.689
"Geoscan"	3.750	.381	117.960	1.288

The (χ^2) test is a measure of the randomness of a set of numbers (in this case, the number of fission tracksrecorded over a unit area).

$$\chi^2 = \frac{(n-1)s^2}{\sigma^2}$$

where s^2 = the variance

σ = the population variance

n = the degrees of freedom

The normal deviate (n.d.) - i.e. the standard deviation - of the value χ^2 may be calculated (for values on n 30) when:-

$$\text{n.d.} = (2\chi^2)^{\frac{1}{2}} - (2n-1)^{\frac{1}{2}}$$

then for a random situation, the value of n.d. should lie between zero and two standard deviations. This is in fact seen to be the case (table2.6 column 5).

The uranium content in the "Geoscan" 48 x 26 mm. glass slides were calculated by fission track analysis and found to contain $0.149 \pm .002$ p.p.m. uranium.

2.5. Choice of Detector

Pieces of makrofol and mica were tested for their suitability as S.S.T.D.'s. Both were irradiated in contact with standard microscope glass slides and in contact with each other. Tracks were revealed on etching with a suitable etchant - mica in 40% HF for two hours at room temperature; makrofol in 6N NaOH for ten minutes at 70°C - and counted at x400 magnification using the Quantimet 720 (at Birkbeck College).

Table 2.7 shows that at the dose of 6×10^{16} thermal neutrons.cm^{-2}, the track density between the mica and makrofol S.S.T.D.'s varied by only approximately 0.2%. The difference between the mean track length (column 4) was insignificant at the magnification used (x400). At lower magnifications however, tracks in makrofol may be easier to resolve.

Table 2.7

detector	(ρi) tracks.cm^{-2}	uranium (p.p.b.)	mean track length (μm)
makrofol/glass	2.718×10^5	333	18
mica/glass	2.726×10^5	334	15
mica/mica	1016	1.23	-
makrofol/makrofol	120	.15	-

The main qualitative difference was in the appearance of the detector. Makrofol was virtually free of any dislocations, whereas mica frequently had dislocation defects, and also a tendency to be easily scratched when handled. These defects may be mistaken for fission tracks especially when automatic counting is used. What is perhaps more important is that the makrofol has a lower intrinsic uranium content (column 3) than the mica. Makrofol is therefore a more sensitive S.S.T.D., particularly when applied to minerals with concentrations of uranium in the low p.p.b. range.

The track registration qualities of the two detectors at various doses were examined by track counting after irradiation adjacent to standard glasses over a range of thermal neutron doses between 7×10^{15} and 5×10^{17} neutrons.cm^{-2} (figure 2.15). From the graph it can be seen that the track count for makrofol deteriorated at high ($> 4 \times 10^{17}$ neutrons.cm^{-2}) doses. The makrofol, in fact, with increasing dose became more brittle and less manageable. It has been reported (Seitz and Hart, 1973) that severe track fading may occur with the use of plastic detectors. Although figure 2.15 may be interpreted in this manner, a more likely explanation is that instead of tracks being lost through fading, excessive irradiation damage affects the makrofol plastic, such that an increase in R_b (the etching velocity of the bulk of the detector) over R_t (the etching velocity along the damaged trail) occurred. This would have the effect of increasing the critical angle of incidence (θ_c - Fleischer et al., 1964) and fewer tracks would result. This hypothesis is backed, qualitatively, by the appearance of the fission tracks in the makrofol at doses in excess of 4×10^{17} neutrons.cm.$^{-2}$. A lower etching time was needed to reveal the tracks, and once formed, they appeared shorter and were conical in shape.

The maximum workable dose for makrofol S.S.T.D. was then of the order of 4×10^{17} neutrons.cm.$^{-2}$. At doses in excess of 2×10^{17} neutrons.cm.$^{-2}$ however, the epoxy resin binding the rock thin section tothe slides lost its adhesive qualities and the thin section began to crumble. So any apparent advantage obtained by using mica was not considered sufficient at the maximum usable dose (2×10^{17} neutrons.cm.$^{-2}$) to offset its lower sensitivity.

One advantage mica has over plastic S.S.T.D.'s is that

Figure 2.15

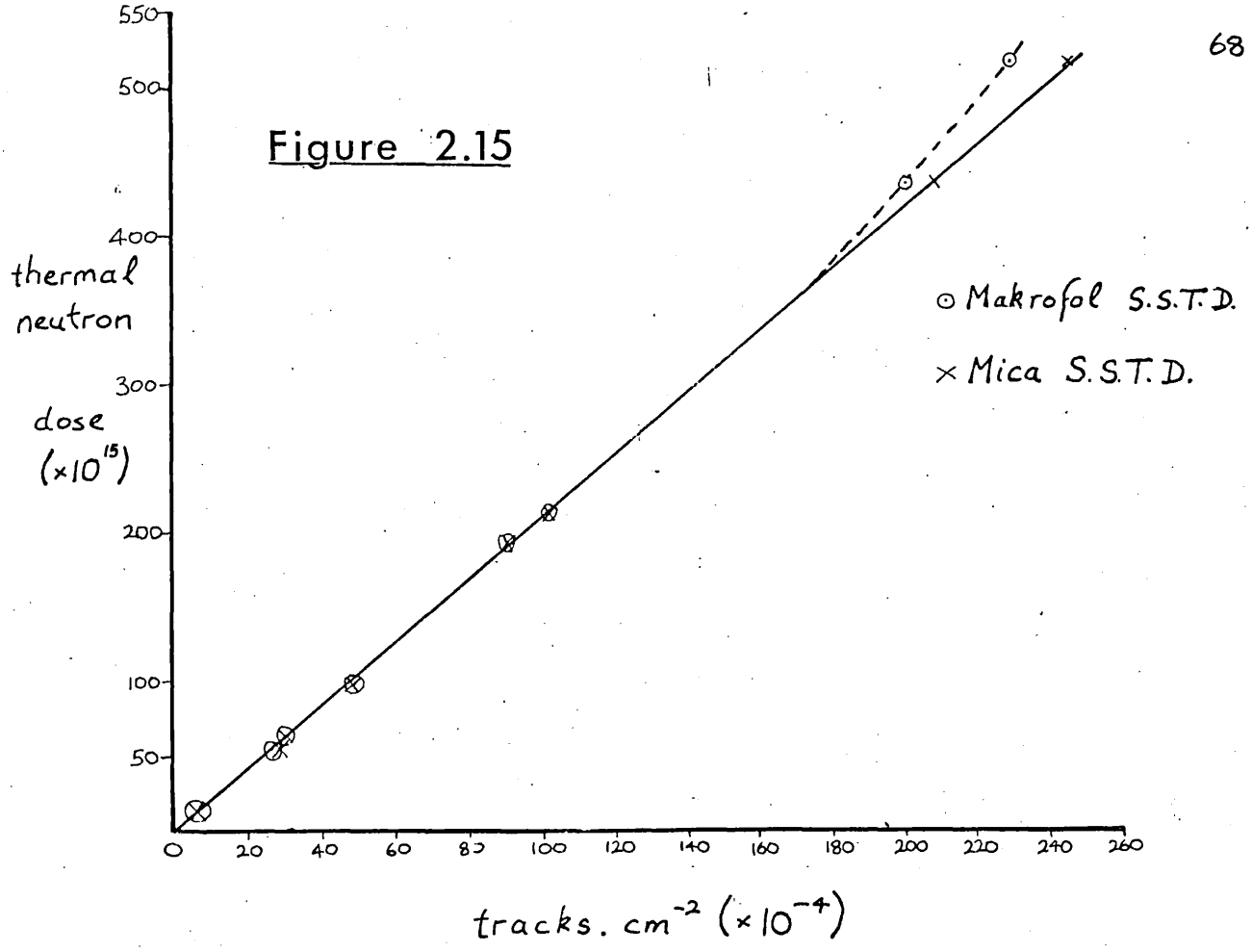

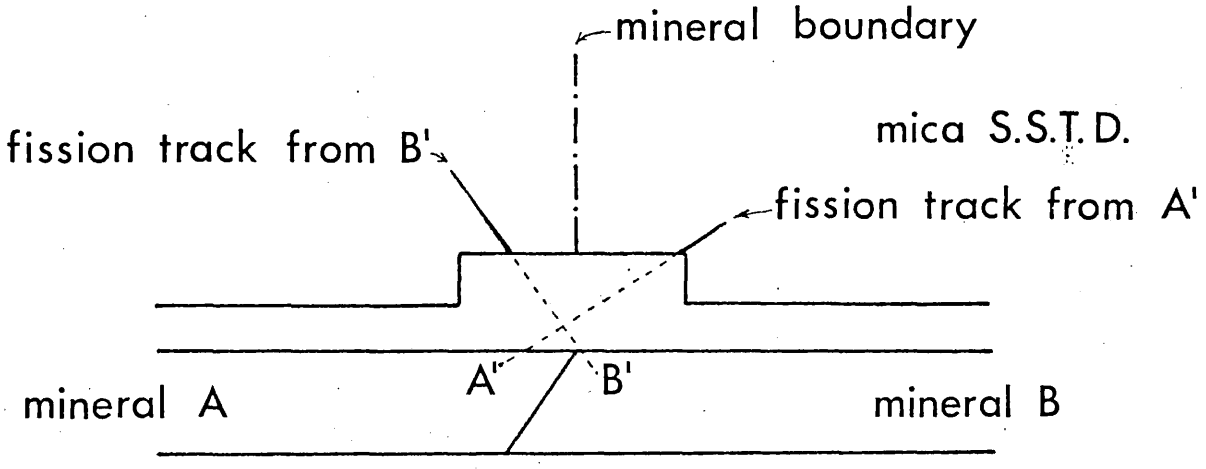

Figure 2.16

it has a higher "saturation value". That is the total number of tracks which may be resolved (and counted) over a unit area is greater for mica than for makrofol. Seitz et al. (1973), using a Scanning Electron Microscope, counted track densities of up to 2×10^{8} tracks.cm.$^{-2}$. The saturation limit for plastic S.S.T.D.'s occurs however, at about 5×10^{7} tracks.cm.$^{-2}$. A major disadvantage however, of using mica was its surface appearance. It was virtually impossible to cleave a piece of mica without it aquiring a stepped surface profile. This can lead to unnecessary relocation errors since the surface contact between the S.S.T.D. is not 100% (figure 2.16). For example, a 2 μm surface step can create a relocation error of up to 8 μm. Since the surface of plastic detectors are essentially smooth with no stepped profiles, errors of this type are advoided. Thus for thermal neutron doses of up to 2×10^{17} neutrons.cm.$^{-2}$, makrofol plastic was prefered to mica as the routine S.S.T.D..

2.6. Sources of Error

The four stages of the technique used to obtain uranium distribution maps (sections 2.3.1. - 2.3.4.) can each introduce errors resulting in inaccurate values of uranium concentrations for the various minerals. In this section is discussed the "individual" sources of error, and the steps taken to avoid or standardise those errors. These can be subdivided into four stages:-

1. Sample preparation errors
2. Irradiation errors
3. Etching errors
4. Counting errors

A discussion of the errors inherent in the technique of fission

track analysis and counting statistics can be found in section 2.7..

2.6.1. Sample preparation errors

As the surface of the polished thin section contain many (small) cracks and intermineral relief boundaries, it was important that the abrasives used to polish the surface contained negligable amounts of uranium, in order to avoid contamination from this source. Samples of abrasives used (section 2.3.1.) were tested for their uranium content by placing them between sheets of makrofol S.S.T.D., irradiating, etching and counting. The track densities for the abrasives were of the same order as those for blank makrofol sheets, the uranium content was therefore, below the detection limit ($<$1p.p.b.). The abrasives used were thus eliminated as being potential sources of error by contamination.

2.6.2. Irradiation errors

As it was possible to have individual standards for each polished thin section irradiated, sample packing was so arranged (figure 413) that relative standard/specimen positions were very close (a few millimetres). This effectively eliminated (or standardised) local flux variations, self-absorption factors and temperature differences. Absolute values for the neutron doses were similarly not required if standards were introduced for each irradiation.

It has been suggested (Wark, private communication) that certain epoxy or araldite resins emit a gas under neutron bombardment which can cause track fading. Initial use of araldite to attach the makrofol S.S.T.D. to the rock or glass surface did in fact result in track fading over a distance of several millimetres around the adhesive spot. When Bostik, or the araldite resin used in preparing the thin sections were substituted as an adhesive, no track fading occurred.

2.6.3. Etching errors

Optimum etching conditions were achieved: the aim being to obtain the maximum value for track length/track width ratio, such that it had a high probability of being recognised (and counted) as an etch figure from a fission fragment.

Once the concentration and temperature track etching parameters had been established (Section 2.3.3.) an experiment, aimed at obtaining the optimum track definition by varying the etching time (the other track etching parameter) was performed. Track dimensions were measured (to within 0.2 μm) using the Quantimet 720 at Birkbeck College over a period of 14 minutes at 1 minute intevals. A plot of etching time against track length is given in fig 2.17, and of etching time against track length/width ratios in fig 2.18. Fig 2.17 shows two distinct phases of etching. There is an initial large increase in track length over a relatively short time inteval. At a track length of 18 μm, further increase in etching time produces only a very small increase in track length. The first phase (represented by the line AB, fig 2.17) of etchant attack corresponds to the solution rapidly etching the damaged region (caused by the fission fragment) until it reaches the end of the fission fragment range in the detector. The second phase (line CD) is governed by the velocity of attack on the undamaged (bulk) of the detector. Thus, both the rate of chemical attack along the track (R_t), and the rate of chemical attack of the bulk of the detector (R_b) can be calculated. From the graph:-

R_t = 18.8 μm in 7 minutes

= 161 μm per hour

R_b = 2 μm for 6 minutes

= 20 μm per hour

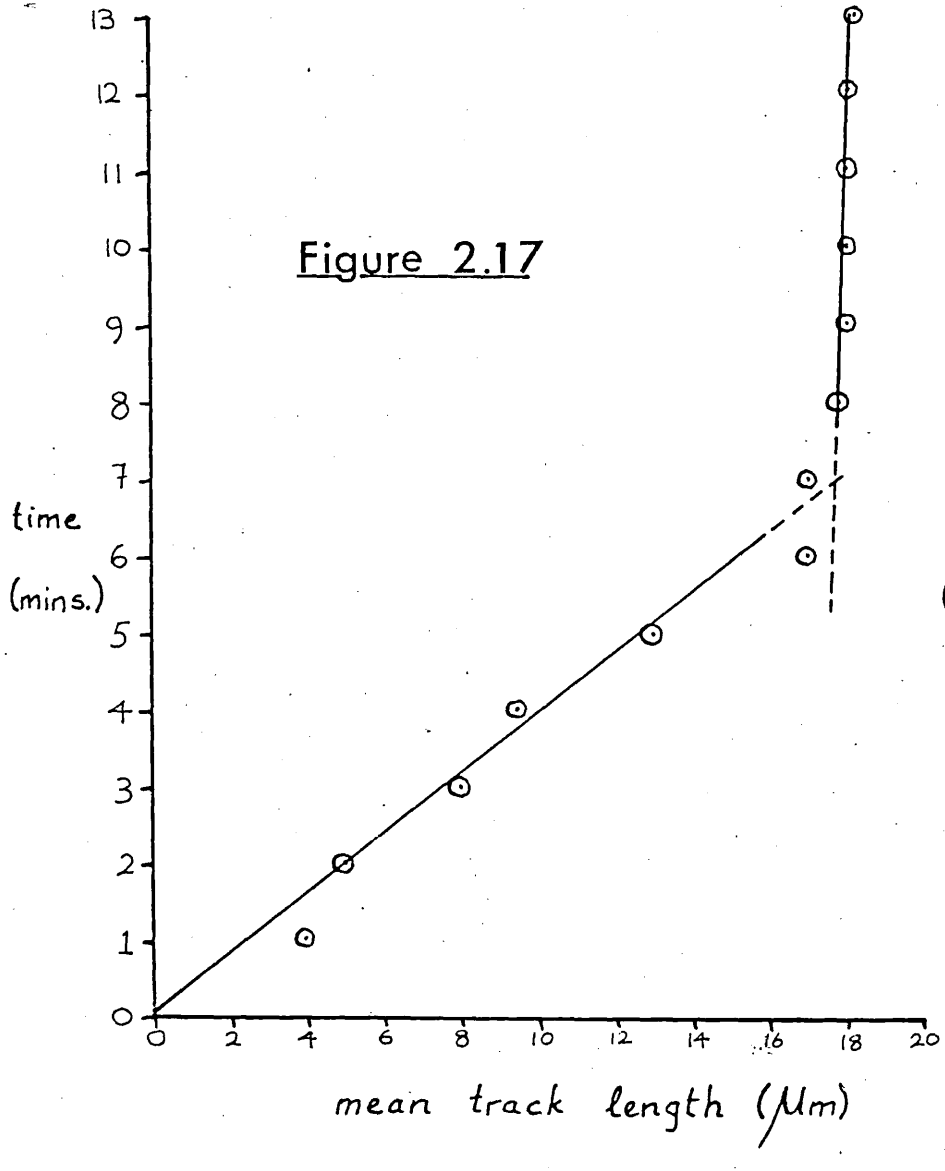

Figure 2.17

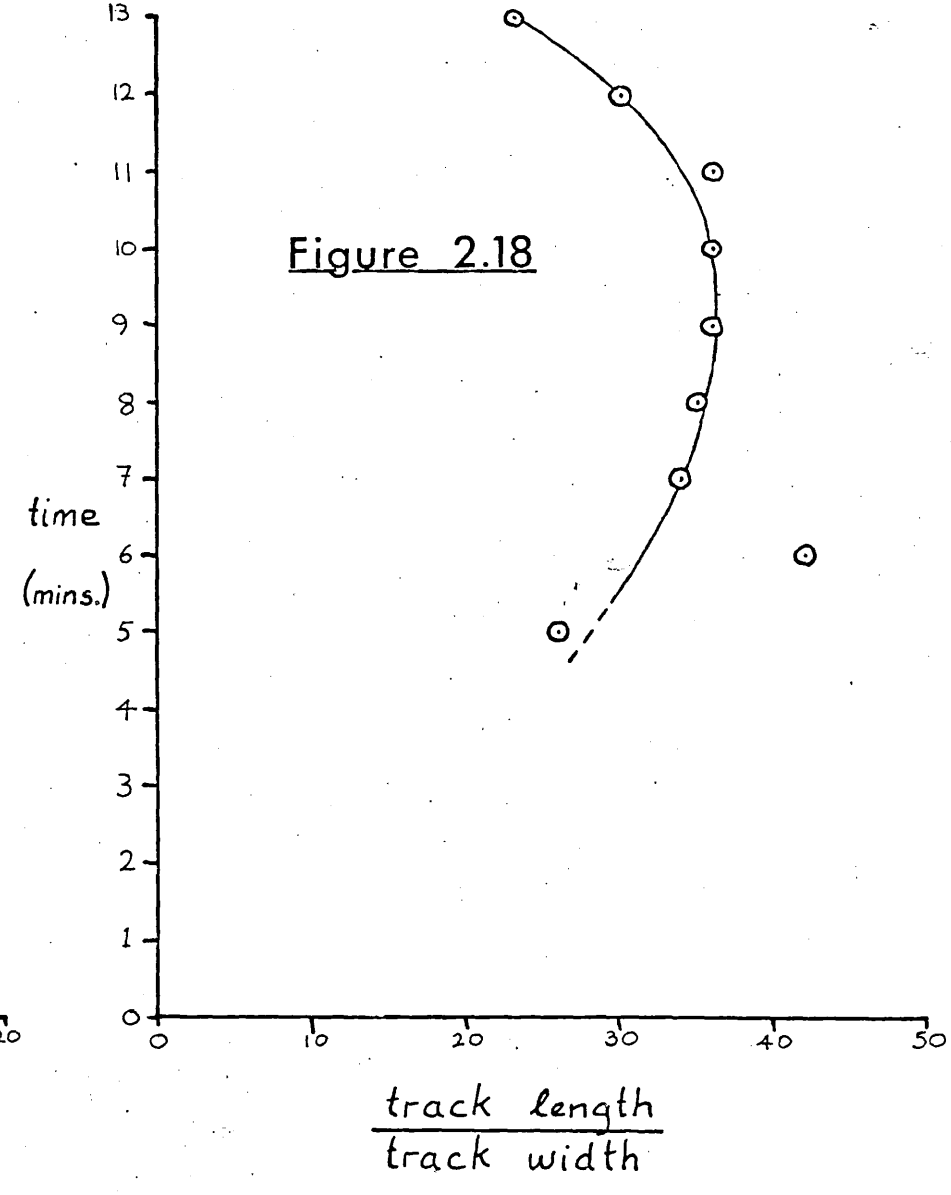

Figure 2.18

By substituting these values of R_b and R_t into Fleischers et al. (1964) formula for calculating the critical angle of incidence θ_c (Section 2.2.3):- $\theta_c = \sin^{-1} \frac{R_b}{R_t}$

θ_c is found to be approximately 7°.

However the value R_b calculated here is at very best an approximation since changes of track length under 0.2 μm cannot be resolved with any degree of accuracy. Thus, large errors will result when attempts to measure very small changes of track length are made. When, therefore, the Paretzke et al. (1973) value of R_b for makrofol at 70°c ($R_b = 1.6$ μm hr $^{-1}$), is substituted into the same equation, θ_c has the approximate value of 1°.

Although R_b appears constant, the track width was seen to increase w.r.t. the length. Fig 2.17 shows with increasing time, a decrease in the track length/width ratio such that an optimum track definition exists. In this case the optimum definition was after 10 minutes ($\pm$ 1 minute).

It was of course important to etch both standards and specimens under idential conditions. Fig 2.19 shows the variation in track density with etching time. A maximum (optimum) density at 10 $\pm$ $\frac{1}{2}$ minute was reached, and which then decreased with further increases in etching time. There appeared to be two factors affecting the shape of the graph (fig 2.19). At low etching times the tracks have not fully developed to their maximum size. The track density will then depend upon the magnification used (in this case X400), and the revolving power of the microscope lenses. At high etching times definition is lost (see fig 2.18, tracks become overetched, overlapping may occur, and tracks with low angles of incidence become "etched out". At the optimum track

Figure 2.19

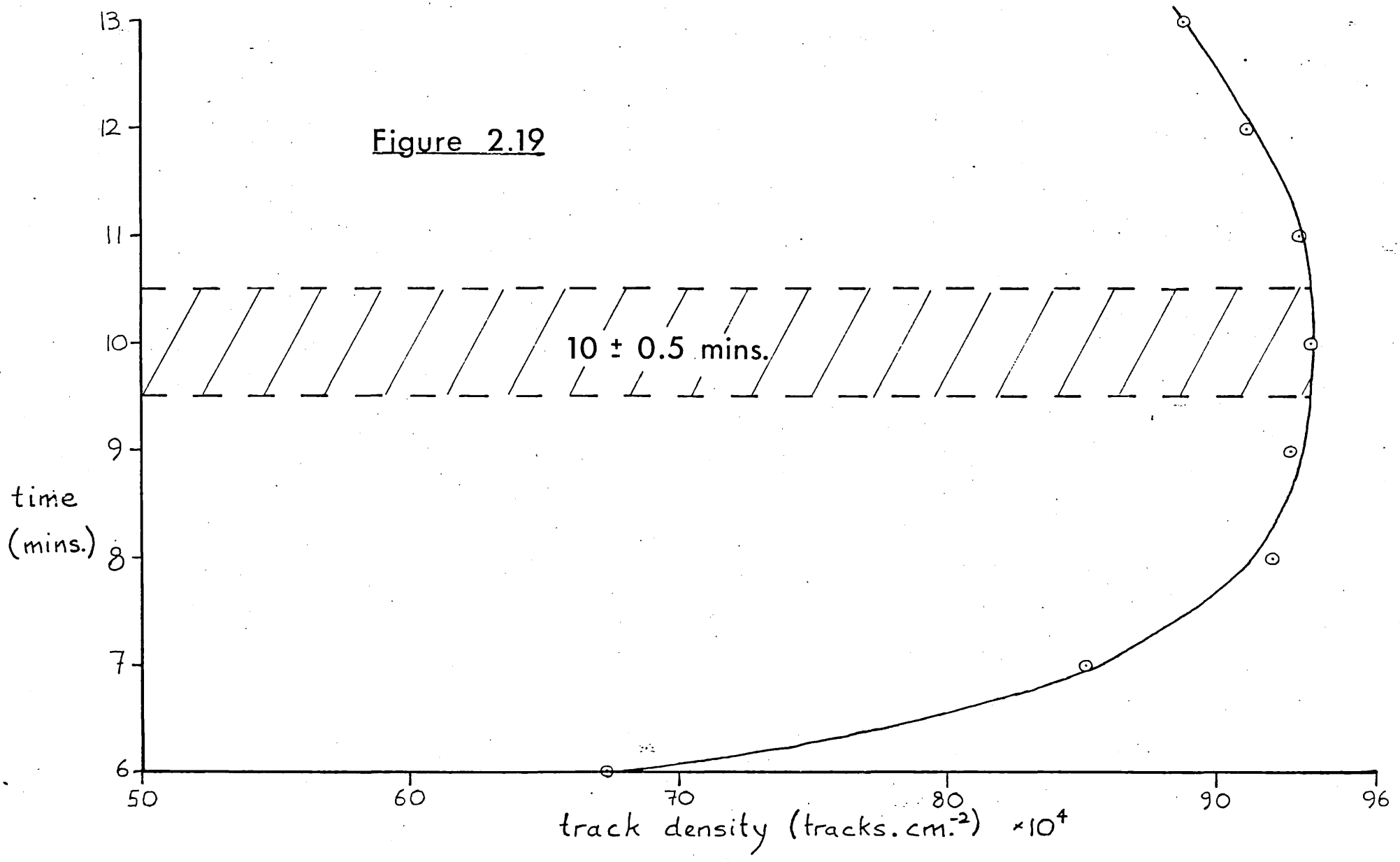
13
12
11
10
9
8
7
6
time (mins.)
10 ± 0.5 mins.
50
60
70
80
90
96
track density (tracks.cm.$^{-2}$) ×10^4

density and time (10 minutes) a variation in etching times of $\pm$ 0.5 minutes results in a variation in track density of only 0.2%.

During routine etching the solution was stirred approximately every 60 seconds to ensure a layer of etch products did not accumulate on the detector surface. Khan (1973) formalised this aspect of etching when he quantitatively showed the adverse effects of an "etch product layer" on the bulk etching rate.

2.6.4. Counting errors

In either visual or (particularly) automatic track counting, probably the greatest source of error arises in deciding whether a feature in the S.S.T.D. is a fission track or a detector defect. This error was minimised by using organic S.S.T.D.'s since they are not so prone to defects as inorganic S.S.T.D.'s. In fact, the vast majority of tracks in a S.S.T.D. are easily recognised as such when viewed visually (at suitable magnification) since they form straight, linear defects; are of limited size; are randomly orientated (in general), and are inclined at an angle to the detector surface. Occasionally however, a subjective criteria needs to be employed to decide whether a feature is to be counted as a track or not. With experience, subjective errors can be standardised, and at low track counts may be eliminated, since there are fewer features and more time can be allocated to their correct identification. So, paradoxically, low track counts are likely to be more accurate than higher track counts. When counting the standard (with a relatively high track density) where up to 50 track counts were often performed, care was taken to correctly identify border line features in order to minimise subjective errors.

When counting tracks with the Quantimet 720 (Section 2.2.5), tracks perpendicular to the detector surface were often not detected (there is a visual display of detected features - fig 2.14). Consequently numerical adjustments to the output were sometimes required. This simply entailed recording manually the excess number of fission tracks in that area count.

2.7. Evaluation of Errors Involved in Fission Track Analysis.

Inherent within any analytical technique is the likelihood of error. A measurement of the degree of error involved is necessary in order that the data presented can be evaluated in terms of reproducibility of results and how close the analysed value is to the "true" or intrinsic value. By the combination of a statistical analysis on a series of results and consideration of errors inherent in the technique itself, an evaluation of the precision and accuracy of the data, and the sensitivity and selectivity of the technique can be made.

2.7.1. Precision and accuracy of results.

Statistical interpretation of results permits an unbiased presentation and the determination of the degree of useful ness of the data collected. The reproducibility, i.e. the precision, and the measure of correctness of the data, i.e. the accuracy, can be expressed in mathematical terms.

In order to determine the precision of results obtained by fission track analysis, 100 area counts over an area of $1.746 \times 10^5 \mu m^2$ were performed on three standard glasses (section 2.4.) using the Quantimet 720 and a magnification of X400. The same specimens were manually counted using the Zeiss photomicroscope again at a magnification of X400 and over an area of 1.44×10^5 μm^2 in steps of $120 \times 120 \mu m^2$ squares. The standard deviations

(S.D.) and coefficient of variations (or mean standard deviations, C) from these results are presented in table 2.8.

$$\text{where S.D.} = \sqrt{\sum d^2/(n-1)}$$

$$C = \frac{\text{S.D.} \times 100}{\bar{x}}$$

where d is the deviation of a specific result from the arithmetic mean, $\bar{x}$, of a number of determinations, n.

Table 2.8.

	S.D.		C %		track density ($\times 10^5$ tracks. cm^{-2})	
	Quantimet	Zeiss	Quantimet	Zeiss	Quantimet	Zeiss
SRM 614	0.18	0.60	.381	1.23	3.370	3.368
50 x 24	0.47	1.58	.380	1.27	8.667	8.635
Geoscan	0.20	0.63	.377	1.17	3.750	3.750

Thus, from the table 2.8, a precision of $\pm$ 1.5% is attainable at a confidence limit of $\pm 2\sigma$ (i.e. 95.4% probability).

The degree to which a particular result corresponds to the true, or intrinsic, value is often difficult to determine since this value is not really known. For this reason, a series of standard rocks (e.g. Flanagan, 1973) came into use having generally accepted values for different elements. An estimation of the accuracy could then be obtained for a particular technique, or batch of samples, by comparing the values obtained for a standard rock with the published values. However, such a procedure could not be used for fission track analysis, since mineral standards with uranium concentrations at the p.p.b. level are not obtainable. Nevertheless, an indication of the accuracy was obtained when six specimens from a batch of 50 x 24 glass slides were analysed by both fission track analysis and delayed neutron activation

analysis, D.N.A.A., (Section 2.4., table 2.5.). D.N.A.A. gave a uranium concentration of 0.362 p.p.m. from an average of six analyses (mean S.D. = 4.3), and fission track analyses a concentration of 0.344 p.p.m. from six analyses (mean S.D. =0.80). These two values are within five percent of each other. It should be noted however, that a much greater degree of precision was obtained using the fission track technique.

2.7.2. Sensitivity and selectivity of the technique.

The sensitivity of the fission track technique depends upon three factors:-

1) the thermal neutron dose

2) the intrinsic uranium concentration of the detector

3) counting a sufficient number of tracks to allow reasonable counting statistics.

Since the number of tracks produced from a given concentration of ^{235}U is proportional to the thermal neutron dose, then, from a first approximation, the higher the dose, the greater will be the sensitivity. However, from experiments on organic detectors (section 2.5.) it was found that doses in excess of 4×10^{17} neutron. cm^{-2} disrupted the structure of these detectors making them unusable. Thus for organic detectors, the maximum workable dose was considered to be 2×10^{17} neutrons. cm^{-2}.

An estimation of the uranium content of makrofol S.S.T.D. gave a value of 0.16 p.p.b. (table 2.7.)

Carpenter (1972) noted that uncertainty due to counting statistics varied directly with the square root of the number of events observed, and that the precision of the results may suffer if an insufficient number of observations are made. Using automated track counting techniques, Besant and Ipson (1970) suggested that at track densities greater than approximately 5×10^{4} tracks. cm^{-2}, overlapping may begin to introduce errors.

Ching-Shen Su (1972) also found that the number of observed fission tracks was proportional to the uranium concentration at low track densities, but that the linearity disappeared at high track densities.

Price and Walker (1962) suggested a detection limit of twice the background level, viz. the tracks emanating from the makrofol S.S.T.D., is attainable. At a thermal neutron dose of 2×10^{17} neutrons.cm^{-2} this corresponds to a density of approximately 700 tracks. cm^{-2}, and is equivalent to approximately 0.3 p.p.b. uranium. A peak to background ratio of 10 indicates a sensitivity of 1.5 p.p.b. (3000 tracks. cm^{-2}) at a dose of 2×10^{17} neutrons. cm^{-2}. Therefore the optimum working range is from 1.5 p.p.b. to 25 p.p.b. (5×10^{4} tracks. cm^{-2} - from Besant and Ipson, 1970). Since this upper limit refers essentially to automatic counting techniques where overlapping of tracks cannot easily be resolved, by careful manual counting, the working range can be extended to 25 p.p.m. (at 2×10^{17} neutrons. cm^{-2}) and 50 p.p.m. (at 1×10^{17} neutrons. cm^{-2}). At concentrations of uranium above this level, the fission tracks overlap to such an extent that the detector is, in effect, saturated.

Although a number of other elements can produce etchable particle tracks in organic detectors (e.g. lithium and boron, Kleeman 1973; lead, Hamilton, 1971; oxygen, Carpenter et al., 1973; thorium and ^{238}U, Hair et al., 1971), only ^{232}Th and ^{238}U form tracks of comparable size to ^{235}U in makrofol and lexan S.S.T.D.'s irradiated in a thermal neutron dose. The error produced by ^{232}Th and ^{238}U are fortunately small since these isotopes only fission under bombardment of fast neutrons (see section 2.1.), and have much lower capture cross-section '

values than ^{235}U (table 2.1.). Assuming Th/U ratios of exceptionally 10 to 1 (Burnett et al., 1971) and thermal/fast ratios of typically 10^2 (table 2.2.), the contribution of fission fragments from thorium is approximately one percent. Assuming also a natural isotopic abundance ratio between ^{238}U and ^{235}U (approximately 140, table 2.1.), the contribution from ^{235}U amounts to only 0.12%. The technique then is very selective using makrofol or lexan S.S.T.D., the only interfering elements, thorium and ^{238}U producing, in general approximately one percent error.

A more serious type of error is introduced in the form of matrix effects when non-silicates are being analysed. Since the range of fission fragments varys according to the media in which they travel, Mory et al. (1970), the term R_{stand}/R_{spec} in equation (5), section 2.1.6., will not be constant. In practice, for most silicates, this term approximates to unity, but may deviate considerably for non-silicates, e.g. for PbS, R_{stand}/R_{spec} has a value of 0.33 (Schreurs et al., 1971). This problem may however, be partially overcome by estimating the value of R_{spec} from Mory et al. (ibid.), and, in calculating the uranium contents of some of the oxide minerals (chapter 5), this estimation was performed.

The precision and accuracy then of fission track analysis is comparable with other techniques for the determination of uranium (Fisher, 1975) and has the added advantage of being able to map the distribution of that element in rock sections. An overall accuracy of $\pm$ 5% for concentrations up to approximately 100 p.p.b. and $\pm$ 10% for concentrations greater than 100 p.p.b. is considered to have been achieved.

2.8. Electron-probe Microanalysis.

An additional technique was employed to determine the concentrations and distributions of elements within mineral phases, that of electron-probe microanalysis. Analyses were performed on the same polished thin sections as those used for uranium distribution studies, and the contact print photographs used initially in the fission track method, were found to be useful for location purposes in the electron-probe microanalysis technique.

The two instruments used in this thesis were the Cambridge "Geoscan" (at Imperial College, London University), and the Jeol 50A Scanning Electron Microscope (at Chelsea College, London University).

2.8.1. Cambridge "Geoscan" electron microprobe.

This instrument was used mainly for quantitative analysis of selected minerals using as standards natural or synthetic minerals. The Geoscan at Imperial College has available two spectrometers, whereby two elements may be analysed simultaneously, and a choice of five crystals (PET, LiF, TlAP, mica and quartz). The details of elements analysed, crystals used etc., are given below in table 2.9. Routine procedure of analysis was undertaken for the major elements.

For the standards, a total of 10,000 counts were accumulated both at the beginning and at the end of the run. Specimens were counted for three or four ten-second counts. For the background, two ten-second counts approximately two degrees 2 θ either side of the peak were determined for both standards and specimens. The data was then corrected for both instrumental (i.e. background, dead-time and drift) and matrix (fluorescence, absorption and atomic number) effects using the Imperial College'

programme (PTMK5) by Mason et al., 1968

For the determination of minor elements Ni and Ca in olivines, a manual scan across the peaks was initially performed in order to locate precisely the apex of these peaks. Three 100-second counts were accumulated and averaged for each point. The data were corrected in the same way for instrumental and matrix effects.

Table 2.9.

Element	X-Ray Line	Crystal	Bragg Angle (2θ)	Standard Used.
K	K	PET	51° 08'	KTANT (synthetic potassium tantalate)
Zr	L 1	PET	83° 30'	PUREZR (Zr metal)
Y	L 1	PET	95° 06'	YIG (synthetic yttrium iron garnet)
Si	K	TlAP	32° 08'	WOLL2 (natural wollastonite)
Mg	K	TlAP	45° 11'	FORST (synthetic forsterite)
Al	K	TlAP	37° 49'	MGALOX (synthetic spinel)
Na	K	TlAP	55° 07'	JAD2 (Natural jadeite)
Fe	K	LIF	57° 15'	FE2O3 (synthetic iron oxide)
Ni	K	LIF	48° 10'	NIOX (Nickel Oxide)
Ti	K	LIF	85° 85'	TIOX (synthetic titanium oxide)
Ca	K	LIF	112° 57'	WOLL2 (natural wollastonite)
Mn	K	LIF	62° 46'	RHODON (natural rhodonite)

2.8.2. Jeol 50A Scanning Electron Microscope.

This instrument was used for three purposes - location of small mineral phases, rapid qualitative analysis of minerals,

and for obtaining elemental distribution maps of a given area within the rock specimen.

In the uranium distribution maps of the Rhum cumulates, a rdatively frequent occurrence is the appearance of fission track "stars". These corresponded to small, uranium-enriched mineral phases (chapter 5, section 5.4.). These minerals were in all cases found to be either phosphorus or zirconium bearing and were often only of the order of 20 - 30 μm in size making them difficult to locate using a petrological microscope. By use of the energy-dispersive detector on the scanning electron microscope (S.E.M.), a window could be set such that only phosphorus (K_α) and zirconium (L_α) were detected (between 1.9 and 2.1 keV). Then, with reference to the fission track contact print, the area of the rock corresponding to the fission track star was scanned at approximately X600 magnification on the P/Zr channel. The uranium source mineral was readily located by an accumulation of dots on the cathode ray fluorescent screen. Rapid identification and qualitative analysis of the phase could then be obtained by displaying the full spectrum from a 100 second spot analysis.

Elemental distribution scans of mesostasis areas were obtained for a variety of elements (chapter 5) using a similar procedure. A window was set at the upper and lower limits on the most intense peak of the element concerned (usuall the K line), and a slow raster (50 seconds for major elements) performed. The image obtained on the cathode ray screen was then photographed. In order to relate elemental scanning pictures to the rock surface, a secondary electron image (S.E.I.) or absorbed electron image (A.E.I.) of the area at the same magnification was photographed.

Use of the energy dispersive detector was made in order to establish whether major element zoning was present in the cumulus phases, in particular the olivines and heteradcumulus feldspars and clinopyroxenes. This was performed by comparing integrated peak areas of selected major elements across the surface of the grain. For olivines, Mg and Fe were determined; for plagioclase feldspar, Ca and Na; and for clinopyroxene Fe, Mg and Ca.

CHAPTER 3 URANIUM DISTRIBUTION - RESULTS.

3.1. Introduction.

Uranium is a strangely paradoxical element. From the immense amount of energy attainable from its nuclear properties, used constructively, it can benefit mankind in a technological society by providing a stable energy source. Used destructively however, it is capable of eliminating organic life on earth.

In spite of its increasing importance in economic aspects of geology there is not a great amount of detailed geochemical data of uranium in major rock-forming minerals. This is undoubtably a result of its low abundance in these minerals (often to sub-p.p.m. levels), and, until the initiation of fission track studies, problems involving its analysis at these very low levels prevented much detailed work.

This chapter presents analytical results for uranium in the major cumulus phases, and also provides a general guide to the manner in which uranium behaves in a crystallising basic magma. Before, however, discussing its behaviour in magmas, some information regarding its electronic configuration and aqueous chemistry is desirable.

3.1.1. Uranium - its electronic configuration.

The electronic configuration of the uranium atom (atomic number 92) is such that there are three/partially filled orbitals, $5f^3\ 6d^1\ 7s^2$, the removal of electrons from which give rise to four oxidation states (table 3.1.).

Table 3.1.

Oxidation state	0	+3	+4	+5	+6
Electronic configuration	$5f^3 6d^1 7s^2$	$5f^3$	$5f^2$	$5f^1$	$5f^0$

A measure of the relative stabilities of the four oxidation states may be obtained by an examination of the oxidation/reduction couples (for an acidic media), table 3.2. - from Moeller, 1963. Although direct comparisons between aqueous solutions and silicate melts can not usually be made, indications of the possible existence of ionic species in silicate melts can be obtained from the aqueous chemistry. From this table then, it can be seen that U^{3+} would act

Table 3.2.

Oxidation/ Reduction couple	Oxidation state	E^{0}_{298} (volts)	ionic radius* (nanometres)
$U^{0} - U^{3+}$	3	-1.80	$U^{3+} = 11.3$
$U^{3+} - U^{4+}$	4	-0.631	$U^{4+} = 10.6$
$U^{4+} - UO_2^{+}$	5	+0.58	
$UO_2^{+} - UO_2^{2+}$	6	+0.063	

* From Whittaker and Muntus (1970).

as a powerful reducing agent and is therefore probably unstable in silicate melts. UO_2^{+} is unstable in the presence of water (Moeller, 1963), being either reduced to U^{4+}, or oxidised to UO_2^{2+}. With few exceptions then, only the U^{4+} and UO_2^{2+} ions are capable of existing in aqueous solutions (and hence, probably in silicate melts). Under oxidising conditions, and in the presence of water (i.e. analagous to late-stage crystallisation of basic magmas, chapter 5), U^{4+} oxidises to produce the doubly-charged uranyl, UO_2^{2+}, ion.

$$U^{4+} + 2H_2O \longrightarrow UO_2^{2+} + 4H^{+} + 2e \qquad (1)$$

where $E^{0}_{278} = +0.64$ volts.

3.1.2. Uranium - its geochemistry in basic and ultrabasic rocks and magmas.

The concentration of uranium in ultrabasic rocks is invariably

lower than in more acidic rocks. Hagland (1972) reports values of between 0.001 and 0.8 p.p.m. uranium for intrusive ultrabasic rocks, and between 0.15 and 21 p.p.m. for intrusive acidic rocks.

In basic and ultrabasic igneous cumulates, although mean uranium concentrations are low, there is also observed a relatively wide range of concentrations. Gijbels et al., (1974) report a range of between 0.011 and 0.066 p.p.m. for the Bushveld intrusion: Henderson et al. (1971) found that values obtained from the Rhum intrusion were lower than those from the Skaergaard intrusion (Rhum mean, approximately 0.040 p.p.m., Skaergaard mean, 0.24 p.p.m.), and that the uranium content gave an indication of the relative amount of mesostasis in the rock, if minerals such as apatite and zircon were not present as cumulus phases.

A summary of uranium concentrations in tholeiitic basalts (Fisher, 1975) shows that average values range from 0.075 to 0.300 p.p.m. Henderson et al. (1971) from an estimation of the amount of pore material in the Rhum cumulates, calculated a minimum value of 0.4 p.p.m. uranium in the contemporary magma. For this study, a value of 0.3 p.p.m. was used in calculations of partition coefficients of various minerals (chapter 4, sections 4.3. to 4.7.).

The behaviour of uranium in the crystallisation of a basic magma appears to be controlled largely by its greater inherant stability in the magma. At the onset of crystallisation, uranium acts as a low-partitioning (low-k) element,

$$\text{where } k = \frac{(M)_{\text{mineral}}}{(M)_{\text{magma}}}$$

where $(M)_{\text{mineral}}$ is the concentration, wt./wt., of element M in the mineral

$(M)_{\text{magma}}$ is the concentration, wt./wt., of element M in the magma.

and in the cumulus phases of Rhum, assuming a value of $(M)_{magma}$ to be 0.3 p.p.m., values of k between 1.3×10^{-2} and 1.3×10^{-1} are found (chapter 4).

Several topics of research have arisen from whole-rock and inter-mineral uranium distribution studies on basic and ultrabasic rocks. Henderson (1968, 1970) and Henderson et al., (1971) showed that the amount of uranium in layered basic intrusions could be correlated with the amount of mesostasis in the rock, and to the degree of fractionation efficiency (Henderson, 1975). Fisher (1970) in comparing K/U ratios for a variety of ultrabasic rocks with crustal and chondritic ratios, found that the data were in disagreement with the concept of a chondritic earth. Studies of uranium distributions and concentrations in basic and ultrabasic rocks of possible mantle origin have aided in the formulation of heat-flow models (e.g. Haines and Zartman, 1973), and in models relating to magma genesis (e.g. Seitz and Hart, 1973). Also in ultrabasic inclusions, correlations between uranium and phosphorus (e.g. Kleeman et al., 1969) and uranium and light rare earth elements (e.g. Frey and Green, 1974) have been observed. In lunar basic and ultrabasic rocks, geochemical coherences have been shown to exist between uranium and potassium (e.g. Lovering et al., 1972) uranium and zirconium (e.g. Thiel et al., 1972) and uranium and mesostasis areas (e.g. Rice and Bowie, 1971).

There is a small amount of data from experimental work on uranium distribution studies involving silicate melts. With the aid of fission track analysis, Seitz and Shimizu (1972) and Seitz (1973, a) obtained uranium partition coefficients of pyroxenes grown from diopsidic melts, and calculated diffusion coefficients for uranium within diopside and zircon crystals

(Seitz, 1973, b). From such experiments, Seitz (1973, a), found that the partitioning behaviour of uranium in silicate melts appears to be independent of the temperature and pressure, and of both its actual concentration in the melt and the chemical composition of the melt itself. In addition, Seitz (1974, a) observed that partition coefficients from natural systems are consistently higher than values measured from synthetic systems under equilibrium conditions of crystallisation. This Seitz (ibid.) suggests may be due to the non-equilibrium conditions in some natural systems, and Seitz (1974, b) in fact observed a disequilibrium growth phenomenon in a study of the thorium distribution in experimental charges.

The oxidation state, or states, of uranium in magmas is uncertain. Cherdyntsev (1971) estimates that 20 - 30% of uranium exists as the hexavalent form in acidic rocks, and since the $U^{4+} - UO_2^{2+}$ couple is sensitive to oxidation (equation (1)), it is predominantly the UO_2^{2+} ion which occurs in ground waters and in sedimentary rocks deposited near to the surface.

However, at the onset of crystallisation of basic and ultrabasic magmas and in mantle or deep-seated environments, reducing conditions are likely to prevail. In such environments, a large proportion of uranium is likely to exist as the U^{4+} ion. The ionic radii of the U^{4+} and Ca^{2+} ions are similar (U^{4+} = 10.6 nanometres, Ca^{2+}=10.8 nanometres-Whittaker and Muntus, 1970), and, there is an apparent geochemical compatability between these two elements in their distribution within the olivine phase (chapter 4, section 4.3.). In the late-stage crystallisation of Rhum, the presence of intercumulus magnetite and evidence of water (as for example in the hydrothermal minerals, chapter 5, section 5.2.1.), indicates that uranium is likely to have

adopted the UO_2^{2+} species. In this form, entry into the final minerals to crystallise, such as the zirconium-bearing minerals (chapter 5, section 5.4.), is possible, and consistent with Wilkins (1971) observation that the UO_2^{2+} ion occurs in uranium-enriched minerals. In the majority of the Rhum minerals however, there is no evidence to indicate whether uranium is present as either in the U^{4+} or UO_2^{2+} species.

3.2. The distribution of uranium in the Rhum and Carlingford cumulates.

A study of the distribution of uranium within the ultra-basic cumulates of Rhum and Carlingford by the fission track technique was undertaken. From the results obtained, four distinct groups (with respect to the uranium concentrations) can be delineated.

Group 1: Extremely-low uranium (less than 0.1 p.p.m.) chapter 4, sections 4.3. to 4.7.

Group 2: Low uranium (0.1 to 10 p.p.m.), chapter 5, section 5.2.

Group 3: Medium uranium (10 - 100 p.p.m.), chapter 5, section 5.3.

Group 4: High uranium (greater than 100 p.p.m. chapter 5, section 5.4.

The salient features of these groups are tabulated in table 3.3.

Table 3.3.

	% of total uranium	% modal volume	U(p.p.m.)	Minerals
Extremely-low	less than 40%	95 -98%	0.001 to 0.1	olivine; clinopyroxene; feldspar; chrome spinel.
Low-uranium	approximately 5%	2 - 5%	0.1 to 10	biotite; ilmenite; chlorite; magnetite etc.,
Medium-uranium	approximately 5%	approx-imately 0.1%	10 to 100	apatite.
High-uranium	approximately 50%	less than 0.01%	greater than 100	zircon; baddeyelite; zirconolite (or zirkelite).

Most of the uranium is located in small discrete phases, often not larger than 50 μm in size and containing greater than 100 p.p.m. uranium (chapter 5, section 5.4.). Mineralogically, these phases are baddeyelite, zircon and zirconolite - or zirkelite (a Ca-Ti-Zr oxide containing minor amounts of Fe and Y). Approximately 5% of the total uranium is contained in apatite crystals having uranium concentrations varying from 25 to 75 p.p.m. (chapter 5, section 5.3.). Approximately 5% of the total uranium is bound up in minerals of the low uranium group (uranium concentration of 0.1 to 10 p.p.m.). The accessory or hydrothermal minerals of this group, such as biotite, ilmenite, chlorite etc., are discussed in chapter 5, section 5.2. The cumulus minerals, i.e. olivine, feldspar, clinopyroxene and chrome spinel, although contributing 95 to 98%

of the modal volume, contain only approximately 40% of the total uranium and have uranium concentrations less than 0.1 p.p.m. This group is discussed in chapter 4.

3.3. Uranium in cumulus minerals.

Uranium concentrations, determined by the fission track (contact print) method, of the cumulus minerals are tabulated in this section.

Track counting was performed visually using the Zeiss photomicroscope at a magnification of x400 with the projection head attachment (chapter 2, section 2.3.4.).

Areas within the mineral free from inclusions and cracks were chosen for analysis and where possible, 100 area counts each 100 μm. x 100 μm. (corresponding to an area on the projection head of 80 mm. x 80 m.m.) determined on the detector using the contact print method (chapter 2, section 2.2.3.). Similar area counts on two standards were performed. An internal standard used was the "Geoscan" or "50 x 24" glass slide, and an external standard the SRM-614.

The area counts for both standards and standard glass specimens were converted to tracks per cm^2 and corrected for background. This was achieved by subtracting from these values the number of tracks expected from the makrofol at the thermal neutron dose used for the specimens. The number of tracks resulting from the makrofol was previously determined as 120 tracks cm^{-2} at a thermal neutron dose of 6×10^{16} neutrons.cm^{-2} (chapter 2, section 2.5.); at a thermal neutron dose of x' neutrons.cm^{-2}, the contribution from the makrofol can therefore be calculated from the formula:-

$$x' (\text{neutron.cm}^{-2}) \times \frac{120 \text{ tracks.cm}^{-2}}{6 \times 10^{16} \text{ neutrons. cm}^{-2}}$$

In calculating the uranium concentration of the mineral (chapter 2, section 2.1.6.) values for the mean fission fragment range were required. This term (R_{spec} in equations (5) and (6), chapter 2), has been evaluated for a variety of minerals from the formula by Mory et al., (1970) and is shown in tables 3.10 and 3.11.

In table 3.5. of uranium concentration within the Rhum cumulus minerals, a note regarding the rock type nomenclature (column 2) is required. The nomenclature used here follows Wager et al.'s (1960) usage of orthocumulate, mesocumulate, adcumulate, heteradcumulate and crescumulate (see chapter 1, section 1.2.) with Wager and Brown's (1968, pp. 553-5) modification of prefixing, in decreasing order of abundance, the cumulus minerals. Classification of a rock into an adcumulate (or heteradcumulate), mesocumulate or orthocumulate is based on:-

1) The extent and degree of optical zoning of the feldspar.

2) The uranium concentration of the feldspars (chapter 4, section 4.5.) in the following manner (table 3.4.)

Table 3.4.

U (p.p.b.) of feldspar	morphology	rock type
less than 15.2	poikilitic	heteradcumulate
less than 18.8	tabular (cumulus)	adcumulate (unless clinopyroxene is poikilitic - then heteradcumulate)
15.2 to 25.0	poikilitic)	mesocumulate
18.8 to 25.0	tabular)	
greater than 25.0	poikilitic and tabular	orthocumulate

Tables 3.5. and 3.6. show, with increasing height in the intrusions, the morphologies and modal percentages of the major cumulus minerals, viz. olivine, plagioclase feldspar and clinopyroxene within the Rhum and Carlingford samples. The uranium concentrations of these minerals, together with the whole rock uranium concentrations are also given in these tables. Microprobe analyses of the olivines (table 3.7.) and plagioclase feldspar (table 3.8.) - details of the procedure are given in chapter 2, section 2.8. - show a relative constancy in composition throughout the Rhum eastern layered series, both with morphological variation and with height, and are compositionally similar to the olivine crescumulate samples (H.1. to H.10) from the Rhum western layered series (table 3.9.). In contrast to the relative constancy of the major and minor element concentrations, the concentrations of uranium, within, in particular, the olivine phase, show a marked variation which can be correlated to the crystal morphology. This relationship is diagrammatically shown in figure 3.1 and is discussed in more detail in chapter 4.

	morphology	U p.p.b. range	mean
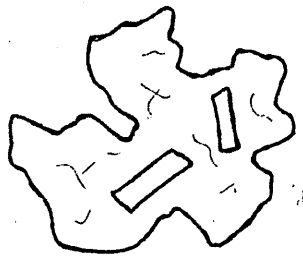	poikilitic	4.30 - 4.52	4.42
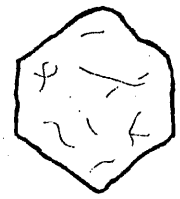	equant	4.88 - 5.33	4.99
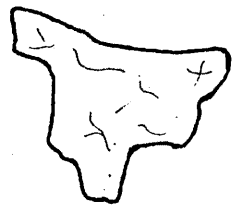	irregular	5.13 - 6.71	5.99
	rounded	5.17 - 6.40	5.92
	tabular	6.35 - 8.03	7.16
	harrisitic	8.21 - 8.43	8.32

Figure 3.1

Table 3.5. (Rhum cumulus materials)

Specimen number	Rock type +	Unit Number and height in metres	Olivine			Plagioclase			Clinopyroxene			
			Morphology *	Modal %	U (p.p.b.)	Morphology **	Modal %	U (p.p.b.)	Morphology **	Modal %	U (p.p.b.)	U whole rock (p.p.b.) ++
R90	feld.-ol.-cpx. ortho.	1 (9.1)	1) rounded 2) equant	2.3 34.1	5.73 5.01	tab.	30.6	25.61	poik.	31.2	33.14	116
R91	feld.-ol.-cpx. ortho.	1 (15.2)	1) equant 2) tabular	24.5 12.4	5.13 6.91	tab.	40.9	29.39	poik.	20.8	35.39	123
R92	ol.-feld.-cpx. ortho.	2 (18.9)	1) equant 2) rounded	59.3 11.1	4.93 5.89	poik.	8.3	28.44	poik.	20.7	36.15	110
R93	ol.-feld.-cpx. ortho	2 (27.4)	equant to irregular	65.8	5.69	poik.	7.6	29.03	poik.	25.9	32.09	-
R94	ol.-feld.-meso.	2 (36.6)	equant	64.3	4.99	poik.	34.8	18.46		absent		80
R95	feld.-ol. cpx. ortho.	2 (48.8)	1) irregular 2) tabular	16.2 12.3	6.71 6.92	poik.	59.2	26.80	poik.	8.6	29.92	101
R11	feld.-cpx.-ol. ortho.	2 (48.8)	equant to rounded	9.3	n.d. (extensive alteration)	tab.	58.0	25.33	poik.	29.8	34.18	'185

Table 3.5 continued .....

R.96	ol.-feld.-cpx. ortho.	3 (53.3)	1) tabular 2) equant to irregular	23.6 35.4	8.03 6.38	poik.	28.3	23.91	poik.	11.0	30.14	131
R99	ol.-feld.-cpx. meso.	3 (64.0)	1) equant 2) rounded 3)irregular	18.4 19.8 3.5	5.27 6.11 5.66	poik.	36.9	21.66	poik.	18.2	29.00	84
R89	feld.-ol. cpx. meso.	3 (187.4)	poik. to sub-poik.	28.3	4.52	tab.	47.1	24.04	poik.	22.3	33.10	73
R86	feld.-cpx.-ol. meso.	3 (195.1)	poik.	18.7	4.47	tab.	52.2	21.31	cum.	25.3	34.5	69
R87	feld. cpx.-ol. meso.	3 (197.2)	poik.	13.8	4.47	tab.	48.8	18.88	cum.	35.1	34.50	46
R83	ol.-cpx.-feld. meso.	5 (213.4)	equant to rounded	80.3	5.17	poik.	8.3	19.18	poik.	9.5	28.77	21
R84	ol.-cpx.-feld. meso.	5 (225.6)	equant to tabular	33.4	6.74	poik.	32.0	17.36	poik.	32.2	31.33	27
R85	ol.-cpx.-feld. meso.	5 (243.8)	1) tabular 2) equant	49.1 13.8	6.32 5.10	poik.	16.4	20.40	poik.	17.9	28.66	29
R82	ol.-feld.-cpx. meso.	6 (292.6)	equant	68.5	5.26	poik.	16.2	21.11	poik.	13.4	29.99	30
R120	ol.-feld.-cpx. meso.	7 (312.9)	equant to tabular	48.7	7.34	poik.	16.3	17.31	poik.	46.3	n.d.	-

Table 3.5 continued.....

R61	ol.heterad.	8 (341.4)	rounded to tabular	72.4	6.41	poik.	23.8	13.64	poik.	2.3	n.d.	-
R62	ol.heterad.	8 (349.0)	1) rounded 2) poik. to sub-poik.	18.2 46.8	5.99 4.39	tab. to sub-poik.	18.7	15.81	cum. to sub-poik.	12.2	29.80	-
R63	ol.heterad.	8 (356.6)	1) rounded 2) poik.	18.0 51.3	6.30 4.30	tab. to sub-poik.	25.0	15.17	cum. to sub-poik.	2.9	32.41	-
R112	ol.-(feld.) heterad.	8 (359.7)	equant	69.8	5.33	sub-poik.	20.3	12.50	poik.	8.6	36.11	-
R110	ol.heterad.	8 (362.7)	equant to irregular	69.1	6.44	poik.	21.7	11.88	poik.	7.3	35.60	-
R.111	ol. heterad	8 (363.0)	equant to irregular	68.9	6.08	poik.	20.9	13.04	poik.	9.1	35.24	-
R64	feld. heterad.	8 (365.8)	poik.	43.3	4.34	tab.	52.7	16.83	poik.	3.2	n.d.	-
R65	feld. heterad.	8 (381.0)	irregular	33.7	5.90	tab.	55.2	14.50	poik.	10.6	32.87	-
R53	ol. heterad.	9 (399.3)	1)rounded 2)tabular 3) equant	14.4 52.0 12.7	6.33 7.86 4.88	poik.	11.1	9.54	poik.	8.0	27.32	15
R54	cpx.-feld.-ol. adcum	9 (411.5)	equant to irregular	6.2	5.13	tab.	45.3	17.19	cum.	47.7	33.19	-

Table 3.5 continued.....

R113	ol.-feld.-adcum.	10 (506.0)	equant to rounded	48.7	6.00	tab.	46.1	15.22	sub-poik.	2.1	n.d.	-
R114	ol.heterad	10 (509.0)	equant to rounded	41.0	5.90	poik.	32.6	12.88	poik.	24.2	31.05	-
R66	ol.heterad.	11 (524.3)	equant	67.3	4.96	poik.	23.8	11.32	poik.	7.8	32.45	-
R68	ol.heterad.	11 (548.6)	1)equant 2)tabular	63.4 10.2	4.88 7.72	poik.	20.0	10.68	poik.	5.2	33.60	-
R.23	feld. adcum.	12 (603.5)	absent	-	-	tab.	96.2	13.61	sub-poik.	2.7	n.d.	'15
R115	ol.heterad.	13 (618.7)	equant	71.6	5.00	poik.	18.7	12.13	poik.	7.9	32.60	-
R116	ol.heterad.	13 (652.3)	equant to rounded	49.3	5.39	sub-poik.	39.2	11.49	poik.	10.0	34.11	-
R17	ol.heterad.	14 (673.6)	elongated	68.4	7.00	poik.	21.6	11.22	poik.	9.0	31.04	'11
H1	ol. cres.	-	harrisitic	78.3	8.32	sub-poik.	17.9	13.73	sub-poik.	1.5	n.d.	24
H2	ol. cres.	-	harrisitic	84.6	8.21	sub-poik.	10.5	13.50	sub-poik.	3.2	n.d.	

Table 3.5 continued.....

H3	ol. cres.	-	harrisitic	76.9	8.37	sub-poik.	20.4	14.17	sub-poik.	1.3	n.d.
H7	ol.cres.	-	harrisitic	82.0	8.35	sub-poik.	16.2	13.26	sub-poik.	0.7	n.d.
H8	ol. cres.	-	harrisitic	74.9	8.43	sub-poik.	2.36	13.59	sub-poik.	1.1	n.d.
H.9	ol. cres.	-	harrisitic	62.4	8.36	sub-poik.	13.9	12.99	sub-poik.	16.9	32.3
H10	ol. cres.	-	harrisitic	70.5	8.31	sub-poik.	16.9	13.40	sub-poik.	11.4	34.0

+ Abbreviations:-

ol. = olivine
feld. = plagioclase feldspar
cpx. = clinopyroxene
spin. = chrome spinel
ortho. = orthocumulate
meso. = mesocumulate
adcum. = adcumulate
heterad. = heteradcumulate
cres. = crescumulate

Table 3.5 continued .....

* The olivine morphologies are diagrammatically shown in figure 3.1 and are described more fully in Chapter 4, section 4.3.

** The plagioclase and clinopyroxene morphologies are described in Chapter 4, sections 4.5. and 4.6 and the abbreviations used in this table are:-

tab.	=	tabular
poik;		
sub-poik.	=	poikilitic; sub-poikilitic
cum.	=	cumulus

++ By delayed neutron activation analysis (after Gale, 1967).

' From Henderson et al., 1971).

Table 3.6 (Carlingford cumulus minerals)

Specimen Number	Rock type	Unit Number (and position in Unit)	Olivine			Plagioclase			Clinopyroxene			U whole rock (p.p.b.)
			Morphology	Modal %	U (p.p.b.)	Morphology	Modal %	U (p.p.b.)	Morphology	Modal %	U (p.p.b.)	
C2	feld.-cpx.-ol. adcum.	1 base-mid.	irregular	17	7.05	tab.	64	17.16	sub-poik.	15	31.88	89
C3	feld.-cpx.-meso	1 mid.	absent			tab.	66	23.12	sub-poik.	31	32.95	113
C4	feld.-cpx.-meso.	1 mid.	absent			tab.	51	18.99	cum.	48	33.73	101
C5	feld. heterad.	1 top	absent			tab.	48	17.68	poik.	49	30.70	125
C6	feld.-cpx.-ol. meso.	2 base	irregular	3	n.d.'	tab.	68	22.43	sub-poik.	26	35.10	148
C7	feld.-cpx.-ol. adcum.	2 mid-top	sub-poik.	9	n.d.'	tab.	47	15.90	sub-poik.	40	34.79	96
C8	feld.-cpx.-ol. adcum.	3 base	irregular	16	6.66	tab.	62	18.08	sub-poik.	19	32.80	-

Table 3.6 continued ....

C9	feld.-cpx. meso.	3	mid.-top	absent			tab.	55	20.14	poik.	41	32.44	-
C11	feld.-cpx. (-ol.) meso.	4	base	irregular	2	n.d.'	tab.	65	21.66	cum.	30	36.60	108
C12	feld.-cpx. -ol. meso.	4	mid.	equant and rounded	8	n.d.'	tab.	50	24.95	cum.	39	35.05	-

Abbreviations as for table 3.5.

' Extensively altered.

Table 3.7. (Microprobe analysis of olivines)

Analysis Number	1	2	3	4	5	6	7	8	9	10	11	12	13	14
SiO_2	39.88	40.13	40.10	39.99	39.80	39.78	40.20	39.92	39.93	39.88	40.10	40.00	39.81	39.93
MgO	45.35	44.74	45.88	44.97	44.83	44.82	44.76	45.55	45.05	45.35	45.08	44.80	45.27	45.10
FeO	14.25	14.21	13.05	13.95	14.41	14.41	13.78	13.94	13.77	14.25	13.85	14.26	13.84	14.00
CaO**	.100	.109	.111	.102	.106	.103	.06*	.092	.088	.04*	.098*	.100	.04*	.101
NiO**	.189	.178	.176	.180	.203	.207	.09*	.166	.171	.13*	.178	.183	.07*	.165
Total	99.77	99.37	99.32	99.19	99.35	99.32	98.90	99.67	98.93	99.65	99.31	99.34	99.03	99.30
Fo content	85.01	84.87	86.06	85.18	84.42	84.42	85.27	85.46	85.46	85.01	85.30	84.87	85.34	85.17

Analysis 1. R.90 equant (average of 3)
2. R.90 rounded (average of 3)
3. R.91 tabular (average of 3)
4. R.91 equant (average of 3)
5. R.92 equant (average of 12)
6. R.92 rounded (average of 3)
(analyses 5 and 6 are produced in full in table 4.6., chapter 4).
7. R.95 equant (average of 5)
8. R.96 tabular (average of 3)
9. R.96 equant to irregular (average of 3)
10. R.99 equant (average of 3)
11. R.99 rounded (average of 3)
12. R.99 irregular (average of 6)
(analyses 11 and 12 are produced in full in table 4.10, chapter 4.)
13. R89 poikilitic (average of 3)
14. R.86 poikilitic (average of 3)

Table 3.7. continued

Analysis Number	15	16	17	18	19	20	21	22	23	24	25	26	27	28
SiO_2	39.91	40.23	39.86	40.06	39.76	39.90	39.94	39.90	39.81	40.04	40.08	40.40	40.30	39.78
MgO	45.38	44.91	45.74	45.50	45.40	45.77	45.38	45.35	45.34	45.23	44.71	43.84	45.10	45.66
FeO	14.01	14.38	13.71	13.86	14.47	14.25	14.12	14.01	13.98	14.00	14.23	14.88	13.79	13.96
CaO**	.098	.05*	.101	.089	.096	.05*	.04*	.05	.06*	.030	.080	.07*	.109	.04
NiO**	.177	.10*	.160	.164	.155	.12*	.11*	.10	.11*	.114	.160	.11*	.140	.09
Total	99.56	99.67	99.57	99.67	99.88	99.99	99.59	99.41	99.30	99.41	99.26	99.27	99.44	99.54
Fo content	85.25	84.99	85.60	85.39	86.34	85.30	85.28	85.10	85.25	85.21	84.84	84.19	85.41	85.66

Analysis 15. R.87 poikilitic (average of 3)
16. R.83 equant to rounded (average of 3)
17. R.84 equant to tabular (average of 3)
18. R.85 tabular (average of 3)
19. R.61 rounded to tabular (average of 3)
20. R.62 poikilitic to sub-poikilitic (average of 3)
21 R.62 rounded (average of 3)
22 R.63 poikilitic to sub-poikilitic

Analysis 23. R.63 rounded (average of 3)
24. R.64 poikilitic (average of 15)
(Analysis 24 produced in full in table 4.5., chapter 4)
25. R.53 equant (average of 3)
26. R.53 rounded (average of 3)
27. R.53 tabular (average of 3)
28. R.54 equant to irregular (average of 3)

Table 3.7 continued

Analysis Number	29	30	31	32	33	34	35	36
SiO_2	42.51	41.31	39.94	39.92	40.01	40.41	42.40	40.86
MgO	44.74	45.38	45.53	45.17	44.94	44.98	44.34	44.13
FeO	11.64	12.51	13.84	14.06	13.99	13.98	12.38	14.20
CaO**	0.05*	0.02*	.102	.05*	.113	.108	0.07	.111
NiO**	0.10*	0.12*	.162	.11*	.164	.139	0.08	.169
Total	99.04	99.34	99.57	99.31	99.21	99.62	99.27	99.47
Fo content	87.26	86.60	85.39	85.13	85.06	85.13	86.46	84.92

Analysis 29. R.66 equant (average of 3)
30. R.68 equant (average of 3)
31. R.68 tabular (average of 15)
32. R.120 equant to tabular (average of 3)
33. R.110 equant to irregular (average of 3)
34. R.111 equant to irregular (average of 3)
35. R.115 equant (average of 3)
36. R.116 equant to rounded (average of 3)

(Analysis 31 produced in full in table 4.14, chapter 4).

** Ca and Ni counted for three 100-seconds counts (chapter 2, section 2.8.1.)

* Ca and Ni counted as for routine major element analysis (chapter 2, section 2.8.1.)

Table 3.8 (Microprobe analysis of feldspars). *

Analysis Number	1	2	3	4	5	6	7	8	9	10	11	12
SiO_2	48.13	48.78	47.42	46.17	47.75	45.93	45.68	45.85	46.31	45.81	45.80	45.78
Al_2O_3	32.51	32.58	33.21	34.71	33.32	34.13	34.18	33.90	33.69	34.30	34.07	34.12
CaO	16.20	16.20	17.00	15.81	16.90	17.91	17.83	17.75	18.00	18.26	17.93	17.84
Na_2O	2.69	2.77	2.61	3.14	2.33	1.73	1.78	1.82	1.69	1.54	1.73	1.77
K_2O	0.08	0.03	0.04	0.04	0.05	0.05	0.04	0.05	0.02	0.04	0.03	0.04
FeO	0.29	0.22	0.25	0.30	0.23	0.36	0.34	0.41	0.38	0.38	0.40	0.34
Total	99.90	100.59	100.53	100.17	100.58	100.11	99.85	99.78	100.09	100.33	99.96	99.89
An	76.51	76.24	78.09	73.40	79.81	85.13	84.74	84.37	85.58	86.79	85.20	84.78
Ab	23.00	23.59	21.69	26.38	19.91	14.59	15.04	15.35	14.30	12.99	14.63	15.00
Or	0.45	0.17	0.22	0.22	0.28	0.28	0.22	0.28	0.12	0.22	0.17	0.22

Analysis 1. R.90 tabular (average of 3)
2. R.91 tabular (average of 3)
3. R.94 poikilitic (average of 3)
4. R.96 poikilitic (average of 3)
5. R.87 tabular (average of 3)
6. R.61 poikilitic (average of 3)

Analysis 7. R.65 tabular (average of 3)
8. R.54 tabular (average of 3)
9. R.68 poikilitic (average of 3)
10. R.23 tabular (average of 3)
11. R.115 poikilitic (average of 3)
12. R.17 poikilitic (average of 3)

Table 3.8. continued

Analysis Number	13	14	15	16	17
SiO_2	47.17	45.22	46.44	48.03	47.41
Al_2O_3	33.03	35.08	34.42	32.56	33.90
CaO	17.05	17.74	15.69	16.12	14.94
Na_2O	1.78	1.38	2.77	2.84	3.18
K_2O	0.05	0.07	0.02	0.02	0.04
FeO	0.82	0.64	0.18	0.21	0.22
Total	99.90	100.13	99.52	99.78	99.69
An	84.5	88.1	75.59	75.61	72.03
Ab	15.0	11.5	24.31	24.25	27.24
Or	0.5	0.5	0.12	0.12	0.23

Analysis 13. from Wager and Brown (1968) table 20, analysis No. 3.

14. from Wager and Brown (1968) table 20, analysis No. 4.

15. Olivine crescumulate - H.1 to H.6. (average of 6)

16. Olivine crescumulate - H.7, H.8. (average of 2)

17. Olivine crescumulate - H.9, H.10 (average of 2)

* For each plagioclase analysis, a preliminary scan was undertaken with calcium on one spectrometer, and sodium on the other spectrometer to determine the most calcic-rich portion of the crystal. This position was then analysed.

Table 3.9. Microprobe Analyses - Olivine crescumulate

Analysis Number	1	2	3	4	5	6	7	8	9	10	11	12	13	14	15
SiO_2	42.54	41.68	41.51	41.80	41.63	42.03	41.79	46.55	47.01	46.61	46.19	46.02	46.40	48.31	50.50
Al_2O_3	-	-	-	-	-	-	-	34.57	34.29	34.20	34.78	35.00	34.73	33.17	3.04
TiO_2	-	-	-	-	-	-	-	-	-	-	-	-	-	-	2.05
FeO	14.33	14.62	14.59	15.02	14.26	14.26	14.24	-	-	-	-	-	-	-	3.12
MgO	42.07	42.34	42.49	42.27	42.96	42.82	42.54	-	-	-	-	-	-	-	17.86
CaO	0.15	0.19	0.22	0.21	0.19	0.19	0.19	14.98	13.52	15.25	16.20	16.38	15.04	14.10	22.36
MnO	-	-	-	-	-	-	-	-	-	-	-	-	-	-	0.03
NiO	0.22	0.25	0.25	0.27	0.25	0.28	0.28	-	-	-	-	-	-	-	-
Na_2O	-	-	-	-	-	-	-	3.46	4.49	3.25	2.54	2.43	3.15	3.67	0.24
K_2O	-	-	-	-	-	-	-	0.14	0.07	0.03	0.05	0.04	0.04	0.01	-
Cr_2O_3	-	-	-	-	-	-	-	-	-	-	-	-	-	-	0.75
Total	99.31	99.08	99.06	99.57	99.29	99.58	99.04	99.70	99.38	99.34	99.76	99.87	99.75	99.26	99.95
Fo content	83.96	83.77	83.85	83.38	84.30	84.26	84.19								
An								69.97	62.22	72.05	77.68	78.66	71.60	67.94	
Ab								29.25	37.39	27.79	22.04	21.12	28.12	32.00	
Or								0.78	0.38	0.17	0.29	0.23	0.28	0.06	
En															50.05
Fe															4.91
Wo															45.04

Table 3.9. continued

Analysis Number	16	17	18	19	20	21	22	23	24	25	26
SiO_2	51.06	51.11	49.57	0.02	0.43	0.05	0.03	0.03	0.10	0.80	0.24
Al_2O_3	2.79	2.71	3.59	7.81	13.39	12.27	12.76	19.76	0.05	0.82	0.04
TiO_2	1.59	1.59	1.89	6.35	3.58	5.67	4.41	3.49	49.96	53.11	51.84
FeO	3.60	3.10	3.15	26.48	25.14	23.87	22.40	20.99	32.64	32.23	38.37
Fe_2O_3*				16.16	17.60	16.54	14.74	12.97	8.86	3.87	3.52
MgO	17.99	17.29	17.81	7.98	7.96	9.84	10.18	11.23	6.42	8.95	5.06
CaO	21.89	22.19	22.73	-	-	-	-	-	n.d.	-	-
MnO	0.08	0.06	0.07	-	-	-	-	-	0.95	0.50	0.41
NiO	-	-	-	-	-	-	-	-	-	0.04	n.d.
Na_2O	0.23	0.27	0.29	-	-	-	-	-	-	-	-
K_2O	-	-	-	-	-	-	-	-	-	-	-
Cr_2O_3	0.72	0.74	0.76	34.83	32.65	31.71	35.69	31.51	0.33	0.32	0.21
Total	99.93	99.06	99.86	99.63	100.75	99.95	99.98	99.98	99.31	100.64	99.69
En	49.61	49.42	50.00								
Fe	5.51	4.99	4.96								
Wo	44.82	45.59	45.04								

Analyses 1 to 7 olivines (H1-3; H7-10)
analyses 8 to 14 plagioclase feldspars (H1-3; H7-10)
analyses 15 to 18 clinopyroxenes (H1; H3; H7; H10)
analyses 19 to 23 chrome spinels
analyses 24 to 26 ilmenites.

*Fe_2O_3 recalculated using the Imperial College program AUTOCAL.

The specimen of olivine crescumulate from the Rhum western layered series (kindly provided by Dr. J. Wadsworth, University of Manchester) was prepared such that ten polished thin sections (numbered H.1 to H.10) from three mutually perpendicular directions were obtained (chapter 4, section 4.3.1.5). Specimens H.1 to H.6 correspond approximately to the olivine (100) crystal face; H.7 and H.8 to (001), and H.9 and H.10 to (010) - figures 4.19 and 4.20. Olivine analyses 1, 2 and 3 are from specimens H.1, H.2 and H.3 respectively; analyses 4 and 5 from specimens H.7 and H.8; analyses 6 and 7 from specimens H.9 and H.10.

From the microprobe analyses, it can be seen that the composition of the major minerals in the olivine crescumulate are similar to those of the other cumulates. The mode of origin and crystallisation processes involved in the formation of the olivine crescumulate is discussed in chapter 4 (sections 4.3. and 4.4.).

Table 3.10. Calculation of mean fission fragment ranges in various elements from Mory et.al. (1970).

Element	Atomic weight	Proportion of element in Oxide	Atomic Number (Zi)	$r_i = (0.8\sqrt{Zi})$
H	1.01	.1121	1	0.800
O	16.00	-	8	2.262
Na	22.99	.7418	11	2.529
Mg	24.31	.6031	12	2.771
Al	26.98	.5292	13	2.884
Si	28.09	.4674	14	2.993
P	30.98	.4366	15	3.098
Cl	35.46	-	17	3.298
K	39.10	.8301	19	3.487
Ca	40.08	.7147	20	3.577
Ti	47.90	.5995	22	3.752
Cr	52.01	.6843	24	3.919
Fe	55.85	.7773*	26	4.079
Fe	55.85	.6994**	26	4.079
Zr	91.22	.7464	40	5.059

* As FeO

** As Fe_2O_3.

Table 3.11

Calculation of R_{spec} and R_{stand} (from equation (6), p.42)

mineral	R_{spec}	standard	R_{stand}
olivine (chrysotile)	2.507	SRM 614	2.641
plagioclase (bytownite)	2.685	"Geoscan"	2.684
clinopyroxene (endiopside)	2.774	"50 x 24"	2.679
chrome spinel (1)	3.343		
biotite (2)	2.743		
chlorite (3)	2.522		
uralite (tremolite)	2.728		
magnetite ($FeO.Fe_2O_3$)	3.273		
ilmenite ($FeO.TiO_2$)	3.461		
chlor apatite ($Ca_5(PO_4)_3Cl$)	2.943		

(1) from Analysis (6), Table 5.6.

(2) from Analysis (5), Deer etal. (1971) Table 18.

(3) from Analysis (4), Deer etal. (1971) Table 21.

CHAPTER 4: CRYSTAL GROWTH OF CUMULUS PHASES

4.1. Theory of Crystal Growth

4.1.1. Introduction

The crystallisation of a mineral from a magma (or silicate melt) can be most adequately described using a combination of equilibrium (thermodynamic) and non-equilibrium (kinetic) arguments. In classical thermodynamical theory, each "state" of a system has a free energy (G) where:-

$$G = E - TS + PV$$

where E = Internal Energy

S = Entropy

T = Absolute temperature

P = Pressure

V = Volume

A change in state from liquid to solid with a decrease in T (or an increase in P) results in decreasing the free energy. At equilibrium, the stable state of the system is the state of minimum free energy. Then, for a mineral AB to crystallise from a melt containing components A and B, the chemical potentials of both A and B in the mineral (μ_A^{min} and μ_B^{min}) must be the same as, or less than, the chemical potentials of A and B in the melt (μ_A^{melt} and μ_B^{melt}),

i.e. $(\mu_A^{min} + \mu_B^{min}) \leq (\mu_A^{melt} + \mu_B^{melt})$

where $G_{AB}^{min} = \mu_A^{min} + \mu_B^{min}$

and $G_{AB}^{melt} = \mu_A^{melt} + \mu_B^{melt}$

At constant pressure, graphs of G against T may be drawn, the general shape being that shown in figure (4.1.)

Consider decreasing the temperature (at constant P). At values of $T > T_L$ (the liquidus temperature), G_{AB}^{melt} is the stable

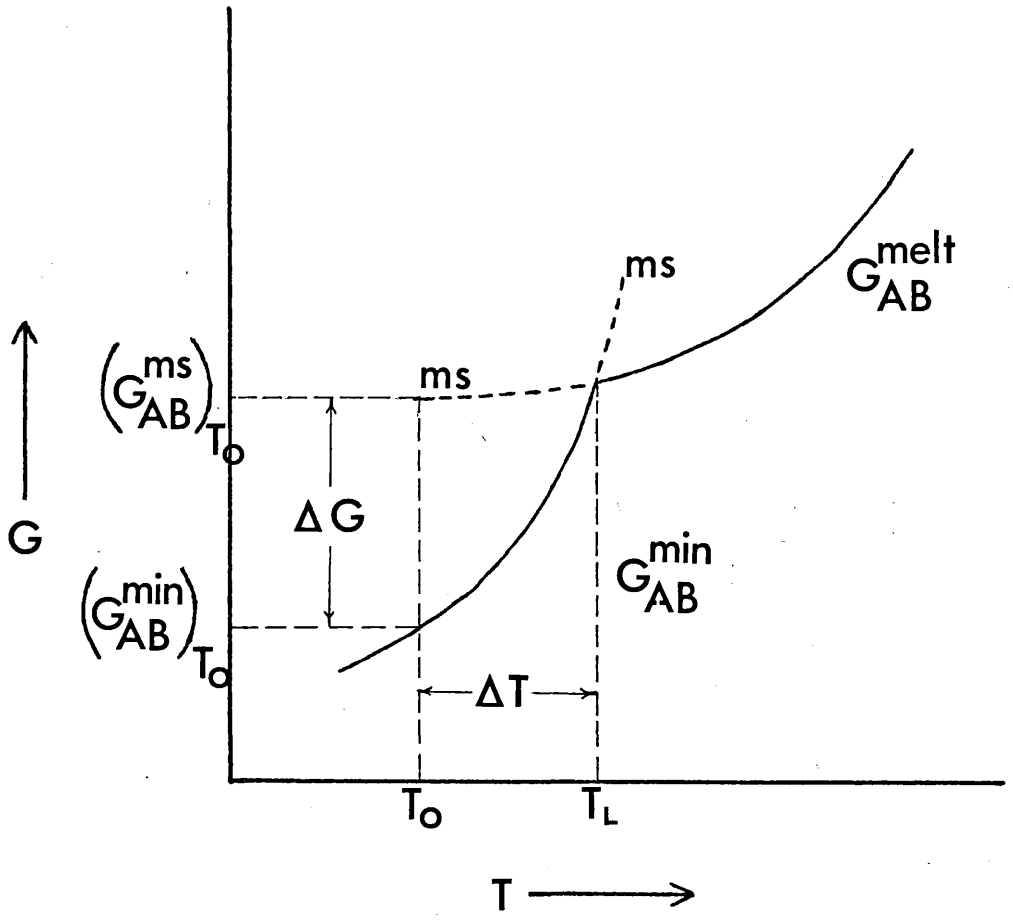

Figure 4.1

after Brice, 1967

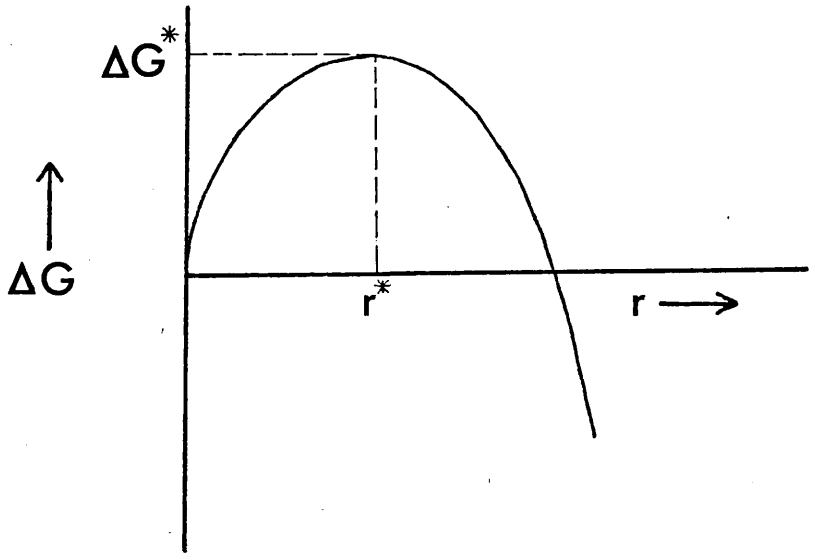

Figure 4.2

after Brice, 1967

state and AB cannot crystallise. At values of T below T_L, $G_{AB}^{min} < G_{AB}^{melt}$ and AB should spontaneously crystallise. In practice however, AB does not crystallise until the melt "supercools" - i.e. until the temperature falls below T_L to some value T_o. The degree of supercooling ($\triangle T$) is given by the relationship:-

$$\triangle T = T_L - T_o \qquad \text{——————(1)}$$

The system is then said to be in metastable (ms), or non-equilibrium condition.

The existence of the metastable region provides the driving force of the transformation $\triangle(G)_{T_o}$ - this being the difference in free energy between the initial metastable state at T_o $(G_{AB}^{ms})_{T_o}$ and the final state $(G_{AB}^{min})_{T_o}$,

where $\triangle(G)_{T_o} = (G_{AB}^{ms})_{T_o} - (G_{AB}^{min})_{T_o}$

4.1.2. Processes involved in crystal growth

There are three basic processes which contribute to the free energy change involved in the transformation from a liquid to a solid state.

(1) The nucleation process ($\triangle G_{nucleation}$).

(2) A crystallisation process at the interface between the crystal and the melt ($\triangle G_{interface}$).

(3) A diffusion process involving transport of material to the interface, and transport of material and heat away from the interface ($\triangle G_{diffusion}$)

The energy evolved (or used) in these processes is dependant upon the magnitude of the free energy difference $\triangle(G)_{T_o}$; and, since the growth rate (Y) of the mineral is a function of the three processes, expressed as:-

$$Y = f\left[\triangle G_{nucleation} + \triangle G_{interface} + \triangle G_{diffusion}\right] \qquad \text{——(2)}$$

then the growth rate is also a function of the free energy difference at T_o within the crystal/melt system, thus

$$Y = f\left[\Delta(G)_{T_o}\right] \qquad \text{——————(3)}$$

4.1.2.1. Nucleation processes

Before crystallisation of a mineral AB from a melt containing components A and B can occur, crystal nuclei of AB need to be created. For their creation, the crystal nuclei require an input of energy to overcome the initial surface free energy of the solid (i.e. nucleus)/liquid interface. Classical nucleation theory (for homogeneous nucleation) involves assigning volume free-energies to the bulk phases and assuming a spherical shape to the embryonic nucleus. The free energy of the system will change by the amount ΔG when the spherical crystallite is formed.

where $$\Delta G = \frac{4\pi r^3}{3}.(\Delta G_v) + 4\pi r^2\sigma \qquad \text{——————(4)}$$

ΔG_v = difference in free energy between the solid and the liquid (per unit volume).

r = radius of the spherical crystallite.

σ = surface tension.

A plot of ΔG against r is of the form of figure (4.2), and shows that an increase occurs with increasing radius of the crystal nucleus until a critical radius (r^*) is attained. Any further growth (or dissolution) of r^* willdecrease the free energy of the system, and is thus thermodynamically favoured. The free energy value ΔG^* corresponding to the critical radius r^*, is termed the free energy barrier (or activation energy) of nucleation. Its existence is one of the reasons why liquids supercool, and it is analogous to the term $\Delta G_{nucleation}$ in equation (2).

Using several valid assumptions, Turnbull and Fisher (1949) restated equation (4) as the more workable equation (5) below:-

$$\Delta G_{nucleation} + \frac{16\pi\sigma^3(v_c)^2.T_L^2.}{3(\Delta H)^2.(\Delta T)^2} \qquad \text{———(5)}$$

where v_c = volume per atom of the spherical nucleus.

$\triangle H$ = heat of fusion.

$\triangle T$ = the amount of supercooling.

$\triangle G_{nucleation}$ then varies sensitively with the amount of supercooling of the melt.

The rate of formation of nuclei, I (nuclei. cm^{-3}. sec^{-1}) depends not only on $\triangle G_{nucleation}$, but also upon the viscosity of the melt, as shown by equation (6) - from Turnball and Fisher (1949).

$$I = N.\frac{k.T.}{h} \exp\left\{\frac{-\triangle G_{nucleation} - \triangle G_{vis}}{k.T}\right\} \qquad (6)$$

where N = Avogadro's number.

h = Planck's constant.

k = Boltzmann's constant.

$\triangle G_{vis}$ = approximately the activation energy for viscous flow.

The dependence of I on the temperature and on $\triangle T$ can be seen from figure (4.3)- after Strickland - Constable (1968).

From values of T_L to T_D (the temperature at maximum nucleation rate), the term $\triangle G_{nucleation} > \triangle G_{vis}$ and will be the rate-controlling factor in equation (6). Below T_D, $\triangle G_{vis} > \triangle G_{nucleation}$ and will be rate-controlling since, at these values, the $(\triangle T)^2$ term in the denominator of equation (5) will be large so decreasing the value of $\triangle G_{nucleation}$. The viscosity of the melt is dependent upon the temperature by the equation:-

$$\eta = A.\exp\left(\frac{-\triangle G_{vis}}{R.T}\right)$$

where η = viscosity

R = Gas constant

A = constant.

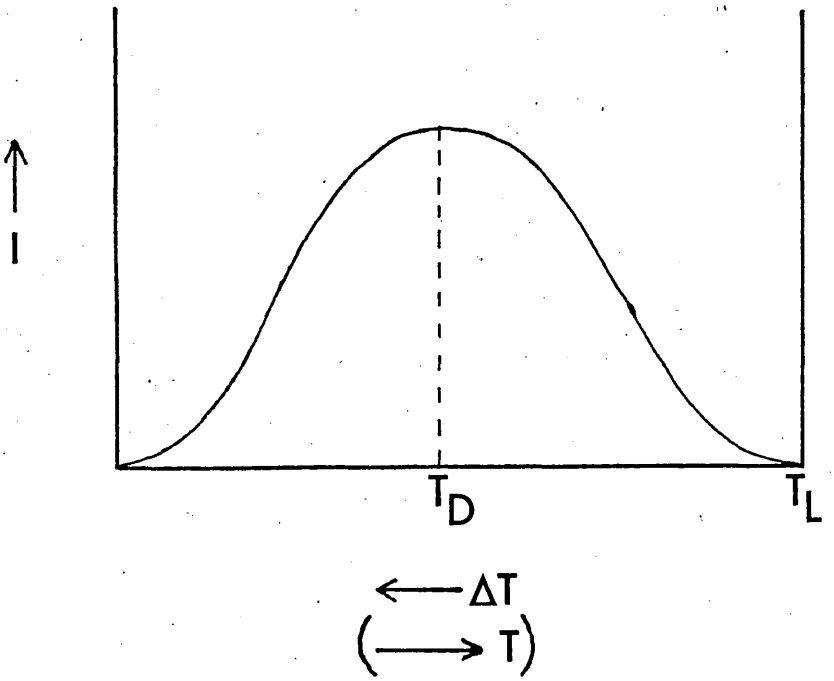

Figure 4.3
(after Strickland-Constable, 1968)

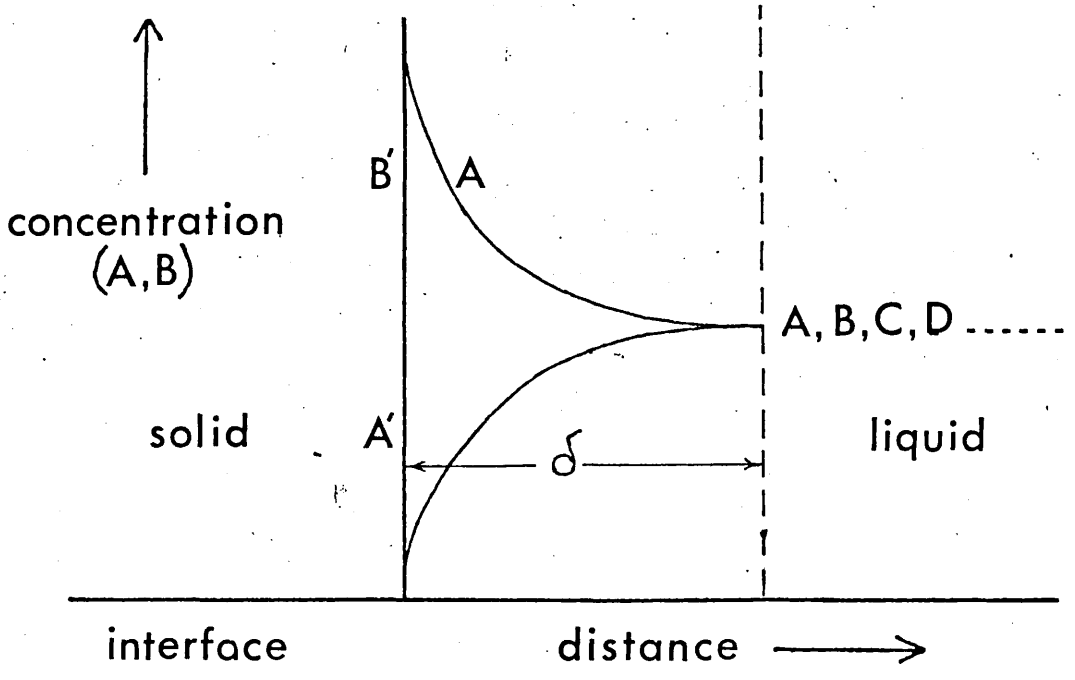

Figure 4.4

Thus the movement of molecules and ions to and from the growing crystal face is inhibited by increasing the viscosity when the temperature is lowered.

The above arguments hold for homogeneous nucleation. For most cases however, nucleation occurs first on impurities present in the liquid or on seed nuclei; nucleation under these conditions is said to be heterogeneous. The impurities (or seed nuclei) act, in effect, to reduce the free energy barrier by a factor of $f(\theta)$. Equation (5) may then be modified:-

$$\Delta G^{het}_{nucleation} = \frac{16.\pi.\sigma^3.T_L^2.f(\theta)}{3.(\Delta H)^2.(\Delta T)^2} \qquad \text{——(7)}$$

where $\Delta G^{het}_{nucleation}$ is the free energy increase for heterogeneous nucleation, and

$$f(\theta) = \frac{(2 + \cos\theta).(1 - \cos\theta)^2}{4}$$

where θ is the contact angle between the nucleus embryo and the substrate surface of the particle (or seed nuclei).

4.1.2.2. Interface mechanisms

There are two main types of crystallisation processes occuring at the crystal/melt interface; these are termed lateral and continuous growth (Kirkpatrick, 1974).

(1) Lateral growth occurs by attaching atoms (and ions) in discrete elementary steps, either as a two-dimensional nucleation process on the crystal surface (Volmar and Marsden, 1931), or by growth on a screw dislocation proceeding perpendicular to the surface (Hillig and Turnbull, 1956)

(2) Continuous growth occurs when atoms (or ions) attach at essentially any position on the crystal surface.

Cahn (1960) and Cahn et al. (1964) showed mathematically that lateral growth mechanisms should occur at small supercoolings, and continuous growth mechanisms at large supercoolings. Uhlmann (1972) and Kirkpatrick (1974) were able to predict which interface

mechanism was involved in several experimental (silicate) systems from the equation:-

$$Yr = \frac{Y.\eta}{1 - \exp\left\{\frac{-L.\Delta T}{R.T_o.T_L}\right\}} = \frac{f.k.T_o}{3.\pi.a_o} \qquad \text{———(8)}$$

where Yr = the reduced growth rate - a conveniently named term describing the modification of the growth rate (Y) by the viscosity , supercooling etc.

L = Latent heat of fusion.

f = fraction of sites on the crystal surface available for molecular attachment.

a_o = thickness of one molecular layer.

Then, a plot of Yr against ΔT will be a function of f, and the supercooling dependence of f can be determined. For a screw dislocation mechanism, f should increase linearly with increasing ΔT; exponentially for a surface nucleation mechanism, and remain constant for a continuous mechanism.

The term $\Delta G_{interface}$ in equation (2) is then again dependent upon the amount of supercooling of the melt.

4.1.2.3. Diffusion processes

In interface controlled growth, the interface advances into regions of the melt having a constant mean composition. The growth rate Y, is then independent of the interface position, and hence of time.

If we have therefore a situation whereby a mineral of composition A'B' grows from a melt containing components A,B,C,D..... (where $A > A'$ and $B < B'$) - i.e. in most natural silicate systems - there will be a region (δ) enriched in component A, and depleted in component B, forming around A'B' as growth proceeds (figure 4,4). For continued growth of A'B', chemical diffusion of A towards, and B away from the interface must occur through δ. The dependence of δ upon various factors is discussed more fully below (section 4.1.5)

but essentially, if the rate by which the interface mechanism occurs is rapid, the volume (or in some cases, heat) diffusion will become the dominating factor as growth proceeds, the crystal growing then only as fast as the diffusion rate allowed.

Christian (1965) showed that the growth rate for a flat interface depends only upon the diffusion coefficient (D) and the time (t), and was proportional to $(D/t)^{\frac{1}{2}}$. However, for minerals consisting of more than one componant (e.g. A'B'C'), the rate-controlling diffusion coefficient will be that of the slowest moving componant necessary for continued growth (D_{slow}), then

$$Y = K\left(\frac{D_{slow}}{t}\right)^{\frac{1}{2}} \qquad \text{———(9)}$$

where K is a constant.

Many mathematical models have been proposed to attempt to obtain solutions to the diffusion equation for spherical, cylindrical and ellipsoidal shapes (e.g. Horvay and Cahn, 1961). However, the existence of too many unknowns and variables in the equations (e.g. the interference between several growing crystals and subsequent overlapping of the diffusion fields) means that results can at best be qualitative, even in controlled laboratory conditions.

4.1.3. The Function of ΔT in Crystal Growth

Figure (43) shows that the nucleation rate is a function of the supercooling, ΔT, of the melt. The various other factors that contribute to crystal growth in terms of the supercooling have been discussed by Tiller (1970) using the coupling equation:-

$$\Delta T = \Delta T_s + \Delta T_e + \Delta T_k + \Delta T_h \qquad \text{————(10)}$$

where ΔT_s = the portion of the supercooling consumed in transporting material to and from the growing crystal interface

(i.e. diffusion)

ΔT_e = the portion of the supercooling consumed in producing a non-equilibrium solid (i.e. for the incorporation of non-equilibrium defects) and the formation of initially curved surfaces of small growing crystals.

ΔT_k = the portion of the supercooling consumed in the driving force for molecular attachment mechanisms of new constituents at the interface.

ΔT_h = the portion of the supercooling consumed in driving the heat liberated by the latent heat of crystallisation.

For some well-defined situations, certain of the components in equation (10) will tend to dominate the growth procedure. For example, in the growth of metal crystals from a relatively pure melt, growth is largely heat controlled and $\Delta T_h \simeq \Delta T$. Growth of oxide crystals from melts of steel is largely diffusion controlled and $\Delta T_s \simeq \Delta T$. Growth of polymer crystals from a well fractionated polymeric melt is largely controlled by the kinetics of interface attachment, and $\Delta T_k \simeq \Delta T$. Growth of lamellar eutectic crystals (these being a growth morphology in eutectic crystals and are analogous to the cellular structures formed in growth from pure metals) is largely controlled by the excess free energy of the solid formed and $\Delta T_e \simeq \frac{1}{2}\Delta T$.

In ill-defined and complex systems found in nature, all four factors may play significant roles in the growth procedure. Figure 4.5, from Tiller (ibid. p.206), shows schematically the regions where various mechanisms are dominant with increasing crystallisation time (temperature and supersaturation being kept constant)

From figure (4.5) it can be seen that initially ΔT_e dominates the crystal growth and with increasing crystallisation time all four factors contribute, until, for non-equilibrium dendritic

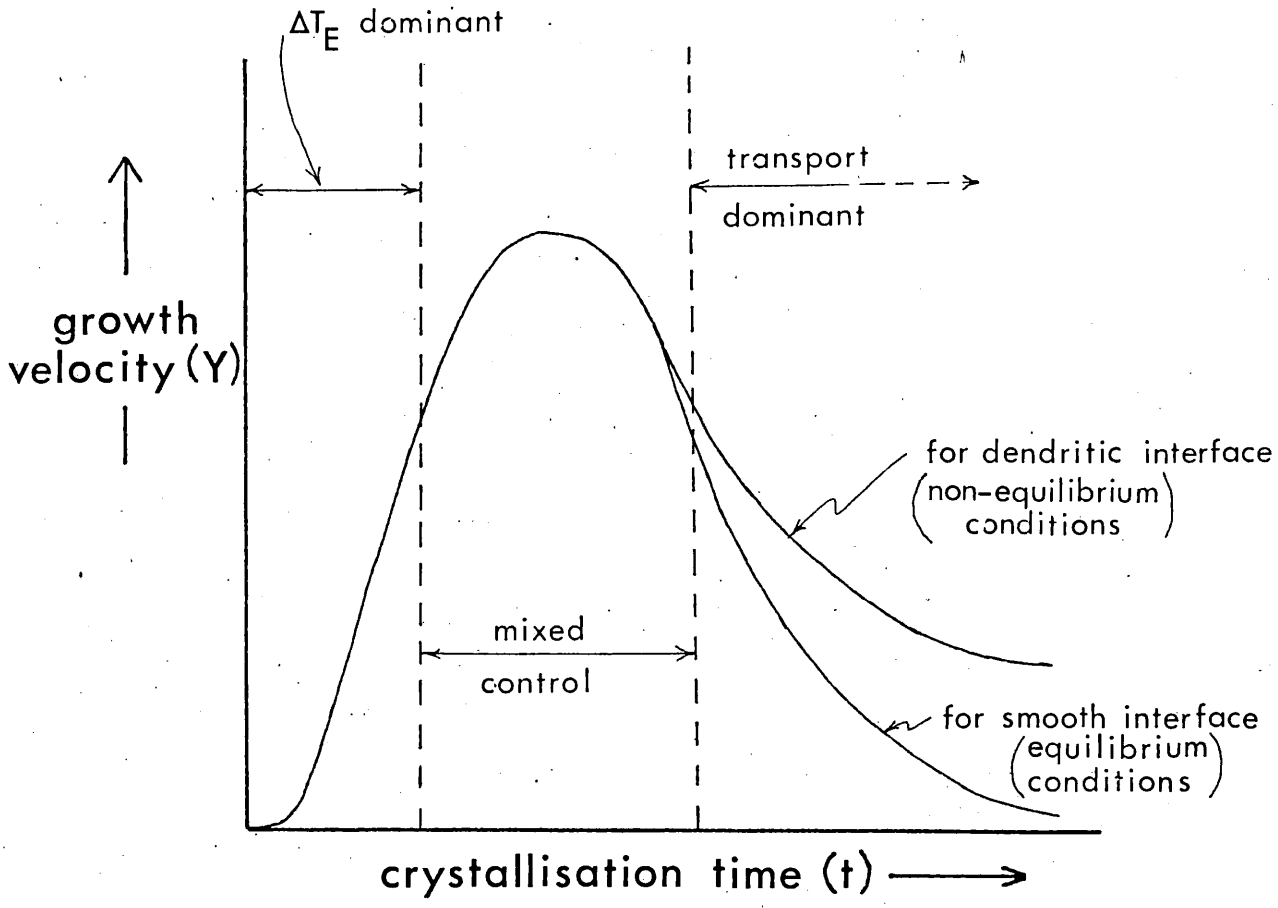

Figure 4.5
(from Tiller, 1970)

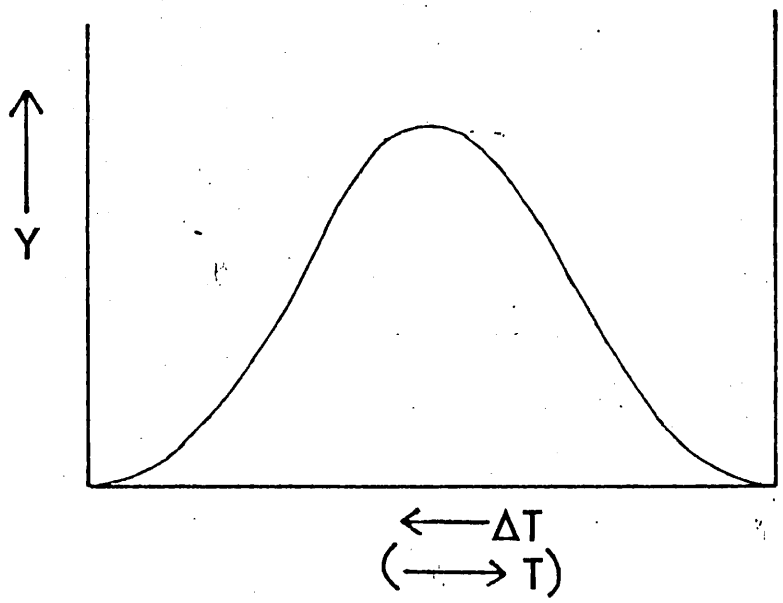

Figure 4.6
(from Tamman, 1925)

type growth, ΔT_s and ΔT_h dominate the growth of the crystal.

Tiller (ibid.) showed also that the crystal morphology would be largely the result of interplays of the above factors, and that a general equation relating the growth velocity to the most stable crystal shape (morphology), S, can be drawn up:-

$$Y(S) = f\left(S, \Delta T_s, \Delta T_e, \Delta T_k, \Delta T_h\right) \qquad \text{——(11)}$$

For silicate melts crystallising in a plutonic environment (in effect, long crystallisation times), the ΔT_e contribution may be neglected. The role that ΔT_h plays in the equation is discussed later (sections 4.1.4. and 4.1.5.), but its significance under equilibrium and plutonic crystallisation conditions will, in general, be negligable. Silicates are at least partly polymeric (e.g. Hess, 1971), and the growth and morphologies of the phases can be interface controlled (e.g. Kirkpatrick, 1974), the ΔT_k contribution then, may be significant. Silicate melts are often complex and the need arises to transfer materials to and from the growing crystal/melt interface such that the contribution from diffusion (ΔT_s) may also be significant.

We then may make the initial assumption that, for silicate melts crystallising under plutonic conditions, there are two extreme cases of growth mechanisms.

(1) Interface controlled growth - where the movement (or growth) of the crystal/melt interface is determined by the mechanism by which the atoms (or ions) attach themselves to the growing crystal.

(2) Diffusion controlled growth - where the movement (or growth) of the crystal/melt interface is determined by the rate at which the atoms (or ions) necessary for continued growth move towards the interface, and those species which are not necessary for growth move away from the interface.

Since for interface controlled growth, the driving potential for growth is obtained by the different free energies/atom in the immediate vicinity (but on opposite sides) of the interface, the interface velocity will be some function of the deviation from equilibrium - which may be measured by the supercooling at the interface, then

$$\Delta G_{interface} = f'(\Delta T) \qquad \text{——————(12)}$$

The diffusion of the atoms (or ions) through a medium is also temperature (and viscosity) dependent (e.g. by the Stokes - Einstein equation $D = k.T/6.\pi.r.\eta$). The growth rate of the interface then, and hence the free energy change for diffusion ($\Delta G_{diffusion}$), would also be some function of the supercooling,

$$\Delta G_{diffusion} = f''(\Delta T) \qquad \text{——————(13)}$$

Tamman (1925) showed experimentally the relationship between the growth rate (Y, in $cm \cdot sec^{-1}$.) and the supercooling (ΔT) - figure (4.6). It can be noted that there is a similarity in shape between figure (4.6) and figure (4.3), the nucleation rate vs. ΔT graph, and the relative juxtapositions of the two curves have been used by Dowty et al. (1974) to interpret a one-stage cooling history for lunar pyroxene-phyric basalts. The significance of these curves in relation to layered igneous rocks is given below (section 4.4.).

In situations where $\Delta G_{interface} \simeq \Delta G_{diffusion}$, the growth velocity will be dependant upon both the local deviation from equilibrium at the interface, and upon the gradients of composition (or temperature) within the phases. It is usually assumed however, (Christian, 1965, p.8) that this situation is transitory, and that the interface mobility will be controlled essentially by either an interface process, or a diffusion process.

4.1.4. Temperature distribution at the interface - constitutional supercooling

As discussed earlier (section 4.1.1.), the nucleation of a mineral species does not occur until some temperature (T_o) below the liquidus temperature (T_L) is reached. If after nucleation and at the onset of crystal growth there is an initial enriched zone of low melting point constituents surrounding the crystal (section 4.1.2.3), from phase diagram arguments the melt adjacent to the crystal interface will have a lower freezing temperature than the bulk of the melt. Thus, the equilibrium liquidus temperature (T_L) rises with increasing distance from the interface figure (4.7). However, curve T, which indicates the actual temperature gradient can be assumed to be linear (Woodruff,1973), or, for a fast growth situation may be convex (Brice, 1967). Although the temperature of the melt rises continuously with distance into the melt, there is a region ahead of the interface in which the actual temperature is below the liquidus temperature. This region (shaded in figure(4.7)) is termed "constitutionally supercooled" (Rutter and Chalmers, 1953).

Keith and Paddon (1963) have shown that there is a relationship between the ratio of the crystal growth rate (Y) and the rate of diffusion (D) to the morphology of the crystal. For a spherulitic morphology $Y \gg D$ and an impurity layer (δ) enriched in low melting point constituents appears at the crystal/melt interface in the region of constitutional supercooling (c.s.). Any pertubations of the interface with dimensions comparable to δ will encounter a region of c.s. liquid, with high ΔT values, resulting in rapid growth of fibers nomal (or at slight angles) to the crystal/melt interface.

During rapid growth, the growth rate may be in excess of the rate of removal of the latent heat evolved during the

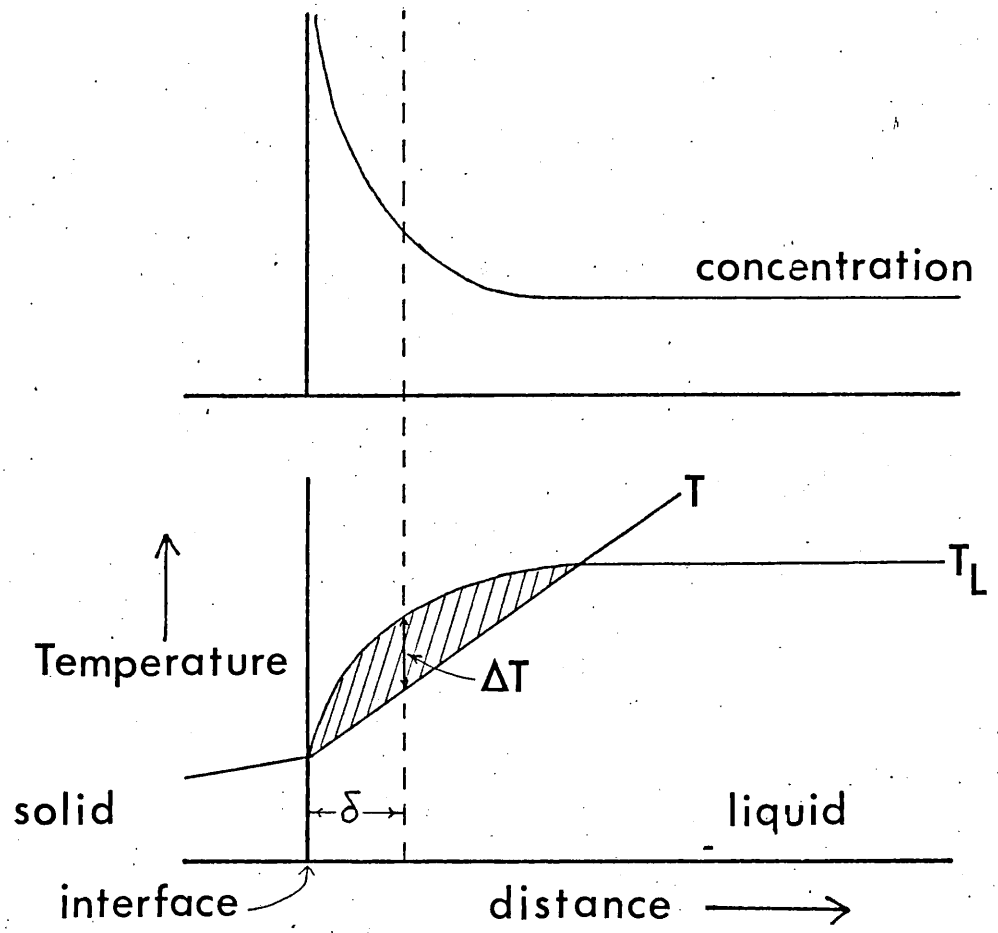

Figure 4.7

(after Rutter and Chalmers, 1953)

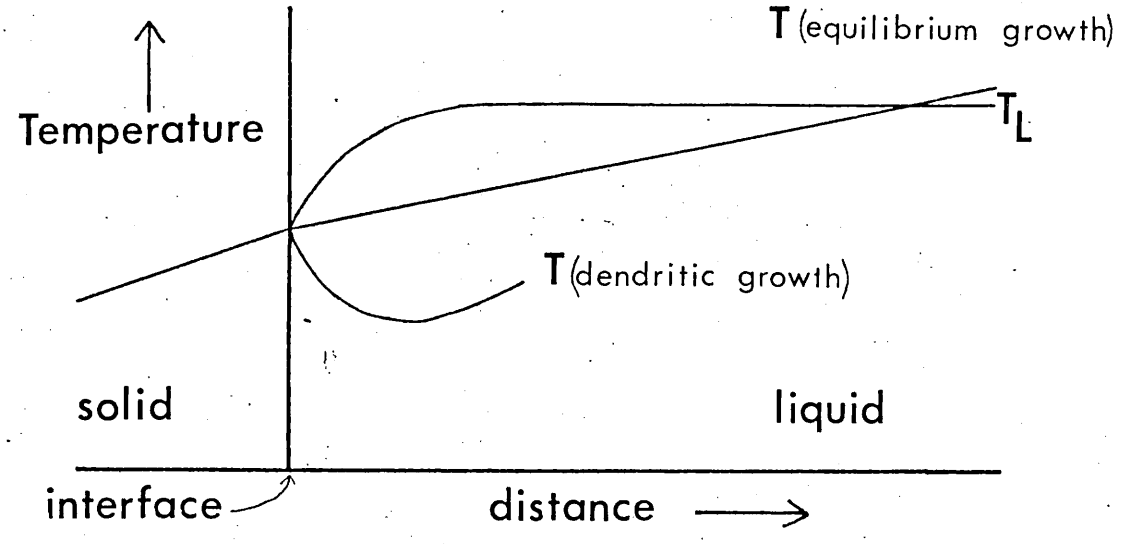

Figure 4.8

(after Christian, 1968)

crystallisation process. Projections will then encounter cooler regions of the melt having negative temperature gradients, the result being to encourage even faster growth. Dendritic crystal morphologies are considered to be the product of rapid growth into negative temperature gradients (i.e. high ΔT) regions of melt (e.g. Christian, 1965), figure (4.8).

4.1.5. Magnitude of δ and its relationship to crystal morphologies.

The magnitude of δ depends upon several factors

(1) The temperature distribution gradient (i.e. the amount of ΔT)

(2) The crystal growth rate (Y)

(3) The convection currents and stirring rates of the melt.

Factors (1) and (2) are to a certain extent interdependant. An increase in growth rate and/or an increase in ΔT will result in a decrease in the magnitude of δ. (figures 4.9(a), (b) and (c)).

Lofgren (1974) has demonstrated experimentally that a whole progression of plagioclase morphologies can be related to progressive changes of $^{D}/_{Y}$ ratio. As ΔT decreases, δ becomes large and the spherulitic fibres increase in size progressing to a dendritic form of morphology. As ΔT approaches zero, the growth rate drops and the morphology observed assumes a more equilibrium (polyhedral) morphology. The sequence observed can be generalised (Lofgren 1974, p. 270) thus:-

equilibrium crystal form

↓

skeletal crystals (generally more acicular than equilibrium form)

↓

dendrites

↓

spherulites

increasing ΔT, Y

decreasing δ

↓

The order of events is then likely to be (for plutonic conditions):-

(1) Initial high supercooling

(2) Nucleation and growth of small crystals

(3) The stablishment of a c.s. region (figure 4.9(a)).

(4) Faster growth encouraged by small δ region, which in turn increase ΔT and decrease δ (figure 4.9(b) and (c)).

(5) The vicious circle broken by the heat loss rate within a large magma chamber being too low, thus T_L (and hence ΔT) becomes in effect too high to crystallise the lower melting point constituents as lower temperature zones around the crystal.

(6) Heat loss within the magma chamber occurs (T_L) drops), or, more likely for plutonic rocks, the growth rate drops until diffussion of the higher melting point constituents into the depleted δ zone occurs.

Figure (4.5) shows schematically the growth rate curve with increasing time.

The morphology of the resultant crystal is then likely to be a result of initial supercooling. A high initial ΔT results in a dendritic or spherulitic growth type and the growth will be interface controlled; a low initial ΔT results in a polyhedral, equilibrium growth type and the growth will be diffusion controlled.

The effects of convection currents arising, for example, from crystals settling within a magma chamber can be of importance to cumulates and its significance is discussed below (section 4.4.)

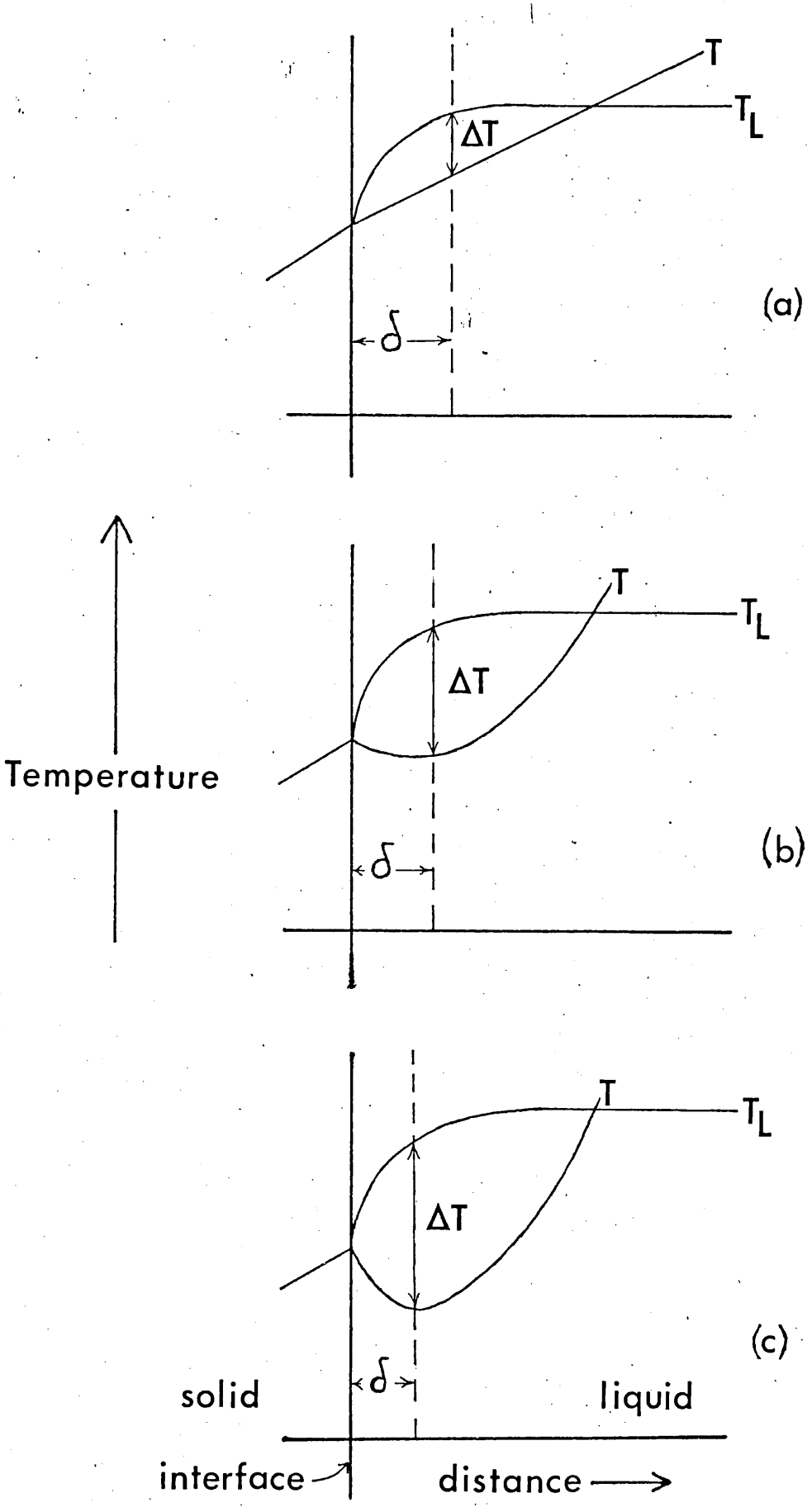

Figure 4.9

Increase in growth rate, Y (a)-(c)
Decrease in δ (a)-(c)

4.2. The Distribution of a low-partitioning trace impurity

The thermodynamic principles governing the partitioning of a trace element between the host mineral and corresponding liquid are fairly well-defined (e.g. Whittaker, 1967 and McIntire 1961). Unfortunately, when applied to natural systems rigid assumptions and a priori conditions are necessorily imposed. This results in formulations of inflexible thermodynamic models based upon constant equilibrium and crystal growth conditions. Albarede and Bottinga (1972) recognised that disequilibrium conditions may exist in trace element partitioning between phenocrysts and host lava, although, in their models they used assumptions that the crystal growth surface is a simple plane and that both partition coefficients and the rate of crystallisation are constant. From the arguments above (Sections 4.1.1. to 4.1.5) it is apparent that under disequilibrium conditions a planar crystal face is unstable; that there is a variation of the growth rate with time (figure 4.5); and, from the variation of uranium (and to a lesser extent Ca and Ni) as trace elements within the olivines (Chapter 3, also section 4.3), observed partition coefficients are themselves not constant.

Most models then are based on the assumption that there is only an equilibrium partition coefficient. It is, however feasible to recognise three partition coefficients (Brice 1967). These are the equilibrium k_{equ}, interface k* and observed (or calculated) k_{obs} partition coefficients.

Consider the distribution of a low-partitioning trace element adjacent to a growing crystal/melt interface (Figure 4.10) where δ_x is a zone enriched in low-partitioning element X.

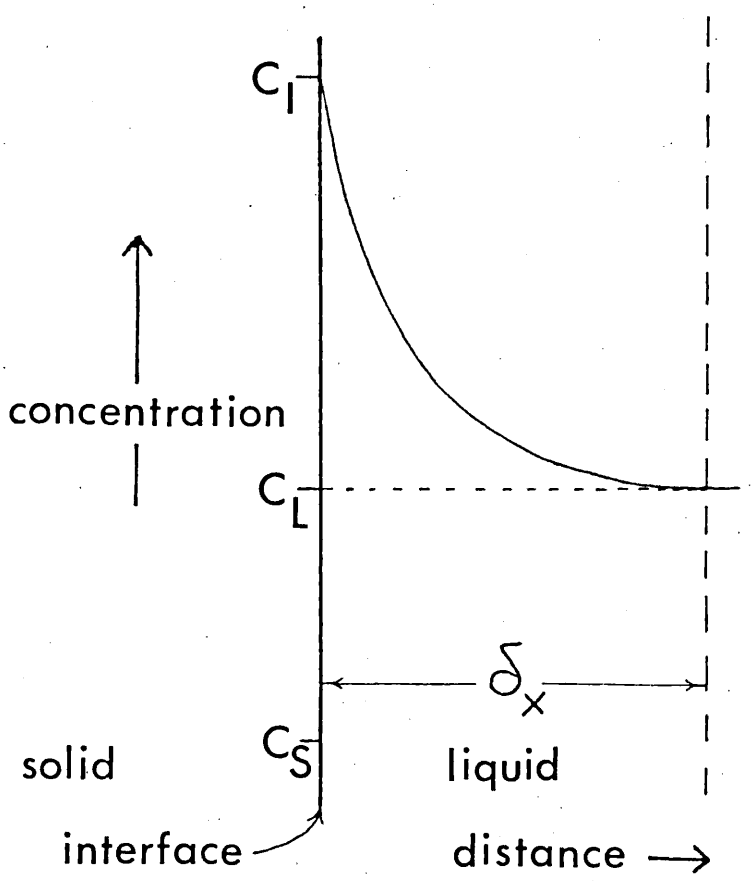
C_l
concentration
C_L
δ_x
solid
C_S
liquid
interface
distance

Figure 4.10

Then $k_{equ} = \frac{C_s}{C_L}$ at Y = 0 (linear growth rate in cm.sec^{-1}).

$k_{obs} = \frac{C_s}{C_L}$ at Y = Y

$k^* = \frac{C_s}{C_I}$ at Y = Y

where C_s = concentration of the element in the solid.

C_L = concentration of the element in the bulk liquid.

C_I = concentration of the element at the crystal/melt interface.

If the growth rate exceeds the diffusion rate of the low-partitioning element (x), then C_I will increase, and the crystal will be forced to incorporate more of the element X. The observed partition coefficient k_{obs} will then vary with the growth rate of the crystal, increasing in value with increasing growth rate and K_{obs} will tend towards unity. The inequality $k_{obs} > k_{equ} > k^*$ will then exist.

and $k_{obs} \rightarrow 1$ —— (14)

If alternatively the diffusion rate of the low-partitioning element exceeds the growth rate Y, then the enriched zone δ_x will decrease and k_{obs} $(\geq k^*) \geq k_{equ}$. Since, from sections 4.1.4. and 4.1.5. above, this is synonomous with equilibrium (low ΔT) conditions, thermodynamical principles of partitioning will be valid.

Thus $k_{obs} \neq 1$ —— (15)

Thus crystallization under slow growth rates and equilibrium (low ΔT, low supersaturation) conditions will give rise to the partitioning of trace elements in response to thermodynamical principles (low values of k_{obs}), whereas more rapid growth (higher ΔT, higher supersaturation) results in larger (and less predictable) partition coefficients (higher values of k_{obs}).

4.3. The Distribution of Uranium in Extremely-low Uranium Phases.

The distribution of uranium within the Rhum and Carlingford rocks has been divided into four distinct groups (or phases). These were outlined in chapter 3 (section 3.1.3.). Group (4) - extremely-low uranium phase - is discussed in the following sections. This group is characterised by the minerals having an extremely low concentration of uranium (between 1 and 100 p.p.b.). The minerals within this group are the major rock-forming cumulus minerals of the intrusions, i.e. olivine, clinopyroxene, plagioclase feldspar, and chrome spinel, rarely contributing less than 95% modal volume.

Because of the extremely low concentrations within these minerals, care had to be taken to ensure that the values measured were from uranium indigenous to that mineral species and not trapped within grain boundaries or cleavage planes, or from small inclusions of uraniferous minerals.

The earlier limitations of the fission track technique (i.e. my inability to obtain prints of the rock surface) meant that tracks were counted only from the middle of the phases, thus excluding any spurious tracks from grain boundaries. The distribution of tracks within the group (4) minerals were homogenous, although the very low concentrations meant that a low magnitude concentration gradient would not be detected over areas smaller than 2 millimetres^2. Similarly, very few fission track "stars" were observed within these phases. Condie et al. (1969) had suggested that the uranium concentration may vary with the crystallographic direction, or be incorporated into cleavage planes. However, measurements of randomly orientated mineral sections give low standard deviations (table 4.2), and constancy of uranium concentrations in three mutually perpendicular directions, both indicate there is no significant variation in uranium concentration with crystallographic direction. Thus it may be concluded that the results obtained by fission track analysis of

the group (4) minerals are an accurate measure of the intrinsic uranium concentrations within these minerals. These results, for the Rhum intrusion, are summarised in table 4.1. Where partition coefficients are quoted, they refer to the observed values (k_{obs})- section 4.2), and the concentration of uranium in the melt is taken to be 0.30 p.p.m. (section 3.3.).

Table 4.1.

mineral	uranium (p.p.b.) range	uranium (p.p.b.) mean	k_{obs} ($\times 10^{-2}$) range	k_{obs} ($\times 10^{-2}$) mean	Average Composition
olivine	4.30 - 8.32	6.30	1.43 - 2.77	2.10	$Fo_{86}Fa_{14}$
clinopyroxene	24.32 - 39.15	33.24	8.11 - 13.05	11.08	$Ca_{44}Mg_{49}Fe_{7}$
feldspar	9.54 - 28.39	18.96	3.18 - 9.46	6.32	$An_{78.6}Ab_{21.2}Or_{.2}$
chrome spinel	approx. 10		3.33		-

4.3.1. Uranium in olivines

Of the group (4) minerals investigated, emphasis was placed on studying the distribution and concentrations of uranium within the olivines, and in particular, the olivines from the Rhum intrusion. The reasons for this were:-

1) The compact nature of the nesosilicate structure and the similarity in M_1 and M_2 sites in olivine are likely to reduce the number of places wherein "foreign" trace elements may accumulate. During the study, on only five occasions were fission track "stars" observed, and on each occasion the source must only have been of the order of 1 μm, or less, in diameter. On these occasions, the mineral areas were scanned using the Jeol microanalyser (chapter 2), for elements phosphorus (P) and zirconium (Zr), since minerals containing these elements (e.g. apatite and sphene) contain comparitively large amounts (greater than 50 p.p.m.) of uranium (e.g. Burnett et al., 1971). No inclusions however, were found. The

probable sources of these "stars" were either contamination from dust, or below surface inclusions.

2) The relative constancy of the Fo/Fa ratio throughout both individual units, and the intrusion as a whole, allowed a means of standardisation - although recently Dunham (personal communication) has found some variation in Fo/Fa in a few units.

3) There exists within the olivine phase a wide variety of morphologies, which may result from different growth rates.

The olivines from samples of the Carligford intrusion were rejected owing to their being often totally altered and comparison could not directly be made with the Rhum olivines because of the reported wide range in forsterite content (Fo_{83} to Fo_{72} - Le Bas, 1960), the result of differentiation within each of the four units.

The range in concentration of uranium within the olivines in this study is comparatively large (from 4.30 to 8.32 p.p.b.). Previously reported values by other workers are scarce, but show also a wide range: e.g. Kleeman et al. (1969) quotes values of 0.2 to 0.7 p.p.b., and Fisher (1970), for dunites, of between 1.4 to 46 p.p.b.

The composition of olivine throughout the layered series of Rhum has been reported as being remarkedly constant (Brown,1956) varying only from $Fo_{83}Fa_{17}$ to $Fo_{86}Fa_{14}$, although more recent detailed work (Dunham, personal communication and Wood, personal communication) has extended this range. The olivines are thus magnesium-rich members of the Fo - Fa series with the name of chrysolite. A systematic detailed chemical analysis of the olivines was not undertaken, but several grains were analysed for Mg, Fe, Si, Ca and Ni using the Geoscan microprobe (chapter 2, section 2.8. for details), these grains being used as standards for other specimens on the more qualitative Jeol S.E.M.. A plot (figure 4.11) of olivine composition verses

Figure 4.11

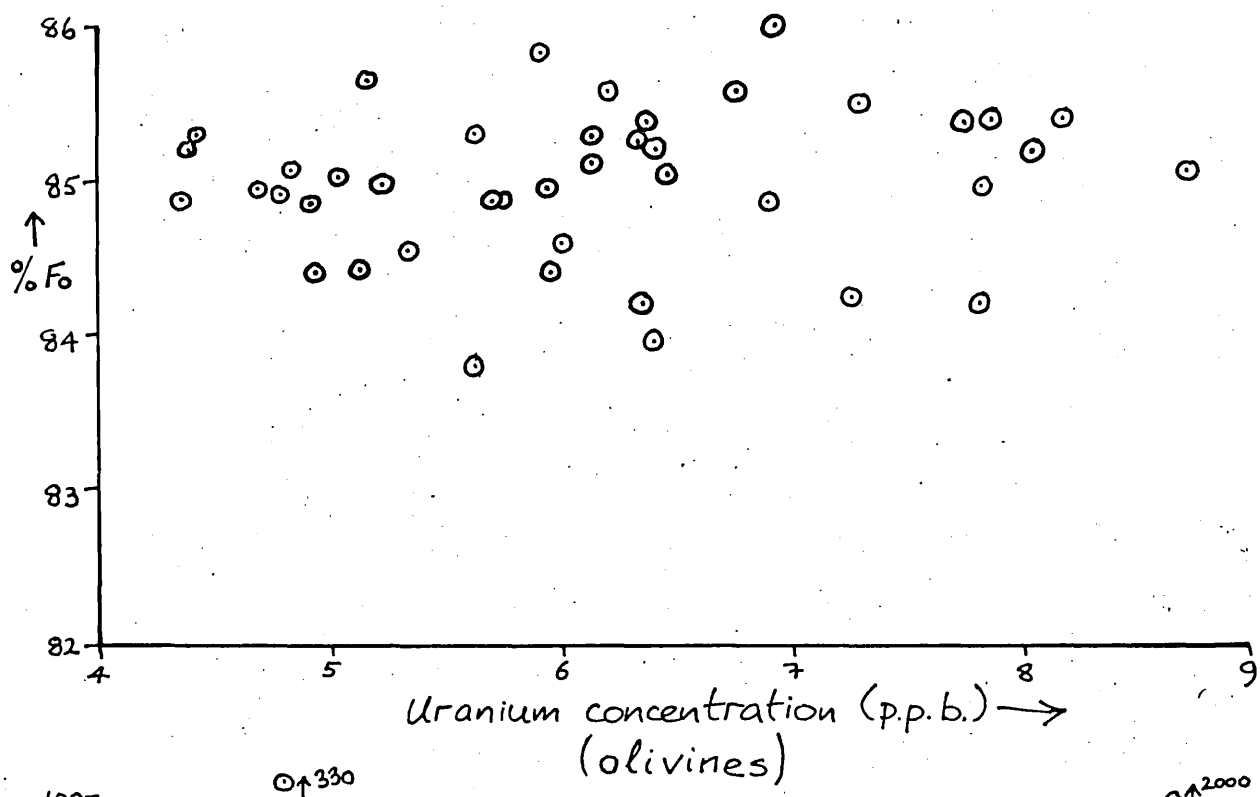

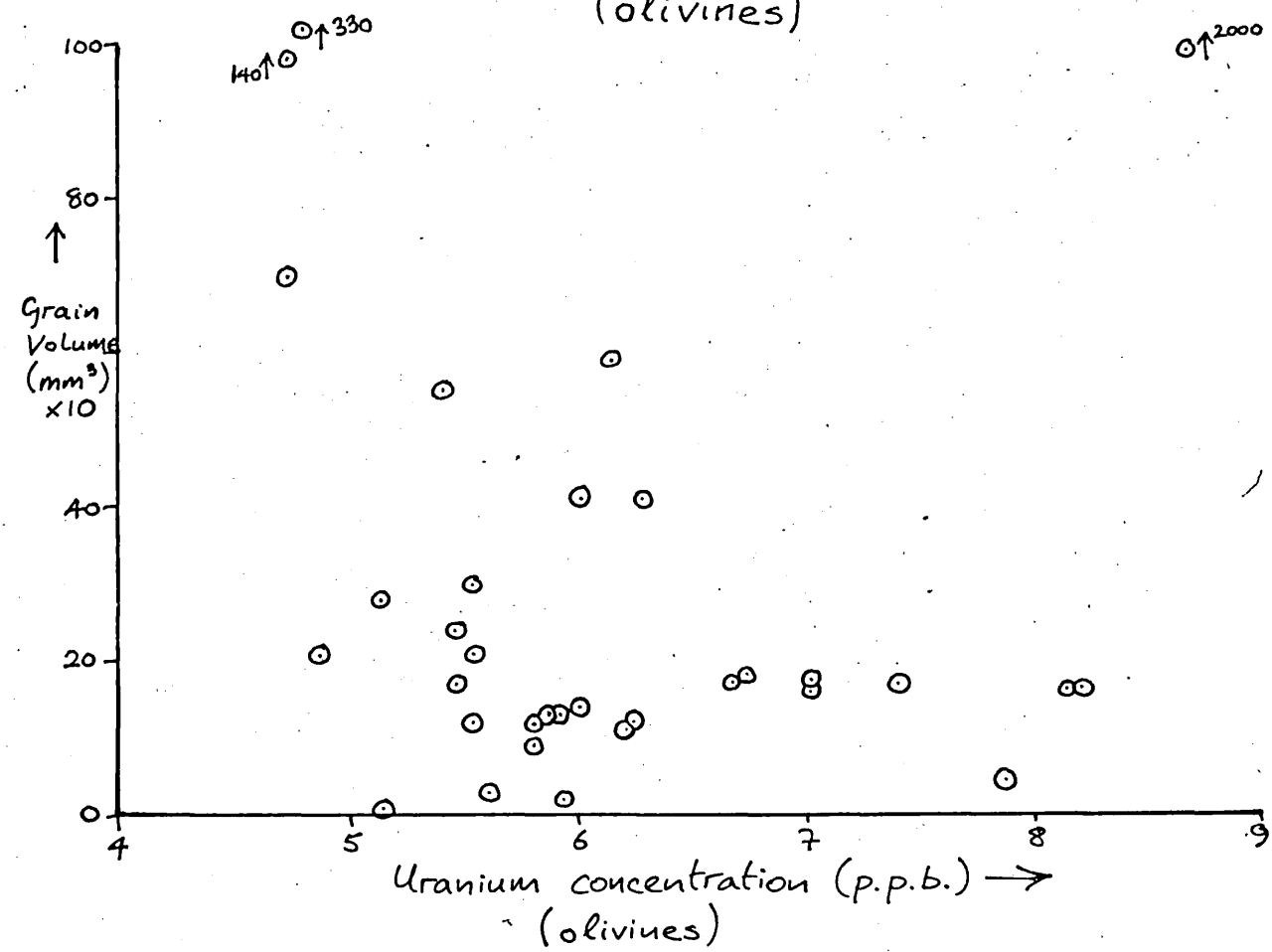

Figure 4.12

uranium content shows no discernable correlation.

One of the striking features of the olivines from the Rhum intrusion, is their marked variation in grain size (and volume). Brown (1956) first recognised this from a detailed examination of olivine size and shape within a single macrorhythmic unit (Brown ibid., figure 3). An inverse relationship between grain volume and uranium content of uraniferous minerals in mesostasis areas (i.e. intercumulus minerals) from lunar basalts was observed by Thiel et al. (1972) and Burnett et al. (1971). In order to see whether this inverse relationship held for cumulus olivine, estimated grain volumes were plotted against uranium concentration (figure 4.12), but again no discernable pattern emerged. Thus, for the olivine phase, grain volume is not the controlling influence in the observed uranium variation.

A plot of uranium concentration against height in intrusion (figure 4.13) similarly shows no correlation (the tie-lines link concentrations for different morphologies within the same rock). However, a feature worth noting (indicated also by the constancy of the Fo content), is the lack of differentiation of the intrusion for over 650 metres, with olivines of unit 1 having similar uranium contents to olivines of unit 14.

Since the method of fission track analysis involves area counting rather than point counting (in e.g. microprobe analysis), and the number of tracks observed for olivines was very low, often several grains were covered during the course of the analysis. Initially, no discrimination was placed over which of the olivine grains were to be counted. The outcome was a set of apparently constant values, the uranium concentrations having a lower mean range and less variation than table 4.1 now shows. When however, preselection of olivine grains for analysis on the basis of morphological type was undertaken, different values were found for

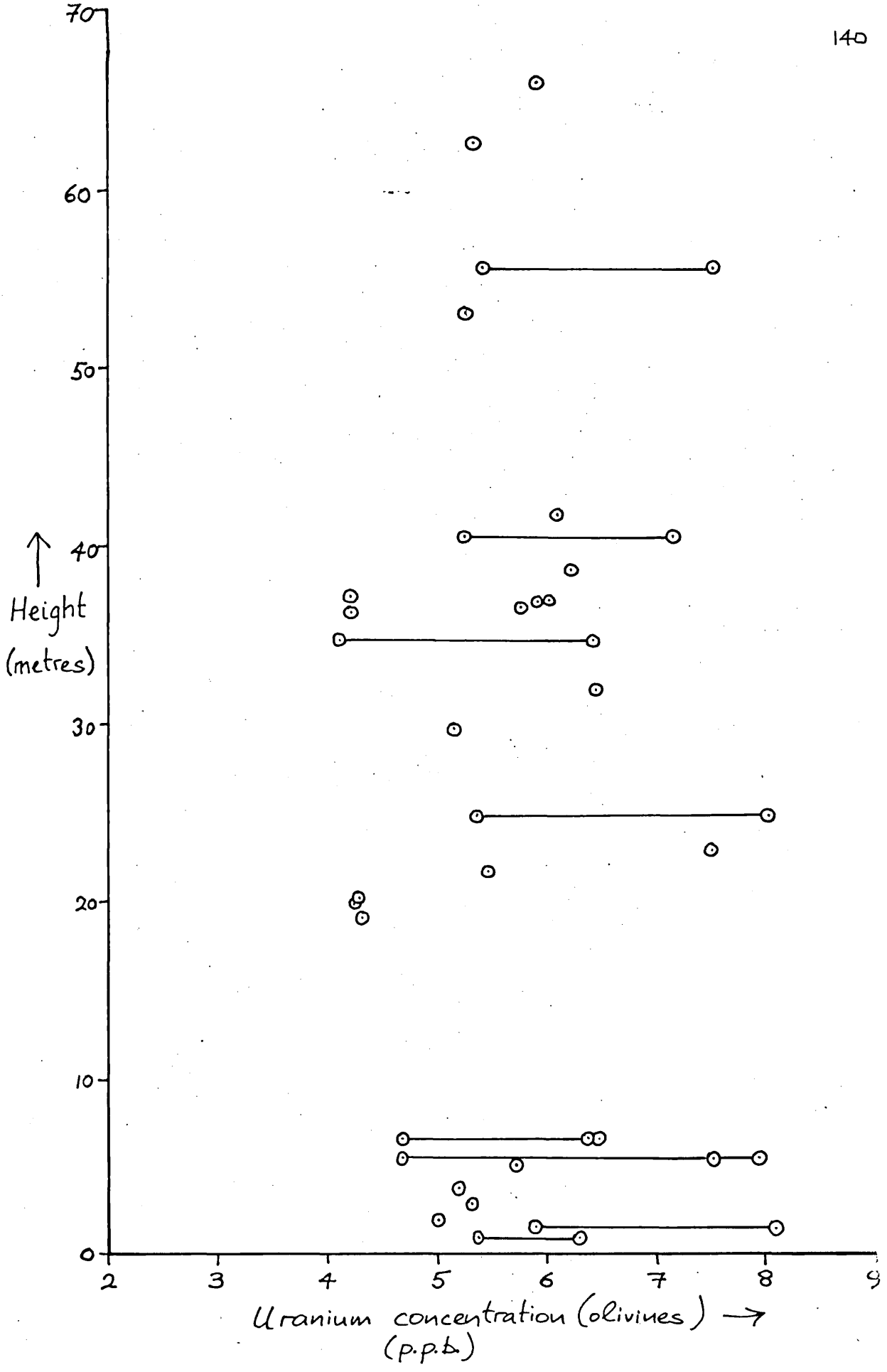
70
60
50
40
30
20
10
0
Height (metres)
2
3
4
5
6
7
8
9
Uranium concentration (olivines) →
(p.p.b.)

Figure 4.13

different morphologies, these often occurring within one rock specimen. On processing the new data by drawing a histogram of the frequency of distribution against the uranium concentration (figure 4.14), distinct groupings are indicated. On the basis of mean concentrations, the groupings can be resolved into six morphological types - table 4.2. (and figure 3.1., chapter 3) - although overlapping of types occur.

Table 4.2.

morphology	uranium (p.p.b.)	mean	S.D.	k_{obs} (mean)
poikilitic	4.30 - 4.52	4.415	.09	.0147
equant	4.88 - 5.33	4.998	.43	.0166
rounded	5.17 - 6.40	5.922	.43	.0197
irregular	5.13 - 6.71	5.993	.42	.0199
tabular	6.35 - 8.03	7.161	1.08	.0239
harrisitic	8.21 - 8.43	8.335	.06	.0227

The morphology of the olivines is considered then to be a fundamental factor in controlling the amount of uranium which enters the olivine structure, and, in the interpretation (section 4,4), arguments are put forward relating the morphology and uranium concentration to the degree of supercooling and crystal growth rate of the phase.

4.3.1.1. Poikilitic morphology

The employment of the textural term "poikilitic" (or "sub-poikilitic") in preference to the term "ophitic" (or "sub-ophitic") here, follows Wager and Brown's (1968) usage. The distinction between the two terms is in any case not clear cut, and is based apparently only on size - e.g. Challinor (1973) mentions that the term ophitic merges into the term poikilitic when "...the individual mafic crystals are very large in comparison with the feldspars and thus completely enclose many of them...". Wager and Deer (1939) for the Skaergaard intrusion, initially proposed the poikilitic habit to be characteristic

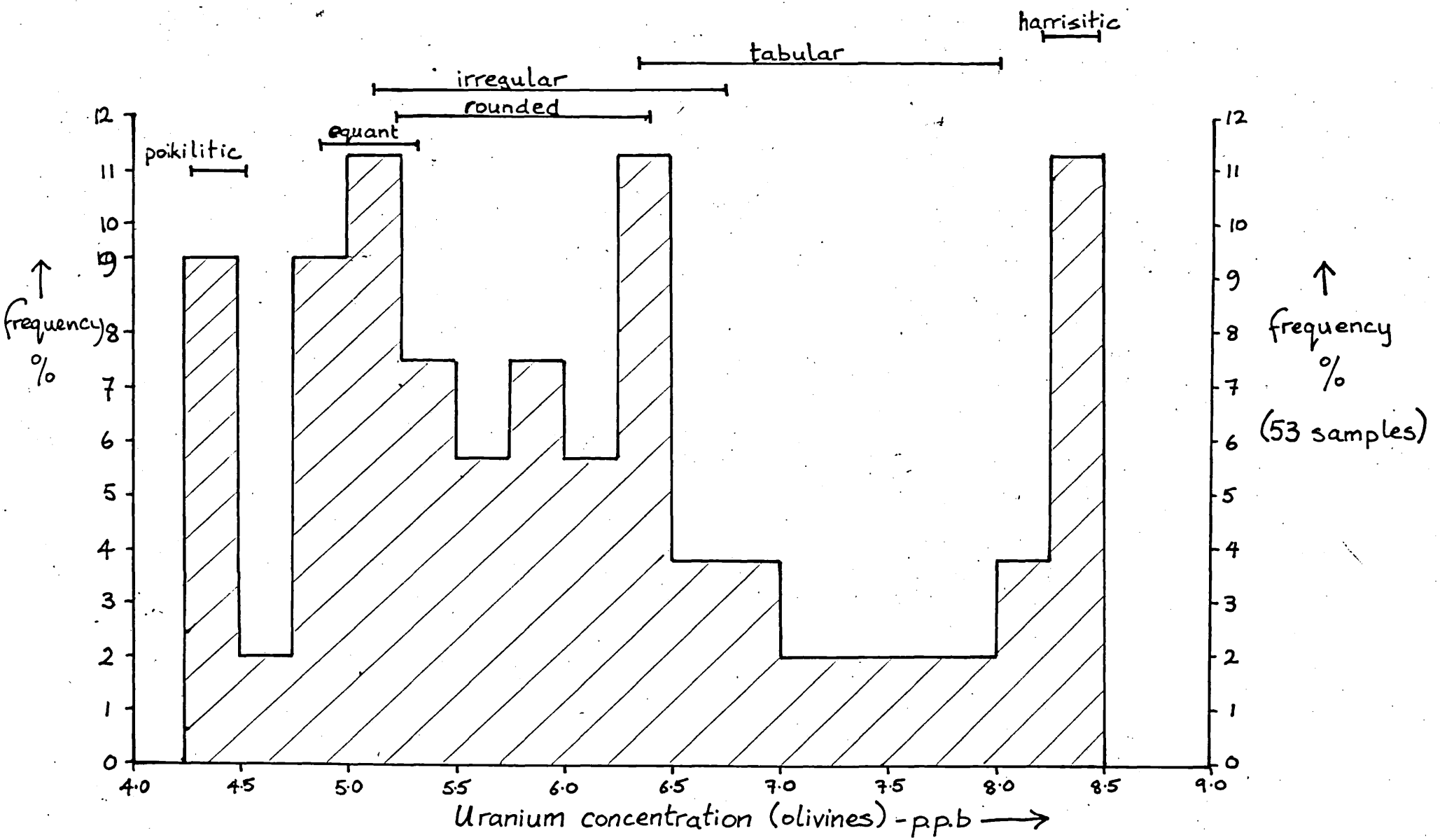
harrisitic
tabular
irregular
rounded
equant
poikilitic
frequency %
0
1
2
3
4
5
6
7
8
9
10
11
12
4·0
4·5
5·0
5·5
6·0
6·5
7·0
7·5
8·0
8·5
9·0
Uranium concentration (olivines) - p.p.b
frequency %
(53 samples)

Figure 4.14

of phases crystallised from intercumulus magma; Wager and Brown (1968, p.60) extended this by using the prefix "sub-" to include those intercumulus crystals which did not develope enough to completely enclose the cumulus crystals, thus, in effect, discarding the use of the term ophitic in layered igneous rocks.

Results presented in table 4.2. and figure 4.14, show that in terms of uranium content, the poikilitic morphology is distinct from other morphologies. These olivines have the lowest uranium concentration and smallest standard deviation of the six recognised types. Detailed analyses of olivines with this morphology are given below in table 4.3.

Table 4.3.

rock no.	unit no.	thermal neutron dose ($\times 10^{17}$ n.cm^{-2}.sec^{-1})	area counted ($\times 10^4$ m^2)	no. tracks	tracks. cm^{-2} ($\times 10^4$) *	U ppb. ($\pm$.331)	Fo content	NiO	CaO
62	8	1.94	100	103	0.990	4.39	85.30	-	-
63	8	1.94	100	101	0.970	4.30	85.10	-	-
64	8	1.94	100	102	0.980	4.34	85.21	.114	.030
89	3	1.73	100	95	0.910	4.52	85.34	-	-
86	3	1.73	100	95	0.900	4.47	85.17	.165	.101
87	3	1.73	100	94	0.900	4.47	85.25	.177	.098

* After subtraction of background from the detector viz. thermal neutron dose $\frac{120}{6} \times 10^{16}$ tracks.cm^{-2} (see section 2,6)

Texturally, this morphological type occurs poikilitically or sub-poikilitically enclosing cumulus feldspar (plate 4.1.). Its modal percentage is low (usually less than 40% volume), and is found towards the top of the units, usually in the feldspar-cumulate. Although its occurrance on Rhum is not plentiful, its occurrence in other layered intrusions appears to be rare. Hess (1960, p.83) records an example from the Stillwater complex of an intergrowth of olivine

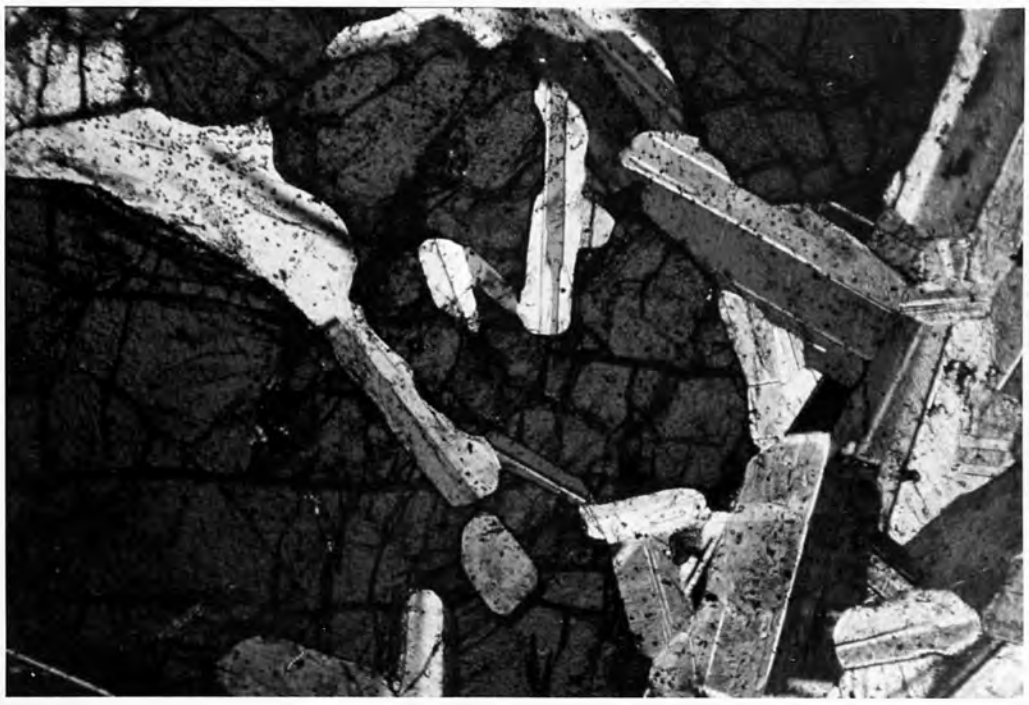

PLATE 4.1. Poikilitic olivine enclosing cumulus feldspar.

0·5 mm.

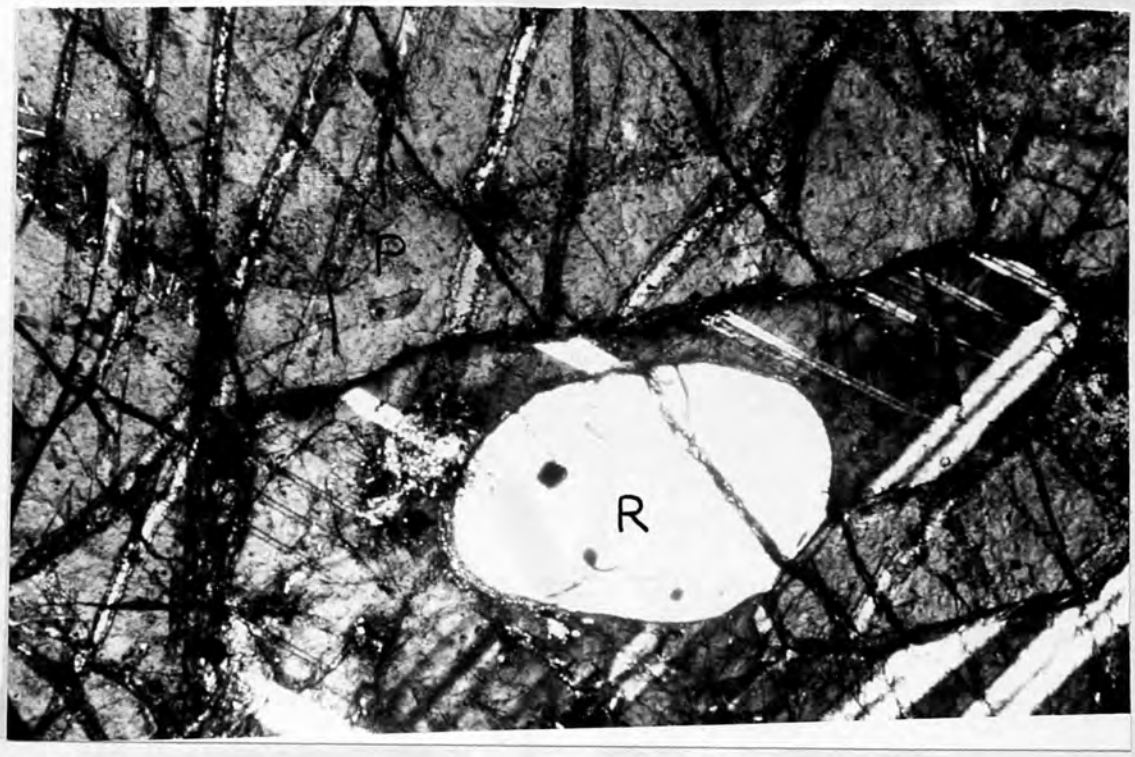

PLATE 4.2. Poikilitic (P) and rounded (R) olivines.

0.2mm.

and plagioclase (ibid. plate 5, figure 1) which he denotes as being poikilitic olivine. Wager and Brown (1968, p.257) suggest that this texture on Rhum may not be sensu stricto poikilitic (i.e. may not have formed from intercumulus liquid), but may have developed through deposition as a composite cluster of olivine and feldspar. Hess (1960) however, believes the Stillwater poikilitic olivines to have settled initially as cumulus crystals (as evidenced by their plagioclase - free cores) but (ibid. p.83) to have grown to a considerable extent from the interstitial liquid. Whilst the poikilitic habit of the olivines is not developed to the extent of the clinopyroxenes or the feldspars of the Rhum intrusion, in two specimens (R.62 and R.63 from unit 8), there is clear textural evidence (plate 4.2) of olivines having both an intercumulus and a cumulus (rounded) morphology within the same rock specimen. The uranium concentrations of these texturally dissimilar olivines differ markedly, whereas their forsterite contents are similar (table 4.4.).

Table 4.4.

rock no.	morphology	modal % (of rock)	U ppb.	partition coefficient ($x10^{-3}$)	Fo content
R.62	poikilitic	46.8	4.39	14.63	85.30
	rounded	18.2	5.99	19.97	85.28
R.63	poikilitic	51.3	4.30	14.33	85.10
	rounded	18.0	6.30	21.00	85.21

Since there is no fall in the Fo content for the poikilitic phase crystallising from the intercumulus magma when compared with the cumulus phase, fractionation had not occurred and using Wager et al.'s (1960) terminology, the poikilitic olivine may be described as a heteradcumulus phase.

An indication of the crystallisation process with which the

poikilitic olivine had formed can be obtained by comparing the uranium contents of the two phases in table 4.4. Uranium, being a low partitioning element, would be expected to accumulate in the intercumulus magma (e.g. Rogers and Adam, 1969), having been "rejected" from the early formed minerals. Use of this simple model predicts therefore, that a mineral crystallising as an intercumulus phase would incorporate more uranium than if it crystallised as a cumulus phase. The data in table 4.4. does not appear to support this. The model however, does not take into account the variety of factors involved in nucleation and crystal growth mechanisms of the different phases, and this aspect is discussed more fully in section 4.4

A comparison of the partition coefficients in table 4.4. for the two phases shows that $(k_{obs})_{cumulus}$ is greater than $(k_{obs})_{poikilitic}$. This in terms of equations (14) and (15), section 4.2., implies that the poikilitic phase had crystallised under slower growth rate and more equilibrium conditions (lower ΔT and lower supersaturation) than the cumulus phase. Implicit also within the above arguments, is the point made initially by Hess (1939), and expanded by Wager et al. (1960), that free access to the main bulk of the magma was necessary in order to allow diffusion of material towards, and diffusion of material (including uranium) and heat (Wager, 1963) away from the growing phase. Were this not to occur, then the intercumulus magma would become trapped and crystallise out as lower temperature mineral phases (or lower temperature zones). Wager et al. (1960) called this process adcumulus growth (or heteradcumulus growth when applied to heteradcumulus phases), and, given the required spatial environment, becomes more probable under equilibrium and slow growth rate conditions. It is proposed therefore to equate the partition coefficient of the poikilitic phase, $(k_{obs})_{poik}$, to the equilibrium partition coefficient (k_{equ}) described above in section 4.2..

Unfortunately, not all observations are consistent with this

model. For example the nature of a microprobe scan (for major elements Fe, Mg and Si, and minor elements Ca and Ni) across a poikilitic olivine of R.64.

The results are given in table 4.5., and shown graphically in figure (4.15). From the results, a slight zoning of the major elements is

Table 4.5.

Analysis no.	Position (mm.)	FeO	MgO	SiO_2	CaO	NiO	Total	Fo content
1	0 (edge)	14.21	44.74	40.13	.054	.102	99.24	84.88
2	.40 (mid)	13.88	44.84	40.39	.074	.083	99.23	85.20
3	.74 (edge)	13.97	44.97	40.41	.043	.104	99.51	85.15
4	2.23 (edge)	14.05	45.16	39.92	.050	.106	99.30	85.13
5	2.39 (mid)	13.99	45.18	40.04	.029	.105	99.31	85.19
6	2.60 (edge)	13.84	45.26	39.81	.042	.067	99.02	85.36
7	3.17 (mid)	14.01	45.34	39.80	.012	.113	99.28	85.22
8	4.06 (mid)	14.01	45.38	39.91	.004	.124	99.43	85.24
9	4.86 (mid)	13.84	45.08	40.10	.000	.133	99.16	85.30
10	5.09 (edge)	13.94	44.96	39.98	.017	.131	99.04	85.18
11	5.48 (mid)	13.94	45.55	39.91	.000	.150	99.55	85.35
12	5.61 (edge)	13.78	44.76	40.20	.059	.087	98.90	85.27
13	7.50 (edge)	13.77	45.05	39.93	.044	.136	98.93	85.36
14	7.78 (mid)	14.25	45.34	39.88	.000	.130	99.61	85.01
15	8.08 (edge)	13.99	14.09	39.94	.019	.134	99.18	85.17

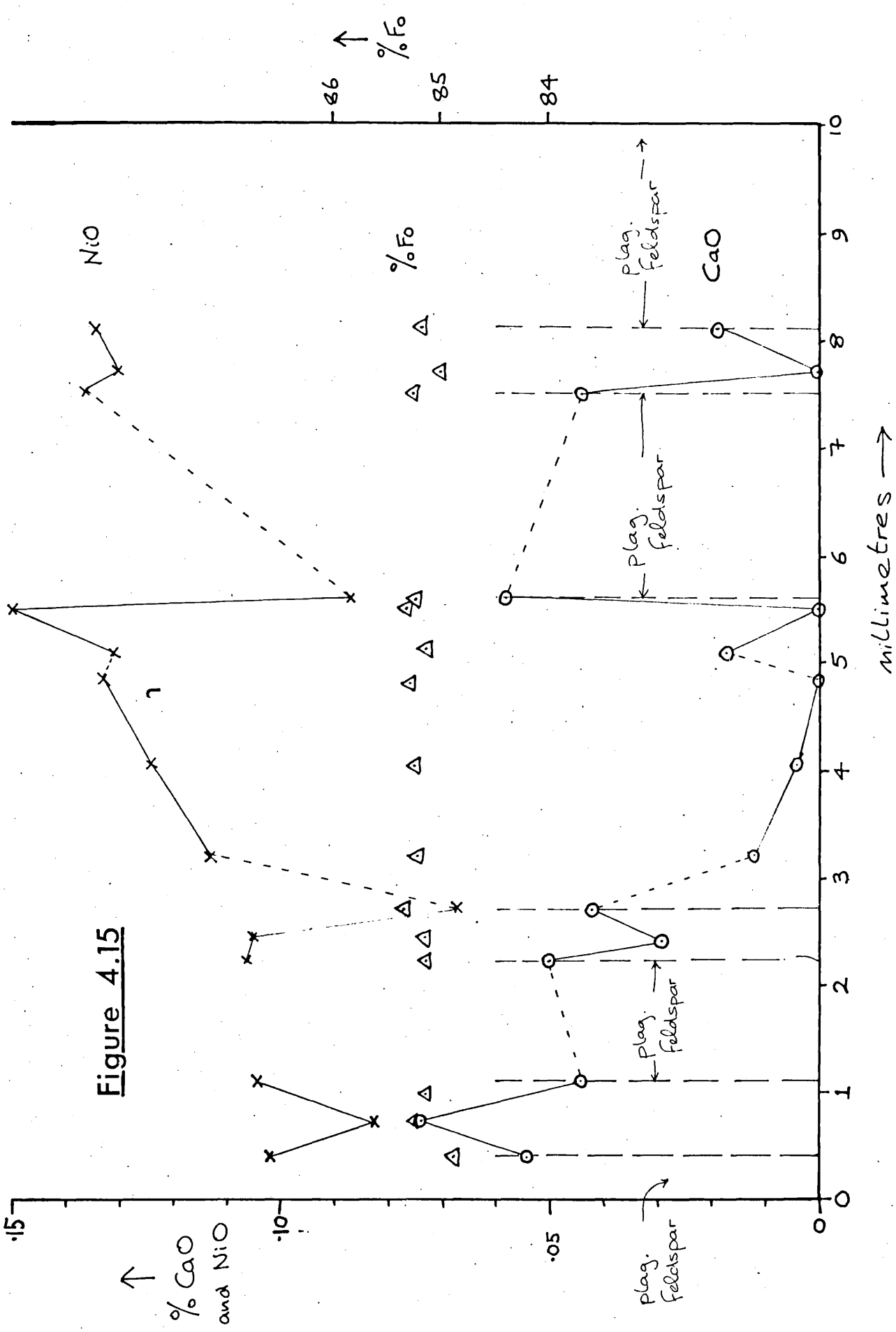
% CaO and NiO
.15
.10
.05
0
NiO
% Fo
86
85
84
CaO
plag. feldspar
plag. feldspar
plag. feldspar
plag. feldspar
0
1
2
3
4
5
6
7
8
9
10
millimetres

Figure 4.15

observed (from $Fo_{84.88}$ to $Fo_{85.36}$), together with an inverse relationship between Ca and Ni. (A uranium gradation, if present, would not have been detected owing to the very low concentration resulting in a small number of tracks). Inverse relationships between Ca and Ni have been observed elsewhere, in e.g. a series of olivines from a lava flow (Shaw, 1975 - personal communication), and can be at least qualitatively predicted in that Ca, with respect to olivine, is a low-partitioning element, and Ni a high-partitioning element. The trace element (Ca and Ni) results are however subject to large analytical errors both from their initial low concentrations and because unpredictable interference effects (in particular for Ca) from the close proximity of the enclosed feldspars would occur. In addition, no quantitative measurements of the three-dimensional aspects of that particular olivine were made. If taken at face value, the resultant fluctuations in Ni and Ca would appear to indicate that small-scale variations in either the intercumulus material or crystal growth rates had occurred during heteradcumulus growth. Future detailed distribution studies of these elements may provide a clearer picture, but these results do not appear to detract from the main features of the uranium results or their genetic implications.

4.3.1.2. Equant morphology

The equant morphological group of olivines were characterised using two separate criteria. Firstly, on the basis of the number (or proportion) of crystal faces developed - olivines having euhedral or subhedral habits (i.e. with two-thirds or more of the faces developed); and secondly on the a:b ratio. (figure 4.16). Olivines with a:b ratios less than 2.5:1.0, together with euhedral or subhedral crystals were classified as equant - plate(4.3) shows an olivine with typical equant morphology.

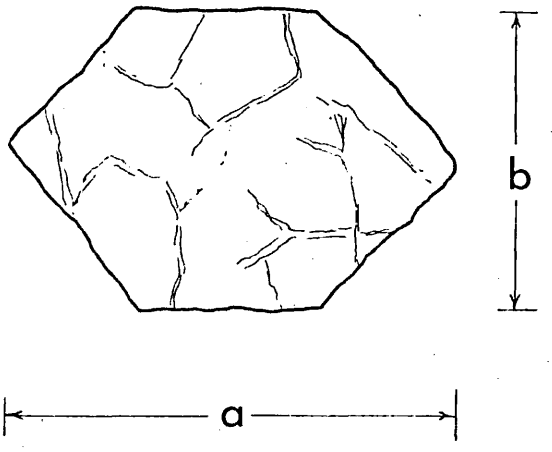

Figure 4.16

The equant morphology was the most common morphological type observed throughout the intrusion. The variation in size was not large, "a" varied from 0.4 to 2.5 millimetres and "b" from o.4 to 1.75 millimetres, Brown (1956) however noted a tendency for the higher units to have a smaller grain size. The equant morphology occurs also more commonly in the lower regions of each unit with a gradation towards more irregular and/or poikilitic morphologies towards the top of each unit. This observation was made also by Brown (ibid) and was well-depicted in his type unit (Brown ibid figure 3). The details of the uranium concentrations and, where analysed, the Fo contents, NiO and CaO concentrations within this morphological group are given in table 4.5 (a).

Unlike the poikilitic and harrisitic (section 4.3.1.5.) morphological groups, the equant olivines, with respect to the uranium concentrations, do not form a totally distinct group, there is overlap with rounded, irregular and tabular morphological types (figure 4.1 4). This may be due in part to errors in assigning an olivine to its incorrect morphology when track counting, since usually only a two-dimensional view is obtained. However, in spite of the limitations of classification on the basis of shape and crystal form, resolution into four groups is possible, and, from the differences in mean uranium concentrations and the low S.D.'s, is quite justifiable. Furthermore, it is contended that the observed differences within each group are a manifestation of differences in genesis of the olivine types.

Perhaps the most striking textural feature of the equant olivines is their frequent tendency to coalesce. Up to five separate olivines are seen apparently intergrown with each other each retaining its euhedral crystal habit (plates 4.3,

Table 4.5 (a) Equant Olivines

Rock Number*	Unit Number	U p.p.b.**	Fo content	NiO	CaO
90	1	5.01	85.01	.189	.100
91	1	5.13	-	-	-
92	2	4.93	84.42	.203	.106
93	2	5.69 (1)	85.31	-	-
94	2	4.99	-	-	-
96	3	6.38	85.46	.171	.088
99	3	5.27	85.01	-	-
83	5	5.17 (2)	84.99	-	-
84	5	6.74 (3)	85.60	.160	.101
85	5	5.10	-	-	-
82	6	5.26	-	-	-
120	7	7.34 (3)	85.13	-	-
112	8	5.33	-	-	-
110	8	6.44 (1)	85.06	.164	.113
111	8	6.08 (1)	85.13	.139	.108
53	9	4.88	84.84	.160	.080
54	9	5.13 (1)	85.66	-	-
113	10	6.00 (2)	-	-	-
114	10	5.90 (2)	-	-	-
66	11	4.96	87.26	-	-
68	11	4.88	86.60	-	-
115	13	5.00	86.46	-	-
116	13	5.39 (2)	84.92	.169	.111

Average (excluding modification) = 4.998 p.p.b. U

* All specimens prefixed "R".

** After corrected for background.

(1) to (3) modifications

(1) to irregular

(2) to rounded

(3) to tabular

and 4.4). An initial cumulus origin for this group is suggested by the tendency for equant olivines to occur in the lower regions of each unit (Brown ibid. p.15) giving rise to a high modal percentage, but the manner in which they interlock clearly could not have resulted from packing during settling as cumulus crystals. A microprobe traverse across three "coalesced" equant olivines (from R.92) for major elements Fe, Mg and Si, and minors Ca and Ni was undertaken to check for zoning. The direction of the traverse is shown in plate (4.4); the results obtained in table 4.6, and figure (4.17): the uranium concentration for equant olivines from this rock was 4.93 p.p.b..

Table 4.6.

Analysis no.	Position (mm.)	FeO	MgO	SiO_2	CaO	NiO	Total	Fo content
1	0	14.33	44.81	39.84	.112	.189	99.29	84.38
2	.2	14.41	44.86	39.71	.114	.195	99.33	84.41
3	.2	14.41	44.79	39.80	.101	.210	99.33	84.41
4	.1	14.42	44.82	39.78	.098	.211	99.34	84.41
5	.1	14.39	44.83	39.76	.098	.224	99.31	84.40
6	.1	14.42	44.84	39.81	.106	.203	99.38	84.42
7	.3	14.43	44.83	39.76	.118	.199	99.36	84.42
8	.3	14.42	44.85	39.79	.112	.215	99.39	84.41
9	.1	14.50	44.83	39.69	.109	.218	99.35	84.44
10	.1	14.44	44.84	39.74	.086	.215	99.33	84.42
11	.1	14.41	44.82	39.81	.104	.190	99.35	84.41
12	.4	14.42	44.83	39.75	.113	.171	99.28	84.40
13	-	14.39	44.83	39.77	.105	.209	99.32	84.41
14	-	14.41	44.81	39.80	.096	.213	99.34	84.42
15	-	14.43	44.82	39.76	.107	.199	99.32	84.42

(Analyses 13 - 15 in table 4.6 are of rounded olivines poikilitic enclosed by clinopyroxene and with a uranium concentration of 5.89 p.p.b.)

The lack of major element zoning across the interfaces of the coalesced olivines (analyses 1 - 12) and the similarity in Fo content with olivines having a rounded morphology (analyses 13 - 15) implies that extension of the rounded cumulus olivines occurred by an adcumulus growth mechanism (Wager et al., 1960, terminology) to produce equant olivines. Post-depositional recrystallisation at grain boundaries in a similar manner to e.g. diagenetic pressure/solution effects in quartz sediments cannot be excluded, but the transport problem of expelling the interstitial liquid and consequently adding the "olivine-rich" material remains.

Table 4.7., a comparison of the two morphologies present, indicates a marked difference in both the uranium concentration and partition coefficients between the rounded and the equant morphology. The partition coefficients for the cumulus rounded

Table 4.7.

morphology	modal % of rock	U conc^{n}. (p.p.b.)	k_{obs} (10^{-3})	Fo content	CaO	NiO
equant	59	4.93	16.43	84.42 (average of 12 analyses)	.106	.203
rounded	11	5.89	19.63	84.42 (average of 3 analyses)	.103	.207

morphology $(k_{obs})_{cum}$ is greater than that for the equant $(k_{obs})_{equ}$ - i.e. cumulus plus adcumulus growth - morphology, and from equations (14) and (15) section 4.2., this suggests for the equant morphology, a slower growth rate under more equilibrium conditions (lower ΔT, lower supersaturation) at the time of crystallisation. The lower uranium concentration of the equant morphology is considered to be the result of combining the (relatively) high uranium content

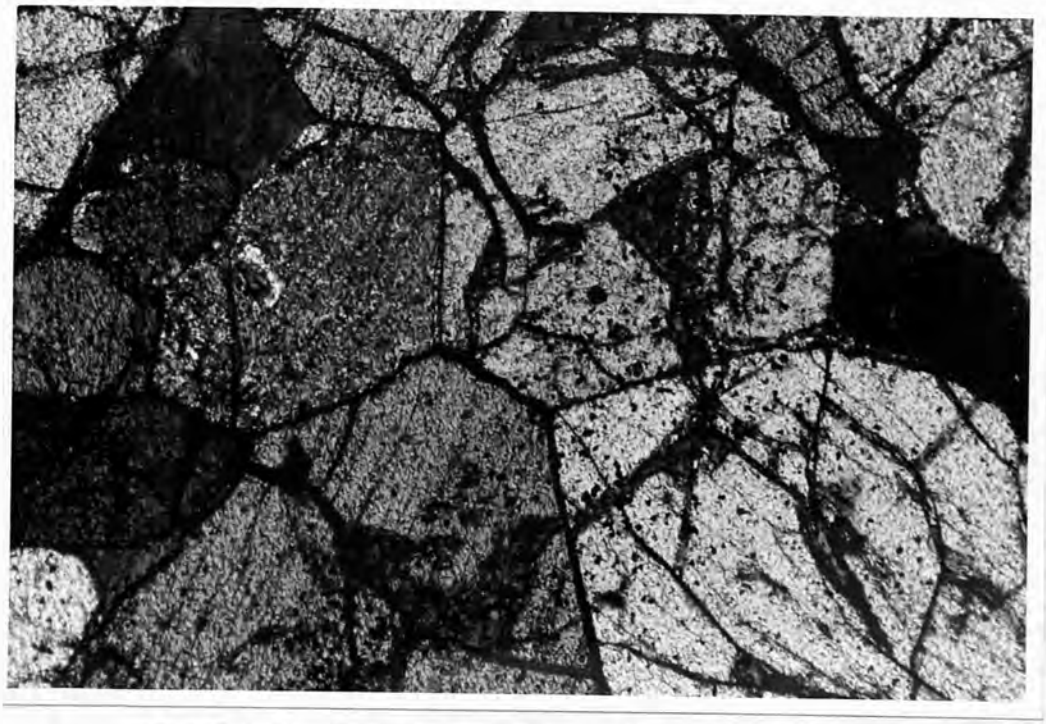

PLATE 4.3. Equant morphology (4 coelescing) 0·2 mm.

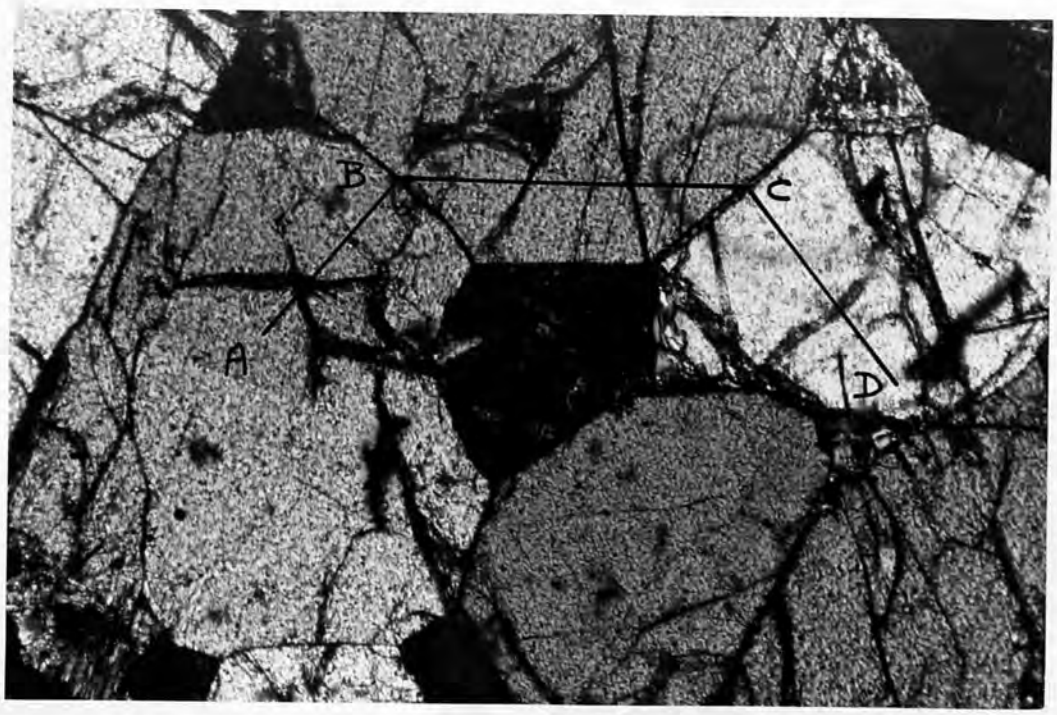

PLATE 4.4. Equant morphology (6 coelescing) 0·2 mm.

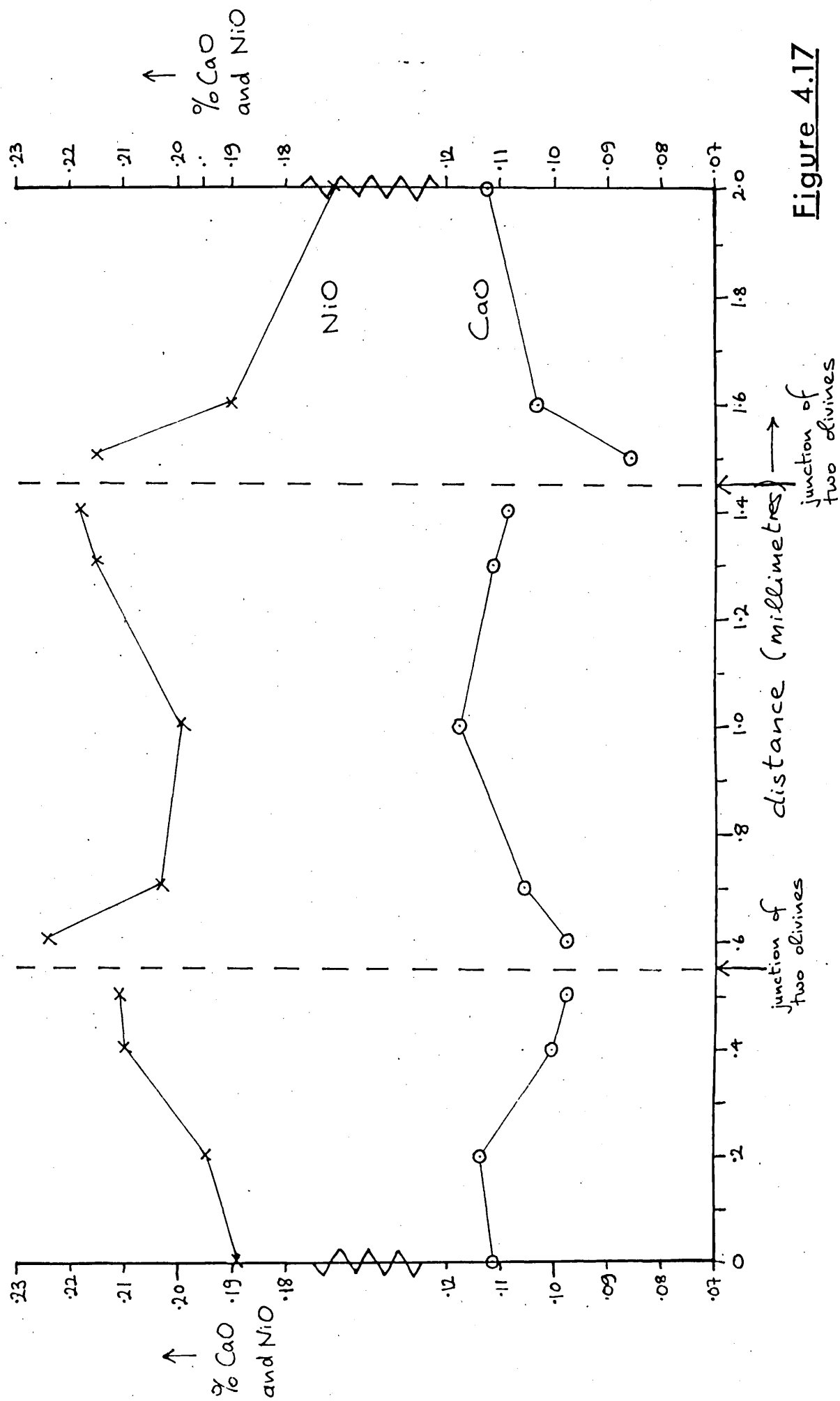
% CaO and NiO
NiO
CaO
distance (millimetres)
junction of two olivines
junction of two olivines

Figure 4.17

of the original cumulus crystal, with the (relatively) low uranium content of the adcumulus overgrowth regions. The conditions under which adcumulus overgrowth occurred would therefore be similar to those for heteradcumulus growth in the poikilitic olivines (section 4.3.1.1.) - viz. equilibrium conditions producing a (slow) diffusion controlled growth mechanism. The relative proportions of uranium within both the original cumulus mineral and its adcumulus growth extension unfortunately could not be distinguished owing to the limitations of the fission-track technique at low concentrations (i.e. a uranium gradient could not be detected). In Figure (4.17.) however, a drop in CaO mirrored by a rise in NiO towards the edge of the equant olivines (i.e. in the zone of adcumulus growth) is observed, thereby suggesting different crystallisation mechanisms for the two morphologies.

4.3.1.3. Rounded morphology

The rounded morphological olivines were characterised by their spherical and anhedral crystal form (plate 4.5). They occur within a rock specimen usually in association with other olivine morphologies (mainly equant, irregular and tabular morphologies) incorporated in the clinopyroxene and feldspar heteradcumulus phases, and often contributing only a low modal percentage of rock. Their size is consistantly small with diameters ranging from 0.1 millimetres to 0.9 millimetres, and this fact, together with the low modal percentage meant that in track counting, the number of area counts which could be performed was low, giving rise to a decrease in the reliability of some of the results. This is a contributing factor to the higher S.D. observed for this morphology (table 2). The details of analyses for rounded morphology are given below in table 4.8.

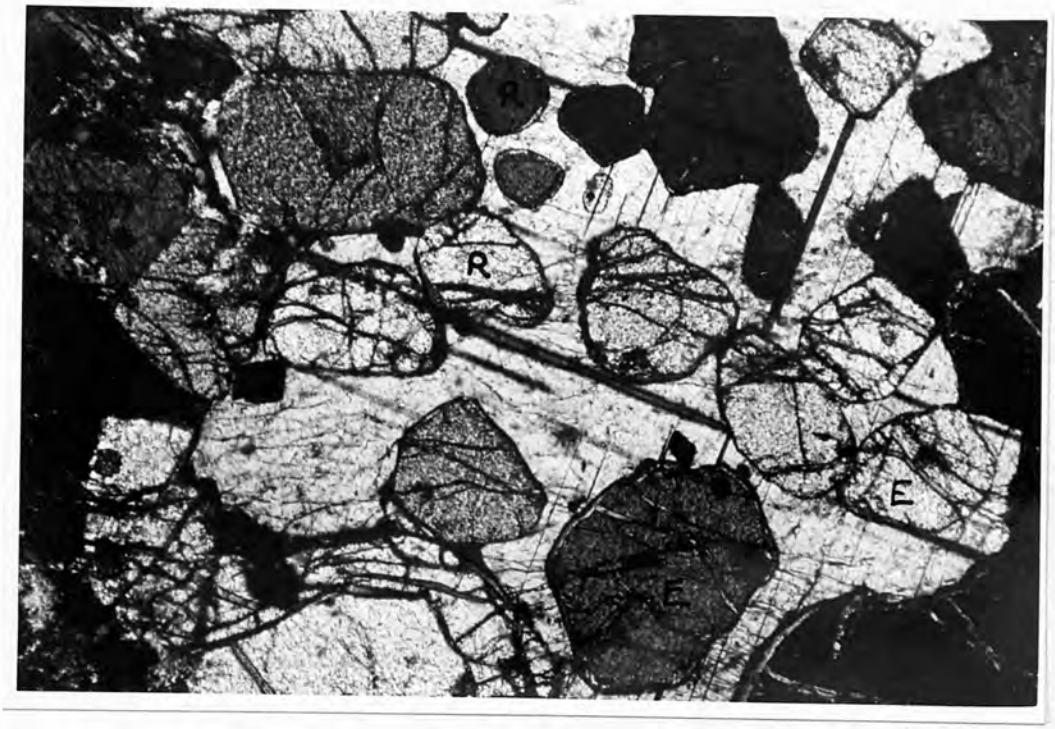

PLATE 4.5. Rounded (R) and Equant (E) morphologies

0·5 mm.

PLATE 4.6. Irregular morphology

Table 4.8.

Rock no.	Unit no.	thermal neutron dose*	Area counted (10^4 m^2)	tracks	tracks per cm^2 (10^4)**	U (ppb)	Fo content	NiO	CaO
90	1	1.94	40	153	1.2912	5.72	84.87	.178	.105
92	2	0.85	50	130	0.583	5.89	84.42	.103	.207
99	3	1.71	100	125	1.2158	6.11	85.30	.178	.098
83	5	1.53	100	95	0.9194	5.17	84.99	-	-
61	8	1.87	100	143	1.3926	6.40	85.34	.155	.096
62	8	1.94	100	139	1.3512	5.99	85.28	-	-
63	8	1.94	100	146	1.4212	6.30	85.21	-	-
53	9	1.80	100	136	1.3240	6.33	84.19	-	-
116	13	1.90	50	62	1.1920	5.39	84.92	.169	.111

*$x10^{17}$ neutrons.cm^{-2}.sec^{-1}. Av.= 5.92

**After subtraction of background from detector - viz.

$$\text{dose} \times \frac{120}{6 \times 10^{16}}$$

Their occurrence, mainly in the lower reaches of each unit, has been interpreted by Brown (1956, p. 15) as having nucleated and then travelled over only a short distance, thus having had little time to grow. When they do appear in the upper horizons, they "..... represent primary crystals which have failed in some way to be fed with olivine-precipitating liquid" (Brown ibid. p. 16). Genetically therefore, there appears little doubt that this morphology represents an initial cumulus phase with little or no post-depositional extension. In fact, the textural appearance of these olivines lends itself to interpretation of some form of post-crystallisation corrosion to produce the spherical form. Whether or not this occurred during deposition or during subsequent heteradcumulus growth of the

enclosing clinopyroxene or feldspar is difficult to say, but, the presence of both rounded and equant olivines incorporated within a single heteradcumulus plagioclase (plate 4.5) suggests that the former explanation is the more probable. It is difficult to envisage a situation whereby simultaneous corrosion of some olivines occurred to give a rounded morphology, and adjacent olivines extended by adcumulus growth to produce equant olivines. With initially rounded olivines, small scale, localised fluctuations in ΔT and supersaturation in the surrounding magma may provide suitable conditions for selective diffusion controlled adcumulus growth to result giving the two morphologies.

4.3.1.4. Irregular morphology

This morphology group is the least well-defined in terms of crystal shape. It varies from a subhedral (plate 4.6. to an anhedral, amoeba-like shape (plate 4.7), and in terms of size, from 0.1 millimetre to 4 millimetres diameter. Although it occurs predominantly in the upper horizons of the units, where Brown (1956) noted a transition from a euhedral shape to a more irregular shape with increasing height in the unit, it may be found in low modal percentages in most of the rock specimens. Because of these low modal percentages, it was often not feasible to calculate the uranium concentrations and in table 4.9. below, results are limited to those rock specimens where a significant number of area counts could be made.

A microprobe scan for major elements Fe, Mg and Si, and minor elements Ca and Ni was made to determine whether zoning was apparent. The trajectory of the scan is given in plate (4.7 the results obtained (analyses 1 to 6) in table 4.10.

Table 4.9.

Rock Number	Unit Number	Thermal neutron dose *	Track density**	U (p.p.b.)	Fo content	NiO	CaO
R.93	2	0.85	0.5630	5.69	-	-	-
R.95	2	1.71	1.3358	6.71	85+	-	-
R.96	3	1.71	1.2658	6.38	85.46	.166	.092
R.99	3	1.71	1.1258	5.66	84.87	.183	.100
R.65	8	1.87	1.2826	5.90	-	-	-
R110	8	1.21	0.9058	6.44	-	-	-
R.111	8	1.21	0.8558	6.08	85.13	.11	.05
R.54	9	1.80	1.074	5.13	85.66	.09	.04

Average = 5.99 p.p.b.

* $\times 10^{17}$ neutrons. $cm^{-2}.sec^{-1}$

** After subtraction of background and $\times 10^{4}$ tracks.$cm.^{-2}$

\+ Estimated using the Jeol S.E.M.

Table 4.10.

Analysis Number	Position (mms.)	FeO	MgO	SiO_2	CaO	NiO	Total	Fo	U (p.p.b.)
1 (A)	0 (edge)	14.20	44.69	40.10	.09	.18	99.26)		)
2	0.2	14.34	44.83	40.05	.09	.20	99.51)		)
3	0.8	14.25	44.81	40.14	.11	.18	99.49)	84.87	) 5.66
4	1.6	14.27	44.78	39.86	.10	.17	99.18)		
5	2.2	14.23	44.83	40.00	.09	.18	99.33)		)
6 (B)	2.4	14.26	44.81	39.94	.11	.17	99.29)		)
7	-	13.80	45.11	40.02	.09	.18	99.20)		)
8	-	13.93	45.06	40.11	.09	.17	99.36)	85.30	) 6.11
9	-	13.84	45.09	39.88	.10	.18	99.09)		)

Analyses 7 - 9: Uranium concentration = 6.11 (± 0.03 ppb.)

Partition coefficient (k_{obs}) = ·0204

The results (analyses 1 - 6, from specimen R.99) show that neither major nor minor element zoning had occurred, and when comparison is made with olivines having a rounded morphology (0.5 millimetres diameter average), analyses 7 - 9, it can be seen that there is virtually no difference in either the major or the minor elements between the two morphologies. Also, the uranium concentrations (and partition coefficients) are similar for the two morphologies despite their marked differences in crystal shape.

Whilst no chemical differences are apparent, the morphologies of the two are clearly different and textural evidence such as coalescing (plate 4.5) indicates some post-depositional overgrowth of original cumulus crystals. Because no zoning occurred, the terminology of Wager et al. (1960) would classify this as adcumulus overgrowth, and Brown (1956) suggests growth from intercumulus liquid had resulted to give the irregular crystal shape. Since the uranium concentrations and partition coefficients for the irregular morphology are greater than for the equant morphology (section 4.3.1.2.) this implied that the overgrowth occurred during larger ΔT and supersaturation conditions and that with respect to the trace element uranium, this overgrowth was not diffusion-controlled to the same extent as for the equant or poikilitic morphologies. Another possible interpretation is that the irregular overgrowth region may have crystallised in areas of trapped liquid and the olivine undergone subsolidus reequilibriation. This alternative explanation however, does not detract from the arguments above; in either situation, growth originally would have occurred under disequilibrium conditions.

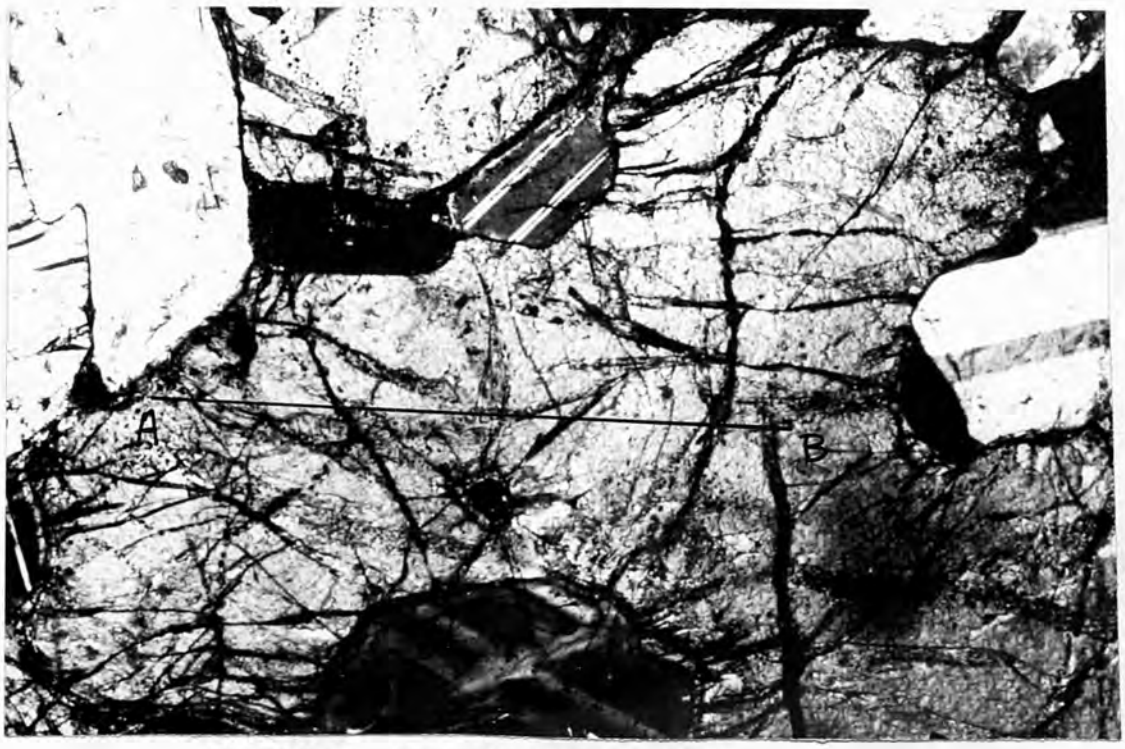

PLATE 4.7. Irregular, ameoba-like morphology showing trajectory of microprobe scan (A - B).

0·5 mm.

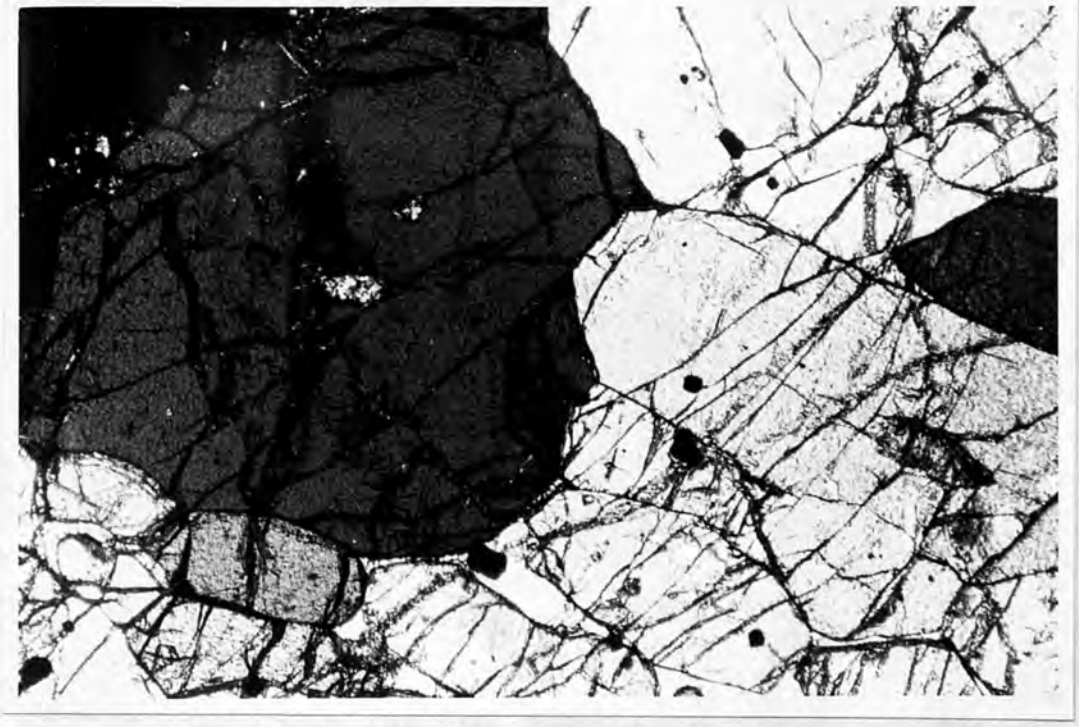

PLATE 4.8. Irregular morphology showing some coelescing.

0·5 mm.

4.3.1.5. Harrisitic morphology

The harrisitic morphology olivines are characterised by their very large, elongated and branching crystal form. They occur usually with the longer axis approximately perpendicular to the plane of layering and with the branches flattened parallel to the (010) crystal face (Wager and Brown 1968 p.257). This morphology is so called after its type location in the Harris Bay area of Western Rhum first observed by Harker (1908). From Wager et al.'s terminology (1960), rocks in which this morphology predominates are called olivine crescumulates. The olivine crescumulates from the Harris Bay area undoubtedly provide the finest example of harrisitic morphology in the world with olivine crystals up to 60 centimetres in length (plate 4.9) although 5 - 10 centimetres is more common.

A detailed study of an olivine crescumulate from the Western layered series of Rhum (kindly provided by Dr. J.Wadsworth, University of Manchester) was undertaken to determine the three-dimensional textural and chemical aspects of this rather unusual morphological type. A rectangular block 10 centimetres by 3 centimetres by 2 centimetres was cut so as to provide ten polished thin sections (numbered H1 - H 10). Six thin sections were cut normal to the x axis (figure 4.18), three at positive x and three at negative x; and two thin sections cut normal to each of the z and y axes. The z axis was found to coincide parallel to the (010) olivine crystal face.

Plates (4.10, 4.11, 4.12) show well the parallel elongated form of the harrisitic morphology. The complexity of the branching is however, difficult to appreciate from the contact print photographs because of the large size (greater than ten centimetres) of the olivines, but in fact in plate 4.10 (H.1), eighty percent approximately of the olivine seen is in

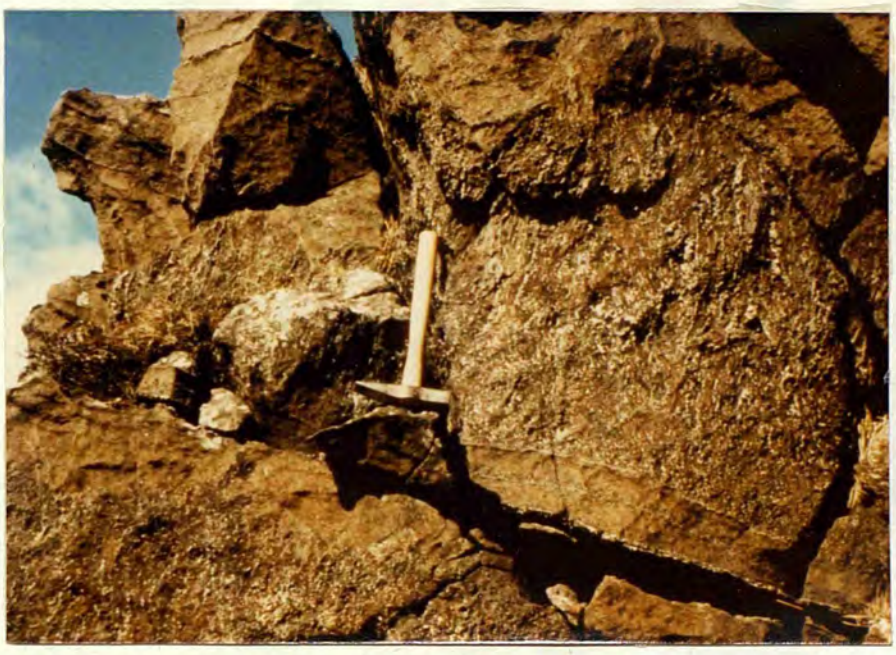

PLATE 4.9. Olivine crescumulate, Harris Bay area - Rhum western layered series.

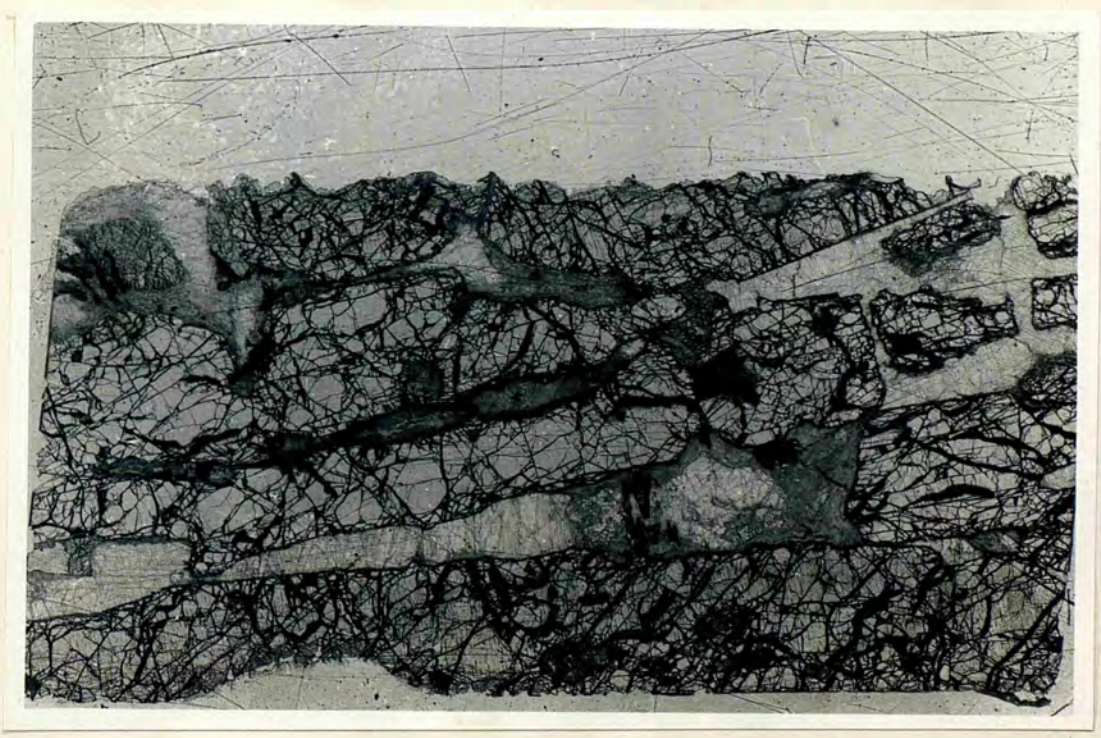

PLATE 4.10. Harrisitic morphology (H.1). 50 mm.

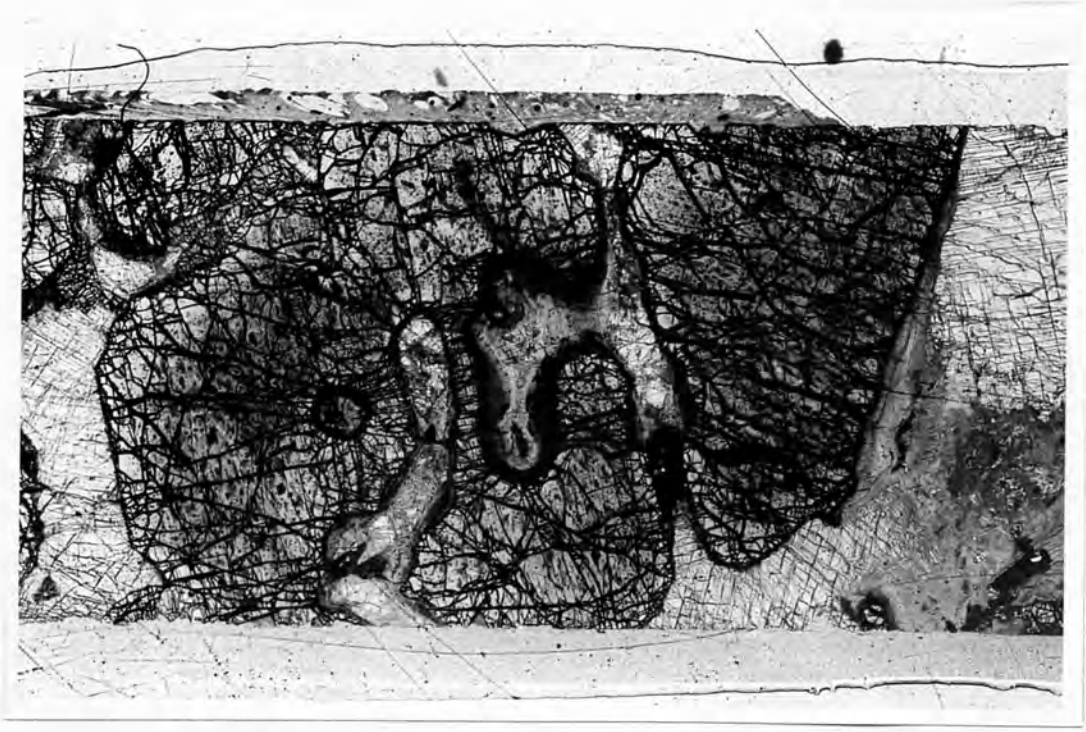

PLATE 4.11 Harrisitic morphology (H.8)

50 mm.

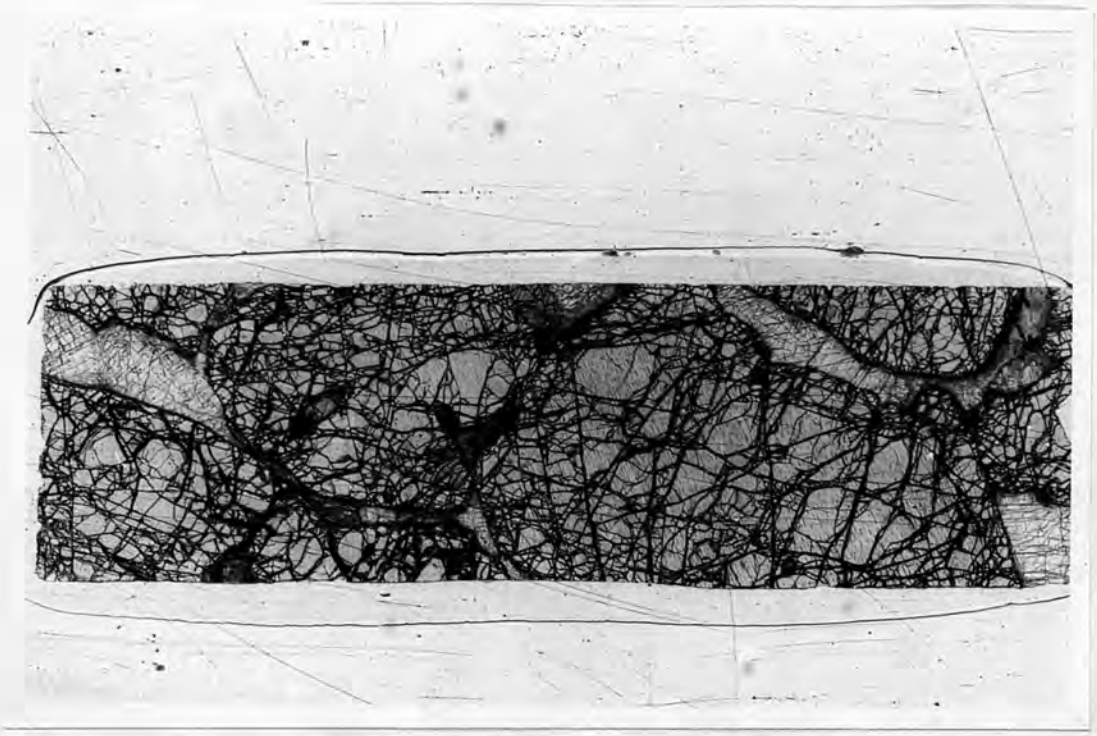

PLATE 4.12 Harrisitic morphology (H.10)

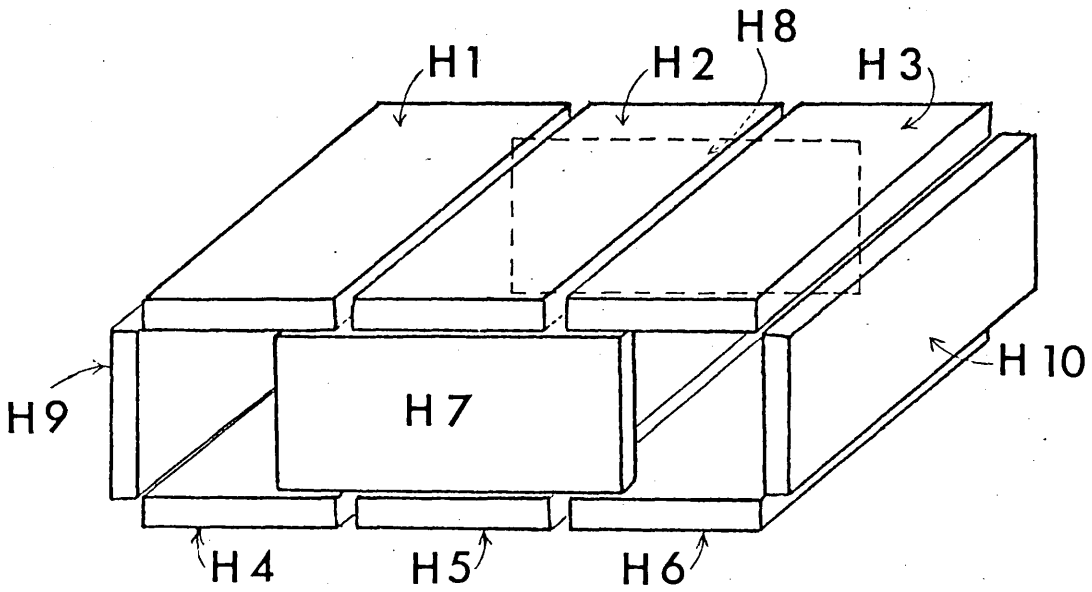

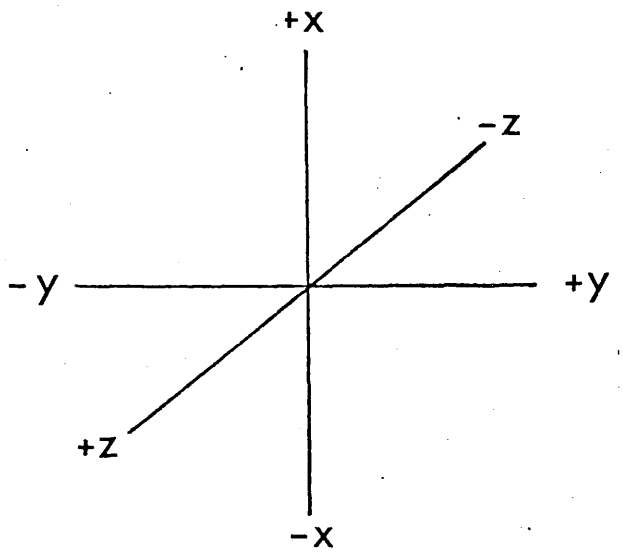

x corresponds approximately to x crystallographic axis.

y —"— —"— y —"—

z —"— —"— z —"—

Figure 4.18

optical continuity, and branching occurs normal to the x,y plane and parallel to (010). The nature of the branching can best be shown schematically in plan, elevation and side views (figure 4.19 a, b, c). The "channels" between the olivine fingers (figure 4.19 b) are filled with large optically (generally) unzoned bytownite feldspar, with occasional clinopyroxene (Ca_{46} Mg_{49} Fe_5) and large (up to three millmetres) irregular shaped ilmenite (plate 4.19). Often encountered within the harrisitic olivines, in particular to (100) crystal plane, were olivine "holes". These are described more fully in chapter 5 (section 5.2.5), but are essentially rounded, or oval-shaped areas of complex mineralogy enclosed two-dimensionally by the olivine, but probably connected in the third dimension to a plagioclase "channel", the hole entrapping intercumulus magma which then crystallised out as low-temperature (and higher uranium) phases.

The major (Fe, Mg, Si) and minor (Ca and Ni) element geochemistry of the harrisitic olivine was studied. Essentially no zoning of any of these elements was detected in microprobe traverses across each of the three axes x, y and z. An average of twenty-seven separate probe analyses are given in table 4.11

Table 4.11

	Average of twenty-seven analyses	Range	U p.p.b. (average of twelve	K_{obs} ($\times 10^{-2}$)
SiO_2	41.85	41.51 - 42.54		
MgO	42.49	42.07 - 42.96		
FeO	14.47	14.24 - 15.02	8.32	6.40
CaO	0.191	0.15 - 0.22		
NiO	0.257	0.22 - 0.28		
Total	99.26			

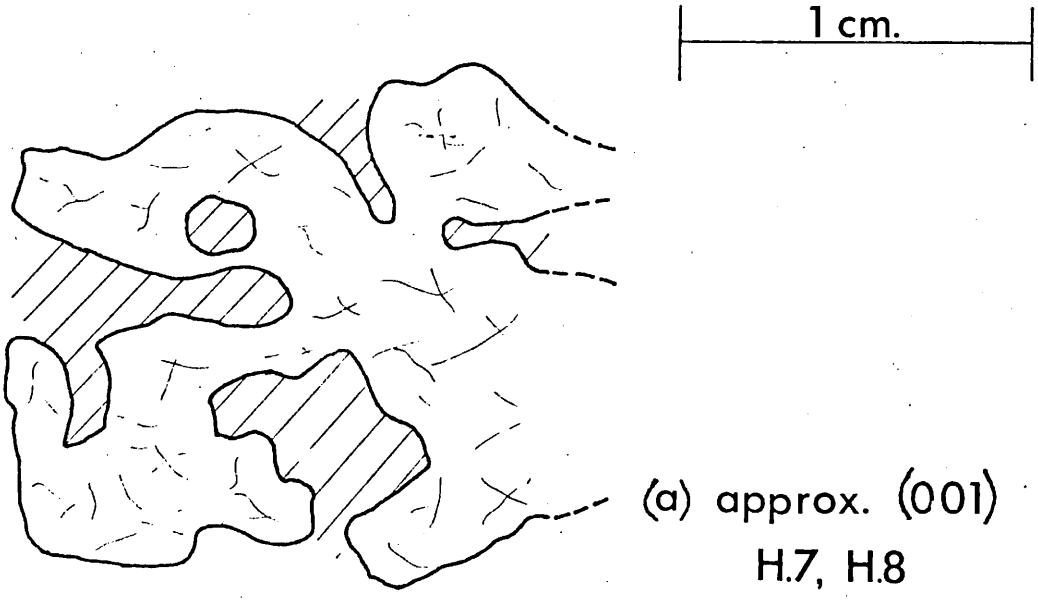

(a) approx. (001)
H.7, H.8

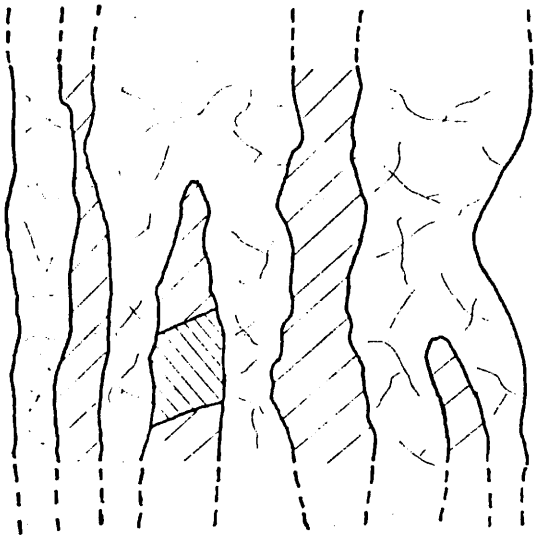

(b) approx. (100)
H.1 to H.6

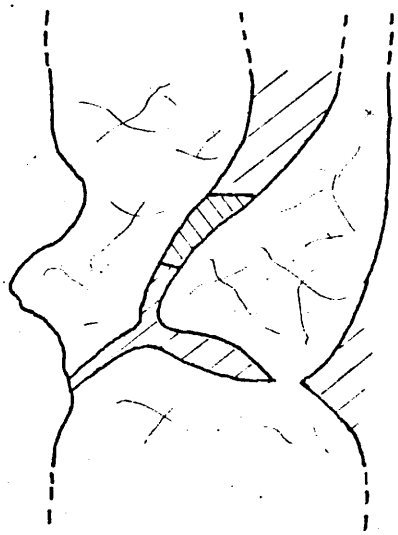

(c) approx. (010)
H.9, H.10

olivine

plagioclase

clinopyroxene

Figure 4.19

Atomic ratios:

Mg = 83.96

Fe^{2+} = 16.04

The uranium concentrations from seven of the thin sections (averaged in table 4.10) however, form a distinct group (figure 4.14) and are the highest values observed within the range of olivine morphologies (table 4.2). The large size of the harrisitic olivines enabled a series of area counts across a single olivine grain to be undertaken, and traverses were performed in three dimensions. 100 area counts (equivalent to an olivine grain area of 1.0 x 1.0 mm^2) for each analysis was made, the details of which are given below in table 4.12.. The crystallographic

Table 4.12

Analysis no.	Position (mm.)	No. of tracks	tracks per cm^2 (10^4)*	approx.) U (ppb.) (± .03 ppb)
H.3. (parellel to z axis				
1	0	158	1.5482	8.37
2	2	156	1.5282	8.27
3	4	155	1.5182	8.21
4	6	159	1.5582	8.43
5	8	156	1.5282	8.27
6	10	160	1.6682	8.43
7	12	156	1.5282	8.27
			Average =	8.32
Thermal neutron dose = 1.54 x 10^{17} neutrons.cm^{-2}.sec^{-1}.				
H.7 (parallel to y axis approximately)				
1	0	184	1.8026	8.29
2	1	186	1.8226	8.38
3	2	186	1.8226	8.38
4	3	185	1.8126	8.33
			Average =	8.35
Thermal neutron dose = 1.87 x 10^{17} neutrons.cm^{-2}.sec^{-1}.				

Table 4.12 (cont.)

Analysis no.	Position (mm.)	No. of tracks	tracks per cm^2 (10^4)*	U (ppb.) (± .03 ppb.)
1	0	177	1.734	8.29
2	1.5	179	1.754	8.38
3	3.0	179	1.754	8.38
4	4.5	1.76	1.724	8.24
5	6.0	178	1.744	8.33
6	7.5	176	1.724	8.24
			Average =	8.31

Thermal neutron dose = 1.80×10^{17} neutrons.cm^{-2}.sec^{-1}.
H.10(parallel to x axis approximately)

directions of the traverses in table 4,12 were identified partly by optical methods, and partly by the orientation of exsolved magnetite (Wager and Brown, 1968) which forms dendritic plates parallel to (010) within the olivine. (Kaaden et al.(1972) has subsequently shown that similar exsolved plates in olivines are Fe-rich chrome spinels of formula $Fe^{2+}(Cr_{0.66}\ Fe^{3+}_{1.34})$). These results show firstly, that like the major and minor elements, no uranium gradient was observed; and secondly, there is no variation in uranium concentration with crystallographic direction (in contrast to Condie et al's., 1969, observations of uranium in pyroxenes).

Although the extreme examples of harrisitic olivine (and the sample analysed in this study) occurs mainly in the western layered series of Rhum (Wadsworth, 1961 - who in fact believed that the western and eastern series were one and the same intrusion), olivine crescumulates do appear in the eastern series (Wager and Brown, 1968) and have been recorded also in the Rogsund gabbro, Norway (Robins, 1971). This morphology may in fact be more common

than initally thought, and has in fact been observed for other minerals; e.g. diopsidic augite from the Duke Island complex - Wager and Brown (ibid p. 512), and bytownite feldspar from a recently recorded macrospherulitic structure on Rhum (Donaldson etal., 1973). The genesis of such extreme structures will inevitably be conjectural since we cannot hope to reproduce in the laboratory the immense sizes of some of the crystals. We can however obtain indirectly, an indication of the kind of conditions that may have prevailed, by certain aspects of the geochemistry and by comparison with, albeit on a very much smaller scale, experimentally produced morphologies.

Of the geochemical clues, the composition (and partition coefficients) of uranium may provide, in a similar manner to the previously described olivine morphologies, information regarding the formation of harrisitic olivines. Wager etal.(1960) suggested that harrisitic olivines resulted from extension of cumulus olivines in a similar manner to that proposed for adcumulus or heteradcumulus growth - i.e. a slow, diffusion - controlled mechanism. However, when comparison of uranium concentration and partition coefficients is made with the poikilitic (or even equant) morphologies, it can be seen that:-

$$(U)_{harr.} \text{ is greater than } (U)_{poik.}$$

$$\text{and } (k_{obs})_{harr.} \text{ is greater than } (k_{obs})_{poik.} \quad \left[= k_{equ}\right]$$

From sections 4.2 (equations (14) and (15)) this indicates that harrisitic olivines grew at a much faster growth rate and under conditions of large ΔT and supersaturation than did the poikilitic morphology which crystallised under equilibrium conditions. Further evidence supporting these non-equlibrium crystallisation conditions is provided by the morphology itself. The elongated branching of the olivines is similar in appearance to a dendritic

morphology observed in experimental systems (e.g. Lofgren, 1974 and Saratovkin, 1959) where dendrites result from rapid growth of high supercooled melts (section 4.1.5.); and also to olivines from volcanic rocks (e.g. Nesbitt, 1971) where rapid cooling is postulated.

Donaldson (1974) in a comparative study of harrisitic morphologies with some Archean spinifex rocks, similarly concluded that harrisitic olivines resulted from rapid growth under supersaturated conditions. He suggested that an elevation in the liquidus temperature (of olivine) relative to the magma temperature was brought about by a decrease in the water content of a water-undersaturated feldspathic peridotite liquid (Donaldson ibid), coupled by adiabatic magma expansion. This would have the effect of increasing the degree of supercooling; but in this model Donaldson, ibid), since the supercooled magma is produced by elevating the liquidus and not by lowering the actual temperature of the system, fast growth may be achieved under low cooling rates. Thus, olivines crystallising under plutonic conditions (i.e. low cooling rates), may produce textures similar to those which crystallised under demonstrably rapid cooling rates (e.g. spinifex texture, Lewis (1971)) - the common factor being the degree of supercooling (or supersaturation) of the magma, and not the rate of cooling.

4.3.1.6. Tabular morphology

Tabular olivines were characterised by their elongated crystal shape where a:b (length to thickness, figure 4.16) ratios were greater than 2.5:1.0 and, in some cases exceed 10:1. A wide range of sizes was observed with "a" values varying from .3 to 5 millimetres and with the direction of elongation parallel to (010). They were often seen to be euhedral with pinacoid faces well developed (plate 4.14). In overall shape, there is

PLATE 4.13. Anhedral ilmenite in olivine crescumulate.

0·5 mm.

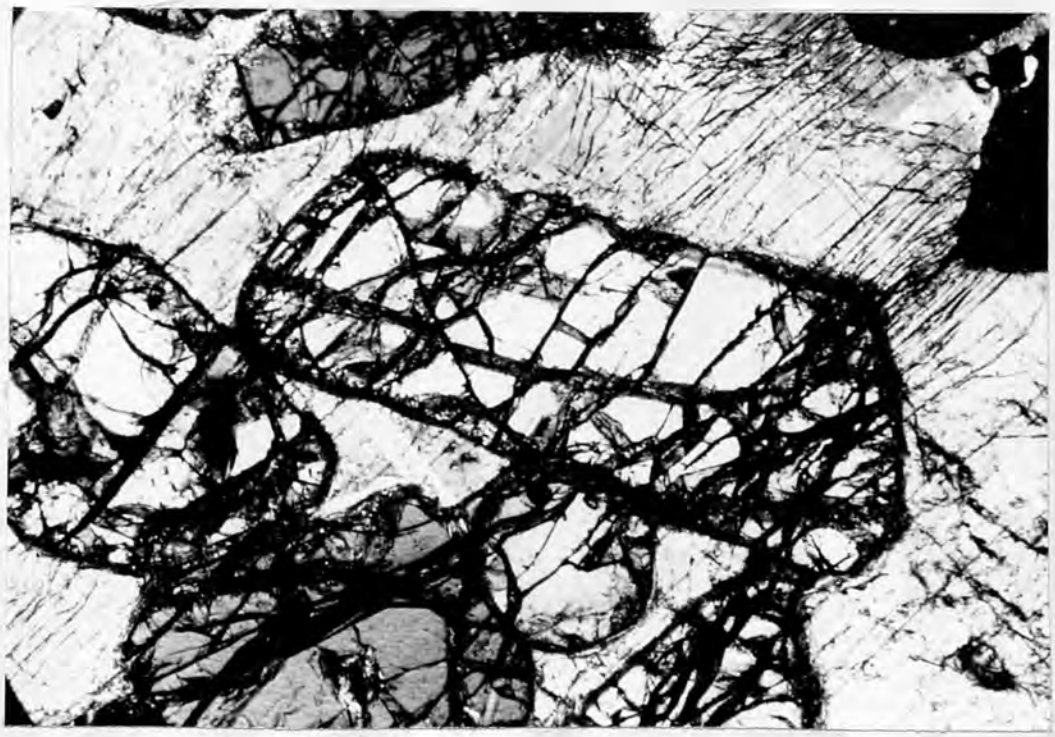

PLATE 4.14. Tabular morphology with well-developed pinacoid faces.

0·5 mm.

some resemblance between this morphology and harrisitic morphology, the major differences being in size, where harrisitic olivines frequently were much larger, and, in that branching was a major characteristic of harrisitic olivines not found in tabular olivines. Brothers (1964) noted also the tabular olivines occurred with (010) planes parallel to the layering, whereas in harrisitic olivines, (010) occurred perpendicular to the layering. A feature of the tabular, and to a lesser extent harrisitic olivines, is the occasional development of strain lamella (plate 4.15) parallel to (100). Wager and Brown (1968) suggest this to be a result of differential stresses brought about by the olivines, whilst still hot, being ovolain by a new deposit of cumulus crystals. Raleigh (1967) showed experimentally, this structure to be parallel to kink bands which formed at temperatures in excess of 1000° Centigrade.

In terms of the uranium content (table 4.13) this group, like certain of the textural aspects, is similar to the harrisitic olivines in that it contains a mean concentration of uranium second highest to that of the harrisitic morphology. The range in concentration is however larger than that observed for the harrisitic morphology, and overlapping of results occur with rounded (and to a lesser extent, irregular and equant) morpholgies (figure 4.14). This may be due to inaccurate designation of some of the olivines into morphological groups during track counting since sections normal to (010) in tabular olivines would resemble a rounded (or equant) morphology. However, the mean uranium concentrations of the two morphologies differ by approximately 16 percent (table 4.2) unlike the forsterite contents (and NiO and CaO where determined) which show no significant variation with any other of the morpholgies studied.

PLATE 4.15 Development of strain lamellae in the olivine crescumulate.

·2 mm.

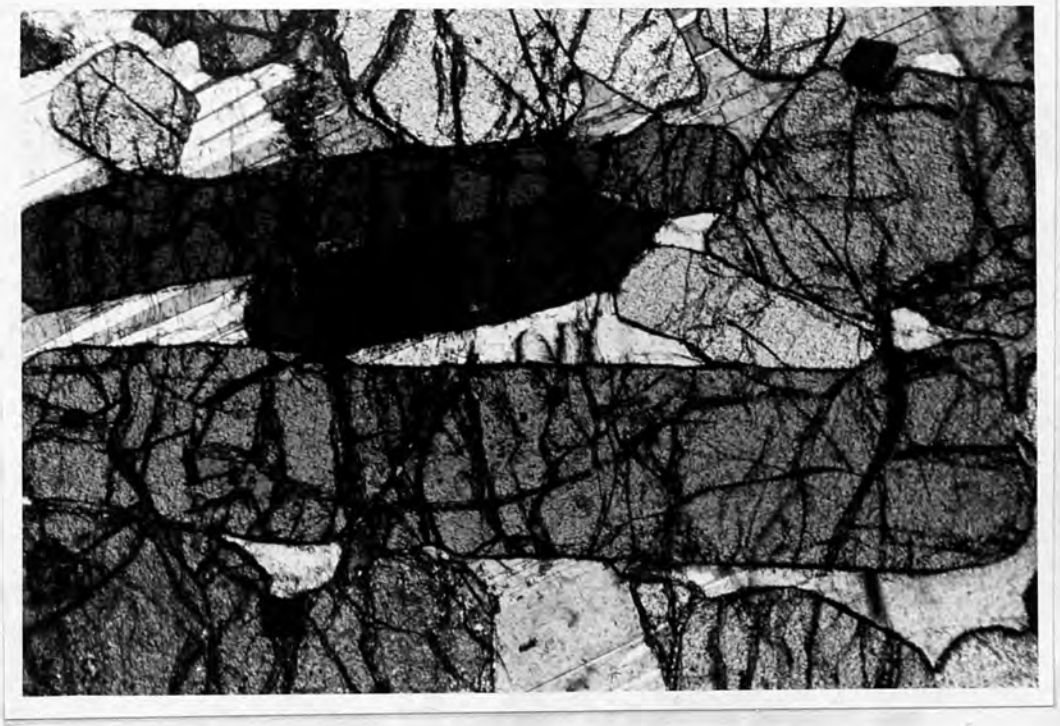

PLATE 4.16 Tabular morphology - igneous lamination.

Table 4.13.

Rock no.	Unit no.	Thermal neutron dose*	Area counted	no. tracks	tracks. per cm^2 **	U (ppb) ± .03	Fo content	NiO	CaO
91	1	0.85	100	70	0.683	6.91	86.06	.176	.111
95	2	1.71	100	141	1.3758	6.92	85.31	-	-
96	3	1.71	100	163	1.5958	8.03	85.46	.166	.092
84	5	1.53	100	123	1.1994	6.74	85.60	.160	.101
85	5	1.53	100	116	1.1294	6.35	85.39	.164	.089
120	7	1.81	100	158	1.5438	7.34	85.13	-	-
61	8	1.87	100	147	1.4326	6.40	85.34	-	-
53	9	1.80	100	168	1.6440	7.86	85.41	.140	.109
68	11	1.81	100	166	1.6238	7.72	85.39	.162	.102

Average = 7.16

* $x10^{17}$ neutrons.cm^{-2}.sec^{-1}.

**($x10^4$) and after background tracks were subtracted.

Traverses of major (Fe, Mg, Si) and minor (Ni and Ca) elements were obtained (using the Geoscan microprobe) with directions both parallel to the elongation, and perpendicular to it. The results are presented in table 4.14, from where it can be seen that essentially the olivine is homogeneous with respect to these elements and no zoning occurs. Analyses 1 to 10 (traverse parallel to the elongation - i.e., to the z crystallographic axis) were analysed at intervals of 0.3 millimetres (± 25 μm), and analyses 11 to 15 (perpendicular to the elongation - i.e., parallel to the x,y plane) at intervals of 0.1 millimetres (± 25 μm). The uranium traverses (only parallel to the elongation) were performed on the basis of 40 area counts (0.4 x 1.0 $millimetre^2$).

Tabular olivines occur sporadically distributed throughout the intrusion, there being no apparent connection between the appearance of this morphology, and its position either within a

Table 4.14

Analysis no.	FeO	MgO	SiO_2	CaO	NiO	Total	Fo content	U (ppb) (± .03)	$(k)_{obs}$
1	13.85	45.53	39.95	.10	.16	99.59			
2	13.85	45.52	39.94	.10	.16	99.57		7.69	
3	13.84	45.53	39.93	.11	.17	99.58			
4	13.86	45.54	39.94	.10	.16	99.60			
5	13.88	45.52	39.93	.10	.17	99.57			
6	13.85	45.53	39.95	.09	.17	99.59		7.71	
7	13.86	45.52	39.94	.11	.15	99.58			
8	13.83	45.55	39.94	.10	.16	99.58			
9	13.84	45.53	39.95	.10	.16	99.59		7.79	
10	13.82	45.52	39.95	.11	.16	99.57			
Average	13.85	45.53	39.94	.10	.16	99.58	85.39	= 7.71	
11	13.84	45.51	39.93	.11	.17				
12	13.84	45.53	39.93	.11	.16				
13	13.86	45.54	39.91	.10	.17			-	
14	13.84	45.54	39.94	.10	.16				
15	13.85	45.52	39.94	.10	.16				
Average of 15	13.84	45.53	39.94	.10	.16	99.57			

Number of ions on the basis of 4 Oxygens

.289 1.699 2.001 .003 .003

Atomic ratios: Mg 85.4

Fe^{2+} 14.6

unit, or within the intrusion as a whole. It is found rarely as the major morphological type and generally contributes only 10 to 35% of the olivine present in any one specimen. A cumulus genesis for this morphology has been proposed by Wager and Brown (1968, p.257) on the basis of alignment within the plane of layering

producing an igneous lamination (plate 4.16, compare also with Wager and Brown ibid., figure 140). The euhedral crystal shape and occasional coalescing (seen e.g. in Wager and Brown ibid., figure 140) of some of the tabular olivines, may however be the result of diffusional modification of the outer edges in a similar manner to that proposed for equant olivines (section 4.3.1.2.).

A comparison of uranium concentrations and partition coefficients between tabular and poikilitic (or equant) morphologies (table 4.2) indicates (from equations 14 and 15) that this morphology crystallised at a faster growth rate and under disequilibrium (large ΔT and supersaturation) conditions. Drever and Johnston (1957 and 1967) suggested also fron textural and field relationships of small basic intrusions that tabular olivines result from rapid precipitation and growth of a supercooled magma. Experimental work by Lofgren (1974) showed that an increase in the acicular habit of crystals resulted from increasing the growth rate (Y) and the supercooling (ΔT) - section 4.1.5.. Wyllie et al. (1963) similarly found that the acicular habit of apatite increases with an increased rate of quenching. One would expect therefore, to find that olivines with high a:b ratios had grown at a more rapid rate than those with lower a:b ratios. Table 4.15 and figure 4.20 show the variation in uranium concentration for different a:b ratios.

Table 4.15

Rock no.	modal % morpn.	a:b	U (ppb) (± .03)	$(K)_{obs}$
96	23.6	8.2	8.03	.0267
68	10.2	5.8	7.72	.0257
84	33.4	2.8	6.74	.0225

("a" and "b" as for equant morphology - figure 4.16).

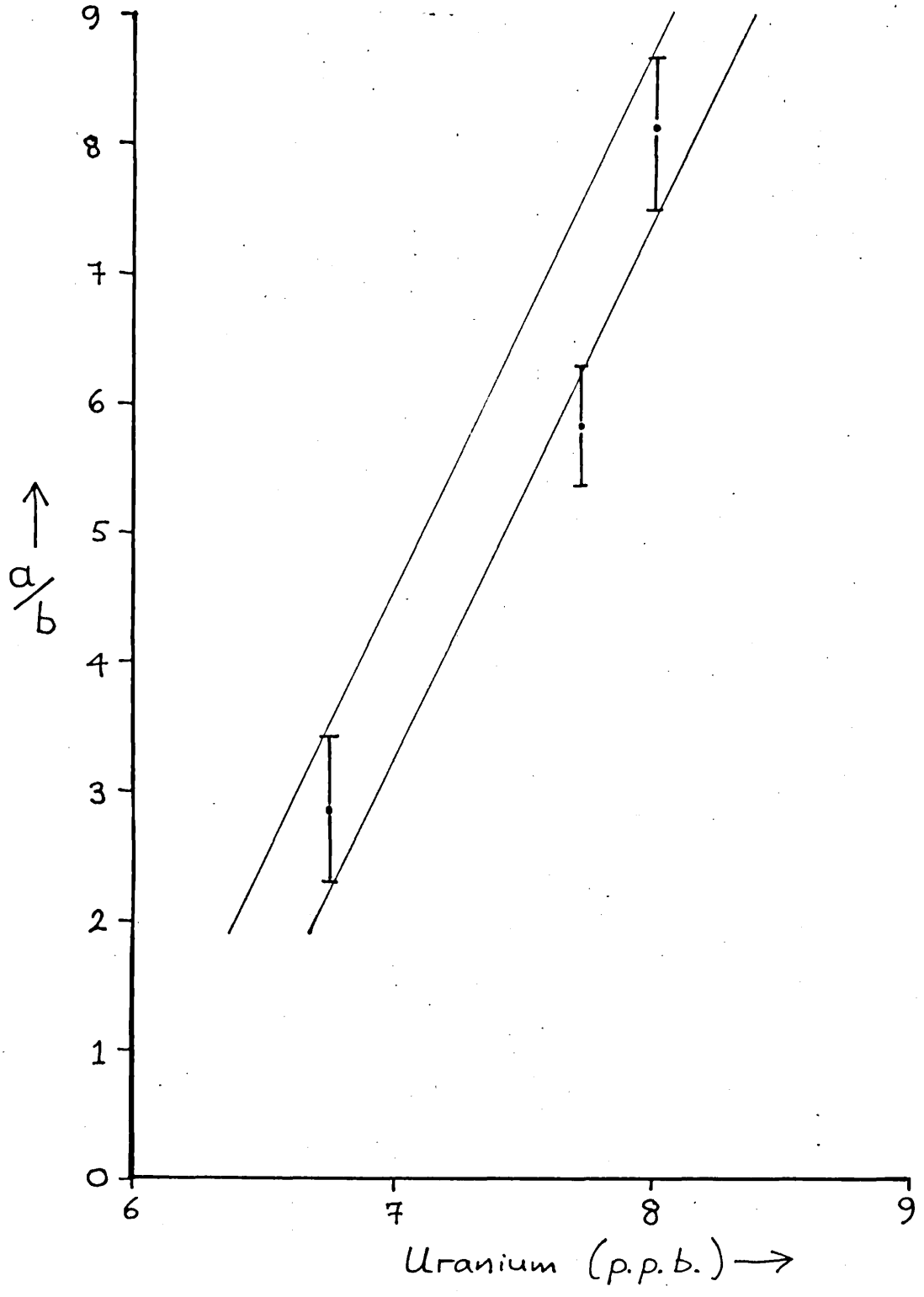

Figure 4.20

An attempt was made to standardise the b values to between 0.3 and 0.4 millimetres for the three specimens. Only three specimens were in fact chosen for this comparison, because the a/b ratio often varied quite extensively within one rock specimen - probably the result of cutting thin sections from unorientated specimens. The three specimens chosen (table 4.15), were fortuitously orientated such that the majority of tabular olivines range within $\pm$ 1.0 a/b, and those counted were within $\pm$ 0.5 a/b. The interpretation of the results in table 4.15 and figure 4.20 is consistant with the above arguments, viz. an increase in growth rate produced an increase in uranium concentration and (texturally) an increase in a/b ratio.

4.4. Summary and discussion

The salient features observed in the geochemical and textural study of the olivine phase from the Rhum basic intrusion can be summarised viz.

(1) A constancy in the major elements (i.e. Fo content), and to a lightly lesser extent, minor element (NiO and CaO) concentration throughout the intrusion.

(2) A variation in both the concentration and the observed partition coefficient (k_{obs}) of uranium.

(3) A correlation between the uranium concentration and the morphology of the olivine phase.

The first point - constancy of Fo content - may give an indication as to the type of mechanism involved in controlling the growth process. In discussing the growth process, whether controlled by the incorporation of the elements involved into the structure of the crystal at the interface (i.e. interface controlled mechanism, section 4.1.2.2.), or by the diffusion of those elements necessary for continued growth towards, and those

superfluous away from, the interface (i.e. diffusion controlled mechanism, section 4.1.2.3.), several factors need to be assessed. In general, the rate-controlling process will be the slower of the two processes. Similarly, in crystallising a mineral consisting of two or more element species from a multi-component system (i.e. a silicate melt), diffusion clearly is going to play an important role. Were the rate of crystallisation to proceed faster than the diffusion rate (i.e. the rate-controlling process to be an interface mechanism), then a metastable phase would result (e.g. Kirkpatrick, 1974). Although situations arise in multi-component systems whereby the rate controlling process is interface-controlled at the onset of crystallisation, and may convert to diffusion controlled as the crystal enlarges (section 4.1.3.), some confusion arises in the literature as to the range of overlap of the two. Christian (1965, p.8) suggests that this range is quite small and that a process is essentially either diffusion controlled, or interface controlled. Mullin (1972 p.195) however, believes that a significant intermediate range exists whereby both processes may be rate-controlling and that the transition from one to the other may be temperature dependent. Intuitively, we would expect, in magmas, the latter to be more likely, because only on rare occasions do metastable phases form from crystallising magmas. Generally, if diffusion is restricted, crystallisation becomes temporarily halted whilst the temperature of the system decreases until an equilibrium assembly is reestablished. Crystallisation can then continue either in the form of lower temperature zones (in e.g. the plagioclase feldspar solid solutions), or as a eutectic system. In the section describing diffusion controlled growth (section 4.1.2.3.), it was noted that the rate-controlling process was taken to be that of the slowest moving component necessary for continued growth. When

therefore traverses of Mg, Fe and Si (i.e. those species which are necessary for continued olivine growth) across different olivine morphologies indicated no significant variation in forsterite content, it may be argued that olivine crystallisation throughout the intrusion was solely the result of diffusion controlled processes - providing sub-solidus reequilibriation had not extensively occurred - however, the U data is more meaniful when assigning growth processes (see also p. 189).

Points (2) and (3), a variation in uranium concentration (and partition coefficient) within the olivine phase, and the corellation of this to the olivine morphology indicate fundamental growth differences between the various olivines not reflected by the major (or minor) element geochemistry. Various observed field and textural relationships (e.g. Drever and Johnston, 1957and 1967) and experimental studies (e.g. Saratovkin, 1959 and Lofgren, 1974) have demonstrated that by a variation in ΔT and in crystal growth rate a variety of crystal morphologies can be obtained (section 4.1.5). A transition from polyhedral (equilibrium crystal shape) to skeletal, to dendritic, to spherulitic morphologies arise by increasing ΔT, and hence the rate of growth. Two of the above factors are likely however, to increase the rate of the interface mechanism at the expense of the rate of diffusion. Firstly, an increase in ΔT results in an increase in the deviation from equilibrium at the interface, thus increasing $\Delta G_{interface}$. Secondly, the transition from a polyhedral morphology to one having a more elongated or acicular form will enable a proportionally larger number of sites to be available for molecular attachment (equation 8). One would expect therefore, to find that interface mechanisms would play a more significant part in the growth process at higher ΔT's.

As growth proceeds by diffusional processes in multi-component systems, it can be seen that an impurity layer (δ) is built up

around the growing crystal (figure 4.4) and that chemical diffusion of the relevant species occurs through δ. In addtion, δ is a function of the constitutional supercooling (section 4.1.4) such that by increasing ΔT, a decrease in δ is observed (figure 4.9(a) to (c)). Consider the effects of this on elements diffusing at different rates (figure 4.27). If B has a slower diffusion rate, and a greater concentration gradient, than A, the distance of the impurity layer δ_B will be greater than δ_A. Then, with a decrease of δ to a value δ_A (caused by an increase in ΔT and/or Y), the incorporation of element A into the crystal structure will be describable in terms of thermodynamic (equilibrium) priciples, and the observed partition coefficient of A will be the equilibrium partition coefficient (k_{equ}). If A is necessary to the continued crystallisation of the mineral, the growth process will be diffusion controlled. The incorporation of element B into the crystal structure will not however, be describable by (or in, thermodynamical principles) when $\delta = \delta_A$, and the observed partition coefficient (k_{obs}) of B will be some value intermediate between k_{equ} and k^* (the interface partition coefficient - section 4.2). If similarly element B plays no significant role in the crystallisation of the solid, then, although the overall growth process can be described as being diffusion controlled, the controlling factor, with respect to element B, will be rate of attachment at the interface. Conversely, decreasing ΔT and/or Y such that δ increases to a value δ_B will result in the partition coefficients of both A and B being that of their equilibrium partition coefficients, and the incorporation of both these elements into the mineral may be described as being diffusion controlled.

There is therefore, a range in rates of growth over which a crystal may develop which will not affect the major (or minor) element concentrations (or partition coefficients), but will be

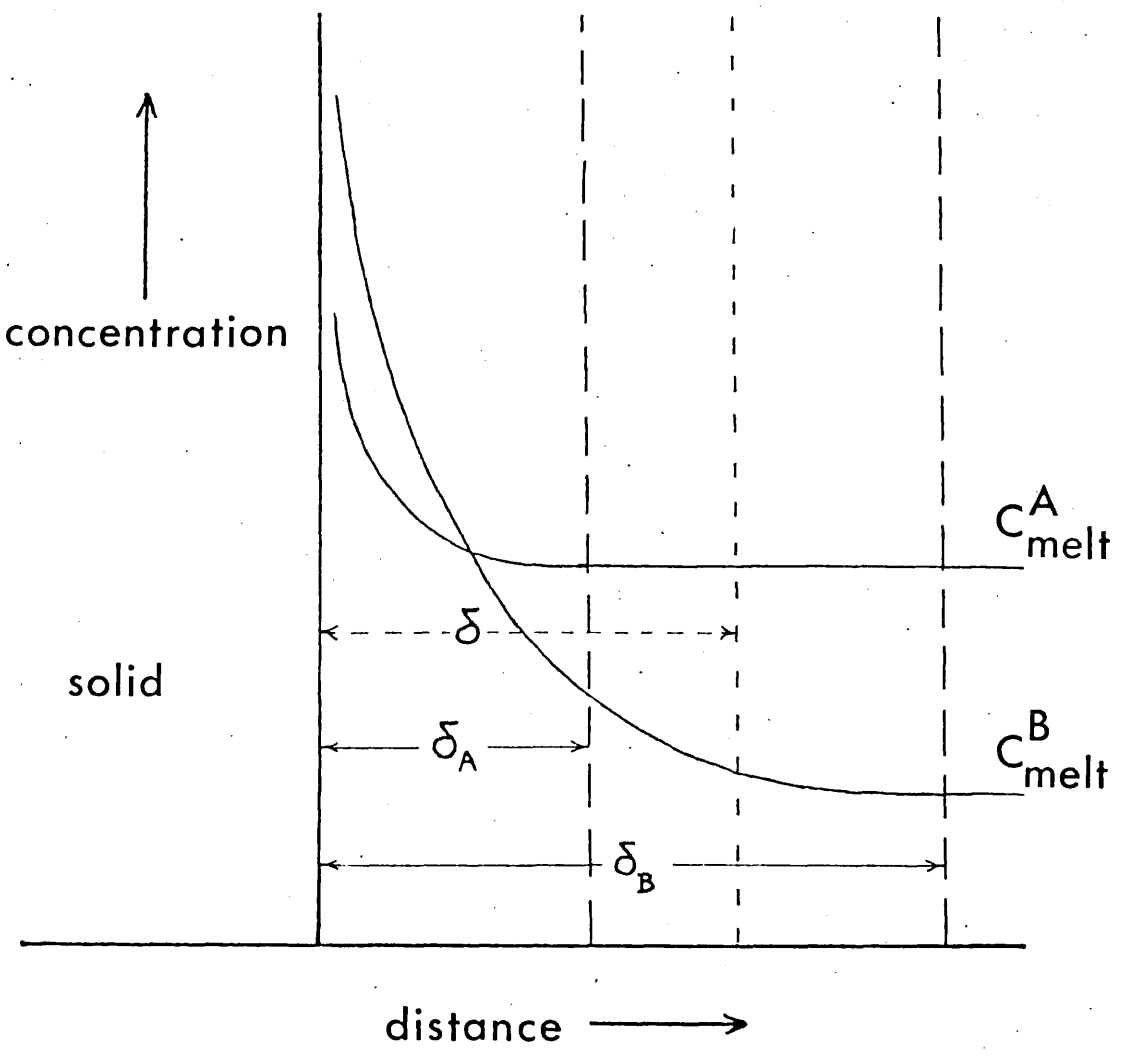
concentration
solid
C^A_{melt}
C^B_{melt}
δ
δ_A
δ_B
distance

Figure 4.21

reflected in the concentrations (and partition coefficients) of low partitioning elements having comparatively lower diffusion rates.

A comparison of diffusion coefficients for Mg, Fe, Ca and uranium are given below in table 4.16. We can therefore, in the general diagram of figure (4.21) substitute Mg (or Fe) as element A, and uranium as element B.

Table 4.16

Element	Diffusion * coefficient (D)	Temperature (° C)	Media	Source
Mg^{2+}	0.091 - 1.4	1200	inter-diffusion in olivine	1
Fe^{2+}	58	1275	iron silicate	2
Ca^{2+}	1.07 - 3.36	1230 to 1423	mugearite melt	3
Th	0.2	1350 and 20 Kbar.	0·5:0·25:0·25 diopside: albite: anorthite melt	4

* $\times 10^{-7}$ cm^2 sec^{-1}
1 = Misner (1972) - recalculated to 1200°C. 3 = Medford (1973)
2 = Matsumara (1969) 4 = Seitz (1974, b)

Using the value for thorium (i.e. 2×10^{-3} cm^2 sec^{-1}) and assuming similar diffusion rates for thorium and uranium (e.g. Seitz, 1973, b), a diffusion coefficient for uranium at 1250°C can be obtained from the Arrhenius equation $D = D_o \exp(-\frac{E}{RT})$ equal to 6×10^{-9} cm^2 sec^{-1}.

The observed variation in uranium concentration of the olivines of Rhum with morphology, therefore, may result from different rates of crystallisation. The morphologies observed ranged from polyhedral through to dendritic; viz. poikilitic and equant (polyhedral) to irregular to tabular (acicular) to harrisitic (dendritic). This trend is indicative of an increase in the supercooling (ΔT) and the growth rate (Y) (section 4.1.5.) and is reflected in a corresponding increase in the uranium concentration. The range in the rates of growth were not sufficient however to significantly affect the concentrations of the other elements (Mg, Fe, Ca and Ni) which remain essentially

constant despite a variation in uranium concentration. These factors can be summarised:-

poikilitic + equant → irregular → tabular → harrisitic

increase in ΔT, Y and Uranium
(Mg, Fe, Ca, Ni constant).

Mg, Fe, Ca and Ni are considered to have been attached to the olivine structure in a diffusion controlled manner throughout the different morphologies, whereas uranium appears to have been incorporated in an increasingly interface controlled manner with increasing olivine growth rate. In terms of crystal morphology, an increase in surface area/volume ratio accompanies the increase in growth rate.

The above arguments lead us to two important considerations:- (1) In multicomponant systems, where a wide range of diffusion rates occur, care has to be taken when assigning a growth mechanism to a particular mineral phase solely on the basis of major element analysis, since, changes in the rates of growth may result in those low-partitioning elements with comparatively slower diffusion rates being incorporated into a mineral by a different growth mechanism than those elements which are necessary for continued growth.

(2) A closer inspection of the variations in partition coefficients of trace, low-partitioning elements may provide more sensitive indicators of the rates of crystal growth of a particular mineral phase.

The second consideration may be put on a more quantitative basis using an equation by Burton, et al. (1953) whereby a limiting value of the effective partition coefficient (t') is obtained from an initial equilibrium partition coefficient (t) as solidification proceeds.

$$t' = \frac{t}{t + (1 - t).\exp(-\frac{Y}{D}\delta_x)} \qquad \text{———(16)}$$

where Y = linear growth velocity ($cm.sec^{-1}$)

D = diffusion coefficient of the element in the liquid

δ_x = effective thickness of the liquid layer in which the solute is transported by diffusion only.

As Y increases t' approaches unity, and, for low-partitioning elements, t' has values intermediate between t and unity. From section 4.2 it can be seen that t is equivalent to the equilibrium partition coefficient (k_{equ}); t' equivalent to the observed partition coefficient (k_{obs}), and δ_x equivalent to the impurity layer δ. Then, by rearranging equation (16),

$$Y = -\frac{D}{\delta} \ln \frac{k_{equ}}{k_{obs}} \qquad \text{———(17)}$$

From theoretical observations Mullin (1972) considered the value of δ to range from approximately 4 - 40 microns in thickness. Donaldson (1975) found, from experimentally grown olivines, δ to be approximately 20 microns. Qualitatively, by keeping D, k_{equ} and k_{obs} constant, an increase in δ produces a proportional increase in Y - a result predicted in section 4.1.5. and above. Growth velocities for the different morpholgies may therefore be estimated from the uranium partition coefficients using values of D (uranium) = 6×10^{-9} $cm^2.sec^{-1}$ and, since no definitive values of δ can be obtained, δ is taken to be 2.0×10^{-3} cm. From the above, however, it will be seen that δ decreases from poikilitic to harrisitic, the overall effect being to increase slightly the rate of growth in that direction. Table 4.17 gives calculated growth velocities and growth to diffusion ratios ($^Y/_D$) for the different velocities using equation (A). The value of k_{equ} is taken to be that of the

partition coefficients of the poikilitic morphology (section 4.3.1.1).

Table 4.17

Morphology	K_{obs} ($\times 10^{-2}$)	Y* $cm.sec^{-1}$	Y $mm.day^{-1}$	$Y/_D$
Poikilitic	1.47	less than 3.83	less than 0.33	less than 64
Equant	1.67	3.83	0.33	64
Irregular	1.97	8.78	0.76	146
Rounded	2.00	9.23	0.80	154
Tabular	2.39	14.6	1.26	243
Harrisitic	2.77	19.0	1.64	317

* $\times 10^{-7}$

The equation breaks down however, when $K_{obs} = K_{equ}$ as this condition yields a zero growth rate. Here crystallisation may be considered to be a steady-state situation with growth by diffusion alone.

Donaldson (1975) estimated that growth rates of the order of 0.45 $mm.day^{-1}$, would ensure complete solidification of Skaergaard

crystal mushes assuming a settling rate of 0.6 mm.day. Wager (1963, figure 5) however, suggests a much slower settling rate giving thicknesses of the order of 0.33 mm.day for adcumulus conditions to prevail. Under these slower conditions, if a packing of at best 65 percent is assumed (Wager etal., 1960), a growth velocity of approximately 0.12 mm.day (equivalent to approximately 1.2×10^{-7} cm.sec^{-1}) is required to ensure complete solidification before a new crystal layer forms. This approximates to the range calculated for the poikilitic and equant morphologies, which were considered to have crystallised, probably around a cumulus olivine nucleus, by an adcumulus (i.e. basically diffusion controlled) process. The cumulus-originated morphologies (i.e. rounded and tabular) give growth rates intermediate between the post-depositional morphologies and the cumulus harrisitic morphology; the latter apparently having grown comparitively rapidly from a layer of settled cumulus olivines (Wadsworth, 1961). The highest calculated growth rate (for harrisitic morphology) is still within the range of recorded olivine growth rates in basalts (Donaldson ibid).

The influence of the growth/diffusion rate ratio ($^{Y}/D$) on the crystal morphology has been shown by Lofgren (1974) and Donaldson (1975) (section 4.1.5.) and values recorded here (table 4.17) agree well with their experimental work. Low $^{Y}/D$ ratios resulted in polyhedral morphologies (poikilitic, equant, and to a lesser extent, irregular and rounded); increasing $^{Y}/D$ ratios resulted in morphologies of increasing surface area/volume ratios (i.e. as tabular and harrisitic morphologies). Donaldson (1974) reports a $^{Y}/D$ ratio for skeletal olivines (intermediate between tabular and dendritic) of approximately 10^{2} per cm.

We can thus, summarise the mechanism of growth and certain magma conditions by subdividing the morphologies into three groups.

Group (1): poikilitic, equant and irregular morphologies. Basically controlled by an intercumulus (heterad or adcumulus) growth mechanism, probably extending original cumulus olivines, under slow, diffusion controlled (with respect to both the major elements and uranium) conditions and with low, but increasing values of ΔT and Y.

If sub-solidus reequilibriation of the olivine had occurred, the observed uranium concentration may not be a true representation of the adcumulus or heteradcumulus overgrowth. A high degree of heteradcumulus growth, e.g. crystallisation of 40 per cent pore space would include a lower contribution of the uranium content of the original crumulus crystal, than would a smaller degree of adcumulus growth (in eg. modification of a rounded crystal to an equant crystal). The amount of overgrowth could not unfortunately be quantified since essentially no changes in either the major or minor element concentrations were detected in microprobe scans. Qualitatively, one would expect the amount of overgrowth for the poikilitic morphology to be less than for equant or irregular morphologies solely on the basis of size.

Group (2): rounded and tabular morphologies. Considered to be phases that crystallised in (and from) the bulk of the magma and subsequently deposited as cumulus crystals. An increase in growth rate with an increase in $^{a}/b$ (and surface area/volume) ratios was observed. With the increase in growth rate, there occurred an increase in the influence of interface growth mechanism for uranium, the major and miner elements were still however diffusion controlled.

Group (3): harrisitic morphology. The most rapid growth rate observed and the result of magma locally developing high values of the supercooling (ΔT). In order to obtain the necessary ΔT values, a period of quiescence in regions of magma free from

suspended cumulus crystals would be required. Alternatively, adiabatic magma expansion plus the removal of water could produce the required high ΔT (Donaldson, 1974).

A qualitative model based on the juxtaposition of the curves of linear growth velocity (Y) and nucleation rate verses degree of supercooling may be proposed for the crystallisation of the observed olivine morphologies. The relevant curves, first obtained by Tamman (1925), have been described above:- homogeneous (and heterogeneous) nucleation as a function of supercooling is shown in figure 4.3., and crystal (linear) growth velocity versus supercooling shown in figure (4.6). The two curves are not in fact identical in shape, the former having a relatively sharp peak, the latter being rather flatter. Tamman (ibid) was able to demonstrate that the maximum rate of crystallisation occurred at a lower ΔT than the maximum rate of nucleation. The relative positions of the two peaks with respect to the degree of supercooling can then be shown schematically (figure 4.22).

The early formed cumulus rounded (and tabular) olivines probably formed in regions of the magma devoid of other crystalline phases, thus their nucleation may be said to be homogeneous. After nucleation (e.g. at point A on the curve), the latent heat of crystallisation generated would decrease the local ΔT and the path of the nucleation would drop to point B, say. The corresponding points A' and B' on the growth rate curve indicate a rapid growth rate for these crystal phases. The combination of rapid growth and high nucleation rate will, result in small crystals, which in the Rhum olivines is manifested as the rounded morphology. If however a higher degree of ΔT were reached, at say point C, without nucleation having previously occurred at point A, a lower number of nuclei would be formed under a rapid crystallisation velocity (C'). Under these conditions tabular olivines can be

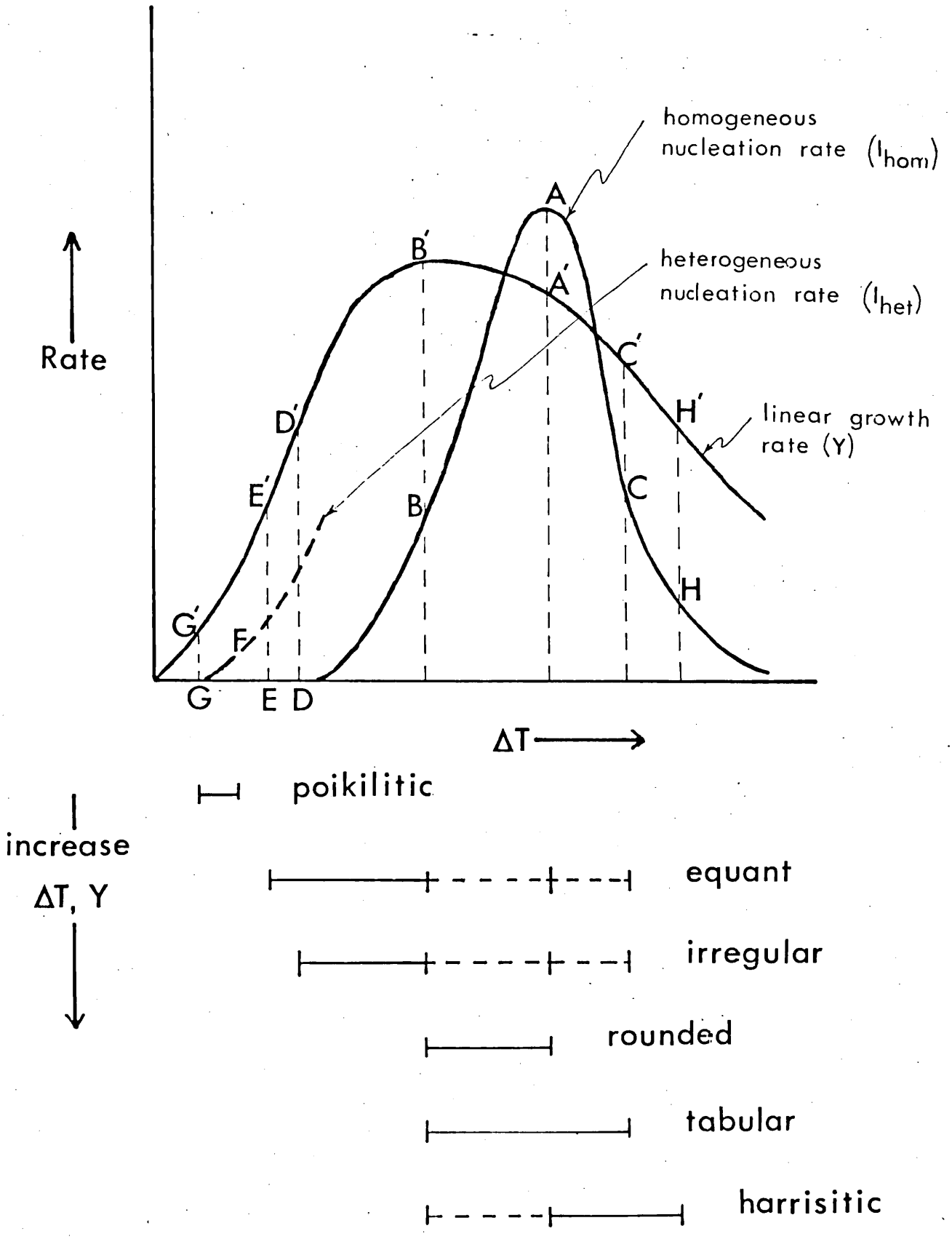
homogeneous
nucleation rate (I_{hom})
heterogeneous
nucleation rate (I_{het})
linear growth
rate (Y)
Rate
A
A'
B'
B
C'
C
D'
E'
F
G'
H'
H
G
E
D
ΔT
poikilitic
increase
ΔT, Y
equant
irregular
rounded
tabular
harrisitic

Figure 4.22

envisaged forming.

Extension of cumulus olivines by adcumulus or heteradcumulus growth can similarly be explained using this model. During settling of the cumulus crystals they would move into regions of relatively fresh melt (i.e. melt replenished in "olivine-constituent" material) and would continue to grow to point D say. Here the growth velocity is lower (D') and it is suggested that adcumulus overgrowth occurred both during and immediately after settling to produce the observed irregular morphology. Irregular in shape since around each crystal the zone of interstitial liquid produced by the effect of interfering diffusion fields from crystals mutually competing for olivine-constituent material would be irregular. After having settled, diffusional adcumulus overgrowth would continue to say point E (slower growth rate, E') giving the euhedral shape and coalescing features characteristic of equant morphology. Heterad-cumulus growth to produce the poikilitic morphology would have occurred after plagioclase feldspar had formed and settled out as cumulus crystals. Although the poikilitic morphology is found in the upper, plagioclase-cumulates of the units, it is probable that cumulus olivine was also present, thus nucleation around the preexisting cumulus olivine crystals would result in heterad-cumulus growth. Nucleation was therefore heterogeneous requiring lower ΔT conditions and would begin at point F say. The reduced pore space would reduce convection and so not allow the heat of crystallisation to disperse quickly and the supercooling would drop to point G say, where slow growth velocities and low ΔT (equilibrium) conditions prevail.

Harrisitic growth of olivine required conditions of rapid growth and low crystal nucleation at high ΔT values. The position where these requirements are met are after the maxima of the nucleation peak (at A) at point H say. (Alternatively,

displacement of the nucleation peak to the right in figure 4.21 would suffice). We need therefore to suppress the nucleation peak in some manner such that, in the quiescent supercooled magma prior to harrisitic growth, early nucleation at point A does not occur. Suppression may be obtained by rapid cooling such that at point H a high growth velocity (H') would act on pre-existing settled olivines and dendritic growth form in the direction of the highly supercooled magma, (i.e. upwards). The large amount of latent heat evolved would be generated in the direction of growth and would "accumulate" in a region above the harrisitic layer. Thus $\triangle$ T would increase to point A (and then to B) and rapid nucleation result. In the field, Wadsworth (1961) observed the frequent appearance of small olivine crystals at the top of harrisitic layers, a feature predicted by the above arguments.

Although many unknowns and variables exist within the model, it is however appealing in its simplicity. Unfortunately the effect of different silicate assemblages on individual peak aspects such as peak height; peak width and peak skewness have not been investigated. Nevertheless, the large range in sizes of the olivines required an interpretation based upon variation in nucleation rate; the observed uranium partition coefficients an interpretation based on variation in growth rate, and the observed morphologies an interpretation based on variation of supercooling. and the model described above is an attempt at combining these.

4.5. Uranium in Feldspars

The distribution of uranium within the feldspars of both the Rhum and Carlingford intrusions was determined using the fission track (contact point) method. A comparison of those resultsis given below in table 4.18. (Details of the analyses are given in table 3.5, Chapter 3). The interpretation of the results

Table 4.18

range	mean *	k_{obs} (mean)	composition **	range	mean +	k_{obs} (mean)	composition ++
9.54 - 29.39	17.99	.0599	$An_{78.6}Ab_{21.2}Or_{0.2}$	12.16 - 23.12	20.31	.0677	$An_{74.6}Ab_{25.3}Or_{0.1}$

* 45 analyses (Rhum)

** 21 analyses (microprobe)
(10 optical)

+ 10 analyses (Carlingford)

++ 3 analyses (microprobe)
(5 optical)

from the Carlingford specimens must be made with care however, because of:-

1) Few analyses were made.

2) Samples which were collected and analysed could not confidently be related to the major rhythmic units of the intrusion. (Details of the Carlingford samples are given in section 1.3).

Previously reported values of uranium concentrations in plagioclase feldspars from basaltic magmas are scarce and show a wide range of values from 2 p.p.b. (Lovering and Kleeman, 1972) to 190 p.p.b. (Nagpal et al., 1973). The values recorded in this work (table 4.17), appear to be more consistant with previously reported values from Rhum plagioclases (Henderson et al., 1970 - i.e. 10 to 70 p.p.b.); with Thiel's (1972) values of approximately 10 p.p.b. in plagioclases from lunar basalts, and with Gibjels et al.'s (1974) values of between 23 and 43 p.p.b. for the Bushveld plagioclases. The wide range of values in the literature probably does not represent accurately the true values of uranium within plagioclase feldspars as a result of several factors.

1) The possibilty of errors caused by contamination is increased owing to the ease of alteration and the common incorporation of inclusions within plagioclase feldspars. Either of these factors would increase the observed uranium concentrations, since uranium

has both a tendency to be associated with alteration minerals (e.g.Kleeman etal., 1969) and within micron-sized inclusions (e.g. in this work).

2) In analytical techniques which involve mineral separation, the degree of normal (Albite) zoning is often not known. This can produce errors in the uranium concentrations as, Henderson etal.(1971) showed, the outer rims of some zoned plagioclase crystals contained a higher uranium concentration than did the cores of crystal. This point is discussed in greater detail below.

4.5.1. Feldspars in the Rhum intrusion

From textural considerations, the feldspars can be divided into two morphological types - tabular (plate 4.17)and poikilitic (plate 4.18). Genetically, these correspond to a cumulus and a heteradcumulus origin respectively. When the uranium concentrations of these two morphological types are plotted against height in the intrusion (figure 4.23), two factors emerge.

1) There is an increase in uranium concentrations with a decrease in height.

2) Although the spread of results is fairly wide and some overlap occurs, in the middle and upper units, two trends may be resolved. There is a tendency for felspars with a poikilitic morphology to contain less uranium than those with tabular morphologies.

These two apparent features may be interpreted from a crystal growth viewpoint - viz. normal zoning (crystallisation of lower temperature zones), and the existence of two crystal growth mechanisms to give the two morphology types. These are discussed separately below.

PLATE 4.17. Tabular feldspar. 0·1 mm.

PLATE 4.18. Poikilitic feldspar. (enclosing olivine) 0·5 mm.

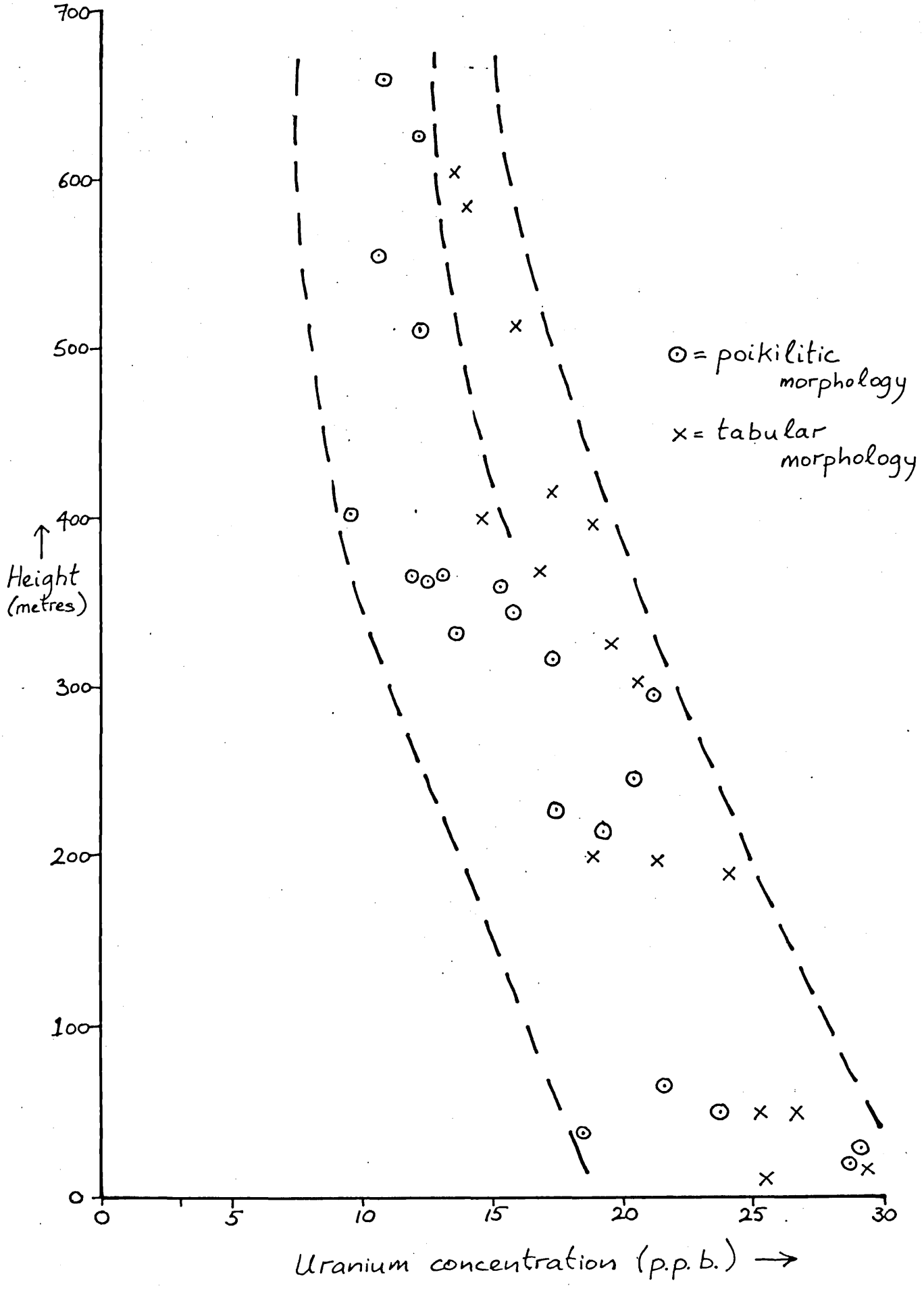
700
600
500
400
300
200
100
0
Height (metres)
0
5
10
15
20
25
30
Uranium concentration (p.p.b.) →
⊙ = poikilitic morphology
× = tabular morphology

Figure 4.23

4.5.1.1. Degree of zoning.

Henderson (1969) and Henderson etal.(1971) discussed the possibility of uranium-- as a low-partitioning element - being incorporated into the outer, lower temperature zones of normally-zoned plagioclase feldspars from the Skaergaard and Rhum intrusions. The argument being that since uranium enters the feldspar crystal in only low concentrations, remaining preferentially in the intercumulus liquid, then, if crystal accummulation occurred rapidly, it was possible to trap intercumulus liquid in contact with the pre-existing feldspar. The resulting lower temperature zones would therefore accumulate a large concentration of uranium.

In figure 4.24 (from Brown, 1956, figure 4) the degree (and extent) of zoning within the Rhum feldspars is plotted against the height in the intrusion. A comparison of this graph with uranium concentration in feldspars against height (figure 4.23) shows a good correlation. With decreasing height in the intrusion there is observed in the feldspars, both an increase in the uranium concentration and an increase in the degree and extent of normal zoning.

Although potentially, the fission track technique is capable of intra-mineral analysis and should thus be able to differentiate zoned and unzoned regions of the feldspar, with such low concentrations it was not practicable to count only those areas where zoning was absent, and inevitably, the resultant uranium concentrations included a variable (unknown) proportion of zoned material. In addition the degree and extent of zoning appears to vary extensively within one rock specimen, and the large spread of results in the lower units may be attributed to this. Thus (perhaps due to the limitations of the fission track technique), it can be seen that an increase in the uranium concentrations of the feldspars is the result of an increase in the degree of zoning.

Henderson (1969) extended the argument to suggest that the existence of zoning in feldspars from cumulates is indicative of the amount of mesostasis material. Whole rock uranium concentrations would then provide an indication of the amount of mesostasis in the rock - providing uranium-enriched minerals such as apatite and sphene were not present as cumulus phases and providing the proportion of clinopyroxene (which contains a higher mean uranium concentration i.e. 33.24 p.p.b.) does not vary extensively. When whole rock uranium concentrations (values given in table 3.5, chapter 3) are plotted against height in the intrusion (figure 4.25) an increase in concentration with decrease in height is observed. If, therefore, zoning in feldspars in cumulates is symptomatic of (low-temperature) crystallisation of trapped interstitial magma, then from the correlation observed between figures 4.25 and 4.24, the zoned portions may be interpretated as being regions of mesostasis material.

The distinction needs to be made here between increasing theAb content as a result of zoning (as e.g. in Rhum) and increasing the Ab content as a result of fractional crystallisation (as e.g. in Skaergaard). Although the uranium concentration appears to increase with increasing Ab content (figures 4.23 and 4.24), this correlation cannot justifiably be extended to encompass fractionated systems, since the Ab-enriched zones of the Rhum feldspars are considered to be mesostasis areas and are not therefore equatable with cumulus originated, lower temperature feldspars of the fractionated intrusions.

4.5.1.2. Variation of Uranium with morphological type.

In the middle and upper units of the intrusion (above approximately 280 metres), optical examination of the feldspars show them to be significantly less zoned than in the lower units. This feature is in accordance with Brown's (1956) observations

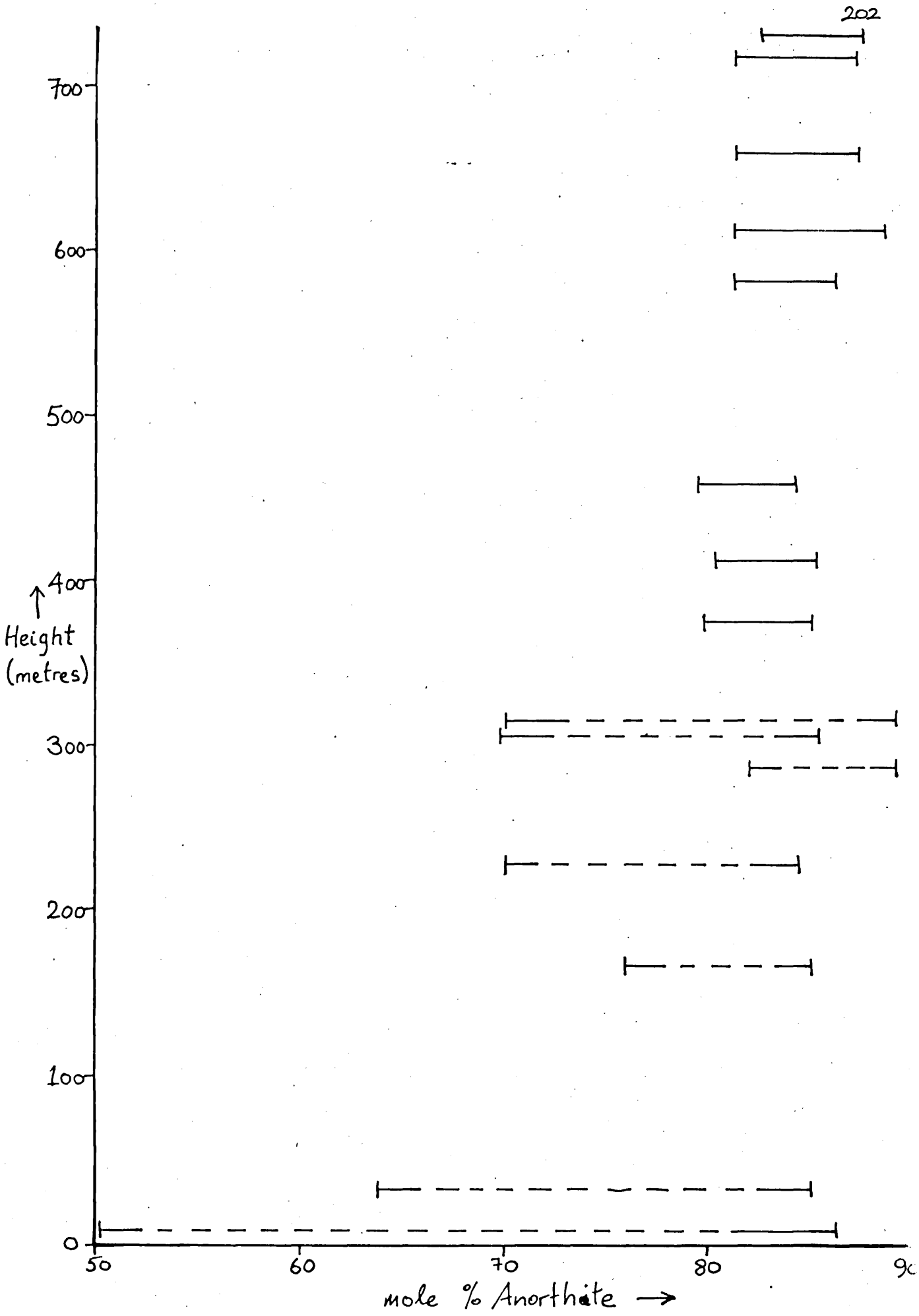

Figure 4.24

(after Brown, 1956)

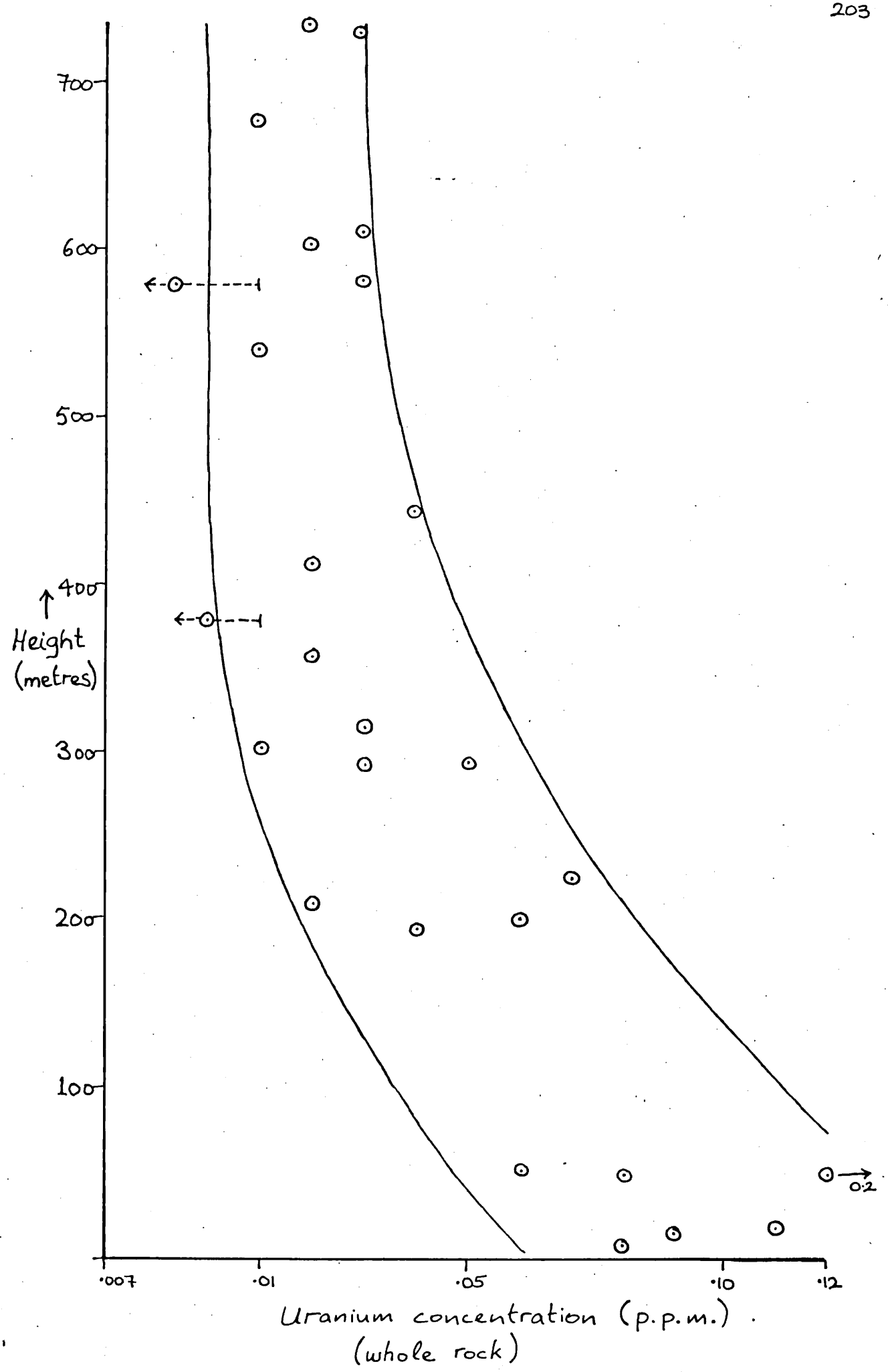
700
600
500
400
300
200
100
Height (metres)
·007
·01
·05
·10
·12
0·2
Uranium concentration (p.p.m.)
(whole rock)

Figure 4.25

(figure 4.24). In these higher units, both the post-depositional crystallisation of the cumulus feldspars in the feldspar-cumulates, and the crystallisation of the intercumulus feldspars of the olivine-cumulates must have occurred at a constant temperature and in an environment whereby there was unrestricted access to the main bulk of the magma. In such a situation, Hess (1939, p431) proposed that free diffusion of material feeding the growing crystals occurred, coupled with a subsequent physical expulsion of the intercumulus liquid. In the nomenclature of Wager et al. (1960), the resulting unzoned cumulates would be termed adcumulates (for unzoned overgrowths of cumulus, i.e. tabular, feldspars), and heteradcumulates (where the feldspar phase takes the form of poikilitic plates). Thus, an analogous situation to that found in the olivines of Rhum arises, whereby both the feldspars and the olivines display poikilitic morphologies, and both minerals have morphologies corresponding to adcumulus overgrowth on pre-existing cumulus phases. In the olivines, the cumulus crystals have rounded (or tabular) morphologies which transform with adcumulus overgrowth, to crystals with an equant or irregular morphology. Habit modification of the cumulus feldspars is not as diverse as the olivines however, the resulting crystal shapes remaining essentially unchanged - i.e. as a tabular morphology.

In these upper units (i.e. above 280 metres) there is a tendency for poikilitic feldspars to have a lower uranium concentration than tabular feldspars (figure 4.23). In the lower units, this trend is destroyed, the uranium concentration having been influenced by the zoning, which varied both in the degree and amount from specimen to specimen. A comparison of the concentrations between the two morphologies (above 280 metres) is given below in table 4.18. In spite of the low number and small degree of overlap of results, the trend is significant, and

an interpretation similar to that for crystallisation of the olivine phase (section 4.4) is proposed. The lower uranium concentrations (and partition coefficients) in the poikilitic morphology suggests crystallisation conditions of lower super-cooling (ΔT) and slower growth rates (Y) than existed for the tabular morphology.

table 4.19

	Uranium p.p.b. (fission track analysis)		
poikilitic morphology*	k_{obs}	tabular morphology**	k_{obs}
11.19	.0428	16.34	.0545
(9.54 - 15.17)		(13.16 - 18.80)	

* 9 results, mean S.D. = 1.73

** 5 results, mean S.D. = 1.36

As observed initially by Brown (1956), the feldspar poikilitic morphology occurs in the lower (olivine-rich) regions of each unit, with the tabular morphology in the upper (feldspar-rich) regions. The feldspars in the olivine-cumulates crystallised interstitially between the olivine crystals and nucleation was likely to be of a heterogeneous nature with olivine grain edges or grain boundaries acting as nucleation sites (e.g. Christian, 1965). Using a similar model to that proposed for the crystallisation of the various olivine morphologies with juxtapositions of nucleation and crystal growth rate curves (figure 4.26), heterogenous nucleation of poikilitic feldspars would occur at some point A(say). In an enclosed environment with restricted convection, the evolved

latent heat of crystallisation would not adequately be able to disperse, and the path of the nucleation curve would decrease to a lower value of ΔT (to point B, say). The corresponding path of the growth rate curve would decrease also from A' to B'. For the formation of the feldspar cumulates in the upper regions of each unit, olivine would have ceased to crystallise and the system reached the olivine-feldspar cotectic join. Thus feldspar would nucleate as a major phase, the mode of nucleation in this case being homogeneous, at point C (say). Again the latent heat of crystallisation evolved would act to decrease locally the value of ΔT of the melt (although the heat dissipation would probably be more effective in a relatively open environment), and the path of the nucleation curve would decrease to point D (say). Adcumulus overgrowth on the settled cumulus feldspars does not appear to have modified the morphology to any great extent, it remaining essentially a tabular morphology, and, in terms of figure 4.26, nucleation and growth rate conditions for adcumulus growth would have been similar to that for poikilitic (heter-adcumulus growth) morphology. Since however, heterogeneous nucleation on pre-existing cumulus feldspars is likely to be thermodynamically more favoured than heterogeneous nucleation on grain boundaries (and edges), the degree of supercooling required would be less for adcumulus growth than for heteradcumulus growth. On the growth rate curve therefore, nucleation would start at some point midway between A and B, and with the decrease in supercooling, continue to point B (say).

The model predicts therefore, that the overall growth rate of the homogeneously nucleated tabular feldspars (with varying amounts of adcumulus growth) would be greater than that for the heteradcumulate phase (poikilitic morphology), with the larger

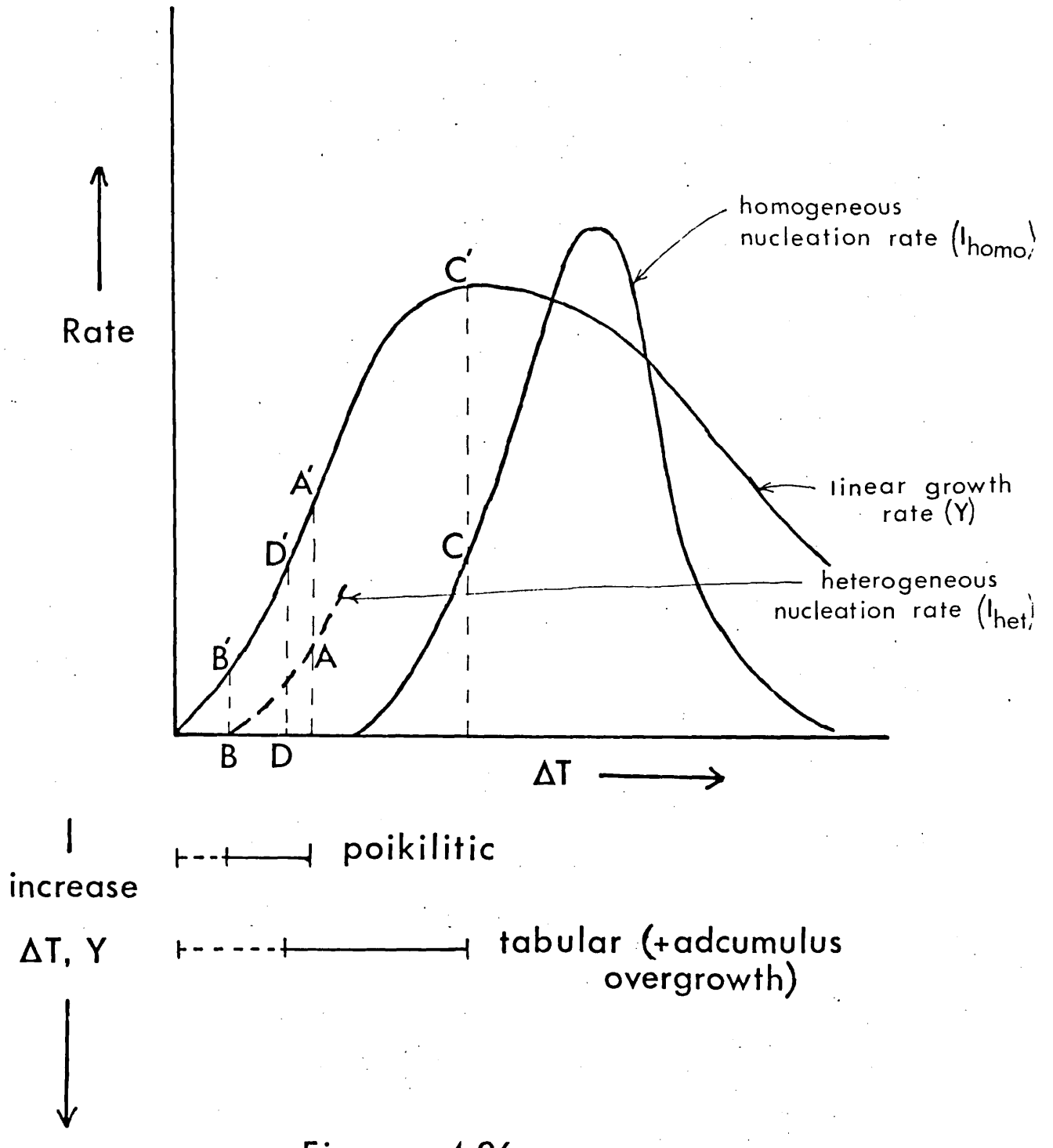
Rate
homogeneous nucleation rate ($I_{homo.}$)
C'
A'
D'
C
linear growth rate (Y)
heterogeneous nucleation rate ($I_{het.}$)
B'
A
B
D
ΔT
increase
ΔT, Y
poikilitic
tabular (+adcumulus overgrowth)

Figure 4.26

uranium concentration for the tabular morphology being a manifestation of the growth rate differences. In both tabular and poikilitic morphologies, the Anorthite content of the plagioclases are essentially the same

As a corollary to this, when the uranium concentrations of the tabular feldspars are compared with the poikilitic feldspars in any one unit (table 4.19), and plotted against the height above the base of the unit, there is observed (with two exceptions) a positive gradient in each of the slopes (figure 4.26 (a) to (h)). In the case of the two exceptions (units 2 and 3), the feldspar zoning varied both in amount and in degree, and the calculated uranium concentrations are not considered to be reliable.

Previous to this study for the uranium distribution in the feldspars of Rhum, an investigation of the distribution of Sr was undertaken on representative feldspar samples separated from both feldspar cumulates and olivine-cumulates of several units, Williams (1971). The analysis was achieved using a Phillips X.R.F. instrument and the results are given in Appendix 2. When a similar graph of Sr concentrations for poikilitic and tabular morphologies are plotted against height above the base of each unit (table 4.19), a mirror-image trend is observed (figure 4.28 (a) to (f)) with negative gradiants to the slopes. An exception to this rule occurs in unit 8 where the slope has a positive gradient. At the present, no explanation can be offered regarding this anomaly. At the time of analysis it was found difficult to interpret these results, but, using the model proposed in this chapter, these trends can be explained.

The distribution at the interface of high-partitioning elements (such as Sr) differs markedly to that of a low-partitioning element (e.g. uranium), and these distributions are schematically shown in figure 4.29. The Sr concentration increases with distance

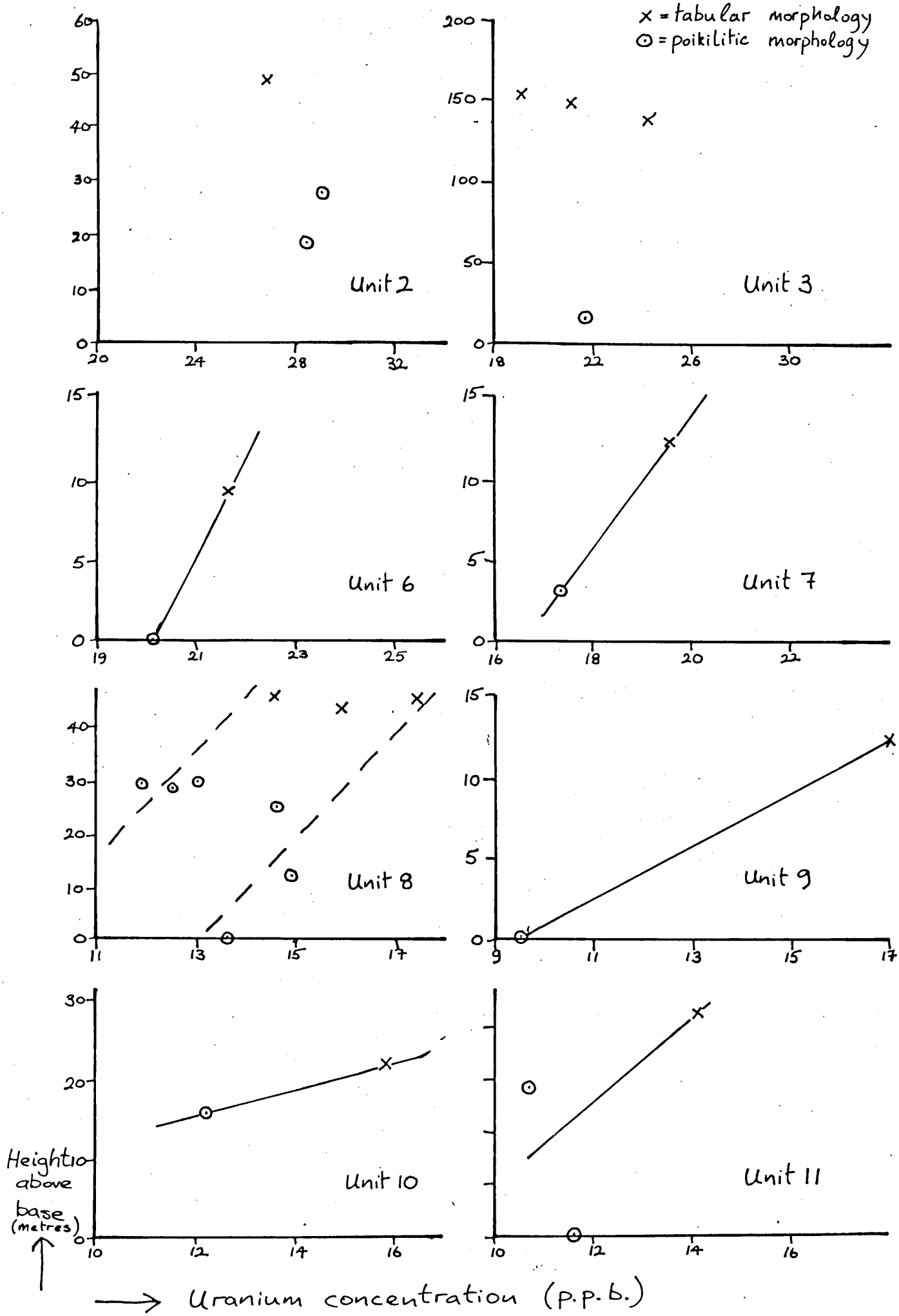
x = tabular morphology
⊙ = poikilitic morphology
Unit 2
Unit 3
Unit 6
Unit 7
Unit 8
Unit 9
Unit 10
Unit 11
Height to above base (metres)
Uranium concentration (p.p.b.)

Figure 4.27

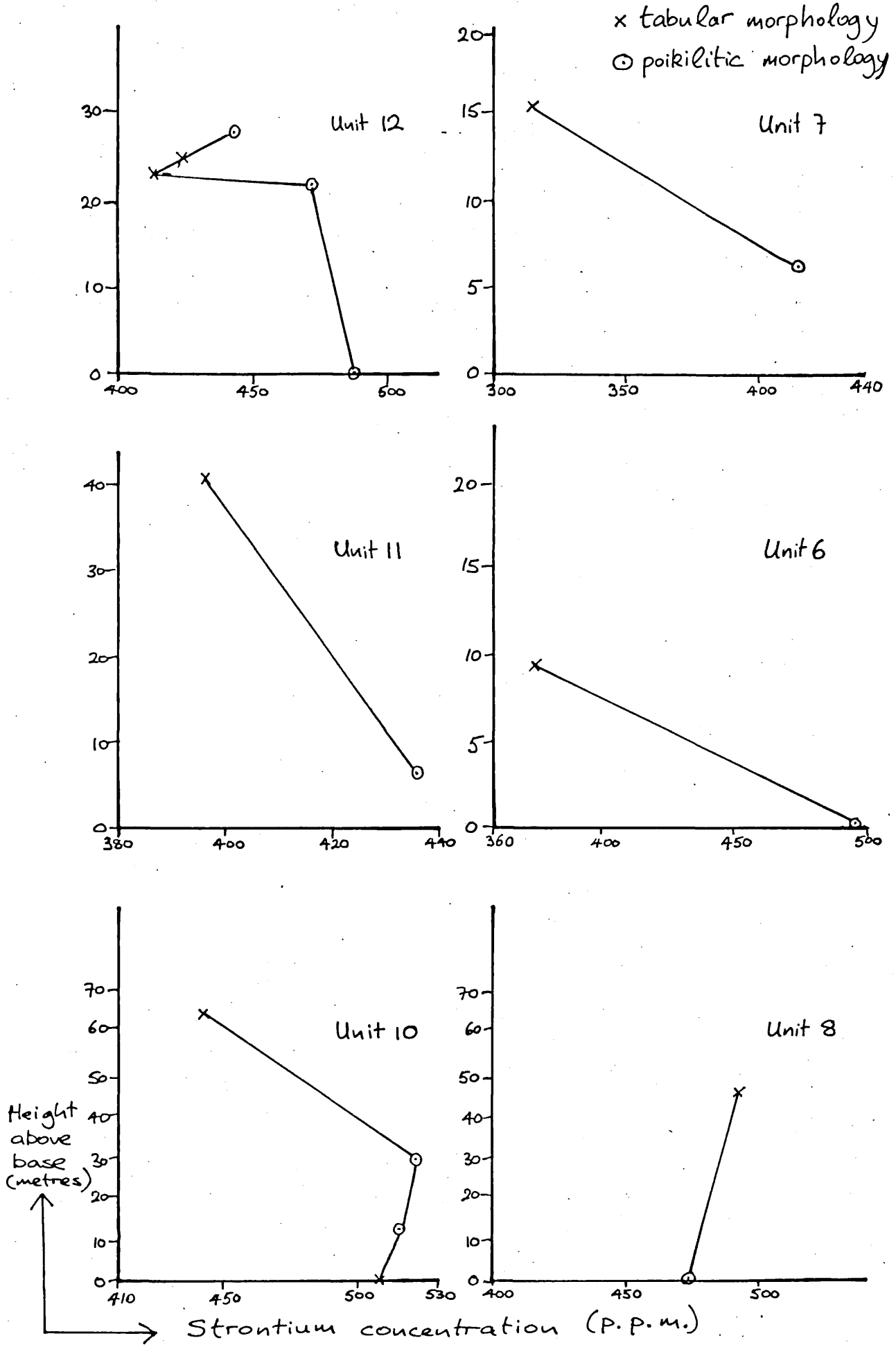
× tabular morphology
⊙ poikilitic morphology
Unit 12
Unit 7
Unit 11
Unit 6
Unit 10
Unit 8
Height above base (metres)
Strontium concentration (P.P.M.)

Figure 4.28

in the melt, whereas the uranium concentration decreases with distance. Under equilibium conditions, i.e. slow growth rate, low ΔT conditions, the observed partition coefficients (k_{obs}) of the two elements will be equal to their equilibrium partition coefficients (k_{equ}), and in figure 4.29 this is schematically represented by the large δ region, δ_A. By increasing the growth rate such that it is more rapid than the diffusion rates of the element species, there is an increase in ΔT and a decrease in δ, to δ_B. This increases the amount of the low-partitioning element (uranium) incorporated in the crystal, but decreases the amount of the high-partitioning element (Sr), and in both cases $K_{obs} \longrightarrow 1$ (equations (18) and (19)).

Therefore, figures 4.27 and 4.28 can be interpreted using crystal growth models such that feldspars with a poikilitic morphology crystallised with a lower (diffusion-controlled) growth rate than the more rapidly grown (more disequilibrium conditions) tabular morphology. This resulted in:-

$$k^{U}_{obs}\ \text{(tabular)} > k^{U}_{obs}\ \text{(poikilitic)}$$

and $$k^{Sr}_{obs}\ \text{(tabular)} < k^{Sr}_{obs}\ \text{(poikilitic)}$$

where k^{U}_{obs} (tabular) = observed partition coefficient or Uranium in the tabular morphology

k^{U}_{obs} (poikilitic) = observed partition coefficient of Uranium in the poikilitic morphology.

k^{Sr}_{obs} (tabular) = observed partition coefficient of Sr in the tabular morphology.

k^{Sr}_{obs} (poikilitic) = observed partition coefficient of Sr in the poikilitic morphology.

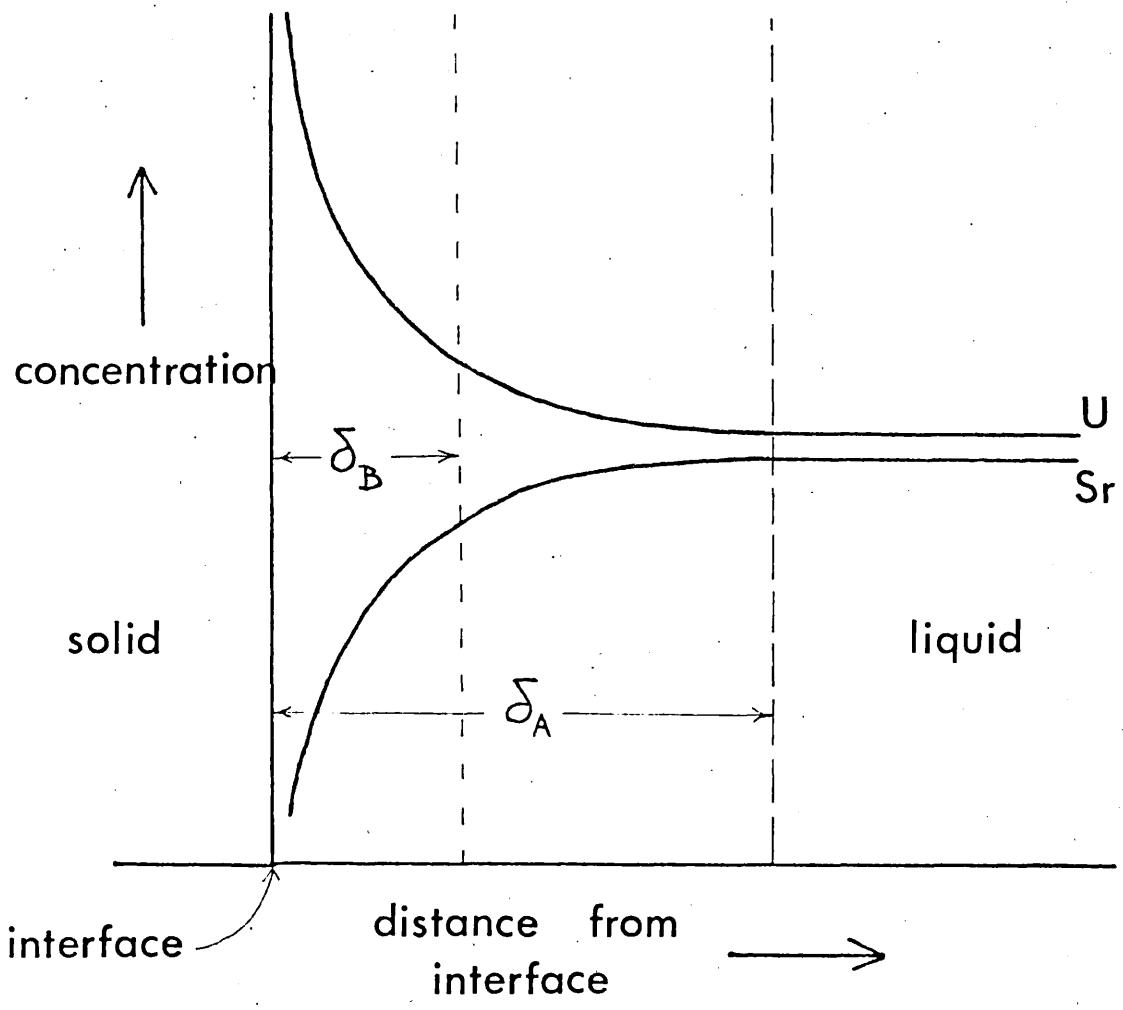
concentration
U
Sr
δ_B
solid
liquid
δ_A
interface
distance from interface

Figure 4.29

Table 4.20.

Specimen Number	Unit Number	Height (metres) above base of unit	Morphology	$U_{p.p.b.}$*	Sr p.p.m.**
R.92	2	0	poik	28.44	-
R.93	2	8.5	poik	29.03	-
R.94	2	17.7	poik	18.46	-
R.95	2	29.9	tab	26.80	-
R.96	3	0	poik	23.91	-
R.99	3	15.2	poik	21.66	-
R.89	3	138.7	tab	24.04	-
R.86	3	140.8	tab	21.31	-
R.87	3	143.0	tab	18.81	-
R.82	6	0	poik	21.11	-
R.42	6	0	poik	-	496+
R.44	6	9.1	tab	21.60	375+
R.120	7	0	poik	17.31	-
R.45	7	9.1	poik	-	415+
R.46	7	18.2	tab	19.48	315
R.30	8	0	poik	-	474
R.61	8	21.3	poik	13.64	-
R.62	8	28.9	poik	15.81	-
R.63	8	36.6	poik	15.71	-
R.112	8	41.1	poik	12.50	-
R.110	8	44.2	poik	13.04	-
R.111	8	44.5	poik	11.88	-
R.64	8	45.7	tab	16.83	-
R.65	8	60.9	tab	14.50	-
R.47	8	60.9	tab	18.43	492
R.53	9	0	poik	9.54	-
R.54	9	12.2	tab	17.19	-
R.35	10	0	tab	-	509
R.34	10	12.2	poik	-	516
R.33	10	27.4	poik	-	522
R.113	10	54.8	poik	12.22	-
R.114	10	57.9	tab	15.88	-
R.30	10	60.9	tab	-	442
R.66	11	0	poik	11.62	-

R.27	11	27.4	poik	-	436+
R.68	11	36.6	poik	10.68	-
R.18	11	41.1	tab	14.13	396
R.19	12	0	poik	-	488+
R.24	12	21.3	poik	-	472+
R.20	12	22.8	tab	-	413
R.23	12	24.8	tab	13.61	424
R.12	12	27.4	poik	-	443

---

* fission track analysis

** X.R.F. Analysis

+ Analyst P. Henderson

poik = poikilitic morphology

tab = tabular morphology

4.6. Uranium in clinopyroxene

The concentrations of uranium in the clinopyroxenes from both the Rhum and the Carlingford intrusions were determined using the fission track (contact print) method. A comparison of the range of concentrations and the mean values for the two intrusions is given in table 4.20 below. (The details of the results are tabulated in chapter3, table 3.4). As in the case of the feldspars, the interpretation of the uranium concentrations in the clinopyroxenes from the Carlingford intrusion must be treated with caution because of sampling difficulties (chapter 1, section 1.3), and because alteration appears to have occurred to a much greater degree than in Rhum.

table 4.21

Rhum *			Carlingford **		
Range (p.p.b.)	Mean	K_{obs} (mean)	Range (p.p.b.)	Mean	K_{obs} (mean)
27.32 - 36.15	32.24	0.107	30.70 - 36.60	33.60	0.112

* 39 analyses (S.D. = 2.33)

** 10 analyses (S.D. = 2.38)

Unlike the other major phases, i.e. olivine and feldspar, the range of uranium concentrations recorded in the literature for clinopyroxenes from basaltic magmas, is not very extensive. Concentrations range from 15 p.p.b. (Kleeman, et al. 1969) to 89 p.p.b. (Nagasawa and Wakita, 1968). However, partition coefficients recorded for clinopyroxene grown from experimental di-an-ab melts (50, 25, 25 wt.%) differ greatly. Seitz and Shimizu (1972) calculated partition coefficients of between 0.15 - 0.19, and Seitz (1973) values of approximately 0.0008 from similar melts. There is therefore a clear need for further experimental work in this field.

By the addition of ^{235}uranium (the uranium isotope measured in f.t. analysis) to experimental melts, the distribution and partition coefficients of uranium using the f.t. technique can be more easily obtained.

The values recorded in this work however, are consistent with those from Henderson (1970) and Henderson et al. (1971), (values range from 32 - 60 p.p.b.). In these cases, the technique used was Delayed Neutron Activation Analysis (D.N.A.A.), and the samples were separated clinopyroxenes from the Rhum, Skaergaard and Bushveld intrusions.

4.6.1. Textural variations in the Rhum clinopyroxene phase

Both the mineralogy and textural variations within the clinopyroxenes of Rhum have been systematically studied by Brown (1956) and Wager and Brown (1968). This section, and section 4.6.2. (Mineralogical and Chemical variations), summarises the previous work and adds some new observations.

In comparison to the olivine and feldspar phases, clinopyroxene as both a cumulus and an inter-cumulus phase, occurs in subordinate amounts throughout the intrusion. Brown (1956) quotes a modal proportionate range of between 1-15% (although he noted one specimen contining 70% clinopyroxene), an "average" olivine-cumulate containing 8% clinopyroxene and an "average" feldspar-cumulate 10% clinopyroxene. In general, he found no significant variation in modal percentage in traverses from the base to the top of the units.

Within each unit, Brown (ibid. p.17) noted a generalised sequence of textural variations:-

1) In the lower regions of the olivine-cumulates, clinopyroxene occurs as large poikilitic plates approximately five millimetres in diameter.

2) With increase in height, although still with a poikilitic morphology, the clinopyroxene usually has a core (up to two millimetres diameter) containing no inclusions, and which he suggests represents the original settled crystals.

3) In some of the feldspar cumulates at the top of the units, clinopyroxene occurs as equidimensional cumulus crystals (averaging 0.6 millimetres diameter) with little intercumulus overgrowth.

In the nomenclature of Wager et al. (1960), these variations would correspond to heteradcumulus, cumulus plus heteradcumulus overgrowth, and cumulus (plus a small degree of adcumulus overgrowth) textures respectively.

In some of the higher units, Brown (ibid,) noted also that clinopyroxene occurs occasionally as a narrow sinuous interstitial rim around both the olivine and the feldspar phases. This feature however, was not observed in any of the specimens examined in this study.

In the field the combination of poikilitic clinopyroxene and poikilitic feldspar enclosing cumulus olivines (i.e. to give an olivine-heteradcumulate) produces a characteristic honeycomb appearance (Wager and Brown, ibid, figure 148). This is due to the clinopyroxenes weathering more easily than the feldspars, the former represented by hollows, and the latter standing out as irregular knobs.

Examination of the specimens collected for this thesis tends to support the above observations. It was noted however, in the lowest three units, there was a higher modal proportion of clinopyroxene (average 22% from eleven specimens), than in the units above (average 11% from twenty-eight specimens) - table 3.5, chapter 3.

Texturally, the general sequence of heteradcumulus to cumulus clinopyroxene with increase in height within a unit, was verified. In addition, field examination of the honeycomb structure near olivine-cumulate/feldspar-cumulate junctions of units 7, 8, 10 and 13 showed there is within the olivine-cumulus, a decrease in diameter of the hollows (i.e. the clinopyroxene) towards the junctions (plate 4.19). Figure 4.30 schematically shows this feature. Below approximately 1 metre beneath the olivine-cumulate/ feldspar-cumulate junction, the diameter of the clinopyroxene stabilises, the honeycomb structure becomes more diffuse, and the rock surface more irregular.

Thin section examination of specimens R.110 to R.112 from unit 8 (the positions are shown in figure 4.30) confirms the decrease in size of both the feldspar and the clinopyroxene poikilitic crystals towards the junction. Although measurements of the poikilitic crystals from the thin section are given in table 4.21, these values are not considered to be as accurate as field measurements of the honeycomb weathering. The reasons can be attributed mainly to the small size of the thin sections (24 millimetres by 48 millimetres) and to problems of obtaining a representative section containing the maximum crystal diameters. In the highest specimen, R.111, the feldspar exists as a cumulus to sub-poikilitic phase, the clinopyroxene retaining a true poikilitic morphology. In the feldspar-cumulate of this unit, the feldspar occurs as a cumulus phase with clinopyroxene poikilitic to it.

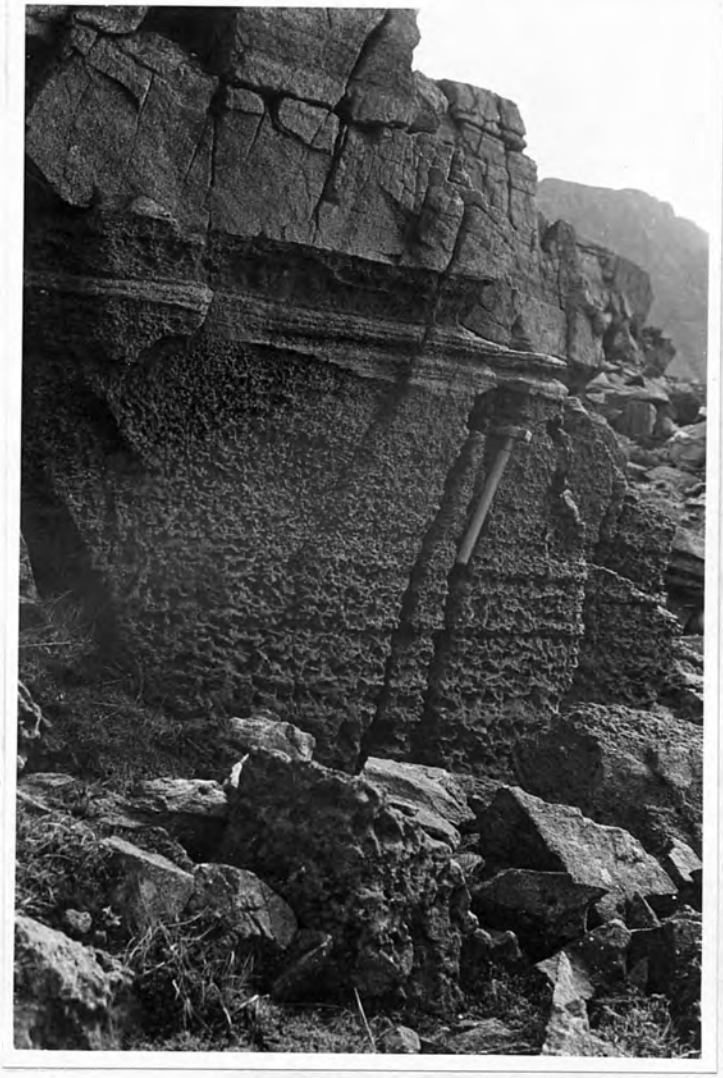

PLATE 4.19

Honeycomb weathering - unit 8.

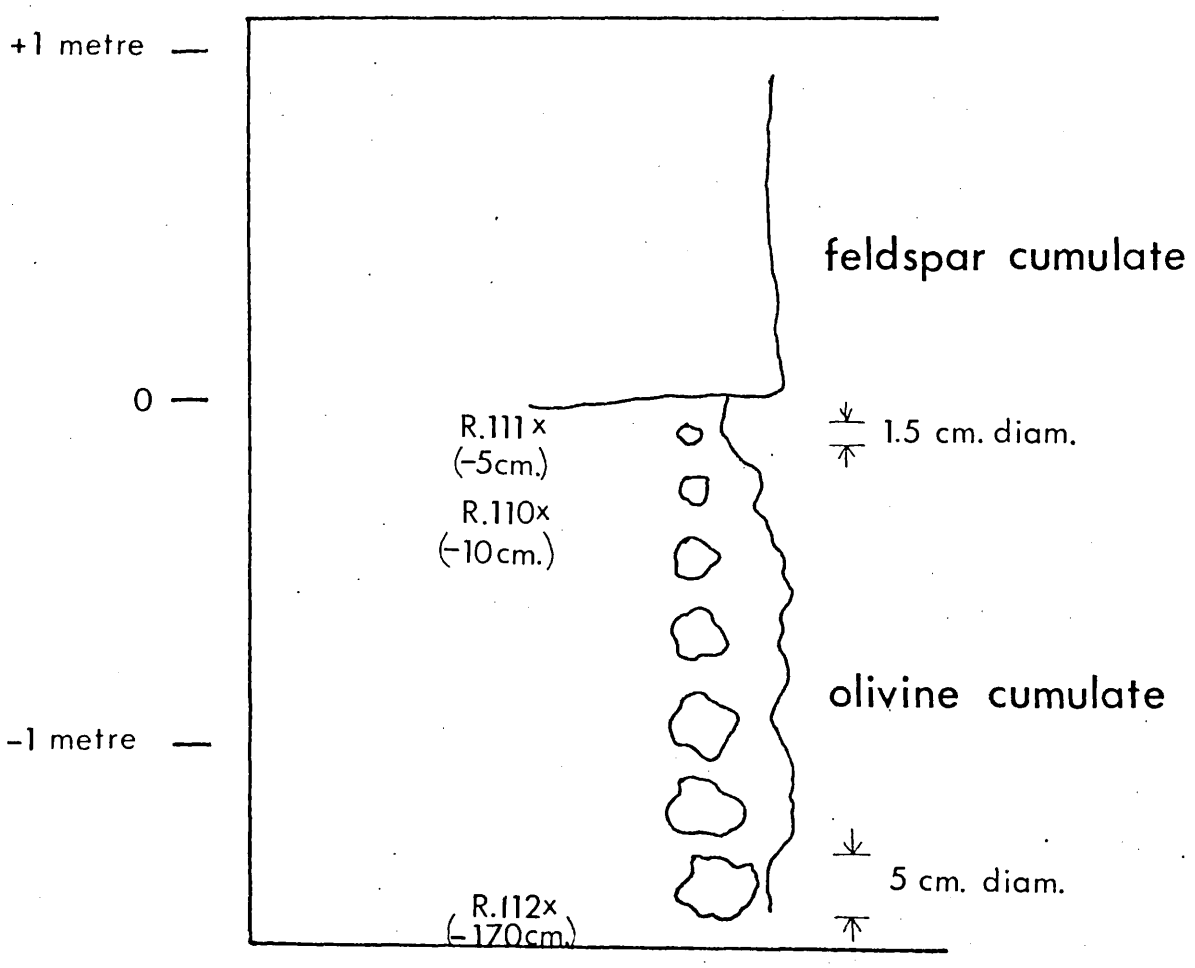
+1 metre
0
-1 metre
feldspar cumulate
olivine cumulate
R.111 x
(-5cm.)
R.110x
(-10cm.)
R.112x
(-170cm.)
1.5 cm. diam.
5 cm. diam.

Figure 4.30

table 4.22.

Specimen Number	Height below junction	Feldspar Approximate size	Feldspar Morphology	Clinopyroxene Approximate size	Clinopyroxene Morphology
R.111	2 - 5 cms	1.5 to 2 mm.	Sub poikilitic	4 mm.	poikilitic
R.110	10 cms.	4 to 5 mm.	poikilitic	6 to 8 mm	poikilitic
R.112	170 cms.	6 to 8 mm.	poikilitic	10 to 12 mm.	poikilitic

Although in only four units was there adequate exposure of the olivine-cumulus/feldspar-cumulus junction this evidence, and the absence within the intrusion of feldspar poikilitic enclosing cumulus clinopyroxene, suggests the order of nucleation of the cumulus phases to have been:-

olivine (and spinel?); feldspar; clinopyroxene.

4.6.2. Mineralogical and chemical variations in the Rhum Clinopyroxene Phase.

Brown (1956) records very little change in mineral composition of the clinopyroxene with either height in the intrusion, or with rock type. The composition throughout the intrusion is essentially $Ca_{44}\ Mg_{49}\ Fe_{7}$, i.e. magnesian augite. The high Mg/Fe ratio is characteristic of high-temperature clinopyroxene such as those formed early in the crystallisation of other fractionated basic intrusions (e.g. Skaergaard, Stillwater etc.). Twinning is rarely seen; zoning in the higher units is absent but is sometimes patchily present in the lower units. Brown (ibid. p.25) noted the absence of exsolution lamellae of orthopyroxene parallel to (100), and suggested this may be due to the calcic nature of the clinopyroxene.

Table 4.23

	1	2	3	4	5
SiO_2	49.15	49.92	48.98	50.25	51.90
Al_2O_3	3.33	3.23	3.42	2.81	3.40
TiO_2	2.05	1.94	1.89	0.81	0.46
FeO	3.60	3.35	3.49	3.14	3.70 (0.53)*
CaO	22.41	22.64	22.35	22.73	21.12
MgO	17.25	17.37	17.41	17.86	17.00
MnO	0.03	0.07	0.11	0.09	n.d.
Cr_2O_3	0.75	0.77	0.88	0.86	0.88
Total	98.57	99.29	98.53	98.55	99.75
Ca	45.53	45.81	45.34	44.86	43.9
Mg	48.76	48.90	49.13	50.30	49.2
Fe	5.71	5.29	5.53	4.84	6.9
U(p.p.b)	31.52	29.33	32.11	32.36	-

* Values in parenthesis are for Fe_2O_3.

Analysis Number	Rock Number	Unit Number	Height (metres)	Morphology
1)	R.91	1	12.3	poikilitic
2)	R.86	3	195.2	equant (cumulus)
3)	R.53	9	399.5	poikilitic
4)	R.54	9	411.7	equant (cumulus)
5)	Analysis from Wager and Brown (1968, p.256, table 20)			

In order to see if the composition of the clinopyroxene is as constant as Brown suggests, a few representative examples of different morphologies from different heights in the intrusion were analysed using the Geoscan microanalyser. (Details of the analytical procedure is given in chapter 2, section 2.8). The results are presented in table 4.23 which shows that the composition remains essentially the same for both different

morphological types and for specimens separated by 430 metres of the intrusion.

Unlike the olivines and feldspars, the uranium concentration within the clinopyroxene was basically constant, and no significant variation of uranium concentration with morphological type was observed. Similarly, no correlation existed between the uranium concentration in the clinopyroxene and the height in the intrusion. These two results may have been due to a sampling bias. From thirty-nine specimens studied with sufficient clinopyroxene present for fission track analysis, on only five occasions was the clinopyroxene a cumulus phase - the remaining thirty-four specimens were the heteradcumulus phase. Until a more rigourous study of cumulus clinopyroxenes within the intrusion is undertaken, these results (table 4.24) cannot unfortunately be interpreted from a crystal growth viewpoint.

Table 4.24.

Rhum clinopyroxene	Uranium concentrations (p.p.b.)		
poikilitic		cumulus	
range	27.32 - 36.15	range	29.80 - 34.50
mean	32.24	mean	33.06

One feature occasionally seen in the uranium distribution maps of the clinopyroxenes, was the existance of a uranium-enriched rim (approximately 300 p.p.b.) around both the cumulus and the heteradcumulus phases (plate 4.20 (a)-(d)). The width of the rim appeared to be fairly constant, ranging from 0.01 - 0.05 millimetres. Where this occurred, the clinopyroxene was probed (both with the Geoscan and Jeol electron microprobes). However, no distribution gradients in either the major elements (Ca, Mg, Fe, Si or Al), or the minor elements (Ti, Cr, Mn, Na)

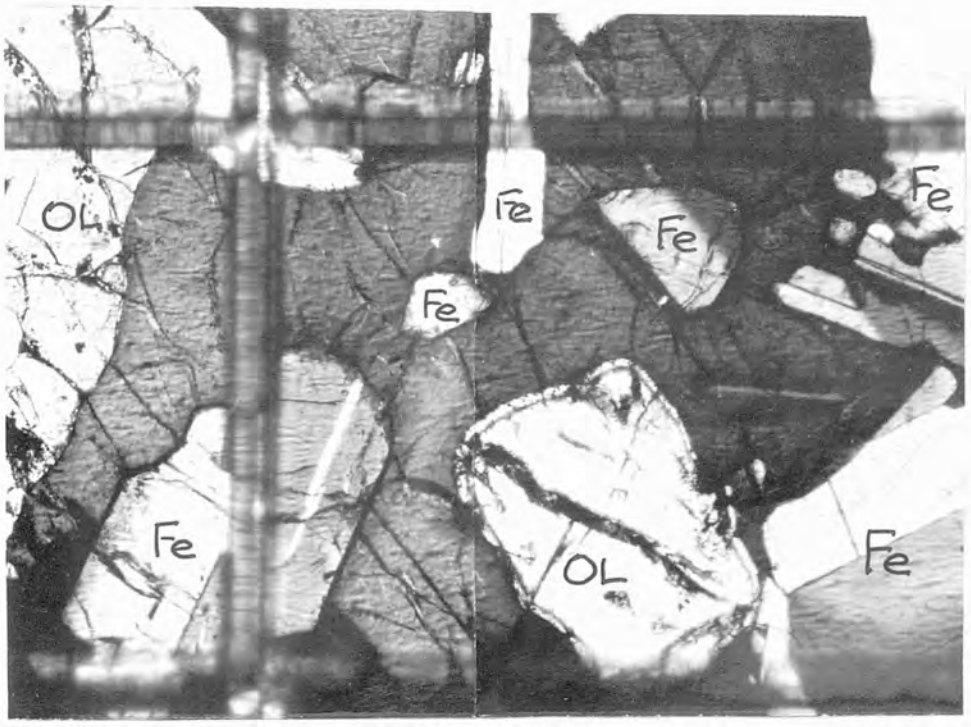

PLATE 4.20 (a). Poikilitic clinopyroxene enclosing olivine (Ol) and tabular feldspar (Fe). 0·1mm

Photomicrograph taken prior to irradiation and showing portion of the makrofol grid.

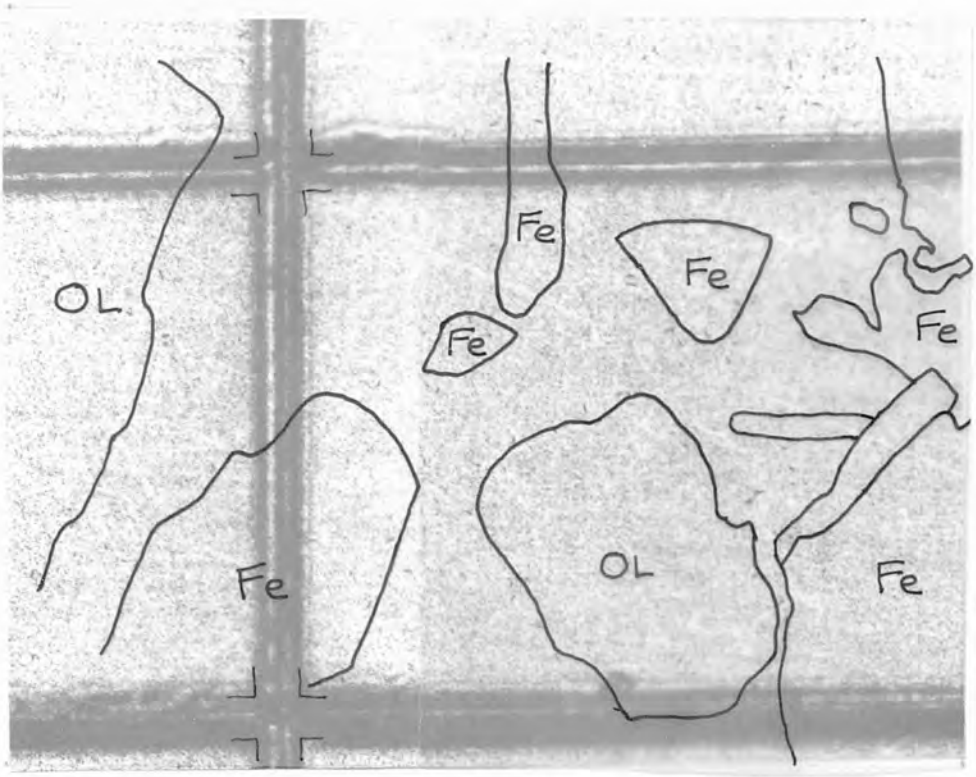

PLATE 4.20 (b). Uranium distribution map.

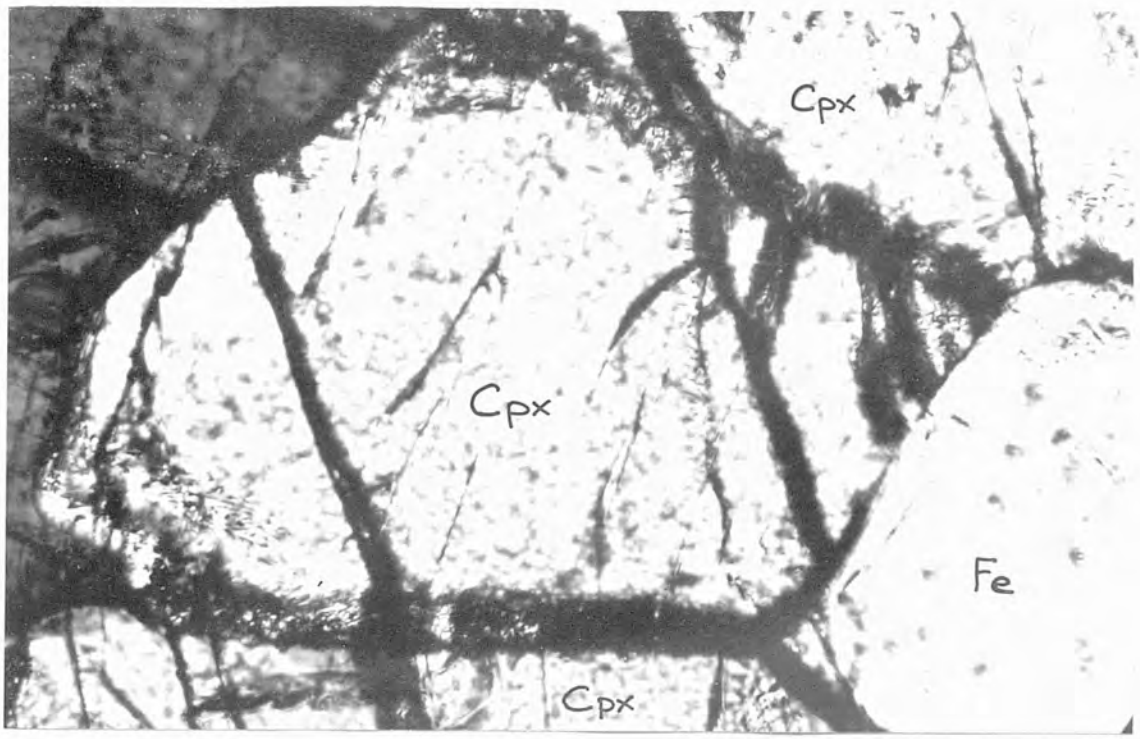

PLATE 4.20 (c). Adjacent cumulus clinopyroxene crystals.

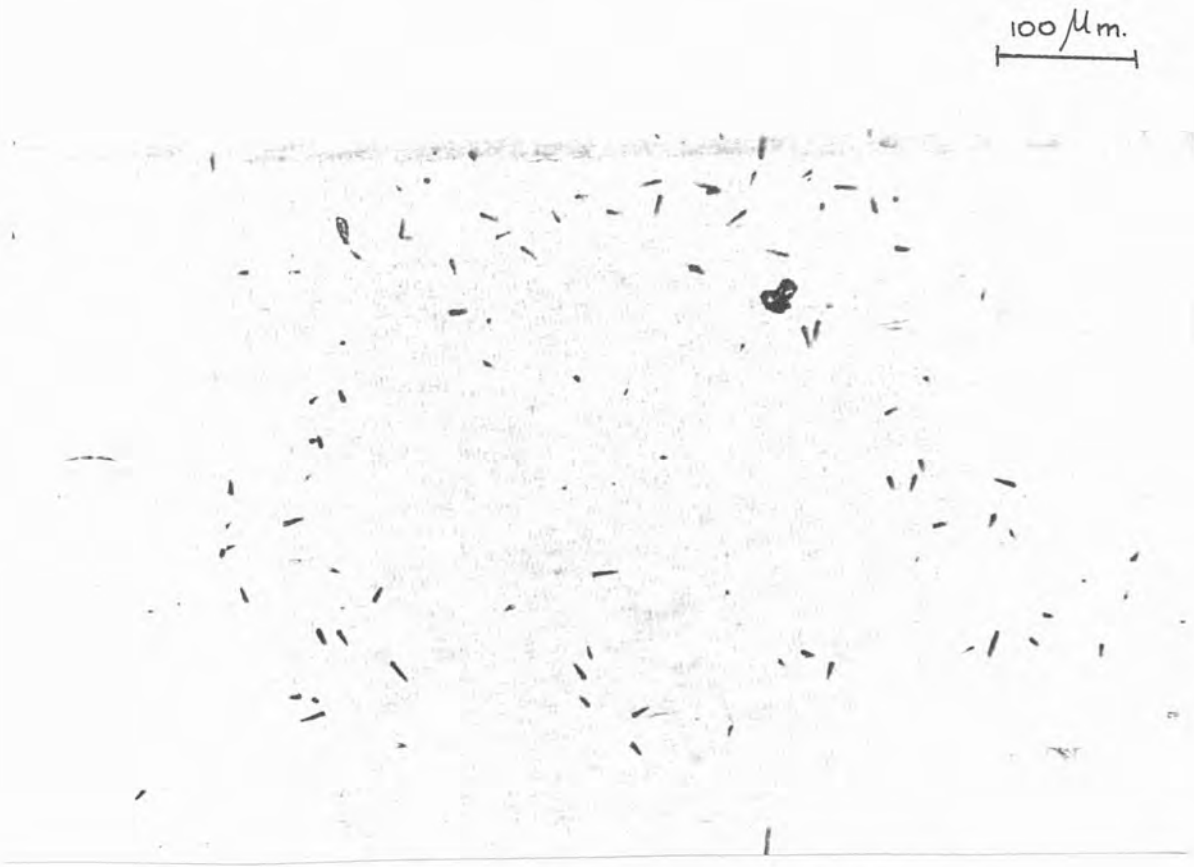

PLATE 4.20 (d). Uranium distribution map. (mirror image)

was detected. In the cumulus phases, the clinopyroxene crystals were distributed inhomogeneously and had formed clusters. Since the junctions between individual crystals were straight and no major element zoning was present, some adcumulus overgrowth of the cumulus crystals had evidently occurred. In the poikilitic phases, growth was of a heteradcumulus nature.

From previous arguments, the diffusion rate of uranium in the interstitial liquid is slower than for the major elements (table 4.7, section 4.4.). Similarly, the existance of a distribution gradient in one element (i.e. uranium) and not others, indicates that sub-solidus reequilibration has not occurred. From a crystal growth viewpoint then, there are two possible interpretations of this feature.

1) More rapid crystal growth in the region of enriched uranium in a similar manner to that proposed for the olivine and feldspar phases.

2) Uranium, in addition to having a slower diffusion rate than the major elements, is likely also to be in the form of a larger complexed species (chapter 3, section 3.2.). Thus, in a physically restricted environment during the latter stages of adcumulus (or heteradcumulus) growth, the final expulsion of interstitial liquid was probably not efficient enough to include all of the uranium. The excess uranium trapped would therefore be incorporated in a non-equilibrium manner, within the clinopyroxenes, as a uranium-enriched rim.

4.7. Uranium in chrome spinel

Chrome spinel occurs within the Rhum intrusion in two dissimilar environments: as disseminated grains in the cumulates, or as occasional thin seams traceable over several metres.

Brown (1956) noted a thin (1.5 to 2.0 millimetres thick) seam of chrome spinel at the junction of unit 11 with unit 12, and forming the base of unit 12. The spinels apparently settled after the accumulation of cumulus feldspars of the unit 11 feldspar-cumulate, and prior to the deposition of olivine to form the unit 12 olivine-cumulate. In conjunction with Dr. P. Henderson, further seams were discovered at the junctions of unit 7/8, unit 13/14 and three seams within the unit 7 olivine-cumulate.

In a microprobe study of the chrome spinel at unit 11/12, Henderson and Suddaby (1971) showed the presence of a large systematic variation in the Cr/Al ratios with only a little variation in the concentration of Fe_2O_3. This trend was seen also in the unit 7/8 chrome spinel seam (Henderson, 1975 b) and interpreted as being the result of a complex post-depositional reaction between the chrome spinel and overlying olivine, underlying feldspar plus intercumulus liquid. This, Henderson 1974 (ibid.) termed "Al-trend". In contrast, disseminated chrome spinel crystals in the cumulates, in particular those cumulates containing crystallised trapped liquid, show a trend involving changes in the Fe^{3+} content, termed"Fe-trend" (Henderson, ibid.). This latter is attributed to reaction between cumulus chrome spinel and trapped liquid.

A comparison of the uranium distribution within chromites would have proved useful in determining the validity of the above hypotheses, however, limitations of the fission track (contact print) method meant that a definitive statement could not be made. Since the modal proportion of chrome spinels in seams was not 100 per cent (typically 70 to 80 per cent), the tracks emanating from the seam could not be precisely referred back to individual chrome spinels. Uranium concentrations

were in fact calculated, but these values (10.3 p.p.b. for unit 13/14 and 9.6 p.p.b. for unit 7 peridotite seam, R.56) relate to chrome spinel plus seam matrix, i.e. feldspar and/or olivine. Uranium concentrations of disseminated grains were similarly found not determinable, in this case due to the low uranium content and small size of the crystals. In the lexan print sample (R.54) however, a large chrome spinel (analysis (2), table 4.25) having a uranium concentration of 19 p.p.b. is seen in close association with a high-uranium phase (zirconolite or zirkelite) and possessing a sieve-like texture with exsolved? silicate phases (section 5.2.4). Both this and another chrome spinel (analysis (1), table 4.25) seen intergrown with ilmenite in a biotite uranium-enriched matrix (section 5.2.3) and within a trapped magma environment, show high TiO_2 and Fe_2O_3 values, table 4.25. Both these grains, like Henderson and Suddaby's (1971) unit 2 grains (table 4.25 analyses (3) and (4)) plot close to the Fe-trend (figure 4.31), and are consistant with Henderson's (1974) interpretation of reaction between chrome spinel and trapped liquid.

A notable feature is that analysis (2) (table 4.25) chrome spinel occurs in unit 9, and from textural considerations (lack of zoning of majority of feldspars), this specimen would be classified as a adcumulate. The fact that a high-uranium phase and a chrome spinel containing a large concentration of Fe_2O_3 and TiO_2 can exist within an adcumulate suggests that pockets of trapped magma can become isolated to such an extent that chemical exchange of material over short distances is totally restricted.

Table 4.2[5]

Analysis Number	(1)	(2)**	(3)+	(4)+	Number of ions on the basis of thirty-two oxygens (1)	(2)	(3)	(4)
Cr_2O_3	26.49	30.94	29.02	24.91	5.89	7.02	6.42.	5.60
Al_2O_3	6.68	4.43	7.60	4.88	2.22	1.50	2.48	1.60
Fe_2O_3*	28.77	24.62	26.96	31.25	6.09	5.29	5.60	6.64
FeO	26.31	29.32	26.70	29.10	6.19	7.05	6.08	6.88
MgO	5.92	4.32	5.08	4.54	2.48	1.85	2.40	1.92
MnO	0.97	0.65	1.11	0.99	0.23	0.15	-	-
TiO_2	4.20	5.08	4.06	5.07	0.89	1.10	0.80	1.12
Total	99.34	99.36	101.33	100.74				

* Fe_2O_3 calculated from total Fe^{2+} assuming stoichiometry.

** Average of four spot analyses (Geoscan microprobe).

+ From Henderson and Suddaby (1971) analyses 1 and 2.

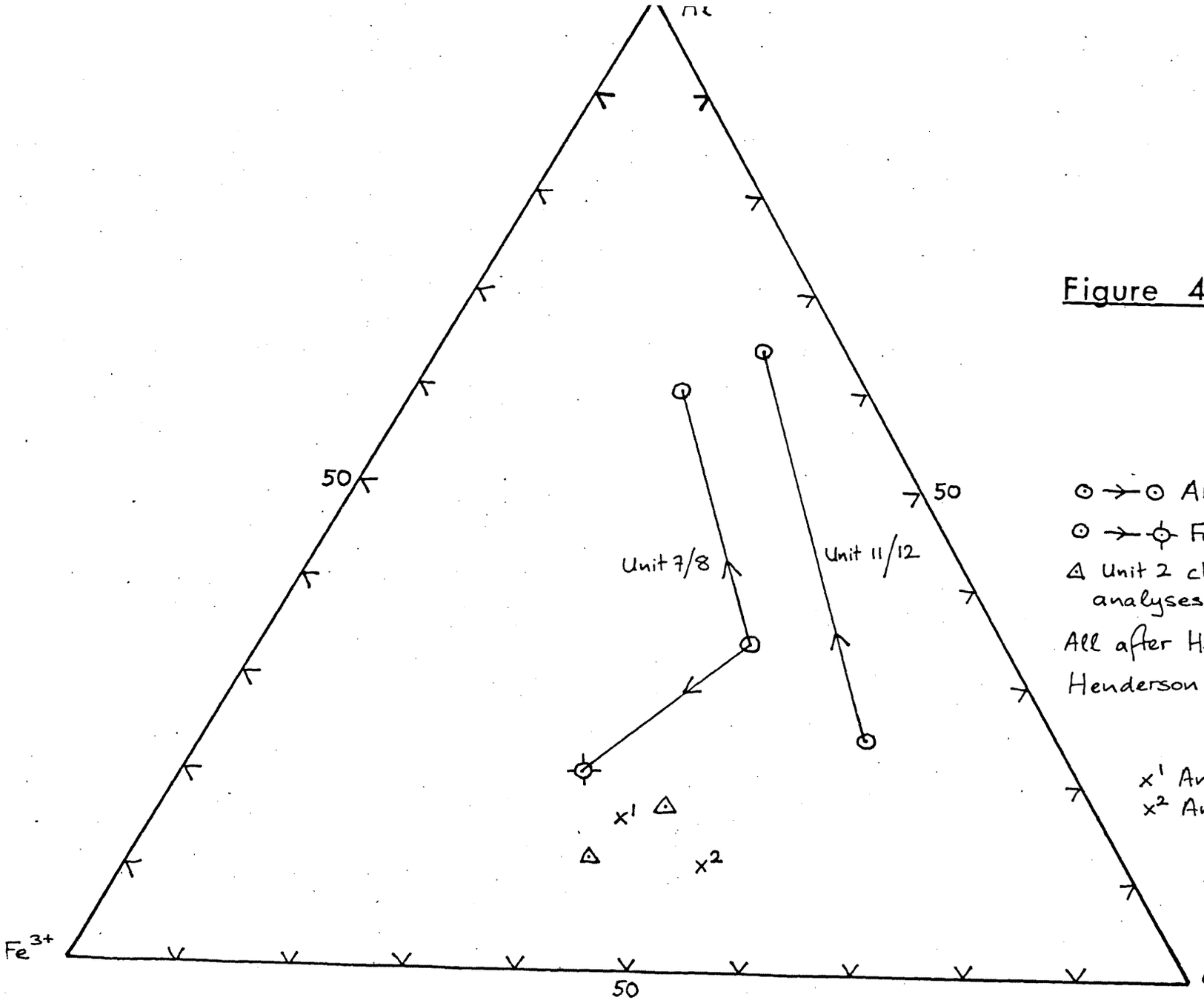

Figure 4.31

⊙→⊙ Al trend

⊙→⊕ Fe trend

△ Unit 2 chrome spinels – analyses (3) and (4), table 4.24

All after Henderson (1974) and Henderson and Suddaby (1971).

x¹ Analysis 1 (table 4.24)

x² Analysis 2 (table 4.24)

CHAPTER 5 THE DISTRIBUTION OF URANIUM WITHIN INTERCUMULUS PHASES.

5.1. Introduction

Although the cumulus phases (i.e. olivine, feldspar, clinopyroxene and chrome spinel) constitute the major proportion of both the Rhum and the Carlingford specimens - usually not less than 95% modal volume - their total contribution to the whole rock uranium concentration is often less than 50%. In table 5.1., an estimation of the contribution of uranium from Group 1 (i.e. cumulus, extremely low-uranium minerals) for an "average" Rhum specimen, i.e. $ol_{50}feld_{30}cpyx_{15}$ chr. $spin._1$ $intercumulus\ minerals_4$, is given. (Intercumulus minerals here is taken to include both primary accessory and alteration minerals).

Table 5.1.

Mineral	Modal %	Average concentration (p.p.b. Uranium)	Contribution to whole rock uranium (p.p.b.)
Olivine	50	6.30	3.15
Feldspar	30	18.96	5.67
Clinopyroxene	15	33.34	4.99
chrome spinel	1	approximately 10	0.1
Total	96		13.91

Thus, for average whole rock uranium concentrations of approximately 40 p.p.b. (e.g. Henderson et al., 1971), the proportion of uranium from the 4% modal volume of intercumulus phases is approximately 65%. This crude estimation is included to show that a very significant amount of uranium is distributed in only a few modal % of rock which is, in fact,

represented by a wide and varied range of minerals. On the basis of the uranium concentrations within these various minerals, a further three-fold grouping may be derived, Group 1 having been previously described in sections 4.3. to 4.7.

Group 2 - low-uranium phases (uranium concentrations from 0.1 to 10 p.p.m.) represented by minerals such as ilmenite, magnetite and biotite.

Group 3 - medium-uranium phases (10 to 100 p.p.m. uranium), e.g. apatite.

Group 4 - high-uranium phases (greater than 100 p.p.m. uranium) represented by minerals such as baddeyelite, zirconolite (or zirkelite) and zircon.

This chapter describes the above groups, and discusses the behaviour of uranium in the late-stage (intercumulus) crystallisation of the Rhum magma.

5.2. Group 2 minerals.

This section describes minerals containing uranium concentrations ranging from 0.1 to 10 p.p.m. After the Group 1 minerals (i.e. the cumulus minerals described in chapter 4), minerals from this group constitutes the second highest modal percentage of minerals from the Rhum cumulates. Minerals from this group are in all cases intercumulus and/or alteration products into which uranium enters in varying amounts.

5.2.1. "Hydrothermal" minerals.

In a locally trapped magma environment small amounts of water-enriched fractionated liquid can become isolated and crystallise as either late-stage minerals, or react with original cumulus crystals to produce hydrothermal alteration minerals. The manner is which interstitial liquid becomes trapped has been discussed by Wager *et al.* (1960) who suggested that crystal

accumulation on top of pre-existing cumulus layers occurred at a more rapid rate than material could diffuse away from the interstices of the settled crystals. An additional mechanism is proposed here (section 5.2.5) and depends mainly upon irregularities in crystal shapes to provide suitably shaped pockets wherein trapping can occur.

Minerals which have crystallised directly from the final dregs of the intercumulus liquid often contain relatively large concentrations of uranium and have partition coefficients (for uranium) greater than unity. These minerals are discussed in sections 5.3. and 5.4., and are invariably found associated with areas of hydrothermal minerals.

Hydrothermal minerals are those minerals which have been formed by reaction between the trapped intercumulus (water-enriched) liquid and earlier cumulus minerals (the magma having passed from the magmatic to the hydrothermal stage - Wager and Brown, 1968, p.52).

Clearly, the possibility exists that such hydrothermal minerals may have formed after consolidation of the intrusion by introduction of water-enriched liquid from an external source. However, several features tend to support a primary alteration genesis. Firstly, the heterogeneous distribution of alteration areas within both thin sections and the intrusion as a whole. In thin section, areas of fairly intense alteration are often located only a few millimetres from fresh, unaltered olivine, feldspar and clinopyroxene crystals. Although the frequency of alteration areas decreases with height in the intrusion, there occur randomly scattered areas of relatively high alteration (i.e. greater than 5 percent) in upper units, and conversely, areas of relatively low alteration (i.e. less

than 2 percent) in the lower units. Secondly, there is the correlation of hydrothermal areas with certain of the olivine morphologies. In the more irregularly-shaped olivines, i.e. irregular, tabular and harrisitic morphologies, hydrothermal areas appear more frequently than in rocks consisting mainly of poikilitic and rounded olivine morphologies. (This feature is discussed more fully in section 5.2.5.). Thirdly, there is the apparent rarity of serpentine minerals (sensu stricto) such as antigorite, chrysotile and lizardite.

In the Rhum cumulates, a frequently occurring hydrothermal mineral assemblage is one of apatite, chlorite, uralite and biotite. Often, only three of these minerals are seen in any one area.

Apatite, chlorite, uralite assemblage. Here, an inner core of a Al-rich (Ca-poor) mineral, identified optically as chlorite is seen surrounded by an outer rim of a Ca-rich (Al-poor) fibrous amphibole, probably tremolite, but given here the general name uralite (e.g. Deer, et al., 1971), with apatite often occurring at the chlorite/uralite junction. A striking example of this is shown in plate 5.1. (a) to (b), where the apatite forms a semi-circular rim (picked out by the uranium-distribution map) separating the internal core of chlorite from the outer rim of uralite. In this specimen from a harrisite sample (H.2.), a three-dimensional view was possible since specimen H.5. was cut parallel to H.2. and approximately 10 millimetres above it (see figure 4.18). The area of H.5. corresponding to the hydrothermal alteration of H.2. consists of sodic plagioclase (approximately An_{58}). Thus, a situation similar to that proposed for olivine holes (section 5.2.5.) is considered to have arisen, whereby crystallisation of feldspar

PLATE 5.1a

·5 mm.

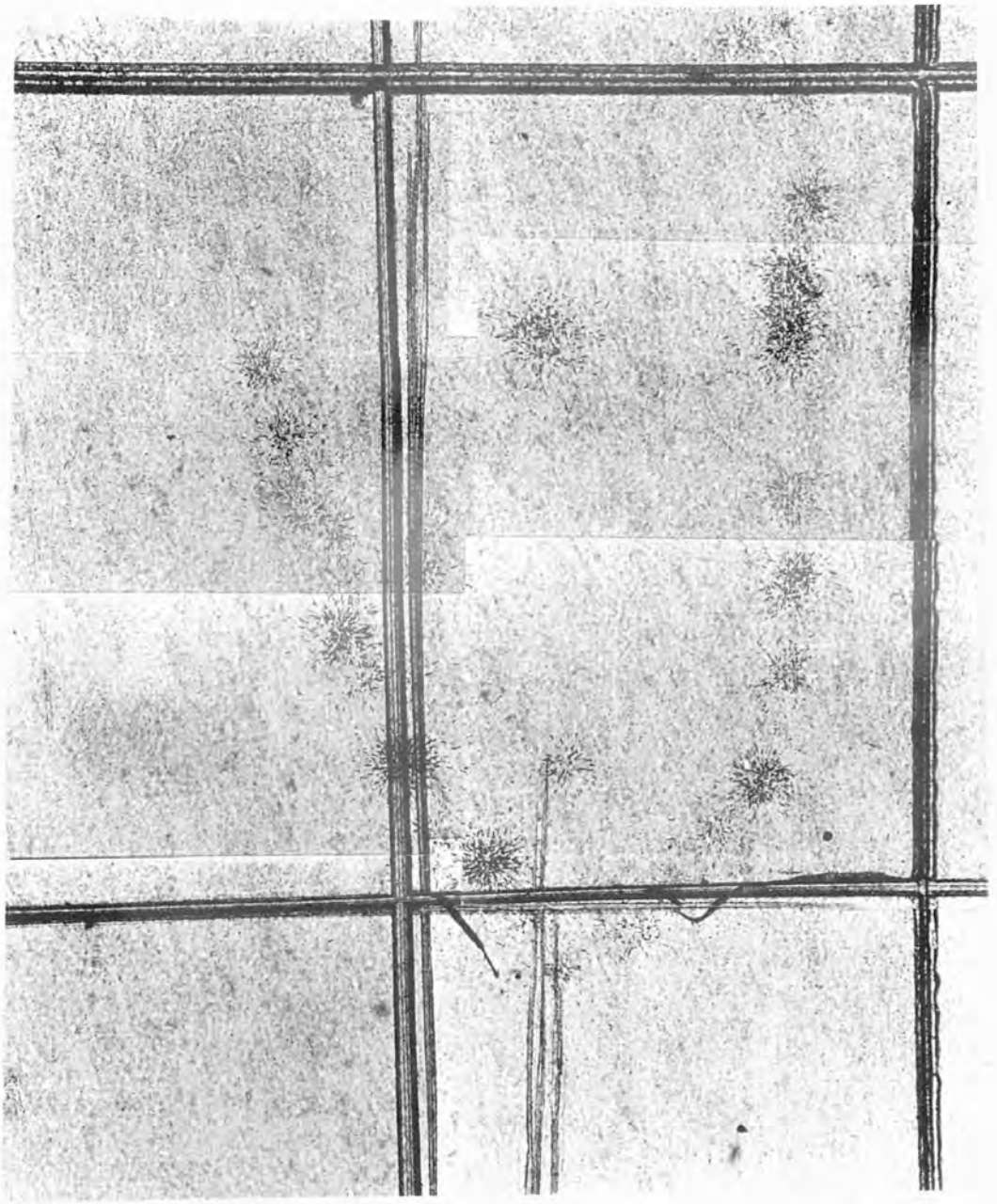

PLATE 5.1 b

·5 mm.

into a hollow created by an irregularity in the olivine crystal shape trapped the interstitial magma. Reaction of the trapped liquid with feldspar, olivine and any primary clinopyroxene present would produce the chlorite/uralite assembly. The excess phosphorus in the locally fractionated liquid forming apatite.

Apatite, uralite, biotite assemblage. This assemblage is shown in plate 5.2. (a) to (f). By comparing the uranium-distribution map with K, Ca and P elemental scans (using the Scanning Electron Microscope), the distribution of uranium between these minerals can be obtained. Uranium enters apatite (80 ± 5 p.p.m.) preferentially to uralite ($0.40 \pm .03$ p.p.m.) and biotite ($0.1 \pm .03$ p.p.m.).

Chlorite, uralite, biotite assemblage. This is shown in plate 5.3. (a) to (f), Chlorite is located from the Al-scan, uralite from the Ca-scan and mica (probably biotite) from the K-scan. Uranium is found essentially only in the uralite phase where a concentration of $0.31 \pm .03$ p.p.m. was determined. Chlorite and biotite contain less than 0.1 p.p.m. uranium.

Rice and Bowie (1971) were able to determine the modal percentage of mesostasis present in a rock from fission track analysis of thin sections in a similar manner to Henderson et al. (1971) who used however, whole rock uranium concentrations. In table 5.2. below, an estimation of the amount of uranium per unit area of mesostasis is given for the three examples above. From this it can been seen that the amount of uranium per unit area of mesostasis varies considerably, and depends to a great extent on the proportion of apatite present. This would indicate that calculation of the mesostasis using fission track analysis is likely to be less accurate than using whole rock concentrations. The reason being that owing to the heterogeneous distribution of the mesostasis and the

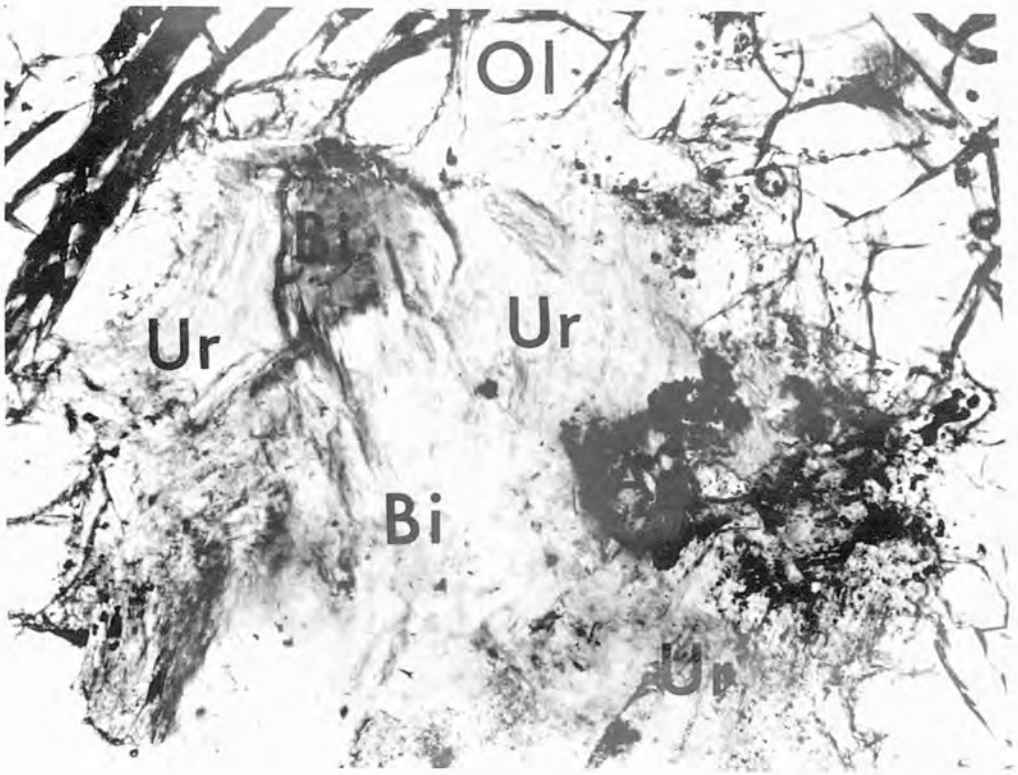

PLATE 5.2 a

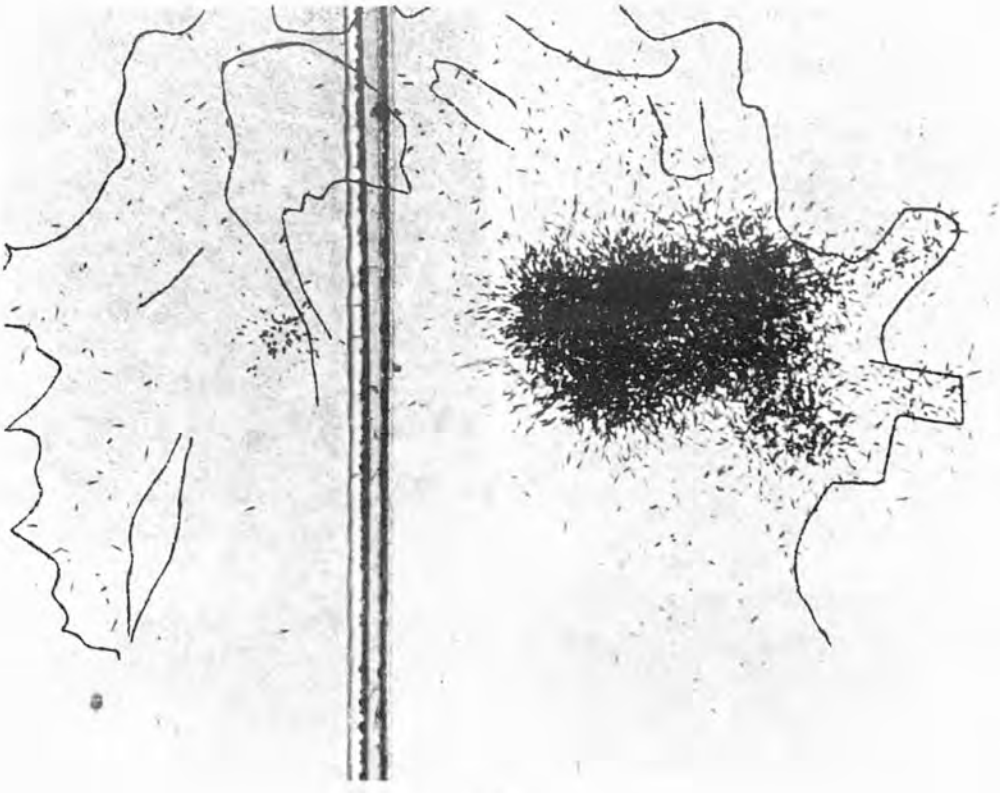

b

·2 mm.

c

d

Ca

e

P

f

Al

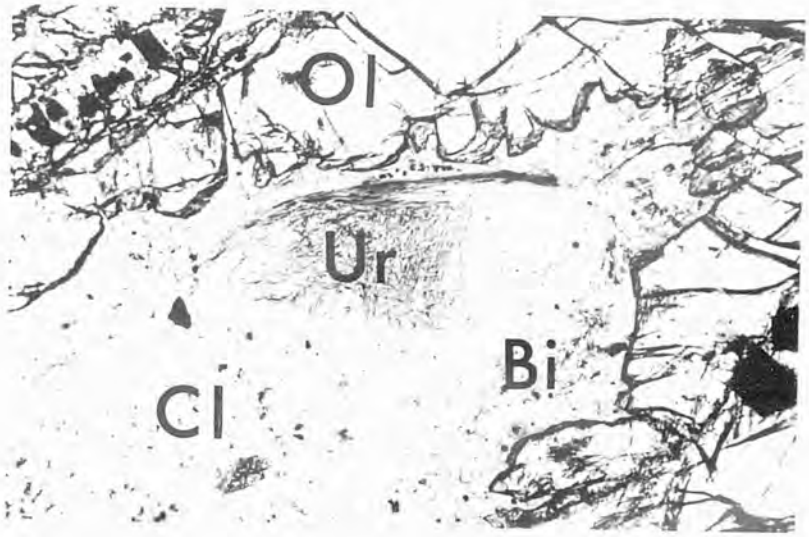

a

·3 mm

PLATE 5.3

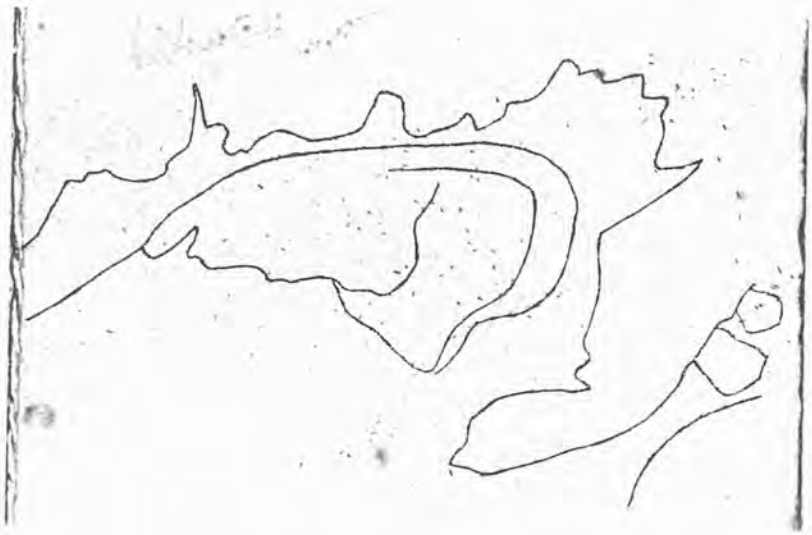

b

c

·3 mm.

d

Ca

e

Al

f

K

large concentration of uranium bound up in a small volume of apatite a thin section would not be representative of the whole rock.

Table 5.2.

	Uralite		Chlorite		Biotite		Apatite	
	Uranium (p.p.m)	modal percentage	Uranium (p.p.m.)	modal percentage	Uranium (p.p.m.)	modal percentage	Uranium (p.p.m.)	modal percentage*
Plate 5.1.	0.3.	65	0.1	33	absent		74± 2	2
Plate 5.2.	0.4	20	absent		0.1	68	80± 5	12
Plate 5.3.	0.3.	28	0.1	64	0.1	8	absent	
Average Uranium	0.38		0.13		0.15		75	
Range	0.31 to 0.46		0.08 to 0.74		0.07 to 0.21		21 to 100	

	p.p.m. uranium per unit area of mesostasis
Plate 5.1.	1.7
Plate 5.2.	10.3
Plate 5.3.	0.16

5.2.2. Magnetite

Magnetite occurs sporadically distributed throughout the intrusion usually having an anhedral crystal shape and associated with late-stage, intercumulus minerals such as chlorite and biotite. The uranium concentrations of the majority of the crystals were difficult to determine owing to their small size (usually less than 0.1 millimetre diameter) and close proximity to associated hydrothermal minerals, but where calculated, varied from approximately 0.2 p.p.m. to (exceptionally) 32 p.p.m. Unfortunately, quantitative analyses of magnetites with differing uranium concentrations were not determined,

however, qualitatively (using the Jeol 50 S.E.M.), they contained essentially only Fe with minor amounts of Ti (less than 5 percent TiO_2) and Cr (less than 2 percent Cr_2O_3).

In a specimen from unit 5, $R.84^A$ (containing cumulus olivine, heteradcumulus zoned feldspar and heteradcumulus clinopyroxene), amagnetite crystal containing 31.8 p.p.m. uranium is seen in association with chlorapatite ($>$ 50 p.p.m. uranium), ilmenite (35.0 p.p.m. uranium) and biotite almost completely enclosed within a branching (or "cup-shaped") olivine. (The uranium concentration of the olivines from $R.84^A$ is 6.74 p.p.b. which in terms of morphological grouping (section 4.3.) classifies them as belonging to the irregular or tabular morphologies.) Plates 5.4 (a) to (c) show the spatial distribution of these minerals and their relationship to the branching olivine, and a noteworthy feature is the plagioclase feldspar which is seen to be normally zoned towards the join of the branches. The significance of this feature, and the fact that the uranium-enriched phases occur also at the join of the branches is discussed below in section 5.2.5. S.E.M. pictures (plate 5.5. (a) to (f)) show the distribution of the minerals apatite (Ca and P phase); ilmenite (Fe and Ti phase); biotite (Al phase) and magnetite (Fe (-Ti) phase), and by comparison with plates 5.4. (b) and (c) (mirror image), the uranium distribution of these minerals can clearly be seen. Their uranium concentrations are given below in table 5.3.

Occasionally, intercumulus magnetite is developed to an extent whereby it poikilitically (in an intercumulus manner) encloses cumulus plagioclase feldspar. Although the poikilitic or sub-poikilitic behaviour of the magnetite appears to develop to a greater extent in the feldspar cumulates of the

PLATE 5.4 (a)

0·5 mm.

Branching or "cup-shaped" olivine with plagioclase feldspar zoned towards the join in the direction of the arrow. The boxed area is shown in plate 5.4 (b) and (c).

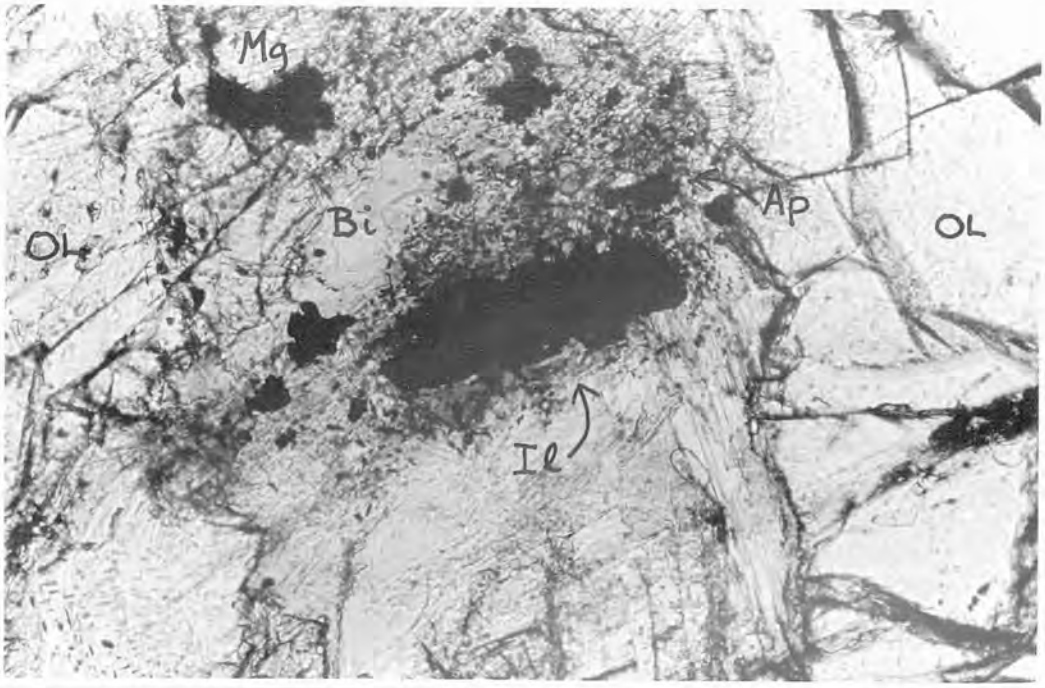

PLATE 5.4 (b)

Magnetite (Mg); apatite (Ap); ilmenite (Il) and biotite (Bi) within a "cup-shaped" olivine (Ol).

0·1 mm.

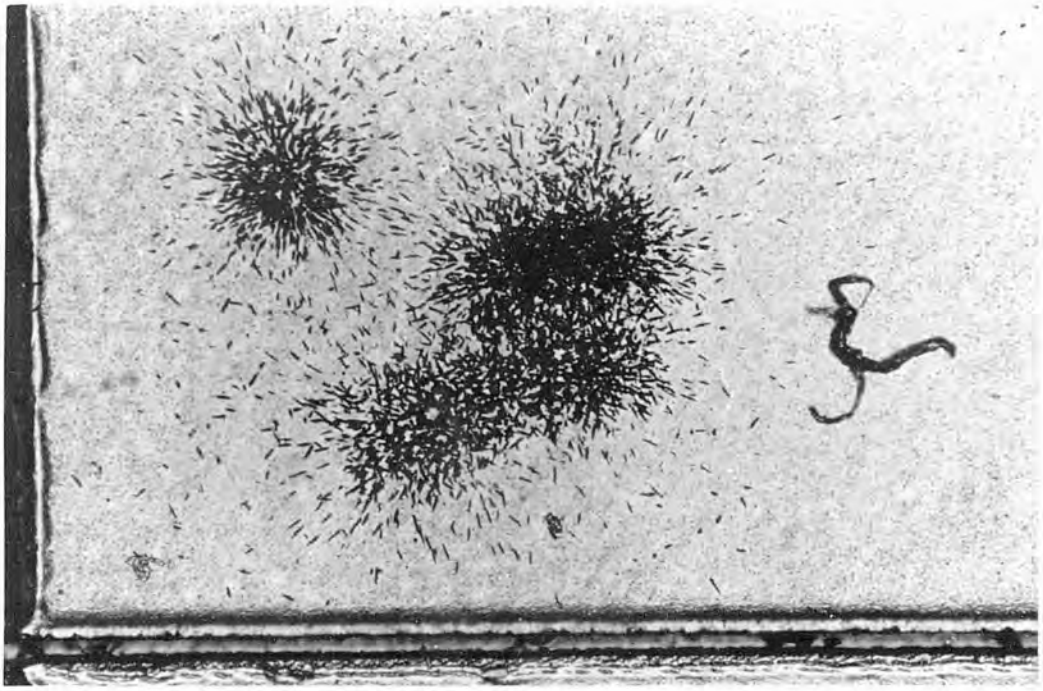

PLATE 5.4 (c)

Uranium-distribution of same area.

PLATE 5.5a

·2 mm.

b

Ca

c

P

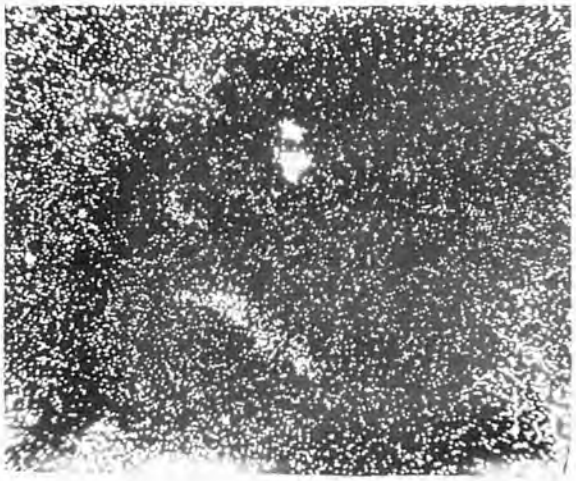

d
Fe

·2 mm.

e
Ti

f
Al

lower units, where the feldspar phase is extensively zoned, it was also observed as high as unit 7. Its occurrence and poikilitic habit within layered intrusions is well documented, e.g. Wager and Brown (1968, figures 32-34) for the Skaergaard intrusion, and Elsdon (1972, figure 1) for the Upper Layered Series, Kap Edvard Holm. Qualitative microprobe analyses (Jeol 50), indicates that essentially only Fe is present with minor amounts of TiO_2 (less than five percent) - S.E.M. pictures plates (5.6. (a), (b) and (c)).

Table 5.3.

Mineral	Uranium concentration (p.p.m.) ± 0.3 p.p.m.
Apatite	50
Ilmenite	35.0
Magnetite	31.8
Biotite *	approximately 0.5

* Uncertain due to interference and overlap of tracks from the other phases.

Uranium-distribution (contact print) maps of intercumulus magnetite show the absence of any uranium gradient, the uranium concentration averaging (for R.121) 243 p.p.b. (table 5.4.). The uranium concentrations of magnetites from layered intrusions have not previously been studied, and a literature search did not yield any data on uranium contents within magnetites.

5.2.3. Ilmenite

Ilmenite occurs throughout the Rhum intrusion as a minor constituent. In general, only two or three grains within any thin section are present, the ilmenite usually having an

PLATE 5.6. (magnetite R.121)

(a) S.E.I.

1mm.

(b) Fe

(c) Ti

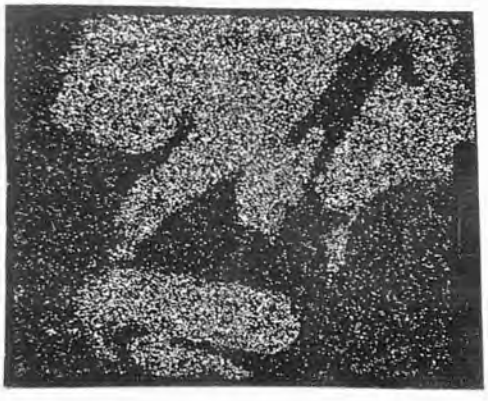

(d) Al

Table 5.4. (Specimen R.121)

Position *	Number tracks centimetre^{-2} ($X10^5$)	Uranium p.p.b.
A5B, A3C	1.3130	203
A4B, A15C	1.3271	254
A10B, A12C	1,3352	271

* On contact print grid.

anhedral shape but displaying a wide range in size - from 0.05 millimetres to 0.2 millimetres. Unlike magnetite, the association of ilmenite with hydrothermal minerals was not so obvious. Like magnetite however, the uranium concentration varied, ranging from 0.13 p.p.m. to 38 p.p.m. Two factors appear to be responsible for this range.

1) The larger the grain size, the lower the uranium concentration.

2) Where ilmenite occurs associated with late-stage intercumulus minerals such as apatite and biotite, the uranium concentration appears to be higher than where no association is apparent.

Uranium concentrations of some ilmenites are given below in table 5.5., compositions in table 5.6.

An inverse relationship between grain size and uranium concentration was observed by Thiel et al. (1972) for ilmenites in lunar basalts. This they considered to be the result of interplay between several factors. The rise in uranium concentration they suggested resulted from an increase in the uranium content of the residual magma as solidification proceeded. The decrease in grain size they suggested was due to an increase in the number of nuclei formed at increased rates

of cooling - the presence of interstitial glass appearing to support this. On Rhum however, interstitial glass was not observed, and the increase in uranium concentration within the Rhum ilmenites is considered to be either a function of an increase in the uranium content of residual magma, or, analogous with the cumulus phases, an increase in the rate of crystal growth.

From textural considerations, analyses (4) and (5) (table 5.5.) represent ilmenites having crystallised from a trapped magma, since on both these occasions, normal zoning of feldspars within "cup-shaped" olivines was observed. (Plate 5.1 is of ilmenite number (4), and plate 5.4. is of ilmenite number (5)). In addition, the trapped magma environment of these ilmenites, has not apparently crystallised high-uranium phases such as baddeyelite or zirconolite (section 5.4.), which would have removed a large proportion of the uranium from the late crystallising magma.

An apparently unique situation was observed in an ilmenite (analysis 2, tables 5.5. and 5.6.) within an olivine-cumulate of unit 6. The specimen (R.82) was collected at the base of this unit and mineralogically consists of equant olivines poikilitically enclosed by heteradcumulus feldspar and clinopyroxene. The uranium-distribution map shows the existence of a pronounced uranium gradient within an anhedral ilmenite (Plate 5.7. (a), (b)). Area counts of 120 μm x 120 μm at X400 magnification were performed in a grid pattern covering the whole of the ilmenite grain. Similar sized area counts were performed on two standards (S.R.M. 614 and "Geoscan"), and an accuracy of $\pm$ 5 percent for each area count was obtained. Figure (5.1) shows the uranium distribution in terms of a contour map, and

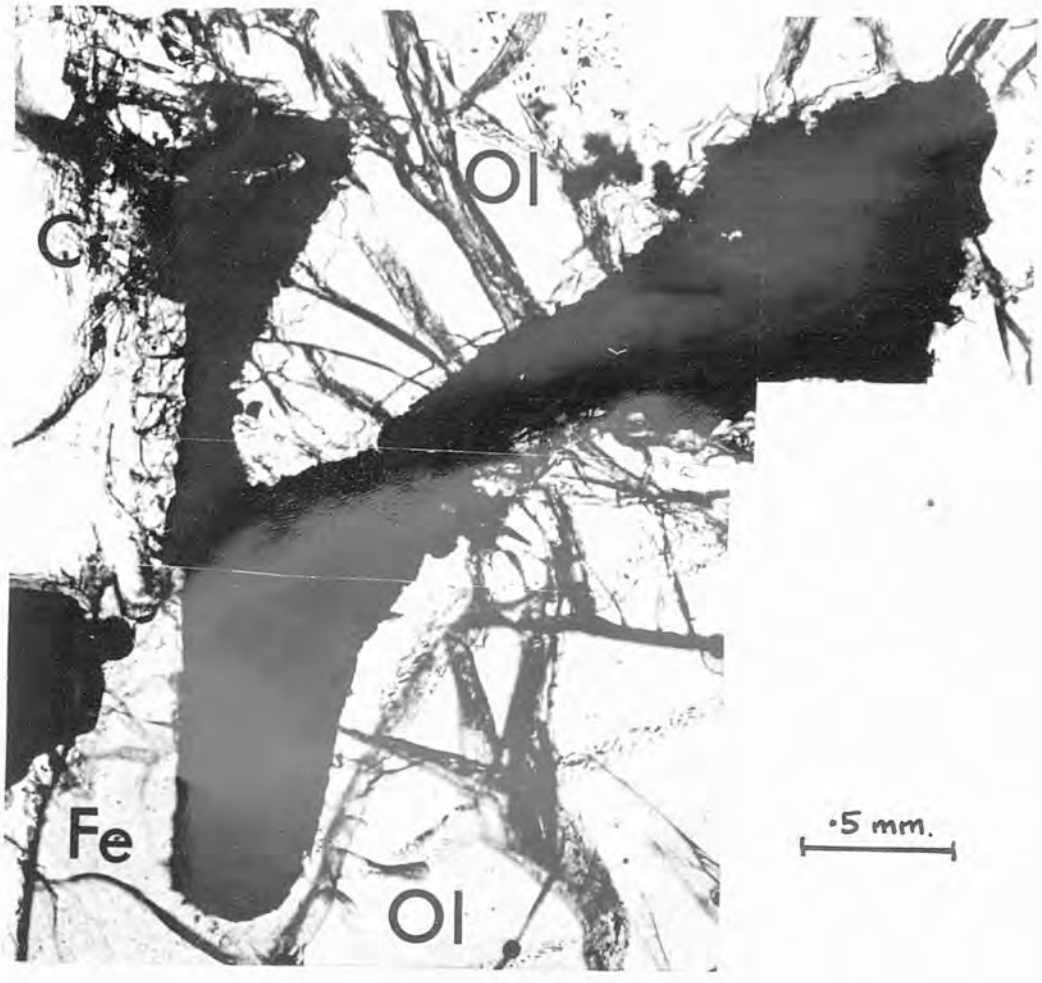

PLATE 5.7(a) Anhedral ilmenite grain surrounded by olivine, Ol, and plagioclase feldspar, Fe, and partially enclosing a euhedral chrome spinel grain, Cr.

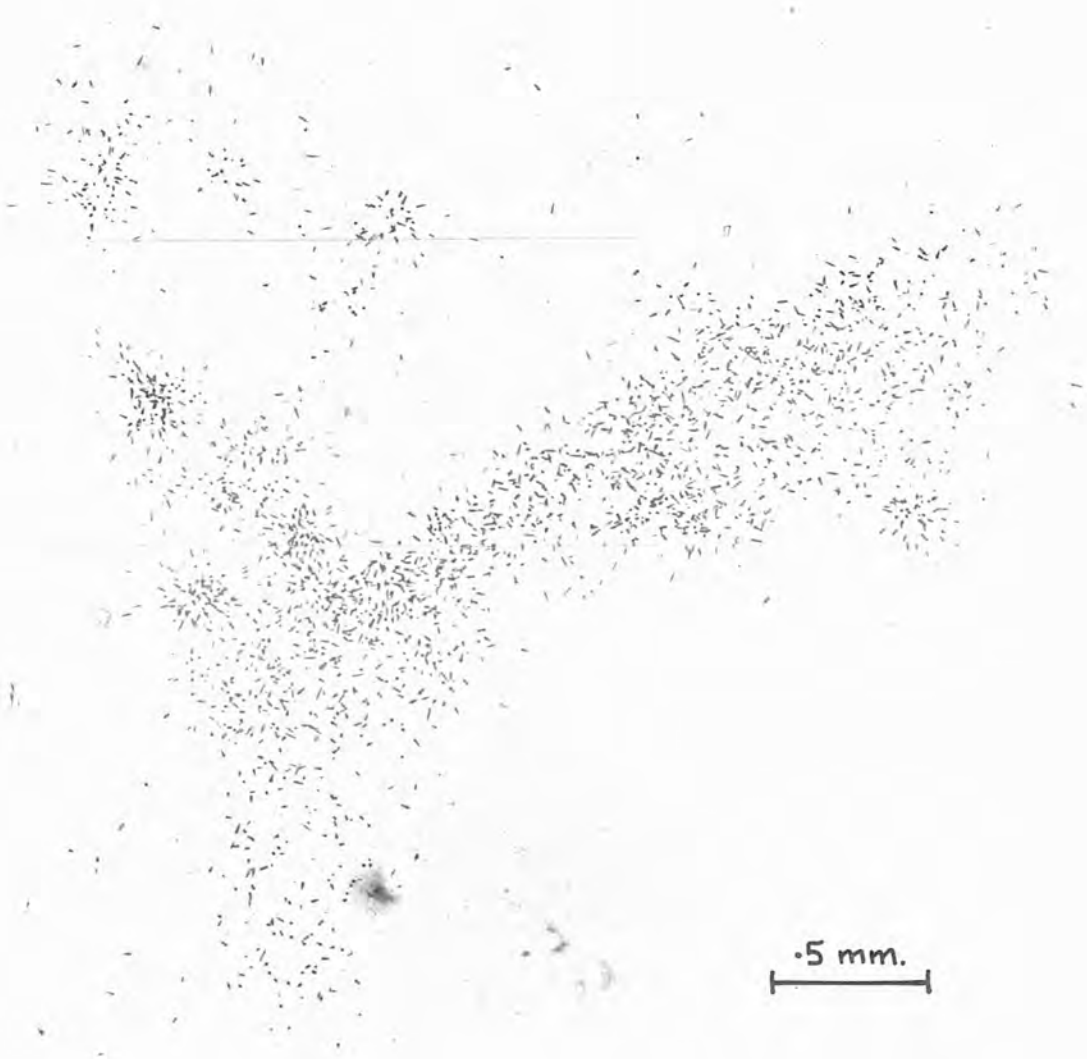

PLATE 5.7(b) Uranium distribution map

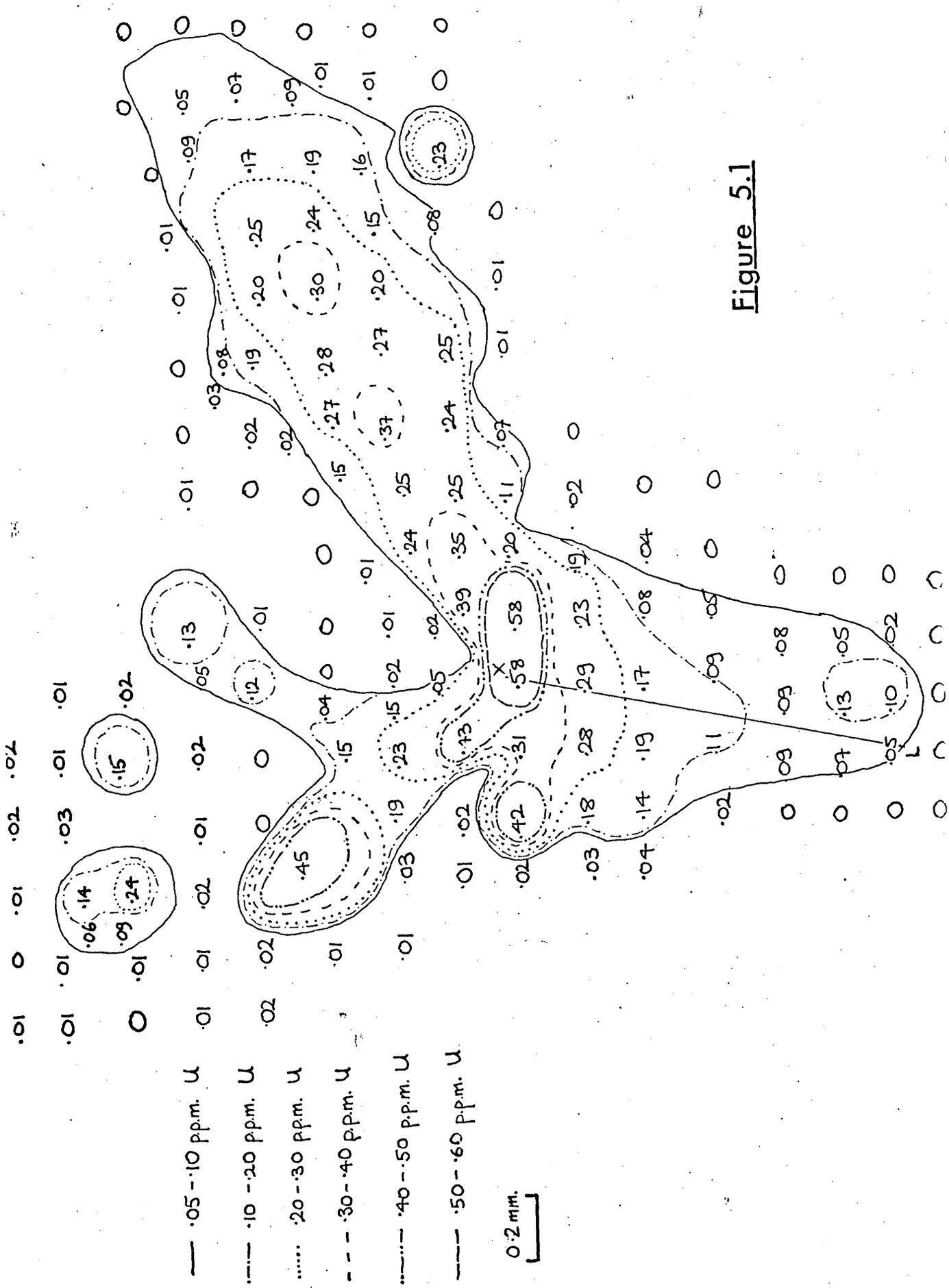
.05 - .10 p.p.m. U
.10 - .20 p.p.m. U
.20 - .30 p.p.m. U
.30 - .40 p.p.m. U
.40 - .50 p.p.m. U
.50 - .60 p.p.m. U
0·2 mm.

Figure 5.1

from this, it can be seen that the uranium concentration varies from .05 to .58 p.p.m. in a uniform profile (figure 5.2.). Using the Cambridge Geoscan, a microprobe traverse across the ilmenite grain covering 16 spot analyses was made, but no major or minor element zoning was detected. The range and average of these analyses are given in table 5.6.

If the natural logarithm of the uranium concentration ($\times 10^{-9}$ wt. %) is plotted against the square of the distance, then with constant growth rate, a straight line should result and the diffusion coefficient (D) may be calculated from the equation (after Matousek, 1970).

$$D = \frac{1}{4kt} \qquad (20)$$

where k = slope of the graph

t = time (seconds)

A plot of ln (concentration) against $(\text{distance})^2$ shows, overall, a large deviation from a straight line (figure 5.3.). If it is assumed that the diffusion coefficient of uranium remains constant, then figure (5.3.) can be interpreted as either a change in growth rate with time (t) or, an increse in the uranium content of the residual magma. The former interpretation is preferred in this instance because of the large grain size and low manganese content of the ilmenite (see discussion below).

An estimation of the rates of growth can be obtained by taking tangents to the curve at the two extremes (i.e. lines X - Y and K - L, figure 5.3.), substituting these into equation (20) and rearranging such that

$$t = \frac{1}{4kD} \qquad (21)$$

Then, assuming D remains constant and has the value 6×10^{-9} centimetres^2. second^{-1} (chapter 4, section 4.4), growth rates of 1.4×10^{-3} millimetres. day^{-1} (for the lower uranium portion

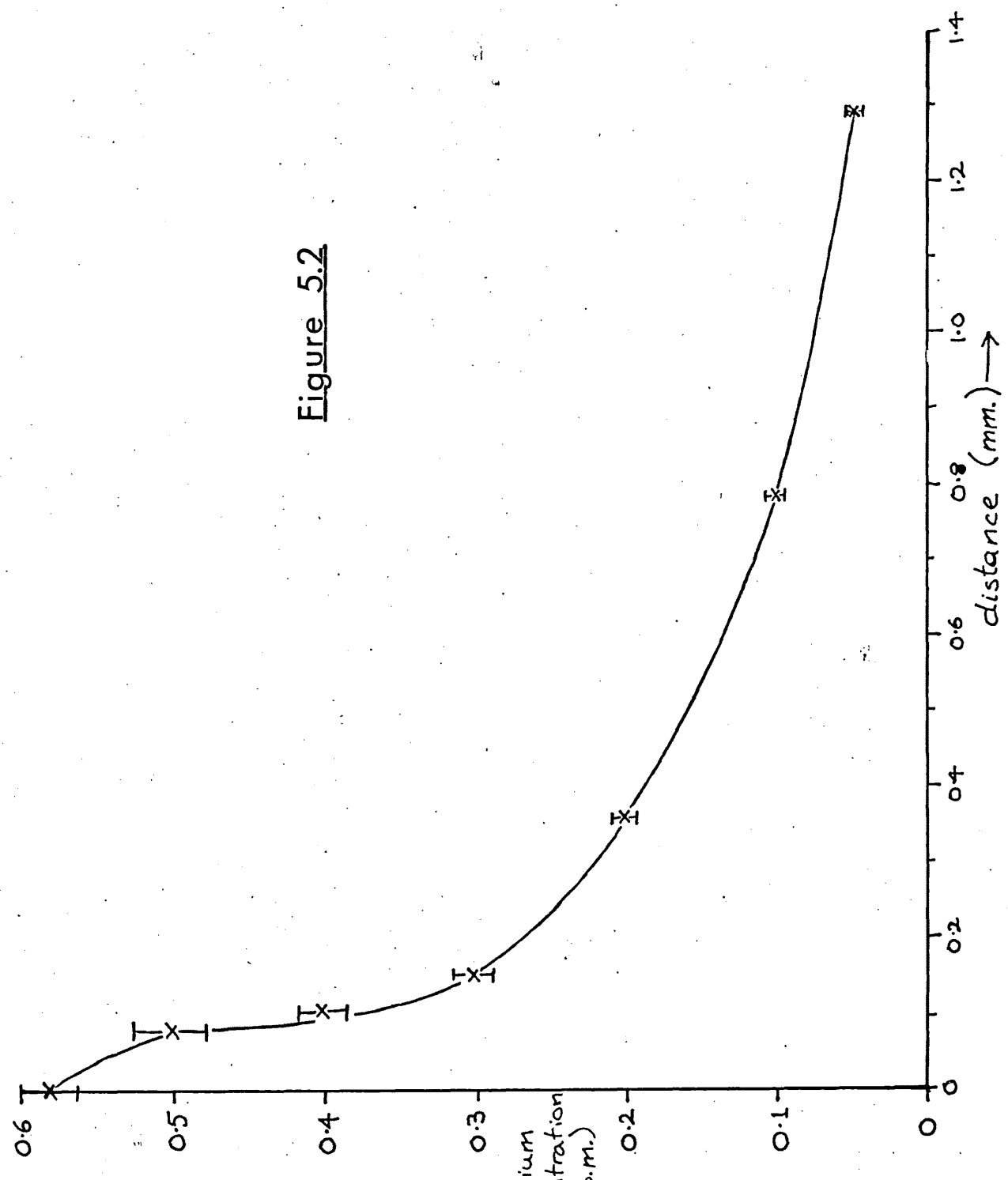
0·6
0·5
0·4
0·3
0·2
0·1
0
Uranium concentration (p.p.m.)
0
0·2
0·4
0·6
0·8
1·0
1·2
1·4
distance (mm.)

Figure 5.2

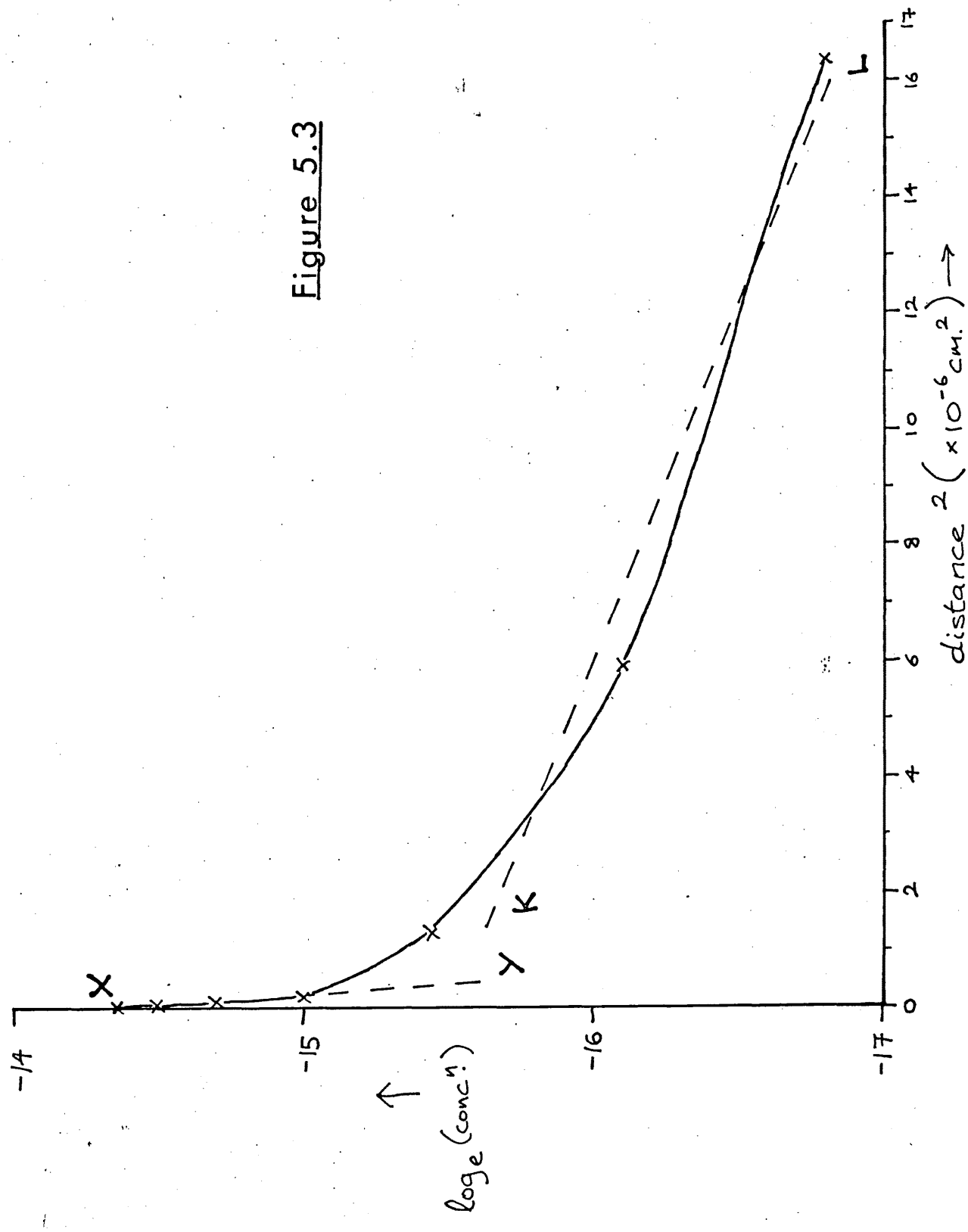
X
Y
K
L
-14
-15
-16
-17
0
2
4
6
8
10
12
14
16
17
log e (conc^n)
distance 2 (×10^-6 cm.^2)

Figure 5.3

Figure 5.4

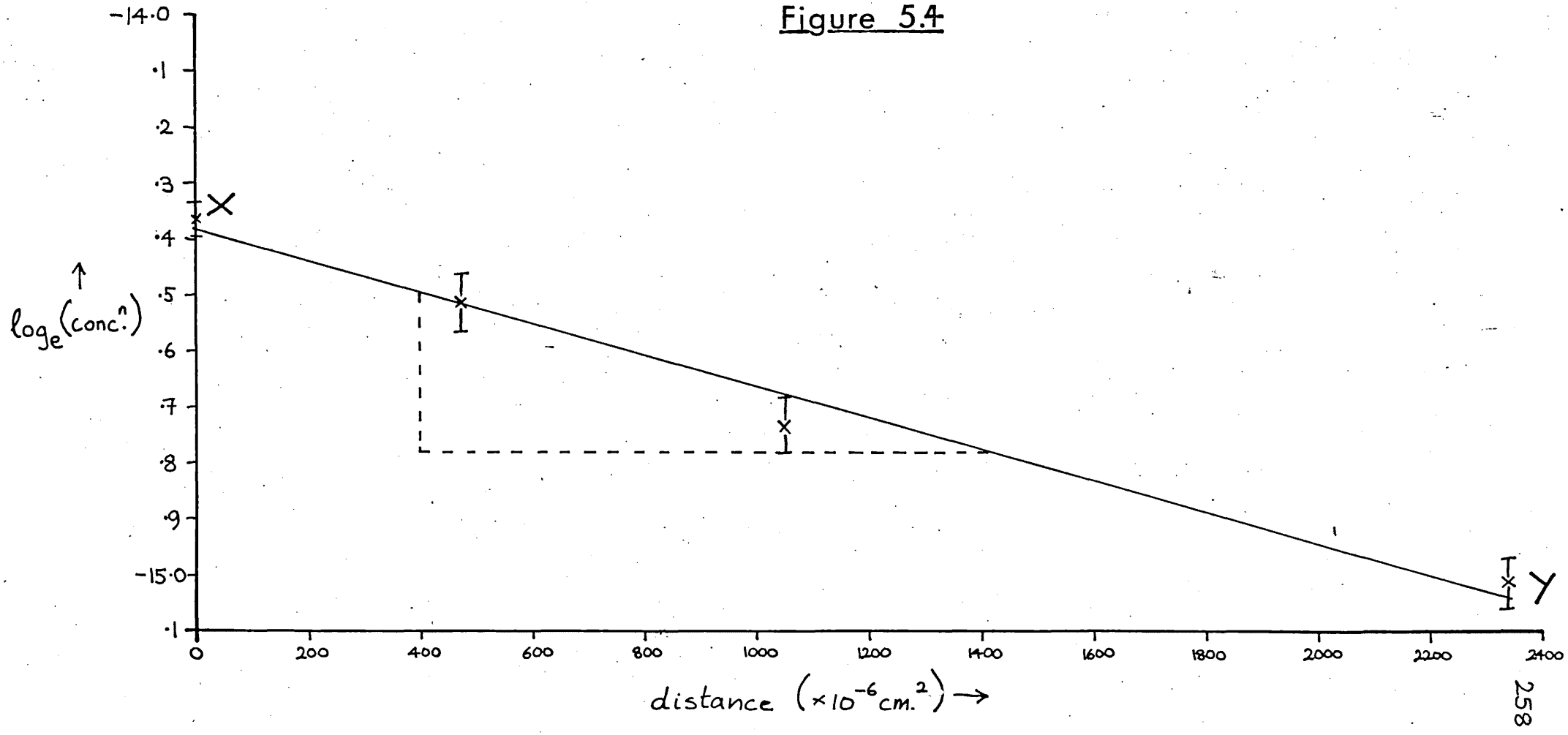
-14·0
·1
·2
·3
·4
·5
·6
·7
·8
·9
-15·0
·1
$\log_e$(conc.n)
X
Y
0
200
400
600
800
1000
1200
1400
1600
1800
2000
2200
2400
distance ($\times 10^{-6}$ cm.^{2}) →

of the grain) and $1{\cdot}03 \times 10^{-2}$ millimetres day^{-1} (for the higher uranium portion, figure 5.4) are obtained. Thus, with an increase in uranium concentration, an order of magnitude increase in the growth rate is observed.

Also within specimen R.82 1a an ilmenite/chromite intergrowth surrounded by a rim of a pale-brown, slightly pleochroic mineral (plate 5.8 (a) to (e)). Qualitative microprobe analysis (Jeol 50) shows this latter mineral to contain the major elements K, Ti, Fe and Si, and minor elements Mg and Al - thus indicating the mineral to be a mica. Microprobe analysis of the two opaque minerals (Cambridge Geoscan) are given in table 5.6. (ilmenite analysis number 3, chromite analysis number 6). The high Fe and Ti content of the chromite indicates (Henderson and Suddaby, 1971) that some post-depositional reaction with the residual magma had occurred, the uranium content of the ilmenite and the presence of surrounding biotite (?) tends to support this.

A noteworthy feature of the ilmenites analysed was their surprisingly high MgO content (average 8.79) Mitchell (1973) notes that ilmenites with MgO concentration of this order in igneous rocks appear to be uniquely confined to kimberlites, and are in fact regarded as a typical kimberlite mineral. Lovering and Widdowson (1968) in reviewing the MgO content in ilmenites for a variety of petrological environments, found that in basic igneous rocks (e.g. Skaergaard) MgO varied from 0.46 to 3.27 percent; for inclusions in basic pipes, MgO ranged from 3.8 to 4.5 percent, and in kimberlites from 7 to 12 percent. In the light of these observations, several ilmenites were reanalysed using the Jeol 50 S.E.M., the results being corrected for fluorescence, atomic number and absorption effects. These analyses (averaged in table 5.8. analysis

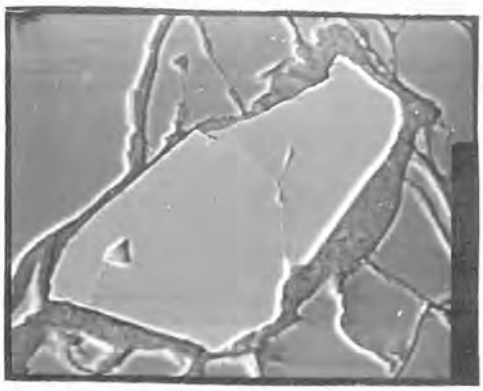

PLATE 5.8.

(a) S.E.I.

0·5 mm.

(b) Ti

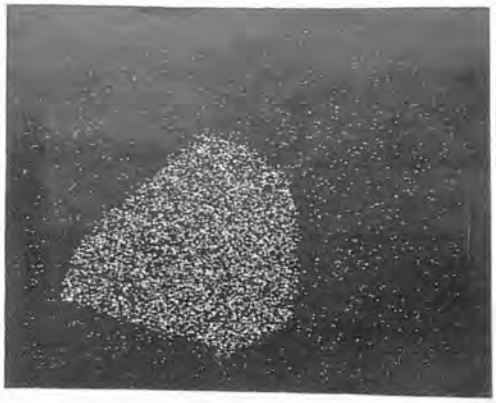

(c) Cr

(d) K

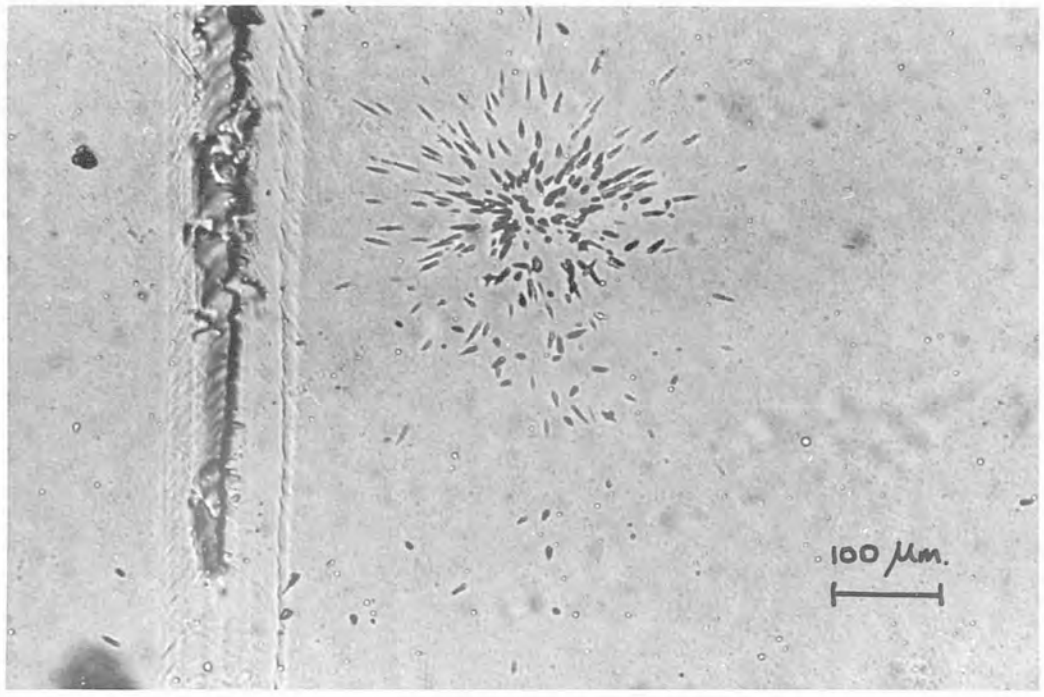

PLATE 5.8 (e)

Uranium distribution map of area from Plate 5.8 (a) to (d). The fission track star apparently corresponds to an area within the K-rich mineral.

number 7) show that the high MgO concentration in the Rhum ilmenites to be real. At present no explanation of this feature is offered.

Another observation was the substitution of MnO for MgO in the high-uranium ilmenite (number 5, table 5.5. and 5.6.). Czamanske and Milralik (1972) suggest that such manganoan ilmenites may have crystallised from a residual magma enriched in Mn relative to Fe. Such an interpretation appears likely in this case. It is hoped however, that future work on the opaque Fe - Ti phases of Rhum will be possible, and that a more comprehensive picture can be obtained.

Table 5.5.

Ilmenite Grain Number	Rock and area (contact print)	Approximate grain area ($millimetres^2$)	Associated Minerals	Uranium p.p.m.
1	H.1 A11B, A4C	.08	olivine, feldspar	$0.13 \pm .03$
2	R.82 A6B, A22C	.06	olivine, feldspar	.05 to .58
3	R.82 A3B, A22C	.0025	chromite, biotite(?)	1.68 ± 0.3
4	H.2 A9B, A4C	.0009	apatite,	5.91 ± 0.3
5	R.84A A3B, A5C	.0001	apatite, biotite, magnetite	35.0 ± 0.3

Table 5.6.

Ilmenite Grain Number	1	2	3	4	5	6**	7***
SiO_2	.02	.09 (.04 - .24)	.08	.09	.18	.05	-
TiO_2	52.11	53.71 (51.60 - 55.19)	54.60	51.53	52.91	4.20	55.88
Al_2O_3	.00	.35 (.02 - .75)	.07	.01	.22	6.68	-
Cr_2O_3	.86	.91 (.33 - 1.44)	.36	.27	1.03	26.49	.31
FeO	28.91	35.42 (32.81 - 35.74)	35.26	28.25	39.64	26.31	32.43
Fe_2O_3*	6.85	-	-	8.43	-	28.77	-
MnO	-	.43 (.15 - .69)	.76	.52	5.75	.97	-
MgO	10.01	8.67 (7.81 - 10.35)	8.33	9.91	0.61	5.92	8.79
CaO	-	-	-	.01	-	.00	-
NiO	-	.10 (.00 - .21)	.09	-	.02	-	-
V_2O_3	-	-	-	-	-	-	0.59
Total	98.76*	99.68	99.55	99.01*	100.36	99.39*	98.00

* Fe_2O_3 calculated using Imperial College program AUTOCAL.

** Chromite associated with ilmenite grain number 3.

*** Jeol 50 S.E.M. analyses average of ilmenite grain numbers 2, 3 and 4.

5.2.4. "Poikilitic" chrome spinel.

The final batch of samples irradiated in the Herald reactor at A.W.R.E. (Aldermaston) for fission track analysis provided two significant observations. The first was the production of Lexan prints (see section 2.2.2.), and details of the flux used etc., are given in Appendix 1. The second was an apparently unique situation (to the Rhum cumulates) of a chrome-spinel exhibiting a poikilitic, sieve-like texture. This is shown in plate 5.9 (a), and the uranium distribution map (lexan print) plate 5.9 (b), strikingly shows that uranium is concentrated in the inclusions.

This particular specimen (R.54) is of an olivine cumulate from unit 9, the absence of zoning in the heteradcumulus feldspar and pyroxenes suggesting that much adcumulus growth must have occurred. The chrome spinel described here has an overall equant crystal shape, like other chrome spinels in this specimen (of approximately 1.5 modal percentage). Unlike the other chrome spinels however, it has a concentric ring of roughly spherical inclusions ranging from 10 to 200 microns in diameter. The concentric nature of the inclusions is probably better seen in the Lexan print and in figure 5.5. (drawn from the photomicrograph). Using the Jeol microprobe, no zoning was detected in major elements Fe, Cr, Al, Mg and Ti across the surface of the spinel. Quantitative analysis of four points using the Geoscan microprobe was undertaken, the positions are shown in figure 5.5., and results given in table 5.7.

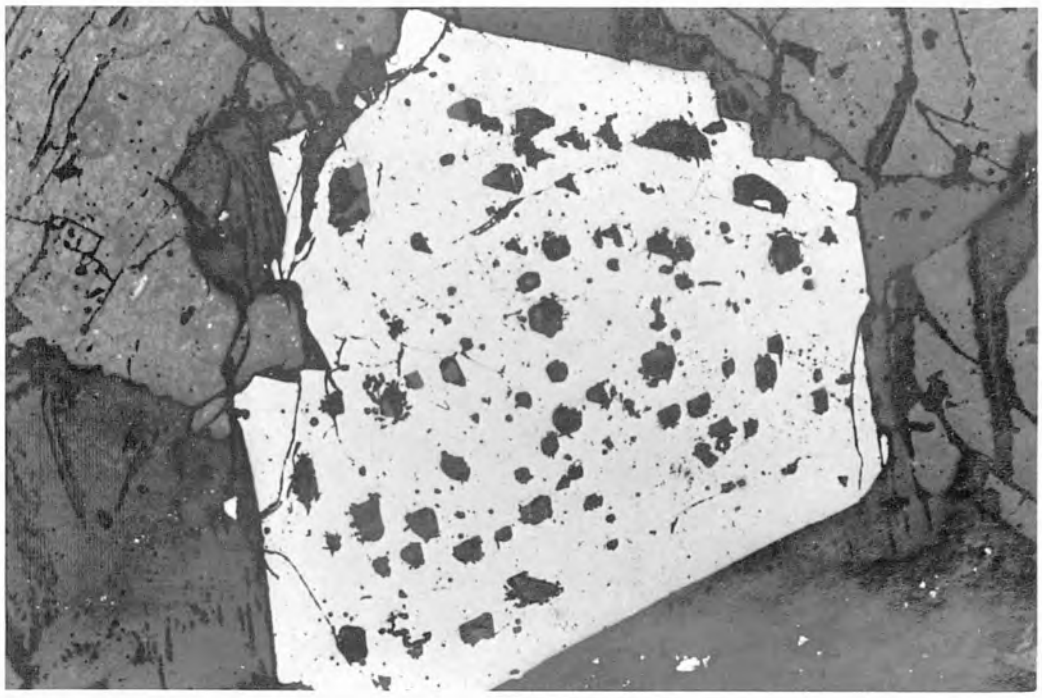

PLATE 5.9 (a)

"Poikilitic" chrome spinel

0·5 mm.

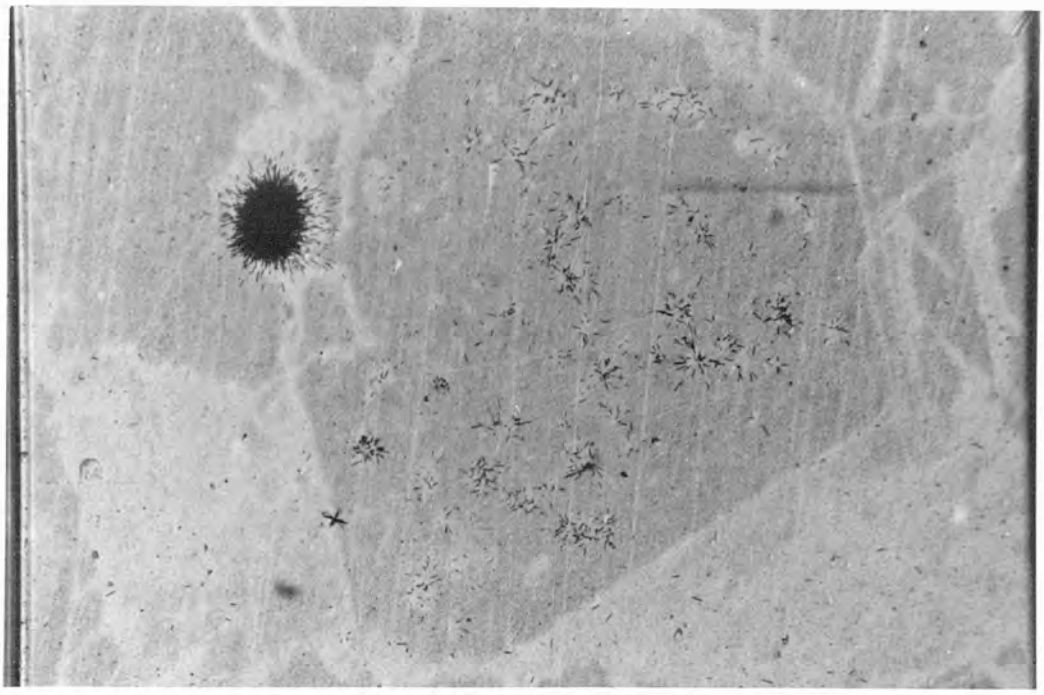

PLATE 5.9 (b)

Lexan print of same area

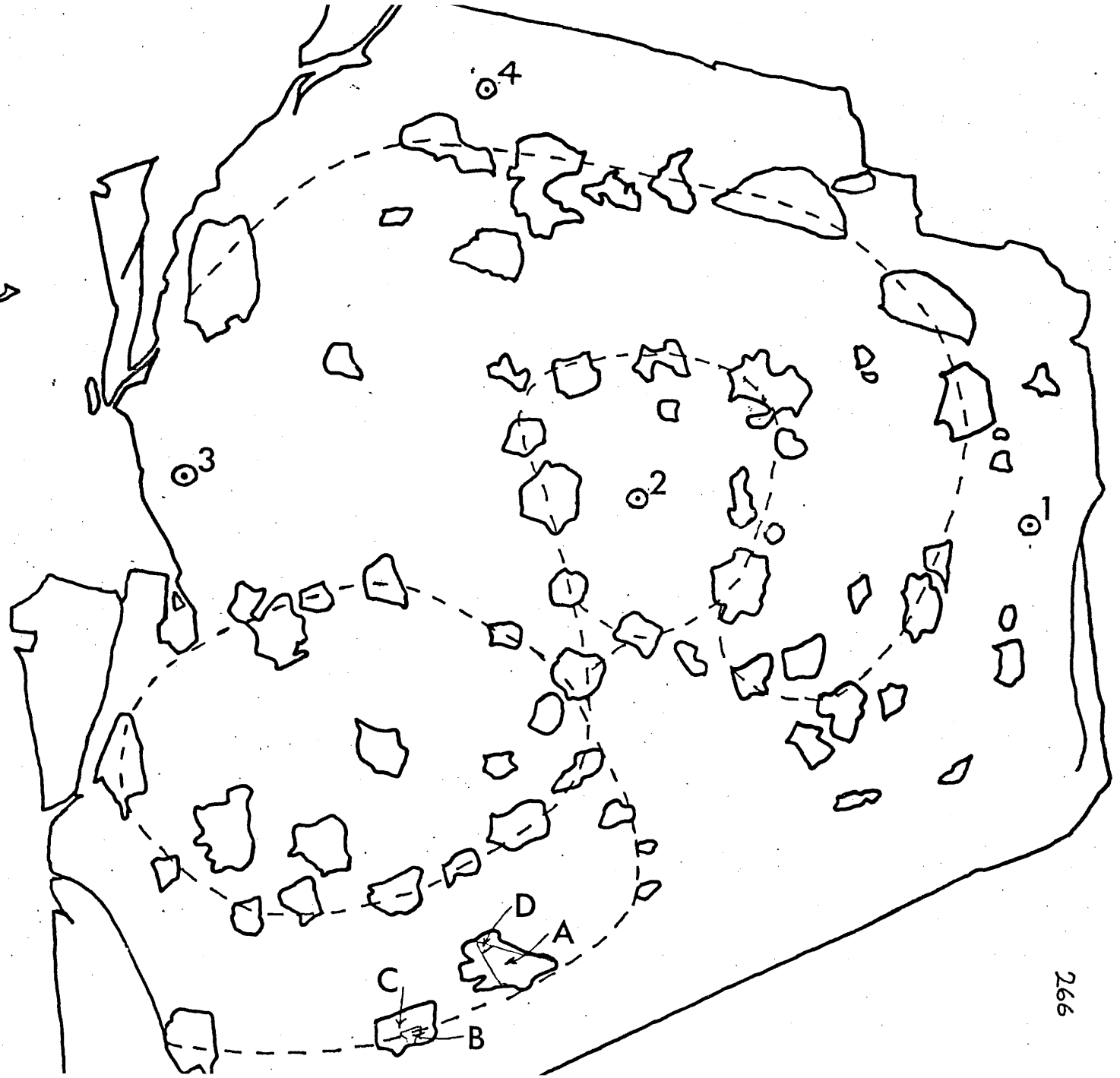
0.1 mm.
zirconolite
(or zirkelite)
indicates concentric
nature of inclusions
analysis positions
(table 5.7)
A, B, C, D – analysis
positions for silicate
inclusions (table 5.8)
1
2
3
4
A
B
C
D

Figure 5.5

Table 5.7.

	(1)	(2)	(3)	(4)	Average
Cr_2O_3	30.85	31.02	30.76	31.14	30.94
Al_2O_3	4.43	4.39	4.48	4.41	4.43
Fe_2O_3*	24.76	24.20	24.53	24.39	24.62.
FeO	29.00	29.32	29.49	30.31	29.32
MgO	4.73	4.42	4.35	3.79	4.32
MnO	0.63	0.66	0.62	0.68	0.65
TiO_2	5.13	5.13	5.08	4.98	5.08
Total	99.53	99.13	99.31	99.70	99.36
Number of ions on the basis of thirty-two oxygen					
Cr	6.97	7.05	6.98	7.08	7.02
Al	1.49	1.49	1.52	1.49	1.50
Fe^{3+}	5.33	5.24	5.30	5.28	5.29
Fe^{2+}	6.93	7.05	7.08	7.29	7.05
Mg	2.02	1.90	1.86	1.62	1.85
Mn	0.15	0.16	0.15	0.17	0.15
Ti	1.10	1.11	1.10	1.10	1.10

* Fe_2O_3 calculated from total Fe^{2+} assuming stoichiometry.
Uranium concentration of 19.3 $\pm$ 0.1 p.p.b.

The included phases are of four distinct types, all of which are silica-rich. Often two, and occasionally three phases are present in one inclusion. The four phases were distinguished by the use of the Jeol S.E.M. and partially analysed using the Geoscan microprobe (table 5.8.).

Phase A contains essentially only Na, Al and Si.

Phase B contains Mg, Fe, Si and minor Ca.

Phase C contains Mg, Fe, Si, Ti, Al and Ca.

Phase D contains Mg, Fe, Si and Al.

Table 5.8.

	A*[1]	B[2]	C[3]	D[4]
Cr_2O_3	0.04	0.76	0.77	0.05
Al_2O_3	17.57	1.58	2.94	9.69
MnO	n.d.	0.09	n.d.	n.d.
TiO_2	n.d.	0.31	8.43	0.86
FeO	0.04	9.63	8.26	18.51
MgO	n.d.	34.20	30.44	16.74
Total	17.65	46.57	50.84	45.85
U (p.p.m.)	17 ± 2	3 ± 1	3 ± 1	Not able to determine owing to overlap from Phase A.

* Average of three inclusions.

1 Other elements present in major proportions are Si and Na.

2 Other elements present in major proportions are Si (and Ca).

3. Other elements present in major proportions are Si and Ca.

4 Other element present in a major proportion is Si.

The included phases cannot be unequivocally identified. However, from similar inclusions recorded in other layered intrusions (McDonald, 1965; Jackson, 1961 and Irvine, 1975), comparisons can be made, and tentative identifications suggested. McDonald (1965) found inclusions of orthopyroxene, clinopyroxene, biotite and plagioclase in chrome spinels from the Bushveld intrusion; Jackson (1961) found olivine and biotite inclusions from the Stillwater intrusion; and Irvine (1975) found combinations of orthopyroxene, chrome-titanium phlogopite (and sodium analogue), sodic plagioclase, pyrrhotite, chalcopyrite, rutile and silica-rich glass from the Muskox intrusion. It is likely therefore that inclusion A is of a

silica-rich glass (a suggestion supported by the high uranium content - approximately 17 p.p.m.); inclusion B an orthopyroxene (enstatite) and inclusion C a titanium-rich (sub-calcic) augite. Phase D requires a fuller analysis before identification can be attempted.

In layered intrusions, the mode of origin of such inclusions, has been under some discussion. McDonald (1965) suggested the existence of an immiscibile chromium-rich liquid within a basic magma, an interpretation considered by Jackson (1966) however, to be not feasible. Recently, Irvine (1975) suggested that chrome spinels of this nature, but of the Muskox intrusion, Canada, may have grown from an "emulsion like mixture of two liquids" (i.e. basic and acidic), whereby droplets of contaminant granitic material become trapped in the spinel during its growth from a basic magma.

In order to interpret the feature described here, several factors need to be taken into consideration.

(1) The concentric nature of the inclusions.

(2) The absence of similar inclusions in nearby chrome spinels.

(3) The fact that this grain is not associated with seam chrome spinels (single inclusions have in fact been observed in chrome spinels from a seam environment in Rhum) unlike those from the Bushveld, Stillwater and Muskox intrusions.

(4) The large amounts of TiO_2 and Fe_2O_3, the grain plotting close to the "Fe-trend" (Henderson, 1974), figure 4.31.

(5) The associated mineralogy. The grain is in contact with a chlorite/biotite assemblage, and adjacent to a high uranium phase (the intense fission track star) identified as zirconolite (or zirkelite) - section 5.4.

A possible interpretation which encompasses all these observations would be a combination of Henderson's (1974) hypothesis

regarding reaction between cumulus chrome spinel and interstitial liquid (i.e. Fe-trend), and Irvine's (1975) hypothesis regarding growth from partially mixed acidic and basic magmas. The close proximity of the zirconolite suggests a trapped magma environment where extreme localised fractionation may have occurred to produce small amounts of acidic liquid. During post-depositional reaction or overgrowth of the chrome spinel, incorporation of this liquid in a globular fashion becomes possible. The concentric pattern is then an indication of either the direction in which the chrome spinel grew, or locates the distribution of exsolved silicate (or silica-rich) phases.

5.2.5. "Olivine Holes".

Inclusions of crystalline material within certain of the olivine morphologies of Rhum were observed on several occasions. As a result of their oval or rounded shape, these inclusions have been termed "olivine holes", and are a relatively common feature in the harrisitic, tabular and irregular olivine morphologies. More rarely are they found in equant olivines, and are apparently absent in the poikilitic and rounded morphologies.

The mineralogy of the included material is varied. Plate 5.10 (a) to (h) is of an olivine hole (maximum diameter of .19 millimetres) within a tabular olivine ($R.84^{A}$), the elemental scans showing apatite, ilmenite and magnetite within a chlorite/uralite matrix. The uranium-distribution map at the lower-power magnification (x10) readily locates the apatite grain of approximately 1.0 millimetre size. A smaller olivine hole (diameter .04 millimetres) within a harrisitic olivine (H.2.) has a more complex mineralogy (plate 5.11 (a), (b)). A combination of elemental spot analyses and optical determinations show the inclusion to consist of brown amphibole (uralite? -

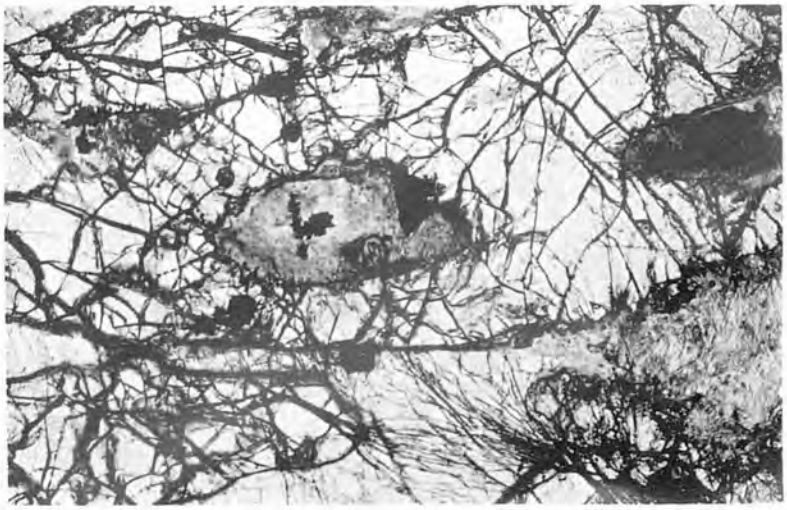

a

·5 mm.

PLATE 5.10

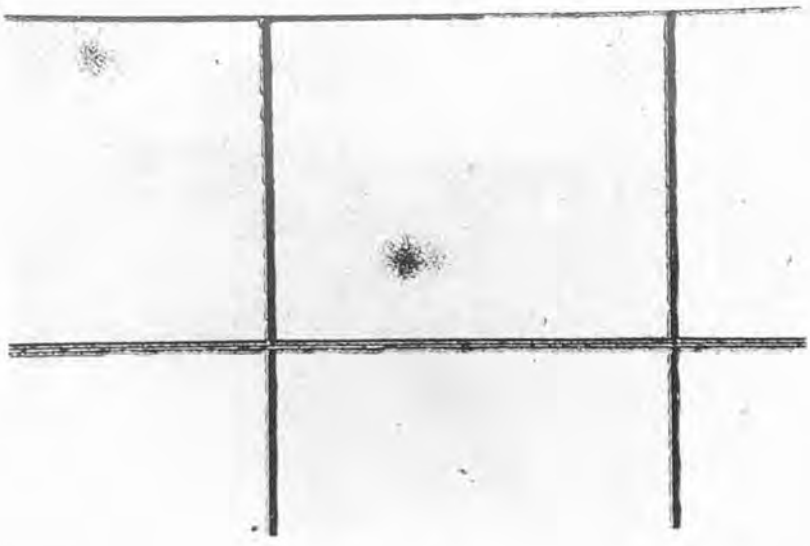

b

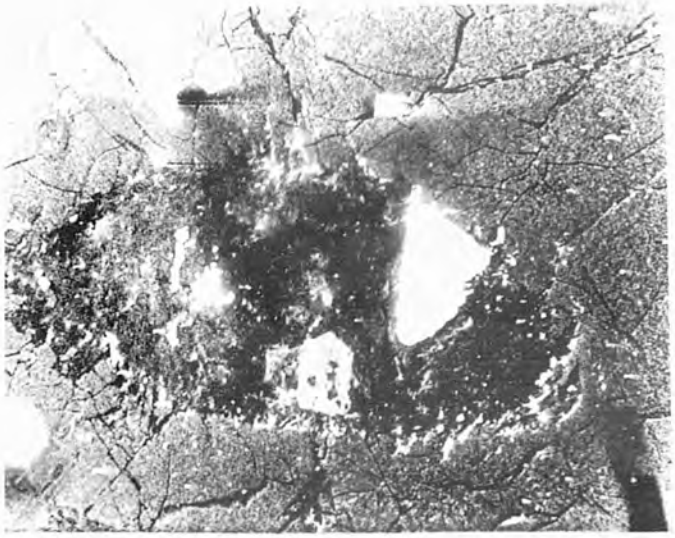

PLATE
5.10

c

·2mm.

d

Ca

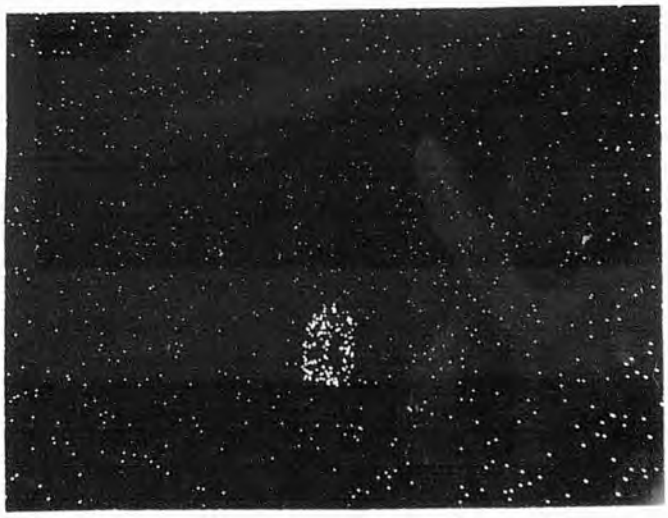

e

P

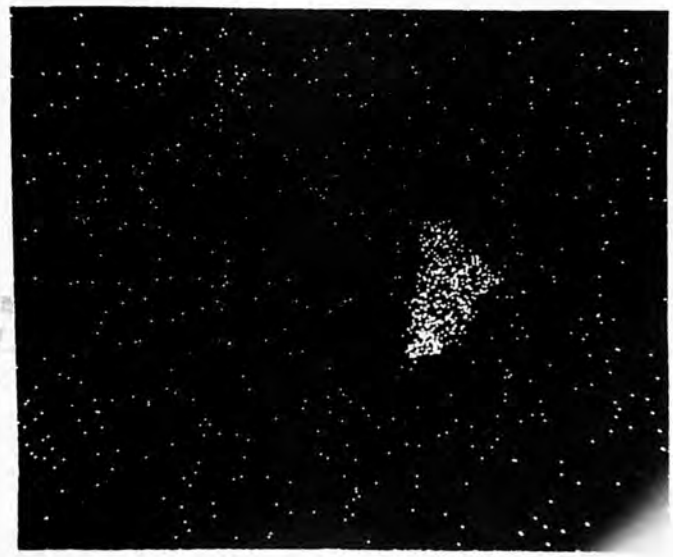

f
Ti

·2 mm.

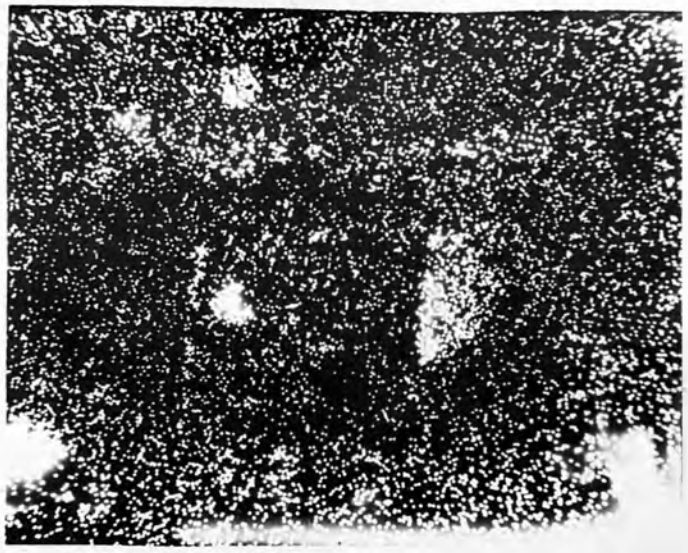

g
Fe

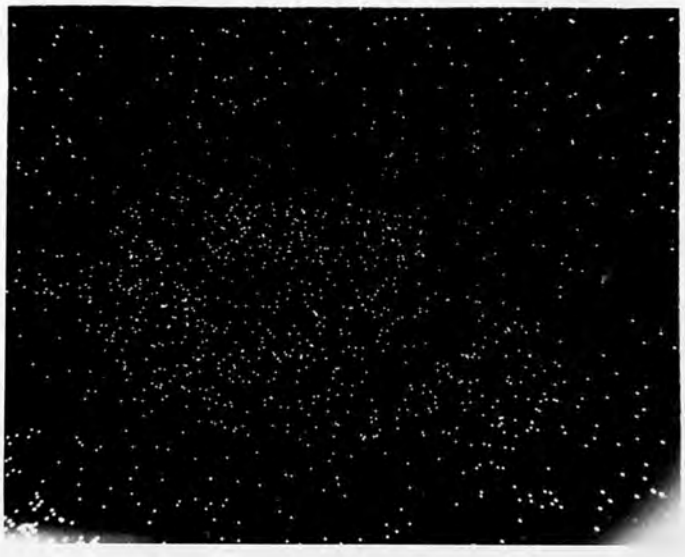

h
Al

spot analysis indicates Ca, Ti, Al, Fe, Si, Ti and minor Mg and K); biotite (K, Ti, Fe, Al, and Si and minor Mg) and chlorite (Al, Mg, Fe and Si).

The frequent appearance of olivine holes within the more rapidly crystallising olivine morphologies would appear to indicate envelopment of liquid during the olivine growth essentially isolating the included liquid. The trapped liquid would then have the composition of the initial magma minus the olivine constituents. This hypothesis is favoured by Drever and Johnston (1957) who described olivine inclusions from picritic dykes. However, three-dimensional views of olivine holes in the harrisitic sample suggests that the shape is in fact a cylinder or cup-shaped hollow within the olivine crystal. Then, during further crystallisation of the rock, interstitial magma becomes increasingly trapped in the hollows and crystallise out as lower temperature mineral phases. Evidence of this is seen in the harrisitic samples where an olivine hole situated directly above (by approximately 10 millimetres) the H.2. hole (plate 5.11 previously) is composed of a more sodic plagioclase (composition An_{62}), plate 5.12. Thus a section cut parallel to the cylinder would be expected to show normal zoning of feldspar towards the bottom of the cylinder (or cup), and, adjacent to the bottom, trapped magma crystallising out as late-stage minerals enriched in low-partitioning elements such as uranium, zirconium or phosphorus. A situation such as this is shown in plate 5.4. (section 5.2.2.) and is a common occurrence in irregular, tabular and harrisitic olivines where minerals such as baddeyelite, zirconolite and apatite are found. Olivine holes, although a growth influenced phenomenon and associated with the more rapidly grown crystals, are considered mainly to be the product of irregularities in the olivine crystal

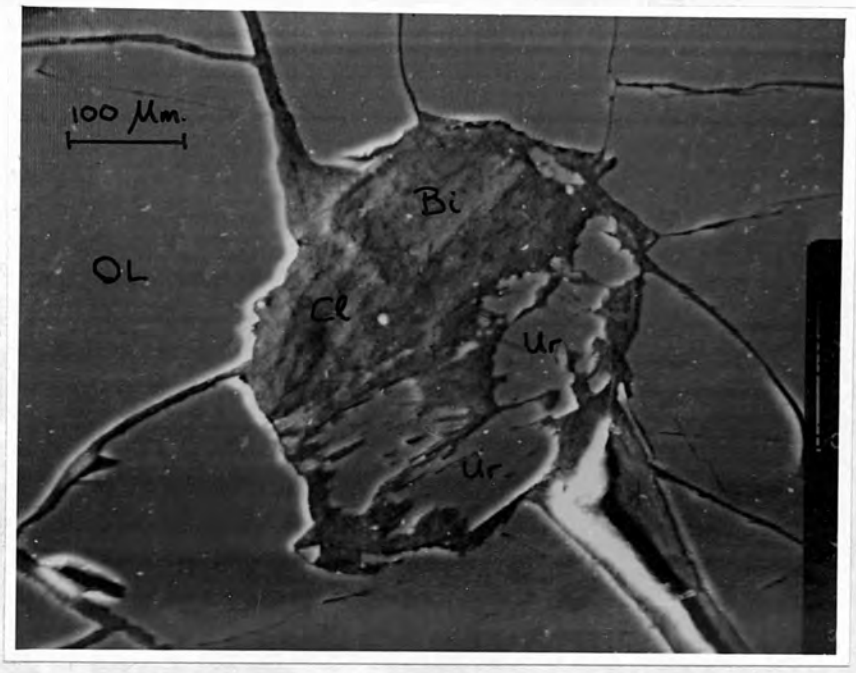

PLATE 5.11 (a)

Secondary electron image (S.E.I.) of olivine hole within a harrisitic olivine. Ur = uralite; Bi = biotite; Cl = chlorite and Ol = olivine.

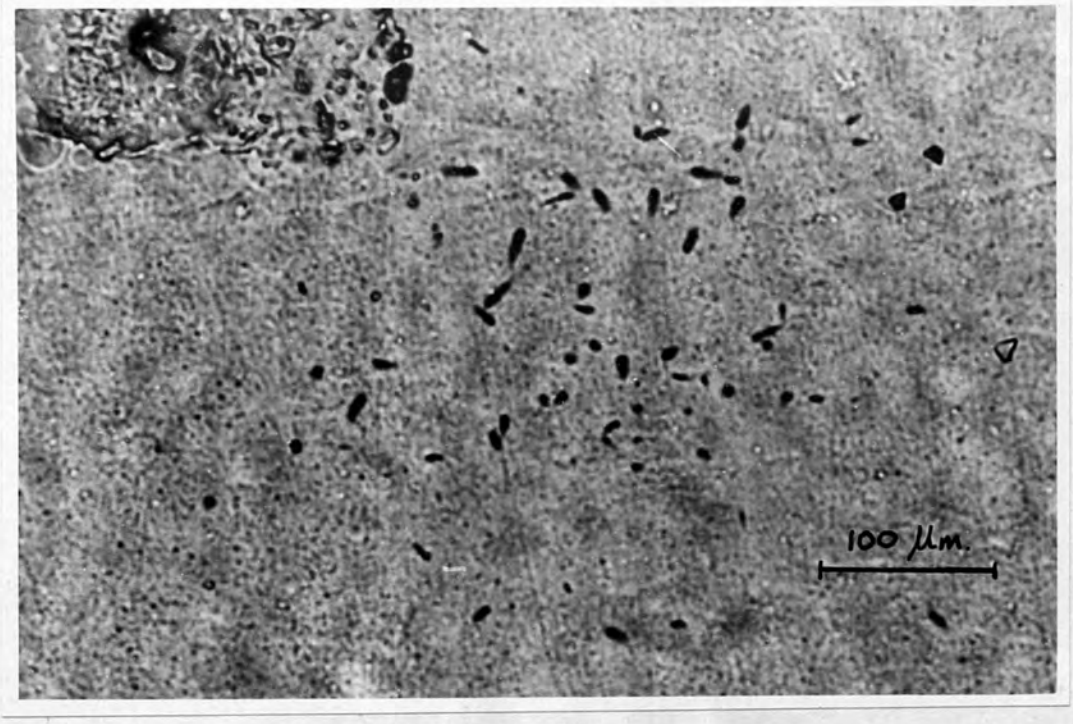

PLATE 5.11. (b)

Uranium distribution map (photomicrograph).

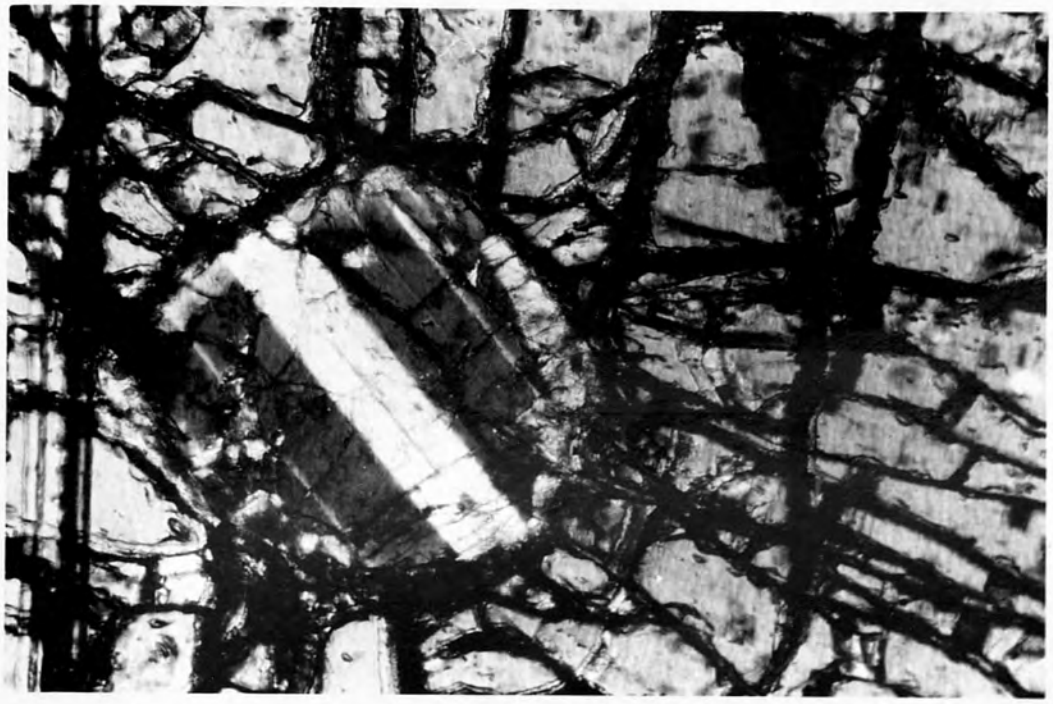

0·5 mm.

PLATE 5.12.

Plagioclase feldspar within an olivine hole, situated approximately 10 millimetres above area shown in plate 5.11.

shape, followed by extremely localised fractional crystallisation in a trapped magma environment, and not solely by enclosing liquid during rapid crystal growth.

The fact that such cross-sections are a relatively common feature, and also that olivine holes are not observed in all the olivine morphologies, suggests that post-consolidation corrosion or alteration was not the major factor in the production of olivine holes.

The range in uranium concentration of olivine holes was from 0.03 to 4.5 p.p.m. and depended upon the included minerals. Because of the varied mineralogy, an average uranium concentration was not calculated.

5.3. Group 3 minerals - apatite

In the four-fold classification based on uranium concentrations derived in this study, group 3 phases are those minerals which contain between 10 and 100 p.p.m. of uranium although overlap of some Group 2 phases occur, e.g. ilmenites and magnetites (section 5.2.2. and 5.2.3.). The vast majority of phases containing 10 - 100 p.p.m. uranium were identified as apatites.

Apatite occurred throughout the intrusion as an intercumulus mineral, and was in fact found in nearly all the thin sections examined. Since the grain size was often less than 100 μm, it can be easily overlooked during preliminary thin section examination - Brown (1956) recorded apatite only from unit 2 of the Rhum intrusion. Using the fission track (contact print) technique however, grains as small as 10 μm were rapidly located since the relatively high uranium concentrations formed distinct features of induced fission tracks in the detector. The smaller grains were then confirmed as being apatite using the Scanning Electron Microscope.

The crystal habit of apatite varied from squat to tabular with length to breadth ratios ranging from approximately 3 to 1 to higher than 15 to 1, the crystals possessing subhedral to euhedral crystal outlines.

Apatite was found associated in assemblages of late-stage intercumulus minerals such as ilmenite, magnetite and biotite (e.g. plate 5.5.); zirconolite and baddeyelite (e.g. plate 5.16. and invariably within a chlorite/uralite matrix. Plate 5.13 (a) to (e) is of a large (0·8 millimetre) apatite crystal (containing 21 $\pm$ 3 p.p.m. uranium) within a harrisitic olivine hole, the surrounding olivine being in optical continuity. The matrix surrounding the apatite consists of two minerals, an inner Mg, Al, Fe, Si phase (chlorite), and an outer Ca, Fe, Mg silicate (uralite). This assemblage of an aluminium-rich inner core and calcium-rich outer core is apparently quite common and has been described above (section 5.2.1.). Plate 5.14 (a), (b) is of two apatite crystals (AP1 and AP2) again in a serpentinised (chlorite?) matrix (S), the surrounding olivines are however several discrete grains and in this case, the matrix can be seen apparently corroding one of the olivine grains (OL 1). The uranium concentration of these two apatite crystals is 85 $\pm$ 10 p.p.m. (the small fission track star in the uranium distribution map is from a hole in the thin section, marked H).

The problem of whether serpentinised areas are primary, i.e. autogenetic and products of late-stage fractionating of the original magma, or secondary, i.e. formed subsequent to the consolidation of the rock has been discussed above (section 5.2.1.). Although in some cases there is evidence to support primary crystallisation, as in the case of feldspar zoning into olivine cups and olivine holes (section 5.2.5.), there is also seen effects of some corrosion by the matrix into the olivines

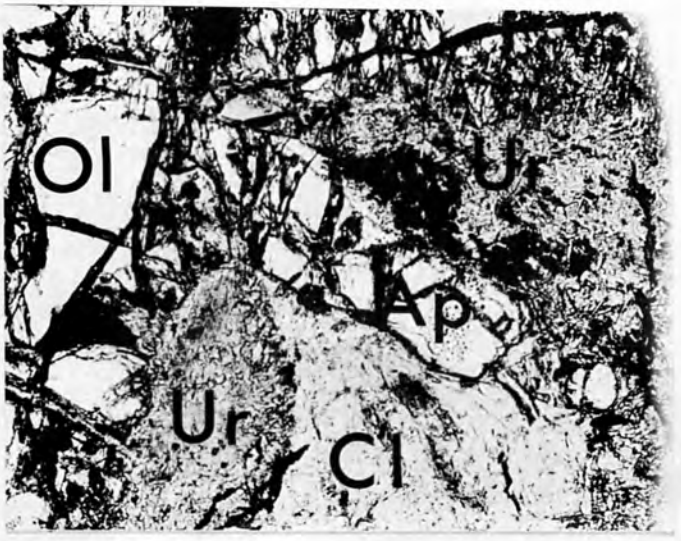

a

PLATE 5.13

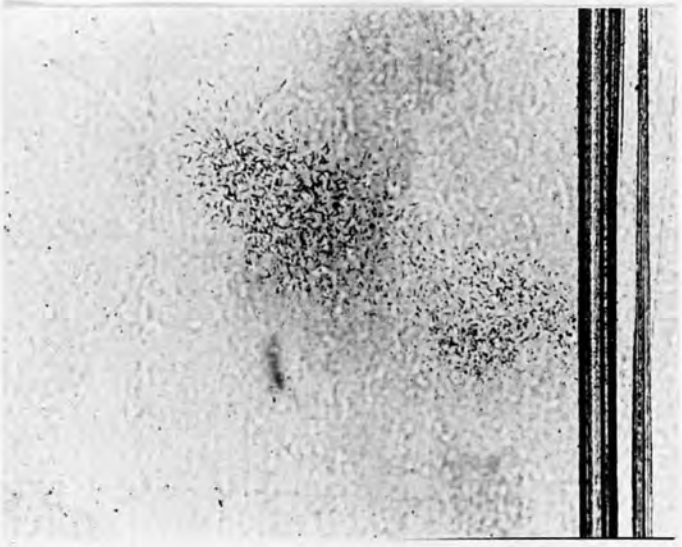

b

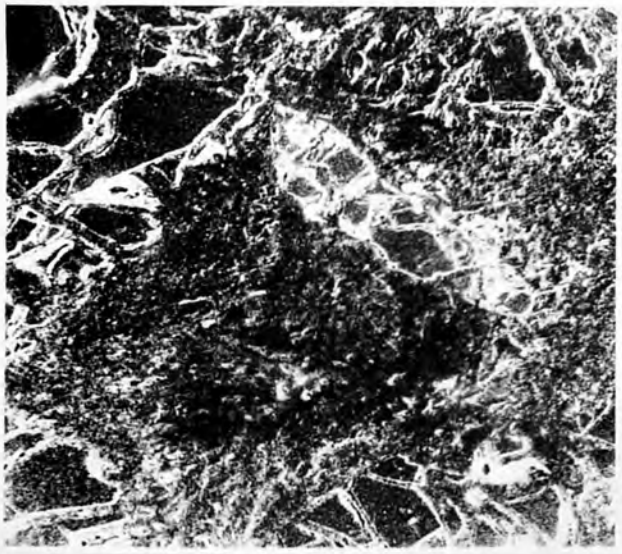

c

·2 mm.

d

Ca

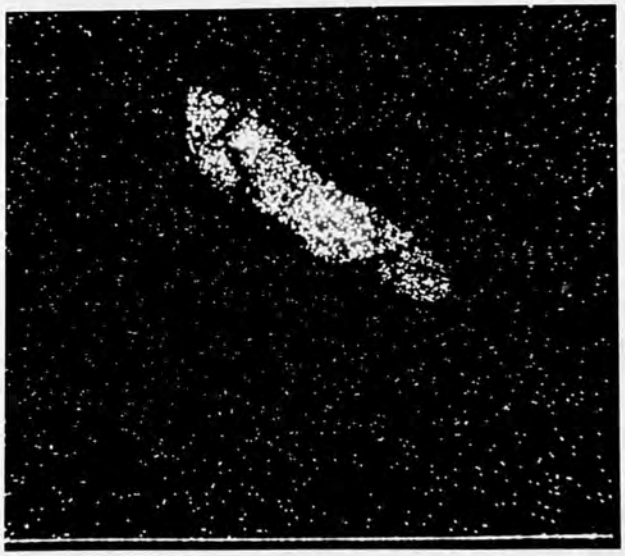

e

P

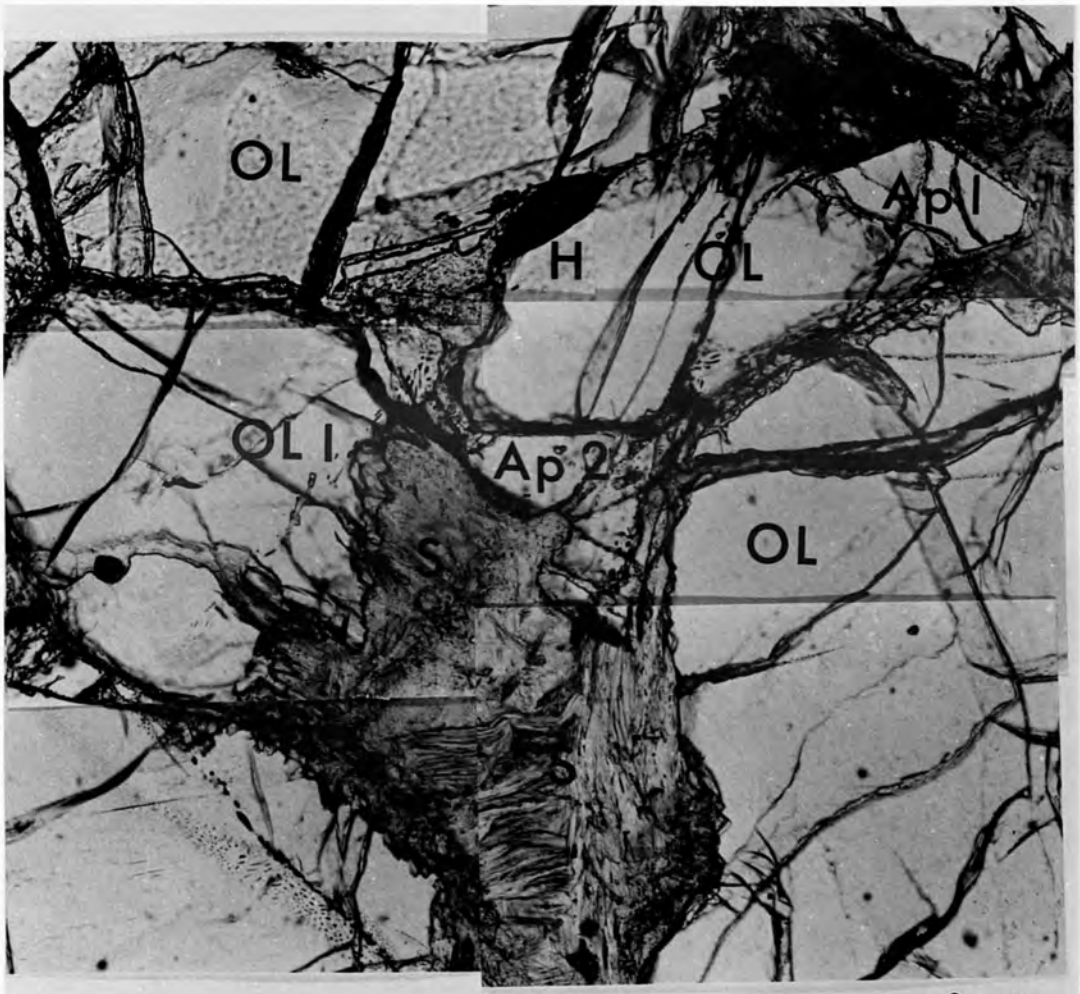

PLATE 5.14 a

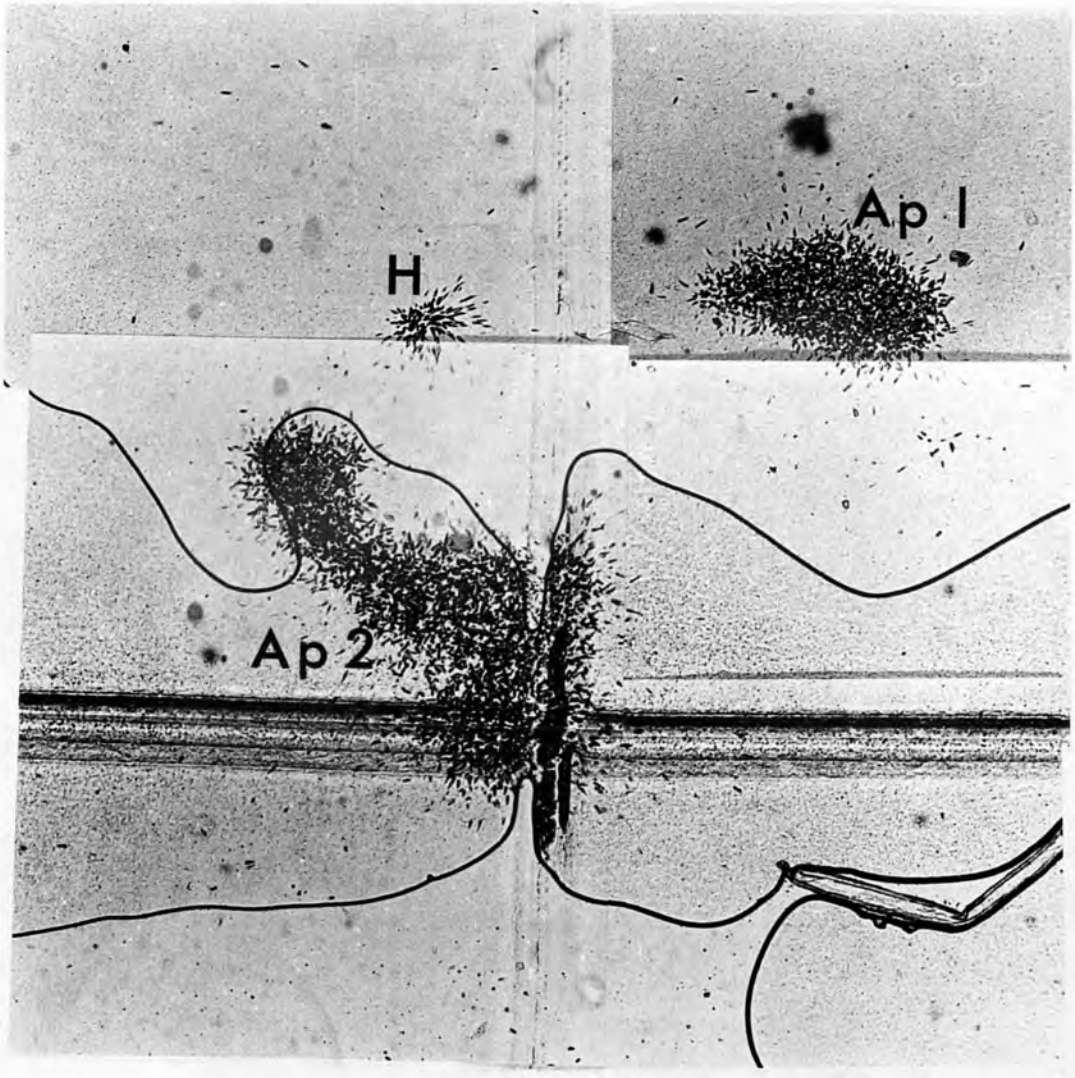

PLATE 5.14 b

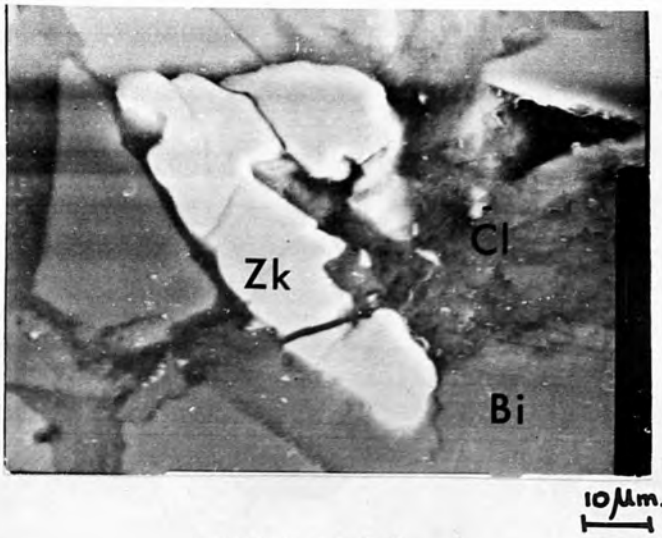

PLATE 5.15 (a)

Secondary electron image (S.E.I.) of zirconolite, or zirkelite (Zk), surrounded by biotite (Bi) and chlorite (Cl).

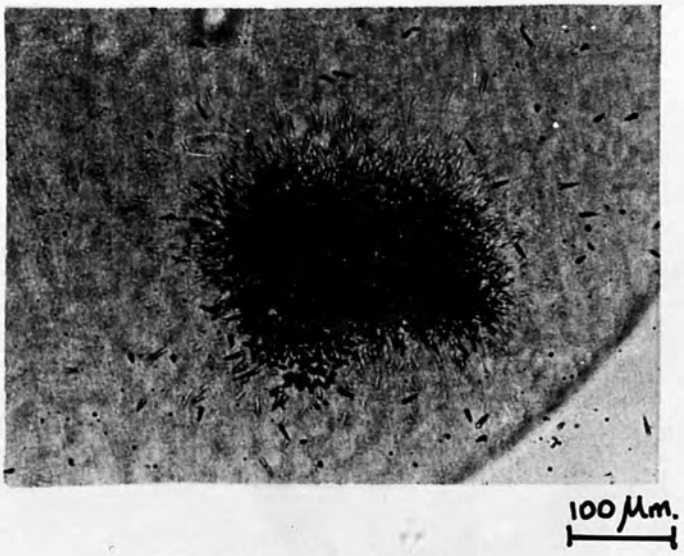

PLATE 5.15 (b)

Uranium distribution map (photomicrograph).

PLATE 5.15 c

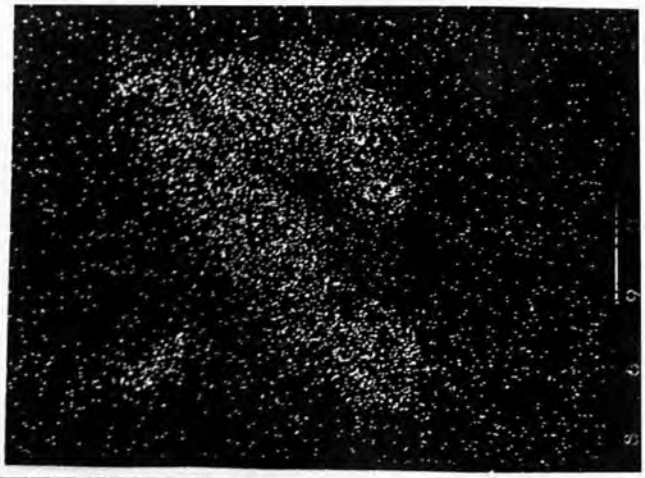

Ca

10 µm.

d

Ti

e

Zr

f

Y

(e.g. plate 5.14) which may possibly be interpreted as alteration through the introduction of hydrothermal solutions from an external source. Although the uranium concentrations of the apatites from plates 5.13 and 5.14 would seem to indicate a correlation between the uranium content and the mode of origin of the matrix, subsequent investigation found this not to be the case. The uranium concentrations of ten apatite crystals from both "primary" (as evidenced by feldspar zoning intocups), and "secondary" areas (as evidenced by corrosion of olivine) were determined. The values ranged from 21 to approximately 100 p.p.m. uranium (averaging 75 $\pm$ 5 p.p.m.) but showed no systematic variation with the mode of origin. It is probable therefore that many other factors were involved such as the degree and extent of trapped liquid, and whether or not phases of high uranium concentrations were formed.

5.4. Group 4 minerals.

A striking feature of the uranium distribution maps of the Rhum rocks was the occasional appearance of fission track "stars". These took the form of star-shaped objects in the detector, and were composed entirely of fission tracks emanating from essentially a point source. It was initially thought that such features were due to contamination of dust-sized particles on the surface of the detector, however, closer examination showed the source to be small (usually less than 50 μm), uranium bearing mineral phases within the rock surface. The shape of these objects led Burnett et al. (1971) to liken them to heavenly stars, classifying them in terms of first and second order magnitudes, and their distribution within the detector as constellations. Burnett et.al. (ibid.) in fact first used the Scanning Electron Microscope (S.E.M.) to locate the source minerals of such stars. They found that by taking elemental

pictures in the P - Zr channel (between 1.9 and 2.1 keV, i.e. the P K_{α} and Zr L_{α} lines) at a magnification of 2000, the uranium fission source was located. In practice, with the Jeol 50 S.E.M. used in this work and the aid of photographic contact prints, a magnification of 600 was adequate for location purposes. The P - Zr channel was used since, in all cases the source mineral was identified as either a phosphate (apatite - section 5.3.), or a Zr-bearing phase (baddeyelite, zircon or zirconolite).

The identification of micron-sized minerals corresponding to fission track stars led to the discovery of new and unusual minerals which would have probably been overlooked using standard microscopic techniques. In particular, fission track mapping was used routinely on lunar samples, and aided in the discovery of a previously unrecorded Fe - Ti - Zr silicate (tranquillityite), e.g. Lovering et al. (1971) and Lovering and Wark (1971).

The high uranium content of these micron-sized phases (often greater than 1 percent UO_2) meant that at the routinely used thermal neutron doses of between 1×10^{16} and 1×10^{17} neutrons. cm^2, the induced fission tracks overlapped to such an extent that resolution of individual tracks became impossible. The S.S.T.D. then became saturated in the area of the fission track star, and only a qualitative (minimum) value of the uranium concentration could be obtained. At the 1 percent UO_2 level however, microprobe analysis becomes feasible, and the possibility arises of mineral dating by e.g. Pb/U of Th/U methods. Chodos and Albee (1972) in fact determined several "microprobe ages" from a high uranium mineral in Apollo rock 12013, and found reasonable agreement with Rb/Sr and K/Ar ages. Since, in basic rocks, these phases are considered to be the product of crystallisation of the final remnants of interstitial liquid,

the calculated microprobe age will correspond to the end of the crystallisation process.

The following sections are a record of the high uranium phases (i.e. group 4 minerals with greater than 100 p.p.m. uranium) found in the Rhum rocks, and includes the first report of the mineral zirconolite (or zirkelite) from a terrestrial basic rock.

5.4.1. Zirconolite (or zirkelite)

In several Rhum specimens intense fission track stars were observed. The corresponding source minerals were located using the P - Zr channel of the S.E.M. Spot analyses of the phases showed the presence of elements Zr, Ti and Ca in concentrations greater than 5 per cent, but an absence of Si. Also observed were peaks corresponding to elements Fe, Y and rare-earth elements (R.E.E.). Elemental scanning pictures of Ca, Zr, Ti and Y are given, together with the uranium distribution map. (Plate 5.15 (a) to (f)).

A total of nine Ca-Zr-Ti oxide grains were recorded throughout the Rhum specimens, although none in the Carlingford samples. The mineral occurs as discrete anhedral grains in localised mesostasis areas, and with a maximum grain size only of the order of 60 μm in diameter. The rock specimens in which these phases occurred were in all cases olivine-cumulates ranging in the intrusion from unit 3 to unit 9 and also within the harrisite sample (olivine-crescumulate). The immediate associated minerals were typically of a mesostasis type varying from chlorite, biotite and apatite to, on one occasion (H.10), the Ca-Zr-Ti oxide was apparently intimately associated with a Mn-rich ilmenite. The crystallising environment of such late-stage intercumulus minerals is discussed more fully below

(section 5.5.) but these minerals are considered to be the product of primary late-stage magmatic differentiation of the Rhum magma.

Quantitative microprobe analyses of four of the grains were obtained using the Cambridge Geoscan instrument. The results are presented in table 5.9., the mineral being identified as either zirkelite ($CaZrTiO_5$) or zirconolite ($CaZrTi_2O_7$).

Confusion has arisen over the years as to whether zirkelite and zirconolite are in fact separate minerals and also over the precise structural formulas. The problem is compounded by the presence of significant amounts of trivalent oxides (often greater than 10 per cent), e.g. Borodin et al., 1960, analysis number 4). The controversy has recently been revived by the identification of oxides from lunar rocks containing varying proportions of the elements Ca, Zr, and Ti. Brown et al. (1972) suggested that the Ca - Zr - Ti phase named as phase β by Haines et al (1971) was equivalent to Ramdhor and El Goresy's (1970) mineral dysanalyte and that they both conform to the zirkelite formula (after Busche et al., 1972).

Wark et al. (1973) however, proposed that the structure more closely corresponds to the zirconolite formula, and since then, both Kirsten and Horn (1974) and Meyer and Boctor (1974) have favoured the use of zirconolite. Since in this work, the totals amount to only 94 per cent, no definitive statement can be made as to whether the mineral is zirkelite or zirconolite.

Although low totals were recorded in this work, it is worth noting that summation of the same elements from Busche et al.'s (1972) average analysis gives a similar total-Rhum average of seven elements = 93.39 per cent; Busche et al. (1972)

Table 5.9.

Analysis Number	(1)	(2)	(3)	(4)	(5)	(6)
CaO	9.47	11.13	10.50	10.75	8.8	12.03
MgO	-	-	-	-	0.72	0.53
FeO	7.02*	6.06*	6.52*	6.13*	6.1*	2.85
Fe_2O_3	-	-	-	-	-	3.44
PbO	-	-	-	-	0.49	-
Cr_2O_3	-	-	-	-	0.54	-
Y_2O_3	2.84	2.24	2.24	0.90	3.6	-
RE_2O_3	-	-	-	-	1.8	3.36
Al_2O_3	0.33	0.53	0.36	0.39	1.36	2.23
TiO_2	35.49	37.71	36.70	38.10	34.5	32.25
ZrO_2	37.27	36.13	37.43	36.22	40.4	35.75
SiO_2	0.26	0.55	0.11	0.19	0.42	1.18
HfO_2	-	-	-	-	0.35	-
UO_2	100 ppm**	100 ppm.**	100 ppm.**	100 ppm.**	0.22	0.10+
ThO_2	-	-	-	-	0.50	0.37
Nb_2O_5	-	-	-	-	1.00	4.25
Ta_2O_5	-	-	-	-	-	0.09
H_2O^-	-	-	-	-	-	0.09
H_2O^+	-	-	-	-	-	1.56
K_2O	-	-	-	-	-	0.24
MnO	-	-	-	-	-	0.12
Total	92.68	94.35	93.86	92.68	100.79	100.44

Table 5.9. (continued)

Analysis Number		(1)	(2)	(3)	(4)	(5)	(6)
Number of ions calculated on the basis of 7 oxygens							
A	(Ca	.651	.740	.709	.726	.567	.812
	(Mg	-	-	-	-	.062	.049
	(Fe	.377	.315	.344	.323	.307	.150
	(Pb	-	-	-	-	.008	-
		1.028	1.055	1.053	1.049	0.944	1.011
B	(Zr	1.166	1.094	1.151	1.113	1.185	1.098
C	(Ti	1.712	1.760	1.740	1.806	1.560	1.528
	(Y	.097	.074	.075	.030	.115	-
	(Al	.025	.039	.027	.029	.096	.165
	(R.E.	-	-	-	-	.038	.077
	(Cr	-	-	-	-	.026	-
	(Si	.017	.034	.007	.012	.025	-
	(Hf	-	-	-	-	.006	-
	(U	-	-	-	-	.003	.001
	(Th	-	-	-	-	.007	.005
	(Nb	-	-	-	-	.027	.121
	(Fe^{3+}	-	-	-	-	-	.163
		1.851	1.907	1.849	1.877	1.903	2.060

* All iron calculated as FeO

** Fission track analysis (minimum value).

\+ Calculated as U_3O_8

Analysis (1) R.82 area A11B, A23C

(2) R.82 area A5B, A21C

(3) R.82 area A4B, A21C

(4) H.10 area A9B, A29C

(5) Average from Busche et.al. (1972) - lunar zirkelite

(6) Analysis number 1 from Borodin et.al. (1960) - terrestial zirconolite.

of some seven elements = 95.18 per cent. It is clear from Table 5.9. that analysis of the Rhum specimens for Rare Earths and niobium would help precise identification.

In table 5.9. the number of ions have been calculated on the zirconolite formula (i.e. ABC_2O_7), where A corresponds to Ca^{2+}, Fe^{2+} and trace $^{2+}$; B to Zr^{4+}, and C to Ti^{4+} plus the other trivalent, quadravalent and pentavalent cations. On this basis, the Rhum specimens averaged can be represented as $A_{1.046}\ B_{1.131}\ C_{1.871}\ D_7$ where A + B + C = 4.048. As a comparison, table 5.8. gives also the average of Busche et al.'s (1972) analysis, and an analysis by Borodin et al. (1960), both of which appear to fit reasonably well with the zirconolite formula. (Busche et al. (ibid) however argues for the use of the zirkelite formula).

Although zirconolite (zirkelite?) occurs in lunar ultramafic rocks exhibiting cumulate textures (e.g. Kirsten and Horn, 1974), this is the first record of such a mineral from a terrestrial ultramafic cumulate, the previously reported examples of terrestrial zirconolite (zirkelite?) were from metamorphosed pyroxenites (Borodin et al., 1960).

The large and diverse range of elements entering the zirconolite structure, and the wide range of concentrations observed (e.g. Meyer and Boctor, 1974), suggests that the structure is not rigidly either $CaZrTiO_5$ or $CaZrTi_2O_7$. The mineral appears to act in a sponge-like manner accommodating the final dregs of trapped intercumulus magma, and incorporates many of the low-partitioning elements which have not entered the cumulus phases.

5.4.2. Baddeyelite

In addition to zirconolite, baddeyelite (ZrO_2) was also located as being the source mineral to several fission track stars. With the S.E.M., the same procedure of mineral location and identification was used. In conjunction with the photographic contact print, the area of the rock corresponding to the fission track star was scanned at approximately x 600 magnification

using the P - Zr channel, the source mineral located by an accumulation of dots on the cathode ray fluorescent screen. The identity of baddeyelite was confirmed by a spot analysis which showed essentially only the element zirconium present.

A total of seven baddeyelite grains were recorded throughout the Rhum specimens, usually occurring as small anhedral grains, and averaging approximately 20 μm in diameter. The associated minerals were the same as those found associated with zirconolite - i.e. apatite, biotite and chlorite. The rock specimens in which baddeyelite occurred were again olivine-cumulates ranging from unit 3 to unit 9, and also within the harrisite sample. Five of the baddeyelite grains were found within the same rock specimens as zirconolite. Quantitative microprobe analyses of two baddeyelite grains are given in table 5.10 below, from where it can be seen that the analysed grains are almost pure ZrO_2.

The uranium concentration of the baddeyelite can only be given as a minimum value (i.e. greater than 100 p.p.m.), since overlapping of fission tracks within the detector had occurred. Fisher (1975) in a recent review of fission track analysis reports a range of uranium concentrations within lunar baddeyelites of 60 to 840 p.p.m.

In one harrisitic sample (H.1. - analysis (1)), a baddeyelite grain 100 μm in diameter with a subhedral crystal outline developed is seen in close association with two euhedral (basal) apatite crystals and several anhedral zirconolite crystals within a chloritised matrix. Plate (5.16 (a) to (h)) show the three separate phases: the Zr elemental scan (d) locates the baddeyelite grain; Ti scan (e) the zirconolite grains, and Ca scan (f) the two apatite crystals. The degree of development of crystal faces of these three average

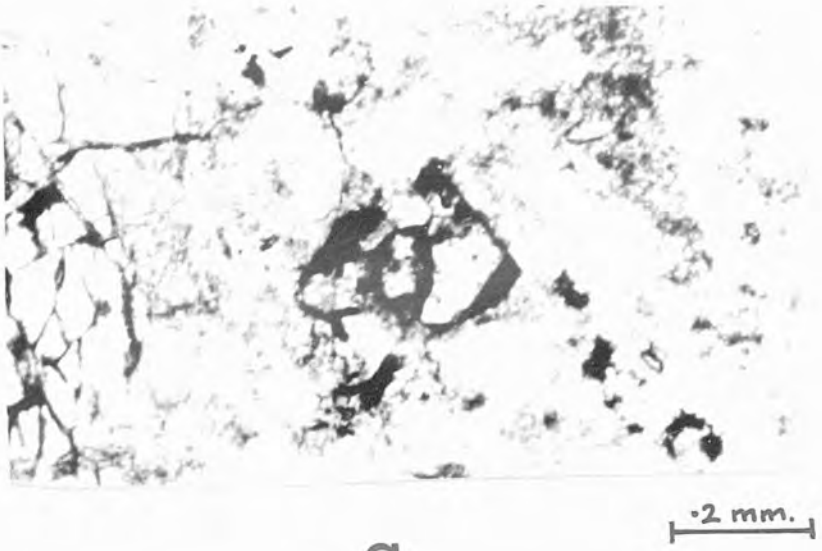

a

PLATE 5.16

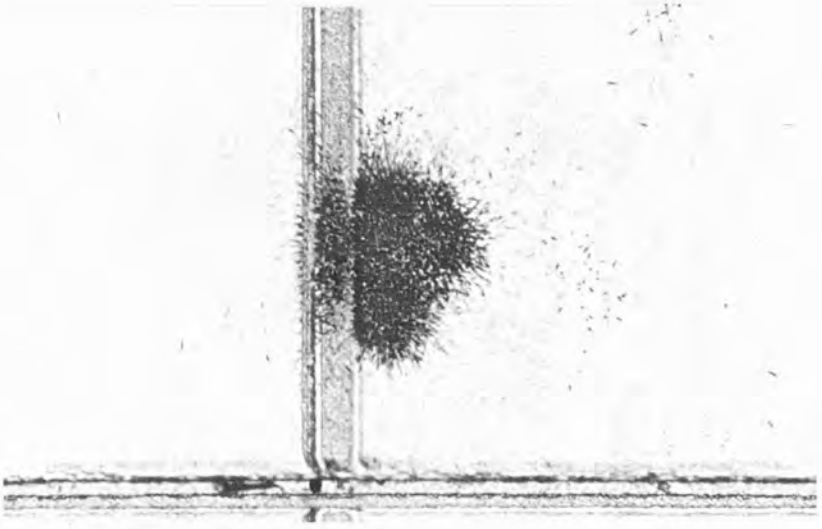

b

c

S.E.I.

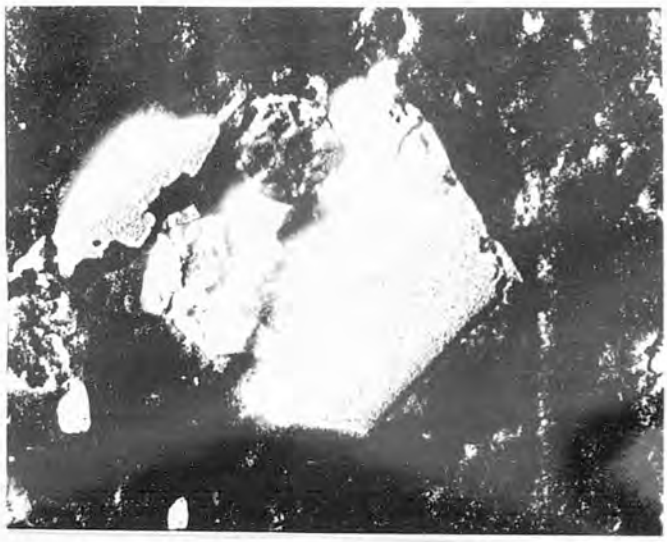

20 µm.

d

Zr

e

Ti

f

Ca

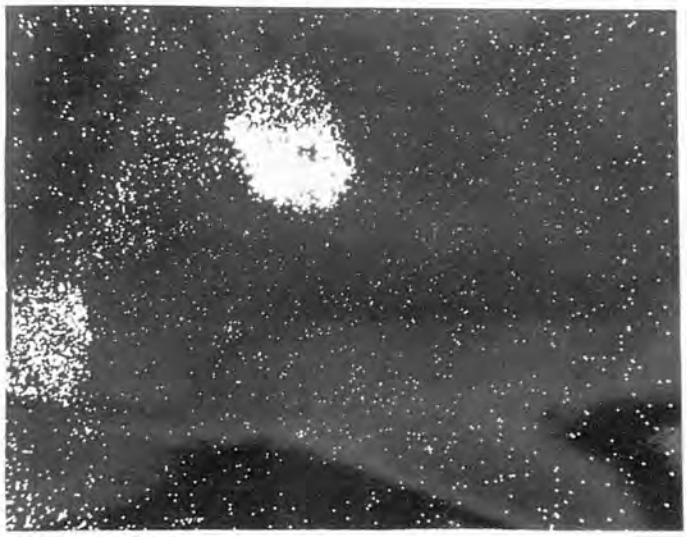

20 μm.

g

P/Zr

h

Fe

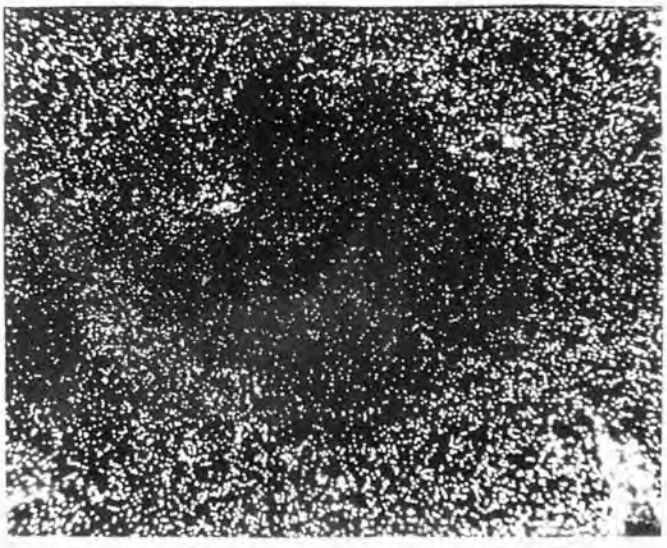

Table 5.10.

Analysis Number	1	2	3	4
ZrO_2	98.12	97.94	97.8	92.07 (85.1 - 95.7)
TiO_2	1.73	1.89	0.56	2.43 (5.46 - 0.83)
FeO*	0.54	0.43	1.3	1.52 (3.22 - 0.39)
Y_2O_3	0.00	0.00	-	1.06 (2.65 - 0.29)
Al_2O_3	0.00	0.00	-	- - -
SiO_2	0.00	0.01	0.08	0.23 (0.29 - 0.16)
CaO	0.00	0.00	-	0.12 (0.14 - 0.08)
HFO_2	-	-	0.93	1.85 (2.07 - 1.52)
UO_2	100 p.p.m**	100 p.p.m.**	-	- -
	100.39	100.27	100.67	99.28

* All Fe calculated as FeO

** From fission track analysis and not included in total.

(minimum value)

Analysis (1) H.1.

(2) R.84[A]

(3) From Keil and Fricker (1974) in a gabbro from Axel Heibert Island (Canada).

(4) From Meyer and Boctor (1974 - lunar baddeyelite).

minerals suggests the order of crystallisation to be apatite followed by baddeyelite followed by zirconolite.

Baddeyelite has been identified on several occasions in lunar basalts and fines (e.g. Ramdohr and El Goresy, 1970 and Meyer and Boctor, 1974), and is considered to be a relatively common accessory mineral associated with late-stage minerals such as silica-rich glass, apatite etc. Reports of its terrestrial occurrence however, are uncommon, this apparently

being the first report from a terrestrial ultrabasic cumulate. Keil and Fricker (1974) record the occurrence of fourteen baddeyelite grains from a gabbro which they considered to be the first report from terrestrial basaltic rocks. However, in a note added in proof, Keil and Fricker (ibid.) suggest that baddeyelite may be a relatively common trace mineral in basaltic rocks (they located further samples in alkali basalts), but because of its small size, it apparently has been overlooked in the past.

Thus the presence of small, late-stage crystallisation minerals, such as zirconolite and baddeyelite, which are easily overlooked using standard microscopic techniques can be readily located using fission track mapping.

5.4.3. Zircon

A third zirconium-bearing phase located as a source mineral of fission-track stars was identified as zircon. Only five grains were detected, these all occurring in unit 8 olivine-cumulates (specimen numbers R.62 and R.64) and having a maximum grain size of 100 microns and possessing subhedral crystal outlines. Like zirconolite and baddeyelite, the minerals associated with zircon were apatite and biotite, and, on two occasions, magnetite and Mn-rich ilmenite. Thus, zircon is similarly considered to be the product of late-stage fractional crystallisation of the Rhum ultrabasic magma, within a localised, trapped magma environment.

Although a quantitative analysis using the Geoscan mico-analyser was not undertaken, S.E.M. spot analyses showed that essentially only Zr and Si were present. Deer et al. (1971) note that yttrium and hafnium enters the zircon structure often in concentrations greater than one per cent

weight oxide. These two elements were not however detected on the S.E.M.

The uranium concentration of the zircon grains can only be estimated at being greater than 100 p.p.m., although the intensity of fission-track stars from zircon grains were lower than for either baddeyelite or zirconolite grains of comparable size. This indicates that the uranium concentration of zircon is less than that for the other Zr-bearing phases - a feature seen also in lunar rocks. The range of uranium in lunar zirconolite (i.e. phase B, Lovering and Wark, 1971) is quoted as 400-2800 p.p.m. (Lovering and Wark, ibid); lunar baddeyelite from 60 - 840 p.p.m. (Fisher, 1975), and lunar zircon from 30 - 330 p.p.m. (Fisher, ibid.).

Although zircon has not previously been reported from the Rhum layered intrusion, it commonly occurs as an accessory mineral in other layered intrusions. In Skaergaard for example, Wager and Brown (1968) records that it can usually be found at all horizons and is associated with minerals crystallised from the trapped intercumulus liquid.

5.5. Summary and Discussion

In the mesostasis areas of the Rhum cumulates, there are present a wide range of minerals containing large variations in uranium concentrations. The proposed sub-division of these minerals into groups based on uranium content, although to a certain extent arbitrary, has some validity in that the cumulus minerals of group 1 were the first minerals to crystallise; group 2, in general, the second; group 3 the third, and group 4 the final crystallisation products of the Rhum interstitial magma.

There is also observed a correlation between the crystal size and the concentration of uranium - the smallest mineral

phases are those from group 4 (high-uranium phases), and the largest from group 1 (extremely low-uranium phases). Such an inverse relationship between uranium concentration and grain size has been previously recorded for mesostasis areas of lunar basalts (e.g. Burnett et al., 1971 and Thiel et al., 1972) and also within terrestrial zircons (e.g. Silver, 1963). Since uranium partitions strongly into the melt during crystallisation of the major mineral phases, the uranium content will increase in a decreasingly smaller volume of intercumulus liquid, until final crystallisation of the residual magma occurs to form the group 4 uranium-enriched, mineral phases.

In addition to uranium being enriched in the intercumulus liquid, there is also an accumulation of water. This is manifested by the close association of uranium-enriched phases of groups 3 and 4 with the hydrothermal minerals described in section 5.2.1. Seitz and Hart (1973) noted a close affinity between uranium and serpentinized areas (not specified mineralogically) within oceanic ultramafic rocks. In these cases, they considered the uranium to have been introduced into the ultramafic rocks from an external source during serpentinization of the consolidated rocks. A primary crystallisation genesis has however, been proposed for the formation of the hydrothermal minerals (and hence groups 3 and 4 minerals) in the Rhum cumulates, the reasons for this can be summarised:-

1) Heterogeneous distribution of the hydrothermal minerals.

2) Correlation between hydrothermal minerals and certain of the olivine morphologies.

3) The appearance of hydrothermal minerals within olivine "holes" (Section 5.2.5.)

4) The absence of serpentine minerals sensu stricto.

Such a primary alteration process has been proposed for other layered intrusions; e.g. Wager and Brown (1968 p.51, p.62) for Skaergaard, and Elsdon (1971) for the Kap Edvard Holm intrusion, East Greenland.

In spite of the strong affinity of uranium with minerals containing significant amounts of water (e.g. apatite, uralite), and in view of the recorded geochemical compatibility between uranium and potassium (e.g. Green et al., 1968), a surprising feature was the relatively low concentrations of uranium in the only potassium-bearing mineral, i.e. biotite. This is well seen in plate 5.2. where the uranium is apparently more stable in both the apatite and the uralite minerals suggesting a stronger geochemical affinity between uranium and calcium than between uranium and potassium.

Uranium concentrations vary considerably in the Rhum oxide minerals, there being observed at least two orders of magnitude more uranium in the zirconium oxides (baddeyelite and zirconolite) than in the iron, titanium oxides (magnetite and ilmenite).

In the ilmenites the controlling factor for uranium variation appears to be either the geochemical compatibility with another element, i.e. manganese in late-crystallising ilmenites, or variations in crystal growth rates (figures 5.1. to 5.3.). In addition, in both ilmenites and magnetites, the uranium concentration increases with decrease in crystal size, a feature attributed to an increase in uranium content of trapped residual magma (see discussion above).

The strong geochemical compatibility between uranium and zirconium is well known from uranium distribution studies of lunar rocks (e.g. Haines et al., 1971). The routine use of

fission track mapping in lunar material has led to identification of many "exotic" (Chodos and Albee, 1972) lunar phases. Many, if not all of these phases, contain ten per cent or more ZrO_2 - e.g. Phase β (Haines et al., ibid.); Phase B (Lovering and Wark, 1971); baddeyelite (Burnett et al., 1971); tranquillityite (Lovering et al., 1971); zircon (Burnett et al., ibid.) zirkelite (Busche et al., 1972) or zirconolite (e.g. Kirsten and Horn, 1974).

In the Rhum cumulates, three zirconium-bearing minerals with uranium concentrations in excess of 100 p.p.m. were observed - i.e. zircon, baddeyelite and zirconolite (or zirkelite), none of which have been recorded before from the Rhum cumulates. From textural considerations of coexisting zirconium minerals, the order of crystallisation appears to be zircon, baddeyelite, zirconolite (zirkelite). From estimated uranium concentrations, the order of uranium partitioning appears to be zirconolite (or zirkelite) $>$ baddeyelite $>$ zircon. This latter observation is consistant with results from Haines et al. (1971) and Fisher (1975).

Thus zirconolite (or zirkelite) is apparently the final mineral to have crystallised from the Rhum intercumulus magma. The flexible nature of the structure (section 5.4.1.) would suggest that this mineral acts in a sponge-like manner to crystallise the final dregs of intercumulus magma. The low analytical totals obtained in this study (table 5.8.) is probably a reflection of the large number of elements accommodated into the structure. In addition to the many reported examples of zirconolite (zirkelite) occurring associated with late-stage crystallisation products (e.g. Lovering and Wark, 1974 and Brown et al., 1972), Kirston and Horn (1974) described zirconolite

from a lunar troctolite as an apparently early-crystallising primary mineral. Duncan et al. (1974) uses this observation to propose a hypothesis for the genesis of lunar basalts from partial remelting of a cumulate containing cumulus ilmenite and zirconolite. In Rhum however, zirconolite (zirkelite) is without doubt not a cumulus phase but, as suggested above, the final mineral to crystallise from the intercumulus magma.

Thus, even in the late-stage crystallisation of the Rhum magma, the behaviour of uranium is influenced by its greater stability within the magma, only entering mineral phases in significant amounts when unable to diffuse away into the main bulk of the magma. Like the cumulus phases (Sections 4.3. to 4.7), uranium distributions in intercumulus phases can act as an indicator of both crystal growth rates (e.g. "zoned" ilmenite, section 5.2.3.), and mechanisms (e.g. "poikilitic" chrome-spinel, section 5.2.4.).

CHAPTER 6 CONCLUSIONS

This chapter outlines the major conclusions obtained from an investigation into the distribution of some trace constituents in the ultrabasic igneous complex of Rhum (Inner Hebrides). The chapters and sections presenting the relevant information are shown in brackets.

6.1. Cumulus phases.

It is shown that the incorporation of trace constituents into cumulus minerals crystallising from a magma in a sub-crustal environment may occur in a non-equilibrium manner. In particular, there exists a variation of uranium concentration in different olivine morphologies although the major elements, Mg, Fe and Si, and minor elements, Ni and Ca remain essentially constant (chapter 4, section 4.3.). In the feldspars, an inverse relationship exists between the uranium and Sr distributions (chapter 4, section 4.5.), and in a function of the crystal morphology.

Using the observed partition coefficients of uranium, growth rates for the various olivine morphologies were calculated (chapter 4, section 4.4., table 4.), and the results appear consistant with those from models involving simple packing of crystals. It is concluded that minerals crystallised by an adcumulus or heteradcumulus growth process, grew at a slower rate and in a more equilibrium, diffusion controlled, manner than those which nucleated and grew directly from the magma (chapter 4, section 4.4.). Olivines displaying a harrisitic morphology grew at a comparatively rapid rate, by an interface controlled mechanism and from a supercooled magma.

In order to interpret these results, a model is proposed incorporating variations in nucleation, supercooling and growth rates for the crystallisation of both the olivine (chapter 4,

section 4.4.) and feldspar (chapter 4, section 4.5.) phases. The distribution of a low-partitioning, slowly-diffusing trace constituent can provide a sensitive indicator to the mechanisms and rates of crystal growth of cumulus phases.

6.2. Intercumulus phases.

The behaviour of uranium in the intercumulus, late-stage crystallisation of the Rhum layered intrusion is controlled largely by its inherent greater stability in the magma. Thus, the proposed four-fold classification based on the concentrations of uranium within mineral groups (chapter 3, section 3.2) shows that minerals containing the lowest uranium contents were the first to crystallise from the Rhum magma, and those containing the highest uranium content, the final minerals to crystallise.

A close association of uranium distribution within areas of hydrothermal alteration is observed. From textural and other arguments (chapter 5, section 5.2. and 5.5.), it is concluded that these areas were of a primary crystallisation genesis, and a mechanism is suggested whereby trapping of intercumulus magma can occur (chapter 5, section 5.2.5.).

Like the cumulus phases, the distribution of uranium provides information regarding both crystal growth rates (chapter 5, section 5.2.3.) and mechanisms (chapter 5, section 5.2.4.).

A geochemical coherance is observed between uranium and manganese (chapter 5, section 5.2.3.); uranium and phosphorus (section 5.3.) and uranium and zirconium (section 5.4.).

A number of unusual geochemical and mineralogical features are seen in the intercumulus phases. The high concentration of MnO and MgO in the ilmenites, and the presence of a uranium-concentration gradient in one ilmenite grain (chapter 5,

section 5.2.3.); a concentric distribution of uranium-enriched silicate inclusions in a chrome spinel crystal (section 5.2.4.); the detection of apatite in all of the thin sections examined (section 5.3.); the presence of zirconolite, or zirkelite, (section 5.4.1.) and baddeyelite (section 5.4.2.) - this being the first record of these minerals from a terrestrial ultrabasic intrusion; and the first recorded appearance of zircon from the Rhum intrusion (section 5.4.3.).

The routine use of a uranium distribution technique highlights many mineralogical features which could otherwise have easily been overlooked using standard petrological microscope techniques.

6.3. Future work.

The results obtained in this study has revealed several avenues of research which could profitably be explored at some future date. These include:-

1) Uranium distribution studies, using Lexan prints (Appendix 1) on experimentally grown crystals from melts enriched in ^{235}U may produce a more quantitative model of disequilibrium partitioning of uranium in basic magmas.

2) A closer study of the oxide phases of the Rhum intrusion is required.

3) The routine use of "microprobe age dating" (Chodos and Albee, 1972) on uranium-enriched Zr-oxides in basic intrusions becomes a strong possibility in the near future. Such an age would correspond to the final consolidation of the intruded magma, and, coupled with dates from other methods, could provide valuable data on rates of heat loss and cooling within specific intrusions.

APPENDIX 1. Lexan plastic prints - conditions for their formation.

The final batch of samples irradiated for fission track analysis at the Atomic Weapons Research Establishment (A.W.R.E.) Aldermaston, produced examples of Lexan plastic prints. This appendix details the reactor conditions prevalent at the time of the production, and assesses the conditions most favourable for their routine formation.

The reactor used was the thermalised part of the VT-1 facility in the Herald reactor at the A.W.R.E. (Aldermaston). A thermal neutron dose of 1.02×10^{17} neutrons. cm^{-2}, and a fast neutron dose of 5.7×10^{14} neutrons. cm^{-2} were recorded for this irradiation.

Four polished thin sections were prepared and packed in a manner similar to that shown in figure 2.13 (chapter 2), using Lexan plastic provided by Professor J.F. Lovering. The sections were tightly wrapped in aluminium foil and placed within a polythene irradiation canister. (The diameter of the thermalised section of VT-1 prevented the use of the constructed nylon canister (figure 2.11, chapter 2), and a polythene irradiation canister supplied by A.W.R.E. personnel was used.) Etching was performed in the routine manner described in section 2.3.3. (chapter 2). After removal from the etching solution and drying, a print of the rock surface on the detector (viz. the Lexan print) was clearly seen even without the aid of a microscope.

The prints were visible in either transmitted or reflected light microscopy, transmitted optics being favoured since fission tracks are more easily seen in this mode. The quality of the prints varied patchily from a clear, precise mirror image of the rock surface (e.g. plate 5.9 (b)), to a fuzzy, indistinct form. This latter feature was most probably the result of

pressure not being evenly applied over the rock surface/detector couple in the initial packing of the samples (for discussion of this see section 2.2.2., chapter 2), and could be overcome by use of an irradiation canister similar in design to those in figures 2.10 and 2.11.

An indication of why Lexan prints were formed in this particular irradiation and not in previous irradiations, can be obtained by examination of relative thermal to fast neutron doses for various irradiations. Both the thermal and fast neutron components were measured for the Lexan print irradiation in the "thermalised" section of VT-1 (table 1). Values obtained from four previous irradiations in the routinely used "non-thermalised" section of J.2 are also shown in table 1 (numbered (1) to (4).

Table 1

	Thermal neutron dose (neutrons.cm^{-2})	Fast neutron dose (neutrons.cm^{-2})	$\frac{\text{Thermal}}{\text{Fast}}$ ratio
Lexan print sample	1.02×10^{17}	5.7×10^{14}	179
(1)	1.21×10^{17}	4.3×10^{15}	28.1
(2)	2.04×10^{17}	7.2×10^{15}	28.3
(3)	2.06×10^{17}	7.68×10^{15}	26.8
(4)	1.05×10^{17}	3.88×10^{15}	27.1
		Average (1) to (4)	27.6

From Table 1 it can be seen that the thermal/fast neutron ratio for the Lexan print samples is approximately a factor of 6.5 higher than for those samples which did not produce prints. A critical factor in the formation of Lexan prints would appear therefore, to be the fast neutron dose (i.e. neutrons possessing energies greater than 0.5 MeV).

As discussed earlier (section 2.2.1, chapter 2), the print of the rock surface imaged on the Lexan plastic detector is considered to be the result of small etch pits produced by alpha-particle and ^{7}Li recoil ions from lithium and boron interactions with thermal neutrons (Kleeman and Lovering, 1970,b; Kleeman, 1973). The different concentrations of these elements in adjacent minerals give rise to variations in the density of alpha-particle (and ^{7}Li ion) pits, hence forming the print fabric within the detector.

Kleeman (1973) was able to catagorise many of the rock-forming minerals into five groups on the basis of their Li and/or B concentrations. These ranged from "very low contrast" (at low Li and/or B contents) to "very high contrast" minerals (at high Li and/or B contents) depending upon the degree of intensity, or contrast, they produced on Lexan plastic prints.

With a large fast neutron component however, several other elements can produce alpha-particles. If their track densities approximate to, or exceed the track densities from Li and B, the Lexan print will become obliterated. In order to test this hypothesis in a semi-quantitative manner, alpha-particle track densities for several elements were calculated using equation (2) (section 2.1.6., chapter 2). These are shown in table 2. (The product $K_{xy}.\alpha_x$ is taken to be 0.3×10^{-4}cm., and q_x equal to 0.25 - see Kleeman, 1973).

Table 2

Element	I* (isotopic abundance)	* millibarns (x 10^{-24})	C++	$(N)_y$ ** (x 10^{20})	expected track density x 10^6 cm. $^{-2}$ ** n_{fast} = (1)	n_{fast} = (2)
$^{16}O(n,\alpha)^{13}C$	.9976	approx 310	449,000	505	848	130
$^{23}Na(n,\alpha)^{20}F$	1.0	220	15,400	12.1	14.3	2.2
$^{27}Al(n,\alpha)^{24}Na$	1.0	120	78,600	52.4	341	52
$^{30}Si(n,\alpha)^{27}Mg$	.0305	45	246,100	148	approx. 1	0.15
$^{31}P(n,\alpha)^{28}Al$	1.0	140	650	0.38	approx 0.3	less than 0.1
$^{39}K(n,\alpha)^{36}Cl$	.9308	85	5,300	2.45	approx. 1	0.15
				TOTALS	1206	185

* Taken from De Soete et al. (1972 values for 14 MeV neutrons.

\+ Assuming density of host phase (i.e. minerals) = 3.0

** Normalised to thermal neutron dose of 2 x 10^{17} neutrons. cm^{-2}.

++ Concentration (p.p.m.) of element from Mason (1966) average diabase.

(1) Fast neutron componant for "non-thermalised" section of J.2 (i.e. for routine irradiations) = 7.24 x 10^{15}

(2) Fast neutron componant for "thermalised" section of J.2 (i.e. Lexan print irradiation) = 1.11 x 10^{15}

A comparison of the sum of the track densities for the two fast neutron doses, with track densities attributed to Li and B for minerals from Kleeman's 1973) five groups (summarised in table 3) can then be made. This shows that for the routine

Table 3 (after Kleeman, 1973)

Group	Minerals present	Track density ($\times 10^6$ cm.$^{-2}$) Thermal neutron dose of 10^{16} neutrons.cm^{-2}	Recalculated to thermal neutron dose of 2×10^{17} neutrons.cm^{-2}
Very low contrast	quartz; ilmenite; spinel; apatite	0.91 - 4.0 average 2.1	18.2 - 80.0 average 41.4
Low contrast	olivine; hornblende; plagioclase; pyroxenes.	4.0 - 12.6 average 8.5	80.0 252 average 170
Medium contrast	plagioclase; pyroxenes; hydrous rim	17 - 45 average 30	340 - 900 average 600
High contrast	pyroxenes; serpentine; garnet; biotite.	70 - 140 average 96	530 - 2400 average 1920
Very high contrast	biotite; micas; "grain boundary"	530 - 2400 average 976	10,600 - 48,000 average 19520

routine irradiations made at Aldermaston, only rocks containing those minerals in the high and very high contrast groups (viz. mica, sepentine, garnet etc.) would be expected to give a Lexan print. In ultrabasic rocks however, minerals of the low and moderate contrast groups (i.e. olivine, plagioclase and clinopyroxene) are present. In order that these rocks produce prints, alpha-particle track densities from reaction with fast

neutrons require to be of the order of 170×10^{6} tracks. cm^{-2}. The approximate calculations in table 2 show therefore, that Lexan prints would be more likely to form in the thermalised section of the reactor.

Thus, for thermal neutron doses of 2×10^{17} thermal neutrons. cm^{-2}, providing that a fast component of less than approximately 1×10^{15} fast neturons. cm^{-2} was attained, most igneous and metamorphic rock sections would be expected to produce Lexan plastic prints.

APPENDIX 2. Strontium in Rhum feldspars - analytical procedure and results.

Plagioclase feldspar was separated from several Rhum (eastern layered series) specimens and analysed by X-ray fluorescence for Sr (Williams, 1971 - unpublished B.Sc. thesis).

Mineral separation was performed on -80 +120 mesh fractions using a Frantz isodynamic magnetic separator and, together with hand-picking, a purity of greater than 99% was achieved. With the aid of a "Spex" model agate ball and container, each sample was powdered (a grinding time of 12½ minutes was used) and made into pellets, duplicated where possible, using the procedure of Norrish and Chappell (1967, pp 204-206). Approximately 2.5 grams of sample were used in making each pellet, this being backed by a layer approximately 5 millimetres thick of high purity boric acid. Application of a pressure of 5 tons per square inch (equivalent to approximately 155 $kg.cm^{-2}$) was found to impart the correct degree of cohesiveness to the pellet.

A Phillips X.R.F. Spectrometer (housed at the Department of Geology and Mineralogy, Oxford) incorporating a molybdenum tube and target and operated at 50 kV and 20 mA was used to determine the concentration of Sr in the plagioclase feldspar samples. The analysing crystal was LiF (110), and the detector a scintillation counter type. Greater than 10,000 counts were accumulated for 40 seconds on both the standard and samples on the Sr K_α line located at 35.70° 2θ. Counts for two background positions were also for 40 seconds and were offset by $1^\circ 20'$ 2θ either side of the peak. The average of the two background counts were subtracted from peak values and the concentration of Sr (in p.p.m.) for the sample were calculated from the equation

below:-

$$(M)_{sample} = \frac{\text{Number of counts for sample}}{\text{Number of counts for standard}} \times (M)_{stand} \times \frac{(A)\ sample}{(A)\ standard}$$

where $(M)_{sample}$ = concentration of Sr in the sample (in p.p.m.).

$(M)_{stand.}$ = concentration of Sr in the standard, AGX (= 181 p.p.m.).

$(A)_{sample}$ = mass absorption coefficient of the sample for the radiation used (= 9.52).

$(A)_{stand.}$ = mass absorption coefficient of the standard for the radiation used (= 7.78).

Table 1

Rock No.	Unit No. (and position in unit)	Height (metres above base of intrusion)	Rock name +	Feldspar morphology **	Sr (p.p.m.)
R.8	1 (top)	15.2	feld.-ol.-cpx.ortho	tab.	507*
R.11	2 (top)	48.8	feld.-ol. ortho.	tab.	417
R.10	3 (base)	51.8	feld.-ol. ortho.	tab.	443
R.39	3 (top)	204.2	feld.-ol.-cpx.ortho.	tab.	503*
R.48	4 (top)	210.3	feld.-ol.-cpx.meso.	tab.	515*
R.42	6 (base)	292.6	ol.heterad.	poik.	496*
R.44	6 (top)	301.7	feld.-ol. heterad.	tab.	375*
R.45	7 (base-mid.)	313.9	ol. heterad.	poik.	415*
R.46	7 (top)	323.1	feld.-ol. heterad.	tab.	315
R.38	8 (base)	326.1	ol.heterad.	poik.	474
R.47	8 (top)	377.9	feld.-ol. heterad.	tab.	492
R.35	10 (base)	441.9	feld.-ol. heterad.	tab.	509
R.34	10 (base-mid.)	454.1	ol. heterad.	poik.	516
R.33	10 (mid.)	469.4	ol.heterad.	poik.	522
R.30	10 (mid.-top)	502.9	feld.- ol. adcum.	tab.	442
R.27	11 (mid.)	539.5	ol. heterad.	poik.	436*
R.18	11 (top)	577.6	feld.-ol. adcum.	tab.	396*
R.19	12 (base)	579.1	ol.heterad.	poik.	488*
R.24	12 (mid.)	600.4	ol.heterad.	poik.	472*

R.20	12 (mid-top)	601.9	feld.-ol. adcum.	tab.	413
R.23	12 (mid-top)	603.5	feld.adcum.	tab.	424
R.12	12 (top)	606.5	ol.heterad.	poik.	443*
R.21	13 (mid.)	640.1	feld.ol. adcum.	tab.	405
R.17	14 (base)	673.6	ol.heterad.	poik.	421*
R.14	14 (top)	731.5	ol.heterad.	poik.	430*
R.15	15 (base)	734.5	ol.-feld.-cpx.adcum.	tab.	431*

+ After Wager and Brown (1968) modified nomenclature (see Table 3.5, chapter 3).

* Analyst, P. Henderson.

** poik. = poikilitic

tab. = tabular

(chapter 4, section 4.5 for discussion).

These results are given in table 1 together with results obtained previously by Dr. P. Henderson. In order that the two sets of results be compatable, several samples were reanalysed, table 2. From these results, it was not considered necessary to nomalise one set of results since an average difference in values of only 2.8% exists.

Table 2

Rock No.	Analysed by P. Henderson Sr (p.p.m.)	mean	Analysed by the author Sr (p.p.m.)	mean
R.18	393.45, 385.84	390	404.53, 404.72	404
R.35	529.90	530	509.05, 508.93	509
R.47	489.54	490	492.90, 496.00	494

BIBLIOGRAPHY

Adams J.A.S., Osmond J.K. and Rogers J.J.W. (1959). The geochemistry of thorium and uranium. In: Rhysics and Chemistry of the Earths (eds. L.H. Ahrens, F. Press, K. Rankama and S.K. Runcorn) vol. 3, pp. 298 - 348.

Albarede F. and Bottinga Y. (1972). Kinetic disequilibrium in trace element partitioning between phenocrysts and host lava. Geochim. Cosmochim. Acta 36; 141 - 156.

Algar R.S. (1965). Radiation effects in polymers. In: Physics and Chemistry of the Organic Solid State (ed. D. Fox). Interscience Publication.

Bailey E.B. (1945). Tertiary igneous tectanics of Rhum (Inner Hebrides). Quart. J. Geol. Soc. Lond. 100 (for 1944); 165 - 191.

Becker K. (1966). Nuclear track registration in dosimeter glasses for neutron dosimetry in mixed radiation fields. Health Phys. 12; 769 - 85.

Becker K. (1968). Nuclear track registration in solids by etching. Biophysik. 5 ; 207 - 22.

Becker K. (1969). Alpha particle registration in plastics and its application for radon and neutron personnal dosimetry. Health Phys. 61 ; 113 - 23.

Benton E.V. (1970). Latent track formation in organic nuclear charged particle detectors. Rad. Effects 2 ; 273 - 80.

Benton E.V. and Henke R.P. (1968). Charged particle tracks in polymers No. 7: Sensitivity enhoncement of Lexan. USNRDL-TR-68-136. U.S. Nav. Rad. Def. Lab., San Francisco, Calif.

Besant C.B. and Ipson S.S. (1970). Measurement of fission ratios in zero power reactors using solid state track recorders. J. Nucl. Energy 24 ; 59 - 69.

Billington D.S. and Crawford J.H. Jr. (1961). Radiation damage in solids. Princetown Univ. Press, 450 pp.

Bohr N. and Wheeler J. (1939). The mechanism of nuclear fusion. Phys. Rev. 56 ; 426 - 50.

Borodin L.S., Bykova A.B., Kapitonova T.A. and Pyatenko Yu. A. (1960). New data on zirconolite and its niobium variety. Dokl. Akad. Nauk. S.S.S.R. 134 : 1022 - 4.

Bowen N.L. (1928, reprinted 1956). The Evolution of the Igneous Rocks. Princetown Univ. Press, 332 pp.

Brett R., Butler P. Jr., Meyer C. Jr. (1971). Apollo 11 igneous rocks 12004, 12008, 12009 and 12002 ; a mineralogical and petrological study. Proc. Second Lunar Sci. Conf. 1 ; 301 - 17. Cambridge, MIT Press.

Brice J.C. (1967). The growth of crystals from the melt. In: Selected Topics in Solid State Physics (Ed.E.P. Wohlbath) vol. 5. North Holland, Amsterdam.

Brinkmann J.A. (1954). Nature of radiation damage in metals. J. Appl. Phys. 25 ; 961 - 70.

Brinkmann J.A. (1959). Fundamentals of fission damage. NAA-SR-4164, U.S. Atomic Energy Commission. 30 pp.

Brother R.N. (1964). Petrofabric analyses of Rhum and Skaergaard layered rocks. Journ. Petr. 5 ; 255 - 74.

Brown G.M. (1956). The layered ultrabasic rocks of Rhum, Inner Hebrides. Phil. Trans. Roy. Soc. Lond. B, 240 ; 1 - 53.

Brown G.M., Emeleus C.H., Holland J.G., Peckett A. and Phillips R. (1972). Mineral chemistry variation in Apollo 14 and Apollo 15 basalts and granitic fractions. Proc. Third Lunar Sci. Conf. 1, 141 - 157. Cambridge MIT Press.

Bruce J. (1975). Rum? Times (London). Readers letters - Monday, July 21st.

Bryan W.D. (1972). Morphology of quench crystals in submarine basalts. J. Geophys. Res. 77 ; 5812 - 9.

Burnett D.S., Monnin M., Seitz M., Walker R., Woolum D. and Yuhas D. (1970). Charged particle track studies in lunar rock 12013. Earth Planet. Sci. Lett. 9 ; 127 - 36.

Burnett D., Monnin M., Seitz M., Walker R. and Yuhas D. (1971). Lunar astrology - U-Th distributions and fission track dating of lunar samples. Proc. Second Lunar Sci. Conf. 2 ; 1503 - 19. Cambridge, MIT Press.

Burton J.A., Prim R.C. and Slichter W.P. (1953). The distribution of solute from crystals grown from the melt. Part 1: Theoretical. J. Chem. Phys. 21 ; 1987 - 91.

Busche F.D., Prinz M., Keil K. and Kurat G. (1974). Lunar zirkelite: A uranium bearing phase. Earth Planet. Sci. Lett. 14 ; 313 - 321.

Cahn J.W. (1960). Theory of crystal growth and interface motion in crystalline materials. Acta Met. 8 ; 554-62.

Cahn J.W., Hillig W.B. and Sears G.W. (1964). The molecular mechanism of crystallisation. Acta Met. 12 ; 1421 - 39.

Campbell I.M. (1968). The origin of heteradcumulate and adcumulate textures in the Jimberlana norite. Geol. Mag. 105 ; 378 - 385.

Carpenter B.S. (1972). Determination of trace concentrations of boron and aluminium in glass by the nuclear track technique. Anal. Chem. 44 ; 600 - 2.

Carpenter B.S., Samual D. and Wasserman I (1973. Quantitative applications of ^{17}O tracer. Rad. Effects 19 ; 59.

Chadderton L.T. and Torrens I. McC. (1969). Fission damage in crystals. Methuen and Co. Ltd., 265 pp.

Challinor J. (1973). A dictionary of geology. Fourth edition. Univ. of Wales Press, Cardiff.

Cherdyntsev V.V. (1971). Uranium - 234. Publishers - Israel Program for Scientific Translations.

Chodos A.A., and Albee A.L. (1972). Automated microprobe analysis and applications to analysis of exotic lunar phases. In: Proc. Sixth Int. Conf. on X-ray Optics and Microanalysis (eds. G. Shinoda, K. Kohra and T. Ichinokawa). pp. 779 - 84.

Christian J.W. (1965). The theory of transformations in metals and alloys. Pergamon Press. 589 pp.

Condie K.C., Kuo C.S., Walker R.M. and Murphy V.R., (1969). Uranium distributions in separated clinopyroxenes from four eclogites. Science 165 ; 57 - 9.

Cross W.G., and Tommasino L. (1967). Detection of low energy doses of fast neutrons with fission track detectors. Health Phys. 13 ; 932.

Cross W.G. and Tommasino L. (1969). A rapid reading technique for nuclear particle damage tracks in thin foils. In: Proc. of the Int. Top. Conf. on Nuclear Track Registration in Solids. Clement-Ferrand, France, May 1969). Vol. 3; 73-84.

Czamanske G.K. and Milralik P. (1972). Oxidation during magmatic differentiation, Finnmarka Complex, Oslo area, Norway: Part 1, the opaque oxides. Journ. Petr. 13 ; 493 - 509.

De Soete D., Gibjels R. and Hoste J. (1972). Neutron Activation analysis. In: Chemical Analysis. A series of monographs on analytical chemistry and its applications (eds. P.J. Elving and I.M. Kolthoff) vol. 34. Wiley - Interscience, London.

Deer W.A., Howie R.A., and Zussman J. (1971). An introduction to the rock-forming minerals. Second edition. Longman.

Donaldson C.H. (1974). Olivine crystal types in harrisitic rocks of the Rhum pluton and in Archean spinifex rocks. Geol. Soc. Amer. Bull. 85 ; 1721 - 6.

Donaldson C.H. (1975). Calculated diffusion coefficients and the growth rate of olivine in a basalt magma. Lithos 8 ; 163 - 74.

Donaldson C.H., Drever H.I. and Johnston R. (1973). Crystallisation of a poikilo-macro-spherulitic feldspar in a Rhum peridotite. Nature (Phys. Sci.) 243 ; 69 - 70.

Dooley J.R. Jr., Taylor R.B. and Jurceka F.J. (1970). Dual microscope comparator for fission track studies. Rev. Sci. Instrum. 41 ; 887 - 8.

Dowty E., Keil K. and Prinz M. (1974). Lunar pyroxene-phyric basalts ; crystallisation under supercooled conditions. Journ. Petr. 15 ; 419 - 53.

Drever H.I. and Johnston R. (1957). Crystal growth of forsteritic olivine in magmas and melts. Trans. Roy. Soc. Edinb. 58 ; 289 - 315.

Drever H.I. and Johnston R. (1967). Picritic minor intrusions. In: Ultramafic and Related Rocks (ed. P.J. Wyllie). John Wiley and Sons, New York.

Drever H.I. and Johnston R. (1972). Metastable growth patterns in some terrestrial and lunar rocks. Meteoritics 7 ; 327 - 40.

Duncan A.R., Erlank A.J., Willis J.P., Sher M.K. and Ahren L.H. (1974). Trace element evidence for a two-stage origin of some titaniferous mare basalts. Proc. Fifth Lunar Sci. Conf. 2 ; 1147 - 57. New York, Pergamon Press.

Elsdon R. (1971). Crystallisation history of the Upper Layered Series, Kap Edvard Holm, east Greenland. Journ. Petr. 12; 499 - 521.

Elsdon R. (1972) Iron-titanium oxide minerals in the Upper Layered Series, Kap Edvard Holm, east Greenland. Mineral. Mag. 38; 946 - 956.

Fisher D.E. (1970). Homogenised fission track analysis of U in some ultramafic rocks of known K content. Geochim. Cosmochim. Acta 34 ; 630 - 4.

Fisher D.E. (1975). Geoanalytical applications of particle tracks. Earth - Sci. Rev. 11 ; 291 - 336.

Flanagan F.J. (1973). 1972 values for international geochemical reference samples. Geochim. Cosmochim. Acta 37 ; 1189 - 1200.

Fleischer R.L. (1966). Uranium micromaps : Techniques for in situ mapping of distributions of fissionable impurities. Rev. Sci. Instrum. 37 ; 1738 - 9.

Fleischer R.L. (1968). Uranium distribution in stone meteorites by the fission track technique. Geochim. Cosmochim. Acta 32 ; 989 -98.

Fleischer R.L. and Hart H.R. Jr. (1970). Fission track dating : Techniques and Problems. In: Proc. of the Burg Wartenstein Conf. on Calibration of Hominoid Evolution (Eds. W.W. Bishop, J.A. Miller, and S. Cole). Scottish Academic Press, Edinburgh.

Fleischer R.L. and Price P.B. (1964). Glass dating by fission fragment tracks. J. Geophys. Res. 69 ; 331 - 9.

Fleischer R.L., Price P.B. and Walker R.M. (1964). Track registration in various solid state nuclear track detectors. Phys. Rev. 133 ; 1443 - 9.

Fleischer R.L., Price P.B. and Walker R.M. (1965, a). Ion explosion spike mechanism for formation of charged particle tracks in solids. J. Appl. Phys. 36 ; 3645 - 52.

Fleischer R.L., Price P.B. and Walker R.M. (1965, b). Fossil particle tracks and uranium distributions in minerals of the Vaca Muerta meteorite. Science 148 ; 629 - 32.

Fleischer R.L., Price P.B. and Walker R.M. (1965, c). Solid state track detectors : Applications to nuclear science and geophysics. Ann. Rev. Nucl. Sci. 15 ; 1 - 28.

Fleischer R.L., Price P.B. and Walker R.M. (1967). Criterian for registration in dielectric track detectors. Phys Rev. 156 ; 353 - 5.

Fleischer R.L., Price P.B. and Woods R.T. (1969). Nuclear tracks in solids. Sci. Amer. 220 ; 30 - 9.

Frank A.L. and Benton E.V. (1969). Int. Top. Conf. on Nuclear Track Registration in Insulating Solids and Applications, Clermont-Ferrand, May 1969.

Frank A.L. and Benton E.V. (1970). Dielectric plastics as high exposure gamma-ray detectors. Rad. Effects 2 ; 269 - 272.

Frey A.F. and Green D.H. (1974). The mineralogy, geochemistry and origin of lherzolite inclusions in Victorian basanites. Geochim. Cosmochim. Acta 38 ; 1023 - 59.

Gale N.H. (1967). Development of delayed neutron technique as a rapid and precise method for determination of uranium and thorium at trace levels in rocks and minerals, with applications

to isotope geochronology. In ; Radioactive Dating and Methods of Low-level counting. International Atomic Energy Agency, Vienna. No. SM-87/37.

Gibb F.G.F. (1976). Ultrabasic rocks of Rhum and Skye: the nature of the parent magma. J. Geol. Soc. 132 ; 209 - 222.

Gijbels etal. (1974) see Addenda p. 329

Green D.H., Morgan J.W. and Heier K.S. (1968). Thorium, uranium and potassium abundances in peridotite inclusions and their hosts. Earth Planet. Sci. Lett. 4 ; 155 - 66.

Greenland L.P. (1970). An equation for trace element distribution during magmatic crystallisation. Amer. Min. 55 ; 455 - 65.

Hagland D.S. (1972). Uranium : Element and Geochemistry. In; The Encyclopedia of Geochemistry and Environmental Studies (ed. R.W. Fairbridge). Encylopedia of Earth Sciences Series, vol. 4A, pp. 1215 - 22.

Haines E.L. (1972). Precise coordinate control in fission track uranium mapping. Nucl. Instrum. Methods 98 ; 183 - 4.

Haines E.L. and Zartmann R.E. (1973). Uranium concentrations and distributions in six peridotite inclusions of probably mantle origin. Earth Planet. Sci. Lett. 20 ; 45 - 53.

Haines E.L., Albee A.L., Chodos A.A. and Wasserburg G.J. (1971). Uranium bearing minerals of lunar rock 12013. Earth Planet. Sci. Lett. 12 ; 145 - 54.

Hair M.W., Kaufhold J., Maurette M. and Walker R.M. (1971). Thorium microanalysis using fission tracks. Rad. Effects 7 ; 285 - 7.

Hamilton E.I. (1971). New technique for determining the concentration and distribution of lead in materials. Nature 231 ; 524.

Harker A. (1908). The geology of the Small Isles of Inverness-shire (sheet 60). Mem. Geol. Surv. Scotland.

Hart S.R. and Brooks C. (1974). Clinopyroxene-matrix partitioning of K, Rb, Cs, Sr and Ba. Geochim. Cosmochim. Acta 38 ; 1799 - 1806.

Henderson P. (1968). The distribution of phosphorus in the early and middle stages of fractionation of some basic layered intrusions. Geochim. Cosmochim. Acta 32 ; 897 - 911.

Henderson P. (1970). The significance of the mesostasis of basic layered igneous rocks. Journ. Petr. 11 ; 463 - 73.

Henderson P. (1975). Geochemical indicator of the efficiency of fractionation of the Skaergaard intrusion, East Greenland. Mineral. Mag. 40 ; 285 - 91.

Henderson P. and Suddaby P. (1971). The nature and origin of the chrome-spinel of the Rhum layered intrusion. Contrib. Mineral. Petrol. 33 ; 21 - 31.

Henderson P., Mackinnon A. and Gale N.H. (1971). The distribution of uranium in some basic igneous cumulates and its petrological significance. Geochim. Cosmochim. Acta 35 ; 917 - 25.

Hess H.H. (1939). Extreme fractional crystallisation of a basaltic magma ; The Stillwater Igneous Complex. Trans. Amer. Geophys. Union. Part 3, pp. 430 - 2.

Hess H.H. (1960). Stillwater Igneous Complex, Montana. Geol. Soc. Amer. Mem. no. 80.

Hilling W.B. and Turnbull D. (1956). Theory of crystal growth in undercooled pure liquids. J. Chem. Phys. 24; 914 - 21.

Horvay G. and Cahn J.W. (1961). Dendritic and spheriodal growth. Acta Met. 9 ; 695 - 705.

Hurford A.J. (1972). A manual of laboratory techniques for fission track dating. Fitch-Miller Rock Dating Group, Report No. FMK/786. Birkbeck College, London.

Irvine T.N. (1975). Crystallisation sequences in the Muskox intrusion and other layered intrusions - 2. Origin of chromitite layers and similar deposits of other magmatic ores. Geochim. Cosmochim. Acta 29 ; 991 - 1020.

Jackson E.D. (1961). Primary textures and mineral associations in the ultramafic zone of the Stillwater complex, Montana. U.S. Geol. Surv. Prof. Paper 358 ; 106 pp.

Jackson E.D. (1966). Liquid immiscibility as one factor of chromitite seam formations. Econ. Geol. 61 ; 778 - 80.

Judd J.W. (1874). The secondary rock of Scotland. Second Paper. Quart. J. Geol. Soc. Lond. 30 ; 220 - 301.

Judd J.W. (1885). On the Tertiary and older peridotites of Scotland. Quart. J. Geol. Soc. Lond. 41 ; 354 - 418.

Kaaden G. v.d., Ottemann J. and Sahoo R.K. (1972). Chromite verschiedener Zusammensetzung und Genese aus einem Dunit von Saruabil, Sukinda, Orissa (Indien). Neues Jahrib. Miner. Mh. 6 ; 256 - 62.

Khan H.A. (1973). An important precaution in the etching of solid

Henderson P. (1975,b) See Addenda p329

Hess P.C. (1971) See Addenda p.329.

state nuclear track detectors. Nucl. Instr. Methods 109 ; 515 - 9.

Katcoff S. (1960). Fission product yields from neutron-induced fission. Nucleonics 18 ; 201 - 8.

Katz R. and Kobetich E.J. (1968). Formation of etchable tracks in dielectrics. Phys. Rev. 170 ; 401 - 5.

Katz R. and Kobetich E.J. (1970). Formation of particle tracks. Rad. Effects 3 ; 169 - 74.

Keil K. and Fricker P.E. (1974). Baddeyelite (ZrO_2) in gabbroic rocks from Axel Heiberg Island, Canadian Arctic Archipelago. Am. Mineral. 59 ; 249 - 53.

Kieth H.D. and Padden F.J. Jr. (1963). A phenomenological theory of spherulitic crystallisation. J. Appl. Phys. 34 ; 2409 - 21.

Kirkpatrick J.R. (1974). Kinetics of crystal growth in the system $CaMgSi_2O_6$ - $CaAl_2SiO_6$. Am. J. Sci. 274 ; 215 - 42.

Kirsten T. and Horn P. (1974). ^{39}Ar - ^{40}Ar chronology of the Taurus - Littrow region II : A 4.28 b.y. old troctolite and ages of basalts and highland breccias (abstract). Lunar Science - 5 ; 419 - 21. The Lunar Science Institution, Houston.

Kleeman J.D. (1973). The role of lithium and boron in forming Lexan plastic prints. Geochim. Cosmochim Acta 37 ; 1321 - 6.

Kleeman J.D. and Lovering J.F. (1967, a). Uranium distribution in rocks by fission track registration in Lexan plastic. Science 156 ; 512 - 3.

Kleeman J.D. and Lovering J.F. (1967, b). Uranium distribution studies by fission track registration in Lexan plastic prints. At. Energy in Australia 10 ; 3 - 8.

Kleeman J.D. and Lovering J.F. (1970). The evaluation of the spatial parameters K and α in equations for fission track uranium analysis. Rad. Effects 5 ; 233 - 7.

Kleeman J.D. and Lovering J.F. (1970, b). Lexan plastic prints: How are they formed? Rad. Effects 5 ; 21 - 6.

Kleeman J.D., Green D.H. and Lovering J.F. (1969). Uranium distribution in ultramafic inclusions from Victorian basalts. Earth Planet. Sci. Lett. 5 ; 449 - 58.

Le Bas M.J. (1960). The petrology of the layered basic rocks of the Carlingford complex, Co. Louth. Trans. Roy. Soc. Edinb. 64 ; 169 - 200.

Lewis J.D. (1971). "Spinifex texture" in a slag, as evidence for its origin in rocks. Geol. Surv. W. Aust. Ann. Rpt. ; 45 - 9.

Lofgren G. (1974). An experimental study of plagioclase crystal morphology ; isothermal crystallisation. Am. J. Sci. 274 ; 243 - 73.

Lovering J.F. and Kleeman J.D. (1970). Fission track uranium distribution studies on Apollo 11 lunar samples. Proc. Apollo 11 Lunar Sci. Conf. 1 ; 627 - 31. New York, Pergamon Press.

Lovering J.F. and Kleeman J.D. (1972). A determination of the decay constant for spontaneous fission of natural uranium using fission track accumulation. Geochim. Cosmochim. Acta 35 ; 637 - 46.

Lovering J.F. and Wark D.A. (1971). Uranium enriched phases in Apollo 11 and Apollo 12 basaltic rocks. Proc. Second Lunar Sci. Conf. 1 ; 151 - 8. Cambridge, MIT Press.

Lovering J.F. and Wark D.A. (1974). Rare-earth element fractionation in phases crystallising from late-stage magmatic liquid (abstract). In : Lunar Science - 5 ; 463 - 5. The Lunar Science Institution, Houston.

Lovering J.F. and Widdowson J.R. (1968). The petrological environment of magnesium ilmenites. Earth Planet. Sci. Lett. 4 ; 310 - 4.

Lovering J.F., Wark D.A., Gleadow A.J.W. and Sewell D.K.B. (1972). Uranium and potassium fractionation in pre-Imbrian lunar crustal rocks. Proc. Third Lunar Sci. Conf. 1 ; 281 - 94. Cambridge, MIT Press.

Lovering J.F., Wark D.A., Reid A.F., Ware N.G., Keil K., Prinz M., Bunch T.E., El Goresy A., Ramdhor P., Brown G.M., Peckett A., Phillips R., Cameron E.N., Douglas J.A.V., and Plant A.G., (1971). Tranquillityte : A new silicate mineral from Apollo 11 and Apollo 12 basaltic rocks. Proc. Second Lunar Sci. Conf. 1 ; 39 - 45. Cambridge, MIT Press.

Mason B. (1966). Principles of Geochemistry (3rd. edition). John Wiley and Sons, London, 329 pp.

Mason P.K., Frost M.T. and Reed S.J.B. (1968). National Physical Laboratory, Report No. IMS 1.

Matousek J.H. (1970). Diffusion in molten sodium oxide-silica glasses. Silikaty 4 ; 333 - 43.

Matsumara G. (1969). Sintering of iron wires with a liquid phase. Int. J. Powder Metal. 5 ; 55 - 61.

McDonald J.A. (1965). Liquid immiscibility as one factor in chromitite seam formation in the Bushveld Igneous Complex. Econ. Geol. 60 ; 1674 - 85.

McIntire W.L. (1963). Trace element partition coefficients - A review of theory and applications to geology. Geochim. Cosmochim. Acta 27 ; 1209 - 64.

Medford G.A. (1973). Calcium diffusion in a mugearite melt. Can. J. Earth Sci. 10 ; 394 - 402.

Meyer H.O.A. and Boctor N.Z. (1974). Opaque mineralogy : Apollo 17, rock 75035. Proc. Fifth Lunar Sci. Conf. 1 ; 707 - 16. New York, Pergamon Press.

Misner D.J. (1972). Cationic diffusion in Fe - Mg olivines at elevated pressure and temperature. Am. Geophys. Union Trans. 53 ; 541.

Mitchell R.H. (1973). Magnesium ilmenite and its role in kimberlite petrogenesis. J. Geol. 81 ; 301 - 31.

Moeller T. (1963). The chemistry of the lanthanides. Chapman and Hall, London. 117 pp.

Mory J., De Guillebon D. and Delsarte G. (1970). Mesure du parcours moyen des fragments de fission avec le mica comme detecteur - influence de la texture cristalline. Rad. Effects 5 ; 37 - 40.

Mullin J.W. (1972). Crystallisation. (Second Edition). Butterworths, London.

Nagasawa H. and Wakita H. (1968). Partitioning of uranium and thorium between augite and host lavas. Geochim. Cosmochim. Acta. 32 ; 917 - 21.

Nagpal M.K., Nagpal K.K. and Melita P.P. (1973). Uranium contents in minerals by the fission track method. Pure and Appl. Geophys. 102 ; 153 - 60.

Nesbitt R.W. (1971). Skeletal crystal forms in the ultramafic rocks of the Yilgarn Block, W. Australia: Evidence for an Archean ultramafic liquid. Spec. Paper Geol. Soc. Aust. 3 ; 331 - 347.

Norrish K. and Chappell B.W. (1967). X-ray fluorescence spectrography. In : Physical Methods in Determinative Mineralogy (ed. J. Zussman) pp. 161 - 214. Academic Press, London 514 pp.

Paretzke H.G. , Gruhn T.A. and Benton E.V. (1973). The etching of polycarbonate charged particle detectors by aqueous sodium hydroxide. Nucl. Instr. Methods 107 ; 596 - 600.

Phillips F.C. (1938). Mineral orientation in some olivine-rich rocks from Rum and Skye. Geol. Mag. 65 ; 130 - 5.

Price P.B. and Walker R.M. (1962). Chemical etching of charged particle tracks in solids. J. Appl. Phys. 33 ; 3407 - 12.

Price P.B., Fleischer R.L., Peterson D.D., O'Ceallaigh C., O'Sullivan D. and Thompson A. (1968). High resolution study of low-energy heavy cosmic rays with Lexan track detectors. Phys. Rev. Letters 21 ; 630 - 3.

Price P.B., Peterson D.D., Fleischer R.L., O'Ceallaigh C., O'Sullivan D. and Thompson A. (1969). Composition of cosmic rays of atomic number 12 to 30. Acta Phy. Acad. Sci. Hung. 29 ; Suppl. 1 ; 417 - 22.

Raleigh C.B. (1967). Mechanisms of plastic deformation of olivine. J. Geophys. Res. 73 ; 5391 - 5406.

Ramdohr P. and El Goresy A. (1970). Opaque minerals of the lunar rocks and dust from Mare Tranquillitatis. Science 167 ; 652 - 4.

Rice C.M. and Bowie S.H.U. (1971). Distribution of uranium in Apollo 11 rock 10017. Proc. Second Lunar Sci. Conf. 1 ; 159 - 66. Cambridge, MIT Press.

Robins B. (1972). Crescumulate layering in a gabbroic body on Seiland, northern Norway. Geol. Mag. 109 ; 533 - 41.

Rogers J.J.W. and Adam J.A.S. (1969). Geochemistry of Uranium ; In Handbook of Geochemistry (ed. K.M. Wedepohl) vol. 2. Springer.

Rutter J.W. and Chalmers B. (1953). A prismatic substructure formed during solidification of metals. Canad. J. Phys. 31 ; 15 - 19.

Saito T. and Maruya K. (1958). Diffusion of calcium in liquid slags. Sci. Repts. Res. Inst. Tohoku Univ. 10 ; 306 - 14.

Saratovkin D.D. (1959). Dendritic Crystallisation. Consultant Bureau, New York.

Schreurs J.W.H., Friedman A.M., Rokop D.J., Hair M.W. and Walker R.M. (1971). Calibrated U-Th glasses for neutron

dosimetry and determination of uranium and thorium concentrations by the fission track method. Rad. Effects 7 ; 231 - 3.

Schulz W.W. (1968). Track density measurement in dielectric track detectors with scattered light. Rev. Sci. Instr. 39 ; 1893 - 6.

Seitz M.G. (1972). Spallation recoil tracks in meteoritic whitlockite. Carn. Inst. Wash. Yearb. 71 ; 294 - 9.

Seitz M.G. (1973, a). Uranium and thorium partitioning in diopside-melt and whitlockite-melt systems. Carn. Inst. Wash. Yearb. 72 ; 581 - 6.

Seitz M.G. (1973, b). Uranium and thorium diffusion in diopside and fluorapatite. Carn. Inst. Wash. Yearb. 72 ; 586 - 8.

Seitz M.G. (1974, a). Fractionation of a rare earth element between diopside and a basalt melt at 20 kbar pressure. Carn. Inst. Wash. Yearb. 73 ; 547 - 551.

Seitz M.G. (1974, b). Promotion of kinetic disequilibrium in trace thorium. Carn. Inst. Wash. Yearb. 73 ; 551 - 3.

Seitz M.G. and Hart S.R. (1973). Uranium and boron distributions in some oceanic ultramafic rocks. Earth Planet. Sci. Lett. 21 ; 97 - 107.

Seitz M.G. and Shimizu N. (1972). Partitioning of uranium in the dipside - albite - anorthite system and a spinel lherzolite system by fission track mapping. Carn. Inst. Wash. Yearb. 71 ; 548 - 53.

Seitz. M.G., Wittels M.C., Maurette M. and Walker R.M. (1970). Accelerator irradiations of minerals : Implications for track formation mechanisms and for studies of lunar and meteoritic materials. Rad. Effects 5 ; 143 - 8.

Seitz M.G., Walker R.M. and Carpenter B.S. (1973). Improved methods for measurement of thermal neutron dose by the fission track technique. J. Appl. Phys. 44 ; 510 - 2.

Silk E.C.H. and Barnes R.S. (1959). Examination of fission fragment tracks with an electron microscope. Phil. Mag. 4 ; 970 - 1.

Silver L.T. (1963). The use of co-genetic uranium-lead isotope systems in zircon in geochronology. In : Radioactivity Dating. I.A.E.A. Vienna ; pp. 279 - 287.

Sinha R.C. and Sastri J.C.V. (1969). Behaviour of trace elements in the differentiated Rajmahal basalts, Santhal Paraganas, Bihar. Indian Min. 10 ; 245 - 51.

Strickland-Constable R.F. (1968). Kinetics and Mechanisms of Crystallisation. Academic Press.

Su Ching-Shen (1972) see Addenda, p.329

Szabo B.J., Dooley J.R. Jr. and Taylor R.B. (1970). Distribution of uranium in uranium-series dated fossle shells and bones shown by fission tracks. U.S. Geol. Surv. Prof. Paper 700B ; 90 - 2.

Tammon G. (1925). Glasses as supercooled liquids. J. Soc. Glass Techn. 9 ; 166 - 85.

Thiel K., Herr W. and Becker J. (1972). Uranium distribution in basalt fragments of five lunar samples. Earth Planet. Sci. Lett. 16 ; 31 - 44.

Tiller W.A. (1970). The use of phase diagrams in solidification. In : Phase Diagrams, Material Science and Technology (ed. A.M. Alper), vol. 1; 199 - 244. Academic Press.

Tilley C.E. (1944). A note on the gneisses of Rhum. Geol. Mag. 71 ; 129 - 31.

Tomkeieff S.I. (1942). The tertiary lavas of Rum. Geol. Mag. 69 ; 1 - 13.

Turnbull D. and Fisher J.C. (1949). Rate of nucleation in condensed systems. J. Chem. Phys. 17 ; 71 - 3.

Uhlmann J. (1972). In: Advances in Nucleation and Crystallisation in glasses (eds. L.L. Hench and S.W. Frieman). Am. Ceram. Soc. Spec. Paper 5 ; 91 - 115.

Volmer M. and Marder M. (1931). Theory of linear velocity of crystallisation of undercooled solid modiciation. Seit. Phys. Chem. 154 A ; 97 - 112.

Wadsworth W.J. (1961) The ultrabasic rocks of southwest Rhum. Phil. Trans. Roy. Soc. Lond. Ser. B. 244 ; 21 - 64.

Wager L.R. (1963). The mechanism of adcumulus growth in the layered series of the Skaergaard intrusion. Min. Soc. Amer. Spec. Paper 1 ; 1 - 9.

Wager L.R. and Deer W.A. (1939). Geological investigations in East Greenland, Part 3. The petrology of the Skaergaard intrusion, Kangerdlugssuag, East Greenland. Medd. Om. Grønland, 105, No. 4 ; 1 - 352.

Wager L.R. and Brown G.M. (1968). Layered Igneous Rocks. Oliver and Boyd, Edinburgh.

Wager L.R., Brown G.M. and Wadsworth W.J. (1960). Types of igneous cumulates. Journ. Petr. 1 ; 73 - 85.

Wark D.A., Reid A., Lovering J.F. and El Goresy A. (1973). Zirconolite verses zirkelite in lunar rocks (abstract).

IN: Lunar Science - 4 ; 764 - 6. The Lunar Sci. Inst., Houston.

Whittaker E.J.W. (1967). Factors affecting element ratios in the crystallisation of minerals. Geochim. Cosmochim. Acta 31 ; 2275 - 88.

Whittaker E.J.W. and Muntus R. (1970). Ionic radii for use in geochemistry. Geochim. Cosmochim. Acta 34 ; 945 - 56.

Wilkins R.W.T. (1971). U - O bond lengths and force constants in some uranyl minerals. Zeit. Krist. 134 ; 285 - 90.

Williams C.T. (1971). Unpublished B.Sc. Thesis. Chelsea College, Univ. of London.

Woodruff D.P. (1973) . The Solid-Liquid Interface. Cambridge Univ. Press, 182 pp.

Wyllie P.J. and Drever H.I. (1963). The petrology of picritic rocks in minor intrusions : A picritic sill on the island of Soay (Hebrides). Trans. Roy. Soc. Edinb. 65 ; 155 - 76.

ADDENDA

Gijbels, R.H., Millard Jr. H.T., Desborough, G.A. and Bartel, A.J. (1974). Osmium, ruthenium, iridium and uranium in silicates and chromite from the eastern Bushveld Complex, South Africa. Geochim. Cosmochim.Acta, 38; 319-337.

Hess, P.C. (1971). Polymer model of silicate melts. Geochim.Cosmochim. Acta, 35; 289-306.

Henderson, P. (1975,b). Reaction trends shown by chrome-spinels of the Rhum layered intrusion. Geochim.Cosmochim.Acta, 39; 1035-1044.

Su Ching-Shen (1972). The determination of uranium concentrations in seaweeds by nuclear track detectors. Rad.Effects, 14; 109-112.

Acknowledgements

I owe a debt of gratitude to many people for their assistance in the completion of this thesis. In particular, I wish to thank the following:

Dr. P. Henderson (Chelsea College, University of London) for initially suggesting the topic, and for continuous encouragement and supervision. I have also benefitted greatly from many fruitful discussions held with Dr. Henderson.

Staff, technicians and fellow research students in the Geology Department, Chelsea College for providing an atmosphere conducive for both stimulating scientific research and entertaining social activities.

Mr. S. Coe (Chelsea College) for help in the photographic work, and Mr. K. Richardson (Chelsea College) for assistance in design and construction of the irradiation canisters.

Mr. M. Wineburg (Chelsea College) for help in use of the Scanning Electron Microscope.

Mr. P. Suddaby (Imperial College, London) for making available the microprobe facilities.

Mr. A. Hurford (Birkbeck College, London) for use of the Quantimet Image Analyser.

Staff and personnel at the University of London Reactor Centre and Mr. P. Roscoe at the Atomic Weapons Research Establishment for assistance in the irradiations.

Mr. J. Cuff (Trinity College, Dublin) for producing the final photographic plates.

The Nature Conservancy for permission to visit and collect samples from Rhum, Inner Hebrides.

The Natural Environment Research Council for providing financial assistance in the form of a Research Studentship Grant.

And to my wife, Patricia for her unceasing patience and moral support during the latter stages of this thesis, and for the final, accurate typing.